

On the Wake of an Inclined Circular Cylinder

vorgelegt von
Dipl.-Ing. Lutz Taubert
aus Tucson, USA

von der Fakultät V
– Verkehrs- und Maschinensysteme
der Technischen Universität Berlin
zur Erlangung des akademischen Grades

Doktor der Ingenieurwissenschaften
- Dr.-Ing. -

genehmigte Dissertation

Promotionsausschuss:

Vorsitzender: Prof. Dr.-Ing. J. Thorbeck
Berichter: Prof. Dr.-Ing. C.O. Paschereit
Berichter: Prof. Dr. I.J. Wygnansky

Tag der wissenschaftlichen Aussprache: 16. Oktober 2009

Berlin 2010

D 83

On the Wake of an Inclined Circular Cylinder

presented by
Dipl.-Ing. Lutz Taubert
from Tucson, USA

by the School V
– Mechanical Engineering and Transport Systems
of the Technical University of Berlin
for the awarding of the academic title

Doctor of Engineering Sciences
- Dr.-Ing. -

approved dissertation

Doctoral committee:

Chairman: Prof. Dr.-Ing. J. Thorbeck

Evaluator: Prof. Dr.-Ing. C.O. Paschereit

Evaluator: Prof. Dr. I.J. Wygnansky

Date of the scientific defense: 16. October 2009

Berlin 2010

D 83

Thanks a lot

to

Prof. Wygnanski, for keeping me pretty busy with a whole lot of great ideas,
Prof. Paschereit, for taking the burden helping to finish this work,
my wife Jenny & my family, for the never-ending support,
the members of the AeroLab, for numerous fruitful discussions,
the HFI-Crew, for giving advice and helping with many details,
and last but not least Prof. Fiedler, for introducing me to
the fascinating world of Fluid Mechanics.

Kurzfassung

Diese Arbeit begann mit einer Machbarkeitsstudie über die potentielle Nutzung aktiver Strömungskontrolle für die Lagekontrolle eines Tankrüssels für die Luftbetankung, der vereinfachend als angestellter Kreiszyylinder betrachtet werden kann. Die Vorversuche an einem einfachen Modell wurden sehr erfolgreich abgeschlossen.

Daran anschließend wurde eine grundlegende Untersuchung der Umströmung eines unendlichen angestellten Kreiszyinders mit aktiver Strömungskontrolle durchgeführt. Druckverteilungen um den Zylinder und im fernen Nachlauf wurden zur Bestimmung der auf den Zylinder wirkenden Kräfte aufgenommen, der Schwerpunkt dieser Arbeit lag allerdings auf den kohärenten Strukturen im nahen Nachlauf. Die Analyse dieser Strukturen ermöglichte ein tieferes Verständnis der Wirbeldynamik in dieser komplexen dreidimensionalen Strömung.

Die Anwendung von asymmetrischer periodischer zero-mass-flux Anregung durch einen einzelnen Schlitz entlang des Zylinders erzeugte deutlichen Auftrieb, die Anregung über zwei symmetrisch auf dem Umfang angeordnete Schlitze reduzierte den Formwiderstand merklich. Auftrieb und Widerstand konnten durch Anregung mit unterschiedlicher Stärke auf beiden Seiten des Zylinders unabhängig voneinander variiert werden. Dies beweist, dass die Kontrolle eines Tankrüssels mittels aktiver Strömungskontrolle möglich wäre und dadurch der Einsatz von hervorstehenden und deshalb leicht zu beschädigenden Kontrollflächen vermieden werden könnte.

Die im Laufe dieser Arbeit entwickelte POD-basierte dynamische Analyse des Strömungsfeldes im nahen Nachlauf enthüllte die Komplexität der kohärenten Strukturen und ihrer Dynamik nahe des Zylinders. Deutliche Fluktuationen der Positionen der kohärenten Strukturen konnten sowohl in radialer als auch in Umfangsrichtung nachgewiesen werden.

Diese Fluktuationen wurden bei grösserer Anregungsstärke unterdrückt und damit die auf den Zylinder wirkenden Wechselbelastungen deutlich reduziert. Da angestellte runde Zylinder in vielen technischen Anwendungen vorkommen, könnte sich die so mögliche aktive Dämpfung strömungsinduzierter Schwingungen als sehr nützlich für die Reduzierung des Risikos von Strukturversagen durch Ermüdung erweisen.

Abstract

This work evolved from a feasibility study targeted at a specific application: the control of a refuelling boom. Presently, the attitude of the refuelling boom on tanker airplanes, basically a finite cylinder with pitch and yaw, is adjusted by means of control surfaces extending from the boom. These control surfaces are bulky and very sensitive to damage by unintended contact with the tanker itself or the refuelling airplanes.

Preliminary experiments were carried out on a relative simple model to evaluate the potential to alternatively control the attitude of the refuelling boom by altering lift and drag of this finite inclined cylinder by means of active flow control. The results were very promising.

Based on these findings, a detailed investigation was carried out to improve the understanding of the general problem of the flow past an inclined cylinder, in particular with application of active flow control. The forces on the cylinder were determined by pressure measurements on the surface and in the far wake to obtain easily comparable quantitative results. To gain a better insight into the vortex dynamics in this complex three-dimensional flow, focus was put on the coherent structures in the near wake of an infinite inclined cylinder and their interaction with it.

Substantial lift was generated by applying periodic zero-mass-flux excitation asymmetrically from a single slot running along the span of the cylinder. Excitation from two slots located symmetrically on the circumference of the cylinder reduced the form drag significantly. Lift and drag were altered independently of each other by adjusting the level of excitation differently on both sides of the cylinder. This proves that the full control of a refuelling boom by active flow control is possible, eliminating the necessity of protruding control surfaces that are easily damaged.

A POD based technique was developed for the dynamic analysis of the flow field in the near wake. It revealed the complexity of the coherent structures and their dynamics close to the cylinder. Considerable fluctuations of the positions of the coherent structures were identified, in radial as well as in azimuthal direction.

These fluctuations were suppressed at higher levels of excitation, reducing the unsteady loads significantly. As inclined circular cylinders are found in many engineering applications the so enabled active damping of flow induced oscillations could prove to be very useful to greatly reduce the risks of structural failure due to fatigue.

Contents

List of Symbols

1	Introduction	1
1.1	Background	1
1.2	Motivation	4
2	Experimental Setup	5
2.1	Test Facilities	5
2.1.1	Closed Loop Tunnel	5
2.1.1.1	Test Section	5
2.1.1.2	Geometry and Coordinate Systems	6
2.2	Cylinders and Mounts	6
2.2.1	Double Slotted Cylinder	6
2.2.1.1	Actuation System	7
2.2.2	The 2-D Cylinder	8
2.2.3	The Swiveling Cylinder	8
2.3	Instrumentation	8
2.3.1	Pressure Measurements	8
2.3.2	Particle Image Velocimetry	8
2.3.3	Hotwire Anemometry	8
3	Experimental Methods and Techniques	9
3.1	The Swiveling Cylinder	9
3.2	Preparatory Experiments	9
3.2.1	Flow Visualization	9
3.2.2	Calibration	10
3.2.3	Variation along individual Slots	11
3.3	Pressure Measurements	11
3.3.1	Surface Pressure Measurements	11
3.3.2	Wake Pressure Measurements	12
3.4	Particle Image Velocimetry	12
3.4.1	Processing and Presentation	13
3.4.1.1	3-D reconstructions	14
3.4.2	Proper Orthogonal Decomposition	17
3.4.3	Data Acquisition	20
4	Results and Discussions	25
4.1	The Experiments – Overview	25
4.2	The Swiveling Cylinder	25
4.3	Preliminary Experiments	27
4.3.1	The Wall Boundary Layer Shedding Fence	28
4.3.2	Flow visualizations	29
4.4	Asymmetric Forcing	30
4.4.1	The Infinite Cylinder	30

4.4.1.1	Forces on the Cylinder	30
4.4.1.2	The Near Wake	38
4.4.1.3	Near Wake Dynamics	47
4.4.1.4	The Far Wake	58
4.4.2	The Finite Cylinder	64
4.4.2.1	Forces on the Cylinder	65
4.4.2.2	The Far Wake	66
4.5	Symmetric Forcing	69
4.5.1	The Infinite Cylinder	70
4.5.1.1	Forces on the Cylinder	70
4.5.1.2	The Near Wake	72
4.5.1.3	Near Wake Dynamics	79
4.5.1.4	The Far Wake	83
4.5.2	The Finite Cylinder	87
4.5.2.1	Forces on the Cylinder	88
4.5.2.2	The Far Wake	88
4.6	Generic Actuation	91
4.6.1	Single-sided actuation with both Slots open	91
4.6.2	Double-sided Actuation with Phase Delay	92
4.6.3	Double-sided Actuation with differing Frequencies	93
4.7	Baseline	96
4.7.1	The Infinite Cylinder	96
4.7.1.1	Forces on the Cylinder	96
4.7.1.2	The Near Wake	99
4.7.1.3	Near Wake Dynamics	104
4.7.1.4	The Far Wake	112
4.7.2	The Finite Cylinder	113
4.7.2.1	Forces on the Cylinder	114
4.7.2.2	The Far Wake	114
4.8	Conclusions	115
4.9	Outlook and Potential Continuation	116

List of Symbols

U_∞	free stream velocity
u_s	slot velocity
D	diameter of the cylinder
R	radius of the cylinder
L	length of the cylinder
L_0	width of test section
b	slot width
Λ	sweep-back angle
γ	yaw angle
α	angle of rotation of the cylinder
X, Y, Z	cartesian coordinate directions with respect to cylinder
x, y, z	cartesian coordinates with respect to cylinder
X_T, Y_T, Z_T	cartesian coordinate directions with respect to test section
Θ	slot location measured from leading edge
x_s	X-coordinate of slot location
y_s	Y-coordinate of slot location
p	local pressure
C_p	pressure coefficient, $\frac{p-p_\infty}{\frac{1}{2}\rho U_\infty^2}$
$C_{p,n}$	normal pressure coefficient, $\frac{p-p_\infty}{\frac{1}{2}\rho U_\infty^2 (\cos\Lambda)^2}$
F_l	lift force
F_d	drag force
C_l	lift coefficient, $\frac{F_l}{L D \frac{1}{2}\rho U_\infty^2}$
C_d	total drag coefficient, $\frac{F_d}{L_0 D \frac{1}{2}\rho U_\infty^2}$
C_{dp}	form drag coefficient
U_n, U_{geom}	velocity normal to cylinder, horizontal (X-direction), $U_\infty \cos\Lambda$
W_{geom}	velocity in spanwise (Z) direction, $U_\infty \sin\Lambda$
u_T, v_T, w_T	velocities with respect to X_T, Y_T, Z_T
u, v, w	velocities with respect to X, Y, Z
u', v', w'	random velocity fluctuations with respect to X, Y, Z
u'_t, v'_t, w'_t	random velocity fluctuations, top part of the wake
u'_b, v'_b, w'_b	random velocity fluctuations, bottom part of the wake
C_μ	momentum coefficient, $\frac{2b}{D} \left(\frac{\sqrt{\overline{u_s^2}}}{U_\infty} \right)^2$
$C_{\mu,n}$	normal momentum coefficient, $\frac{2b}{D} \left(\frac{\sqrt{\overline{u_s^2}}}{U_\infty \cos\Lambda} \right)^2$
f	actuation frequency
F^+	dimensionless actuation frequency, $\frac{f U_\infty}{D}$
F_n^+	normal dimensionless actuation frequency, $\frac{f U_n}{D}$
δ	phase delay between the forcing signals
Ω_z	Z-component of vorticity, $\frac{\delta v}{\delta x} - \frac{\delta u}{\delta y}$
k	turbulent kinetic energy, $\frac{u'^2 + v'^2 + w'^2}{U_\infty^2}$
M	Mach number
A_{ij}	input data to POD
φ	POD phase angle
λ	Eigenvalue
$e_{i,n}$	n th Eigenvector or POD mode
$a_{i,n}$	n th Eigenflow

Acronyms

AFC	Active Flow Control
PIV	Particle Image Velocimetry
POD	Proper Orthogonal Decomposition

Chapter 1

Introduction

1.1 Background

The flow around bluff bodies occurs frequently in engineering and nature. It takes place around buildings, towers, chimneys, masts, cables and pipes whether stationary or being towed both in air and in water. It is a common phenomenon in cross flow heat exchangers and chemical plants. It has even an environmental dimension because wakes from underwater drilling operation or pipes containing effluents or coolants erode beaches or riverbeds, sometimes in an unpredictable manner substantially far from their location.

Therefore it is important to understand the flow around bluff bodies and to use this understanding for efficient control. Passive control by means of shaping the bodies was historically the only option, but this is often limited by the changing direction of the flow. On chimneys for example, parallel vortex shedding is suppressed by installing spiraling ribs that induce spiral flow around the chimneys. The characteristic shape of a bluff body can vary largely, some simplified examples include cuboids like commercial trailers and skewed cuboids that serve as loading ramps on cargo planes and helicopters. The flow around slender bodies or missiles at high angles of attack approximates the flow around yawed cylinders. This was extensively investigated in aeronautics and dubbed as the "forebody problem".

An interesting application that combines a swept-back large aspect ratio cylinder (see figure 1.1) with the necessity to adjust its attitude in a very controlled way is presented by Bennington & Visser [1]. It is concerned with aerial refueling of large commercial aircraft altering its range and productivity. The possibility of controlling the flow around bluff bodies by periodic excitation (Active Flow Control or AFC for short, a good introduction is given by Lachmann [16]) instead of auxiliary lifting surfaces might significantly improve the overall efficacy of the approach. In some cases active flow control gives better result either due to its increased flexibility and adaptability to a given shape or simply by minimizing drag or controlling the lift generated by the body. Another important application is the active damping of flow-induced oscillations by actively changing the Scruton number (reduced damping, $S_c = \frac{m\zeta}{\rho D^2}$). Effective implementation of these techniques requires good understanding of vortex shedding from oblique bluff bodies, properly located sensing devices and the application of modern control theory.

An inclined circular cylinder can be seen as a generic bluff body. The flow around it is three-dimensional and mostly unsteady depending on the sweep angle. The separation location is not determined, thus the interaction between surface curvature and the active means of controlling separation can be investigated under a wide range of independent variables such as locations and types of active flow control devices and possible changes in the coherent structures that they generate in the lee of the cylinder. The two-dimensional flow around a circular cylinder represents the most extensively studied bluff body configuration. At low Reynolds numbers there are many theoretical and numerical investigations but at high Re most of the studies are still empirical or numerical (e.g. Carberry et al. [7], Roshko [23], Thompson & Hourigan [28], Williamson [33] and many others). Despite the numerous publications the understanding of flow separation, vortex



Fig. 1.1: The refuelling boom with control surfaces [5]

formation in the wake and shedding is still limited. This is partly due to the complexity of the flow even at zero sweep-back angle.

It is well known that even a two-dimensional setup will generate three-dimensional vortex structures in its wake. This cellular shedding was analyzed for low Reynolds numbers, for example by Noack et al. [21]. The experimental study by Brede et al. [6] describes quantitatively the different secondary streamwise modes found in the wake of a circular cylinder at low Re . Various Re -dependent mechanisms of vortex shedding and wake instability were investigated by Fey et al. [10] who distinguished among five different types of shedding between $Re = 47$ and $Re = 20000$. For the subcritical range of $Re > 20000$ the relation between Strouhal number and Reynolds number was determined in this paper. The influence of artificial tripping of the flow on the surface of the cylinder was investigated by Igarashi [13]. He describes different patterns of transition, with the flow being sometimes more destabilized by tripping. Since transition affects the width of the wake, empirical relations between Strouhal number and drag are presented in his paper a range $10^4 < Re < 10^6$. One important requirement for the application of AFC to two-dimensional circular cylinders is the spanwise uniformity of the perturbations and the baseline flow. For this reason trip wires are widely used in the subcritical range to provide stable and reproducible conditions along the span.

The experiments presented by Bera et al. [2] use trip wires to pre-condition the flow for the application of active flow control at sub-critical Reynolds number. Detailed results about forces acting on the cylinder and formation of vortices are shown, but the study is limited to the region near to the slot from which the actuation emanates. The identification of vortex centers is covered in detail in this paper. The detection of changes in the vortex locations in complex flows is essential for a better understanding of the physics of active flow control. The occurrence of multi-stable vortex patterns on swept-forward cylinders with a cone at their tip is discussed by Wardlaw & Yanta [31]. The flow pattern in the wake of this body can change significantly by small model imperfections or slightest misalignments. It results in a largely varying side force due to lift generated on the nominally symmetric configuration. The data provided by this investigator is unfortunately limited to time-averaged LDA (Laser Doppler Anemometry) results. Although effects of vortex shedding and flow instabilities were observed, the variations in the measured side force were attributed to globally stable mean vortex patterns while the dynamic behavior of the wake that potentially causes the switching between globally stable states, is mentioned as a possible side-effect.

A theoretical and numerical investigation of the wake of yawed cylinders at low Reynolds numbers was carried out by Marshall [19]. It gives an explanation for the observed breakdown of the Independence Principle at large sweep angles due to the increased axial component of the flow. The vortex dynamics in the wake generate oscillatory forces on the body that may result in vortex-induced oscillations. The flow-induced oscillations of yawed cylinders were investigated by King [15] who was particularly interested in under-water installations. He found out that swept cylinders do not reduce the risk of such oscillations. King's study is one of the few dealing with the swept-back configuration. Extensive experimental study of vortical structures in the wake of a swept-forward, finite cylinder at high Reynolds numbers, was conducted by Thomson & Morrison [29]. They used Schlieren and traversed the flow with Pitot tubes and yaw sensitive pressure probes. This instrumentation restricted the pressure data acquired mostly to time-averaged quantities. A Pitot probe connected to a high-frequency-response pressure transducer enabled the investigators to detect unsteadiness in the flow. This procedure determined the vortex pattern to be stationary in the wake over a wide range of cylinder sweep angles.

High speed Schlieren was also used where the unsteadiness of the flow was apparent. The strongest instabilities occur at sweep angles of 50° to 60° where the different instantaneous patterns were documented. The observed stationary states are separated by unstable regions that extend over a wide range of inclination angles. Even at a frame rate of 1300fps it was not possible to resolve the transition between two stable patterns. The wake instabilities may be caused by the smallest of imperfections in the model or its alignment. At very large sweep-forward angles a symmetric pattern of stationary vortices emerges. Decreasing the sweep angle generates at first asymmetric patterns that degenerate to vortices being shed parallel to the cylinder's axis at sweep angles of 30° or less. Vorticity distributions were calculated from the yaw sensitive meter as well from the spacing observed between individual vortex cores on the Schlieren images. The latter method is based on the sweep-back principle outlined in the paper.

The observations discussed reflect the sensitivity of the flow to asymmetries at the nose, whereupon the Schlieren images give no information about the vortex location along the span (i.e. in the Z-direction), the vortex pattern can be mirrored in the X-Z plane without this being detected. A detailed discussion of nose imperfections on finite swept-forward cylinders having a hemispherical nose, is presented by Hoang et al. [11]. This study is based on extensive surface flow visualizations and scans of the flow field by a seven-hole pressure probe. The study was limited to high sweep-forward angles exceeding 60° . At these angles symmetric vortex patterns were observed in the wake. The paper focuses on describing the flow around the round leading edge where the so-called horn-vortices are being formed.

Pressure fluctuations and vibrations of a swept-forward finite cylinder were investigated by Snarski [25] at different Reynolds numbers. Although the spatial resolution of the used hydrophones was limited to approximately 45° , the differences in the spectra depending on the circumferential location of the hydrophones are significant, especially for small angles of attack. The variation of the vortex dynamics with sweep-back angle are clearly visible in the presented spectra. Vortex shedding was not observed for $\Lambda < 30^\circ$ and $Re > 10000$. Interesting is the observation of disappearing vortex shedding around $\Lambda = 60^\circ$ for $Re = 27600$. This shows clearly the complexity of this 3-D flow. Three different flow regimes, depending on the angle of attack, were observed. The additional dependency on the boundary layer thickness is mentioned but was not investigated.

The available literature on controlling the flow around yawed cylinders seems to be limited to applications dealing with the "forebody problem". Different methods of enforcing flow symmetry to suppress side forces were used. The unsteady bleed technique presented by Williams & Papazian [32] uses an axial row of small holes on the leeward side of the nose cone to generate zero-mass-flux oscillations which force the flow into a parallel shedding mode and suppresses the large side forces resulting from the asymmetry. A closed-loop control scheme based on suction at the tip was presented by Bernhardt & Williams [3]. This experiment used one hole on each side of the tip region while suction was being applied on one control port at a time to force symmetric flow.

The possibility of proportional control of the vortex locations was investigated by Bernhardt & Williams [4], using the unsteady bleed technique from a row of holes located on the leeward side of the tip. The experiments were carried out successfully for a sweep-forward angle of 45° , but failed

whenever the bi-stable situation was found at 35° . The term “micro-asymmetry” used by Ericsson [9] illustrates clearly the problematic instability of vortices on yawed cylinders where the slightest disturbance generates asymmetric modes.

1.2 Motivation

The flow past an inclined cylinder is complex and three-dimensional. For small sweep-back angles the dynamics in the wake are similar to the 2-D flow and the vortices shed periodically from the cylinder. For large sweep-back angles approaching 90° the situation is entirely different and the vortices remain close to the cylinder and do not separate at all. For angles Λ between these two regimes the situation more complex and the vortices peel-off along the span. Starting at the tip of the finite cylinder the spanwise vortices remain close to the cylinder’s surface and separate.

Visualizations like the ones presented by Werlé [30] show clearly the three-dimensionality of the flow, but cannot provide any detailed information about the vortex dynamics in the wake. The streaklines illustrate particle paths, but not necessarily the velocity field, and the visible “structures” depend on the location of the tracer-injection. Thus questions about the peel-off location and spanwise frequency remain unanswered. It is not clear if the shedding is symmetrical for positive and negative vorticity like in the 2-D case or if the vortices separate from the cylinder in an alternating fashion along the span. What are the dynamics of the peel-off process? What is the circulation contained in the vortices? How do the forces vary along the span of the cylinder? Those are some of the questions for which this study endeavors to find an explanation. They cannot be answered neither by surface flow visualizations nor by surface pressure measurements.

Periodic excitation is provided on the surface of the cylinder along a line parallel to its axis. It is used as a diagnostic tool, helping to understand the dynamics in the wake by ordering the process. Furthermore it helps to assess the sensitivity of the flow to excitation and the potential to manipulate and alter it.

The dynamics in the wake and the possibility to control them is of high relevance because oscillating loads can threaten the structural integrity in many technical applications. These dynamics, especially in the near wake can be investigated only by quantitative, ideally time resolved measurement techniques like stereoscopic high-speed PIV systems. Nevertheless the available PIV systems are usually, as in this study, not time resolved. Therefore advanced methods for the dynamic analysis of the acquired PIV data are required.

The identification and explanation of the processes in the wake of an inclined cylinder and the full understanding of the dynamics involved are necessary for an optimized control of this flow. The optimization includes frequency, amplitude location and type of excitation. This work aims at understanding and explaining the details of the flow around a generic bluff body like the inclined circular cylinder. This information is valuable for potential “real world” applications of active flow control on bluff bodies. It is of high technical relevance, taken the fact that bluff bodies are found in many large-scale applications and that the drag is oftentimes a critical design parameter, not to forget its relevance for the energy consumption of almost every vehicle.

Chapter 2

Experimental Setup

2.1 Test Facilities

2.1.1 Closed Loop Tunnel

The experiments were carried out in a closed loop low-turbulence wind tunnel in a test section with a 2' x 3' cross section. The three dimensional nozzle had a contraction ratio of approximately 11:1. The model was mounted horizontally between the walls by means of fully adjustable fixture on one side and simple filler on the other end, as shown in figure 2.1. This setup allowed for the change of the sweep back angle, the yaw angle, and the angle of rotation around the axis of the cylinder. The tunnel speed was computer controlled. The speed was checked before and after each single experiment to ensure a constant free stream velocity even when the drag of the cylinder was changed by the use of active flow control. This feed-back system was integrated into the main LabView data acquisition software.

2.1.1.1 Test Section

The original test section was modified to enable the optical access for the PIV system. The side wall connecting to the downstream end of the cylinder and the tunnel floor were replaced by single piece glass panes to get optimal optical access. This limited the options for modifications of the setup, like mounting a traverse for Hotwire measurements inside the test section. It was not possible to drill any holes into the glass, therefore the cylinder had to be supported entirely from its upstream end. Thus the use of load cells for the direct measurement of the forces on the cylinder was not possible with the available equipment. The side wall holding the cylinder had to be replaced by a 0.5" thick aluminium plate to prevent oscillations of the model due to the single sided support. Figure 2.1 shows the older version of the test section with a transparent side wall. The frame of the test section was modified to accommodate the PIV system below the tunnel floor.



Fig. 2.1: Test section with model and original plexiglass side wall, side view, flow from right

2.1.1.2 Geometry and Coordinate Systems

The orientation of the inclined cylinder with the boundary layer shedding fence around its upstream end and the row of pressure taps at mid-span is presented in figure 2.2. Two different coordinate systems were used during the experiments. The origin of the coordinate system used for the PIV data is located in the center of the most downstream slot. The X-direction for the PIV data is oriented horizontally and perpendicular to the cylinder, the Y-direction vertically and the Z-direction is parallel to the cylinder's axis. The Z-direction for the wake data is oriented horizontally and perpendicular to the free stream, with its origin on the centerline of the test section. The origin of the streamlines computed from PIV data (see for example pages 57 ff) is color coded as marked in figure 2.2.

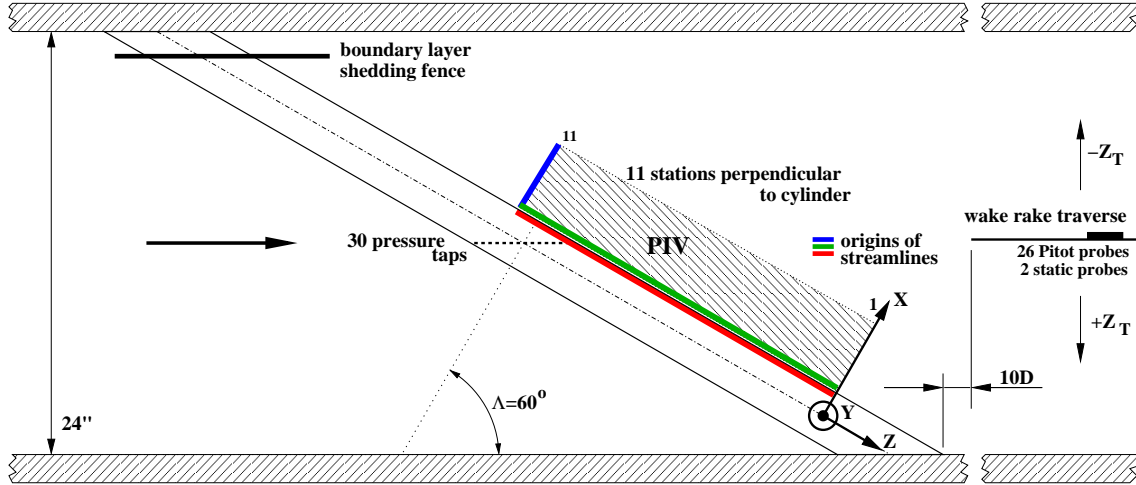


Fig. 2.2: Geometry of the experiments ($\Lambda = 60^\circ$) and coordinate systems, top view

2.2 Cylinders and Mounts

2.2.1 Double Slotted Cylinder

The thin-wall stainless steel cylinder with a diameter of 3" was polished to a mirror finish. It was mounted interchangeably on a central beam that held the 22 internal loudspeakers that served as excitation source, shown in figure 2.5. The excitation was applied through two rows of slots, symmetrically located on both sides of the cylinder. The 0.040" wide slots ran parallel to the axis of the cylinder and were cut at an angle of 30° to the local surface tangent, pointing downstream (see figures 2.3 and 2.4). They were located under $\pm 110^\circ$ on the circumference of the cylinder. Each row consisted of 22 individual 49mm long slots, separated only by 1mm wide bridges.

The slots were laser-cut to maximize the accuracy. The stainless steel tubing was annealed. Still, the deformation due to thermally induced stresses required that all slots were adjusted carefully to the proper slot width. The inactive slot was taped with $25\mu\text{m}$ Kapton tape during asymmetrically forced experiments to avoid unintended actuation from that side.

Three different rows of 30 pressure taps each were located in a plane inclined 0° , 45° and 60° to the axis of the cylinder. These circumferential pressure taps were connected by Tygon tubing to a PSI 8400 pressure scanner for measuring the static pressure distribution around the cylinder. The tubing had to be glued into place one-by-one and the glue had to cure between the individual applications to ensure a proper connection. The glue was brought to the contact point between tubing and the inside of the cylinder by means of a syringe equipped with a thin metal tube of sufficient length. Only the 60° row was connected at first due to the very limited space inside the cylinder. It was later re-used for the experiments with $\Lambda = 45^\circ$ to avoid having to open the model again. This would have required a re-balancing and re-calibration of the actuation system. Additionally, five pressure taps were located at different axial positions on the base of the cylinder.

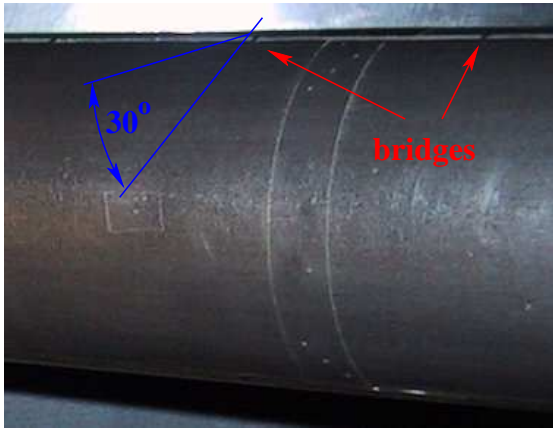


Fig. 2.3: Actuation slots with bridges between slots and taped pressure taps

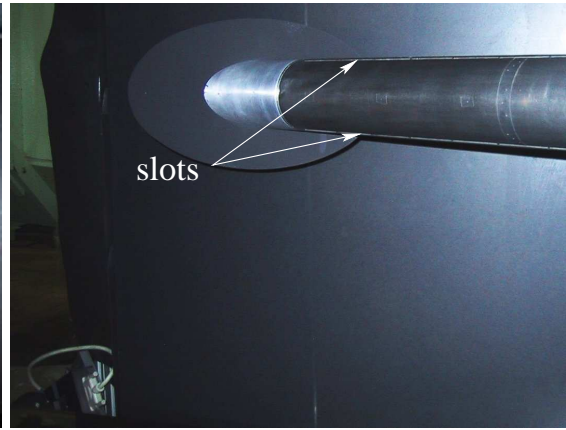


Fig. 2.4: Finite cylinder with endplate, both slots visible, camera in the lower left

The cylinder was mounted either in an “infinite” configuration, spanning the test section from wall to wall, or in a “finite” one with a small endplate mounted to the downstream end of the cylinder (see figure 2.4).

2.2.1.1 Actuation System

Twentytwo miniature sub-woofers (4Ω impedance) were mounted alternating in the central internal beam, as shown in figure 2.5. Each actuator was connected with a separate cable to an external terminal to enable individual fine tuning. This was achieved by connecting resistors in parallel and in series to adjust the effective amplitude for each actuator. The backsides of the actuators were all connected to the same cavity inside the beam, thus a cross-talk between both rows of speakers was inevitable and had to be compensated by modifying the actuation signals.

The actuators were driven in two 3x3 (3 parallel groups of 3 actuators in series) groups by a 660W stereo amplifier. The two actuators remaining on each side were connected in series to one 100W mono amplifier per side. The two outer cavities (between actuators and inside of the cylinder) running along the entire span were each divided into eleven sections by the pink foam visible in figure 2.5 to prevent longitudinal oscillations.

The actuation system was computer controlled and integrated into the data acquisition system for the PSI8400. Therefore the experiments could be run with high repeatability and accuracy due to automated control of tunnel speed, actuation frequency and amplitude.



Fig. 2.5: Internal beam holding the actuators, with dividers

2.2.2 The 2-D Cylinder

The cylinder used for the 2-D experiments (see Taubert [26]) had a diameter of 3" with a 0.4mm wide slot, inclined to the surface at approximately 30° to the downstream direction, which resulted in an almost tangential excitation. It was coupled on both ends with spiral hoses to an external actuator consisting of two combined and modified loudspeakers, driven by a 660W stereo amplifier. A clear disadvantage of this external actuation system were higher modes forming in the long ducting and the high attenuation of the excitation signal.

2.2.3 The Swiveling Cylinder

Preliminary experiments were carried out on the "swiveling cylinder". This model consisted of the aluminium cylinder used for the 2-D experiments with an additional end piece, mounted on a low friction axial roller bearing on the tunnel floor (see figure 2.6) that enabled the free rotation around a vertical axis. The base plate holding the cylinder was chamfered to minimize interference with the flow. The flow was tripped by unwound guitar strings that were mounted on both sides of the cylinder with double-back foam tape. Additionally, a number of 1/4-20 nuts was used to trip the flow over the base plate. Internal actuators were used for controlling the flow by means of zero-mass-flux excitation.



Fig. 2.6: The swiveling cylinder with trip strip, the ruler indicates the horizontal

2.3 Instrumentation

2.3.1 Pressure Measurements

A Pressure Systems Inc. PSI System8400 with two 32 port miniature pressure scanners was used for measuring the surface and wake pressures as well as the static and total pressure in the tunnel. The range of the sensors was $\pm 10'' \text{ H}_2\text{O}$. The system was computer controlled with integrated calibration and accuracy check routines. A Baratron was used for the feed-back tunnel speed control.

2.3.2 Particle Image Velocimetry

A stereoscopic PIV system with two 1024x1024 pixel IDT cameras was used to acquire the PIV image pairs. The cameras were mounted on custom-made adjusting fixtures to obtain optimal flexibility and data quality. IDT ProVision software was used for processing the image data. The light sheet was generated by a Spectra Physics PIV200 NdYAG laser in combination with custom optics (Linos Photonics). Seeding was generated by a Dantec atomizer filled with a 5% Glycerin-in-water solution. The entire PIV system consisting of the two cameras and the laser including the optics was mounted on a horizontal traverse that enabled the data acquisition at multiple stations along the span of the cylinder with a single calibration. The cameras were mounted on a vertical beam. The light sheet was directed vertically up and illuminated the test section through the glass floor, thus the bottom camera visible in figure 2.4 was operated in backscatter-mode.

2.3.3 Hotwire Anemometry

An AA Labs anemometer was used for the Hotwire measurements. The single wire was calibrated in an external calibration tunnel for the higher velocities measured during the calibration of the actuation. For all other measurements the calibration was carried out in the test section. A special fixture that could be mounted to the glass floor was used for measurements inside the test section.

Chapter 3

Experimental Methods and Techniques

The yaw angle of a “swiveling cylinder” was actively controlled in a study of feasibility. Active flow control experiments were conducted on a stationary inclined “infinite” cylinder after this successful demonstration of flow control on a finite inclined cylinder. The natural flow and its alteration due to the application of periodic zero-mass-flux flow control were studied in detail. Pressure data were taken on the cylinder’s surface and in its far wake, Particle Image Velocimetry (PIV) was used to investigate the near wake extensively. The flow on the cylinder’s surface was visualized prior to the quantitative experiments. A series of experiments intended to investigate the stability of the flow past an inclined cylinder did not produce conclusive results. Due to the very low sensitivity of the flow a disturbance in the order of magnitude of the free stream velocity was detectable only 4cm downstream of the location where it was introduced. This does not agree with the idea of a “small” disturbance, therefore the data was not considered.

3.1 The Swiveling Cylinder

For all experiments on the swiveling cylinder, a video camera was mounted outside of the test section and above the downstream, free end of the cylinder. A scale laid out on the tunnel floor was used to determine the yaw angle of the cylinder under equilibrium conditions. It was corrected for the error due to parallax. Different levels of C_μ were applied in ascending and descending order to check for potential hysteresis of this type of control.

To further verify and quantify the results, an “infinite” cylinder was mounted between the side walls of the test section at various preset yaw angles. Free swivel of the cylinder was prevented in this case. The yaw moment acting on the cylinder was determined from the pressure distribution around the cylinder for different C_μ , assuming that the pressure distribution was uniform along the span of the cylinder.

3.2 Preparatory Experiments

3.2.1 Flow Visualization

Surface flow visualization, the so-called “china clay method”, was applied to the finite cylinder in the baseline configuration at sweep-back angles between 60° to 75° to verify the spanwise uniformity of the flow. Titanium Dioxide was dispersed in Kerosene with the addition of a few drops of Oleic Acid for stabilization. This suspension was further diluted with lighter fluid until a suitable viscosity was obtained. It was applied with a paint brush to the surface of a cylinder that was spray-painted in black. Immediately after the application, the tunnel was started and run for several minutes until the solvents evaporated to a degree that the film remaining on the surface

was stable. Photographs were taken for documentation of the three-dimensional “stagnation” and separation lines.

3.2.2 Calibration

The actuation system had to be calibrated to quantify the level of excitation on the flow. Hotwire measurements are commonly used to calibrate the slot velocity versus input voltage to the actuators for zero-mass-flux excitation. This technique depends on the extremely careful positioning of the Hotwire in the exit nozzle, in this case a straightly cut slot. The velocity was measured at a point where the amplitudes and signal shapes of blowing and suction phases matched exactly. This is very important due to the rectifying nature of the Hotwire. Only the absolute value of the velocity can be measured and no information about the precise direction of the flow relative to the surface is available. Thus the actuation level can be determined by calculating the RMS value of the velocity signal only if blowing and suction phases in the time series of the velocity signal are identical. The calibration procedure using Hotwires was carried out initially to reliably determine the properties of the actuation including the distortion of the excitation signal due to resonance in the actuation system consisting of actuators, slots and cavities.

Prior to the final calibration the actuation system had to be fine-tuned for spanwise uniformity by adding resistors in parallel and in series to the individual loudspeakers. This required after every step of adjustment a new evaluation of the uniformity along the entire span because the actuators were coupled through the common back chamber. The procedure of adjustment and verification was repeated until the amplitudes of the excitation signal measured at each individual slot converged and the aimed at spanwise uniformity was obtained.

The time necessary to properly position a Hotwire for every single measurement would possibly have exceeded the total time available for all experiments. Therefore a different system using the dynamic pressure measured at the slot was implemented for the calibration of the actuation. This system enabled the accurate, repeatable and quick positioning of the dynamic pressure sensors at each slot. A special fixture was used to allow for simple spanwise traversing of an Endevco dynamic pressure sensor. The sensor was connected to a short metal tube ending in a soft silicone gasket contacting the cylinder during the measurements.

A careful comparison between simultaneously acquired Hotwire and dynamic pressure data was conducted several times for a single slot. The difference between both data series was comparable to the variation of separate and individually adjusted Hotwire measurements. Thus the accuracy of both methods was considered comparable.

The calibration procedure using dynamic pressure was used for adjusting the spanwise uniformity as well as for the final calibration and proved to be satisfactory in terms of accuracy and repeatability. It saved a significant amount of time compared to the conventional method using Hotwires.

The level of actuation was quantified per slot by the widely used parameter

$$C_\mu = \frac{2b}{D} \frac{\sqrt{u_s^2}}{U_\infty} \quad (3.1)$$

This parameter was adapted to the sweep-back angle by

$$C_{\mu,n} = \frac{C_\mu}{(\cos \Lambda)^2} \quad (3.2)$$

according to the projection of U_∞ perpendicular to the cylinder as described in Schlichting [24] based on geometric considerations and verified experimentally by Naveh et al. [20]).

The calibration of C_μ versus input voltage was conducted for a set of different frequencies and voltages, as presented in figure 3.1. The input parameters were limited by the actuator properties to a minimum frequency of 80Hz and a maximum voltage of 7V at the individual actuator. It was verified later that the maximum calibrated frequency of 500Hz was well above any useful excitation frequency in this experiment. Dynamic pressure data were acquired simultaneously from the two

slots. One was in the process of being calibrated while the other served as a reference to determine the phase delay. Additionally, the signal of one internal sensor per side was recorded to enable later online monitoring of the excitation level.

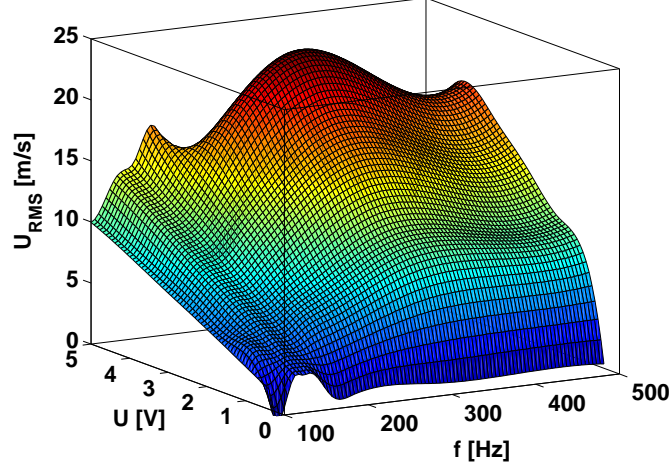


Fig. 3.1: Sample calibration data

3.2.3 Variation along individual Slots

PIV data were taken in 0.5" steps in order to determine the Z-direction intervals necessary to resolve the spanwise variations along the inclined cylinder. No significant variations were found along the individual slots, therefore it was considered sufficient to take representative PIV data at the middle of each slot in the volume being investigated.

3.3 Pressure Measurements

The acquisition time for the pressure measurements was optimized automatically: An initial data set was taken over 30s and averaged, then a second series was acquired over 15s, added to the initial data and averaged again. The difference between the two averages was determined, if it was above the prescribed threshold another data set was taken over 15s. The procedure was repeated until the data either converged or a preset maximum number of iterations was reached. In this case the data point was flagged to be inaccurate.

3.3.1 Surface Pressure Measurements

Three different rows of 30 pressure taps were located around the cylinder, for each of the sweep-back angles under consideration (0° , 45° and 60°). The pressure taps were arranged in streamwise direction (for 0° rotation) and staggered to minimize tap interference. Additionally, several pressure taps were located along the trailing edge, two of which were used during the experiments in order to assess the spanwise pressure gradient.

The pressure taps were connected to the sensors by 0.040" Tygon tubing. Only one set of tubing connected to a single row of pressure taps could be used at a time because the space inside the cylinder was very limited due to the presence of the internal actuators. Only the initially connected 60° row of pressure taps was actually used for the investigated cases of $\Lambda = 45^\circ$ and $\Lambda = 60^\circ$ to avoid inaccuracies due to the re-adjustment of the excitation system that would have been required after installing a new set of Tygon tubing for each sweep-back angle. By using the 60° row for all sets of experiments the lengthy re-calibration was also avoided, since it was not necessary to

disassemble the model for changing the sweep-back angle. Data taken at $\Lambda = 0^\circ$ during an earlier experiment were used for comparison.

Two different projections were used to represent the surface pressure data (see figure 3.2). The natural, streamwise elliptical cross section was used during the experiments and for calculation of lift and drag coefficients. The cylindrical cross section was used in some figures to facilitate comparison of results obtained at different sweep-back angles. In these cases pressure and force coefficients were re-normalized by $U_n = U_\infty \cos \Lambda$. All pressure profiles are presented in cartesian coordinates with the origin being at the leading edge of the cylinder in analogy to airfoil coordinates.

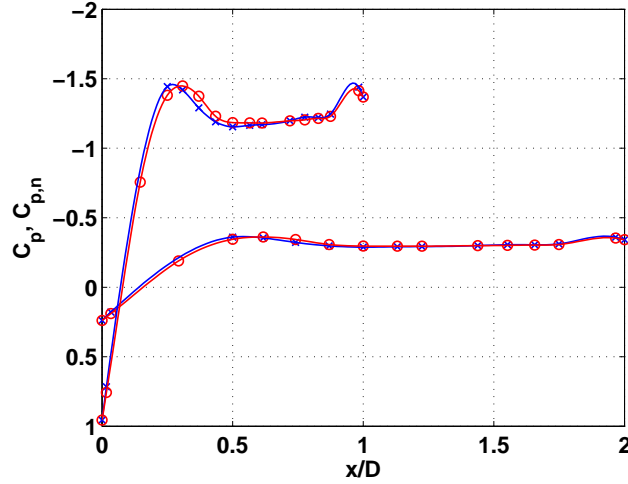


Fig. 3.2: Transformation of C_p distributions, baseline, $\Lambda = 60^\circ$, $Re_n = 35000$

3.3.2 Wake Pressure Measurements

The velocity deficit in the wake of the inclined cylinder was investigated with a vertical wake rake containing 26 Pitot probes at 1" spacing and two static pressure probes at both ends of the rake. The rake assembly was traversed manually across the test section in a plane perpendicular to the free stream, thus scanning the cross section of the tunnel. The rake was located approximately 10 diameters downstream of the downstream end of the cylinder when swept-back at $\Lambda = 60^\circ$, as shown in figure 2.2.

3.4 Particle Image Velocimetry

The basic principle of Particle Image Velocimetry is to determine the velocity components in a plane (exception: a volume for holographic PIV) using two images of a flow field containing particles that were recorded with a preset time delay Δt . The displacements of the particles in the observed plane are generally computed by cross-correlating the two images. These displacements are always determined in the plane that is imaged onto the light recording sensor and not in the plane of the light sheet. A calibration is necessary to map the displacements from the pixel-coordinates of the camera sensor to the physical space. The division of the displacements by the preset time delay Δt results in the vector field of physical velocities.

In most cases the flow has to be seeded with liquid (fog) or solid particles to obtain the required density of particles in the flow. The observed plane is commonly illuminated by pulsed lasers that generate a light sheet of high intensity and quality. The system used in this investigation has to be calibrated by placing a target consisting of a flat surface with contrasting geometric markings in known positions exactly in the center plane of the light sheet. The very accurate alignment of this calibration target is essential because a misalignment between target and light sheet will impair the accuracy. In the case of such a misalignment particles are mapped (by the software) from their

true location in the light sheet to the plane of calibration determined earlier by the (inappropriate) position of the calibration target which causes a significant error.

Stereoscopic PIV is used to determine all three velocity components in the illuminated plane. For this type of PIV two cameras, arranged at a certain distance, are pointed at the same field of view. The velocity component perpendicular to the plane defined by the intersecting optical axes of both cameras can be calculated directly, the other two components have to be computed from the stereoscopic information. Therefore the angle enclosed between the two cameras determines the accuracy of these two velocity components. Usually angles in the range $90^\circ \pm 30^\circ$ are considered a suitable choice.

In the only feasible arrangement of the two cameras and the laser one camera was operated in forward scatter mode while the other had to be operated in the unfavorable backscatter mode. This reduced the raw data quality of the second camera significantly. Particle size and density as well as the field of view had to be adjusted accordingly. All other potential arrangements would have required major modifications of the test section or would have resulted in a severely restricted field of view. The light sheet was oriented perpendicular to the cylinder's axis to minimize reflections. The disadvantage of this setup was that for stereoscopic PIV the optical access to the inclined cylinder was restricted by the geometry of the test section. The distance between ceiling and floor of the test section limited the maximum useful distance between the cameras, and therefore the maximum distance between the cameras and the recording plane, depending on the preset angle between the cameras.

The volume accessible in lee of the inclined cylinder extended from the downstream end of the cylinder (touching the wall) up to 29.5" in spanwise direction, $\pm 2.2R$ in the vertical and $3R$ in the direction downstream of the trailing edge, measured perpendicular to the cylinder's axis.

3.4.1 Processing and Presentation

All raw PIV data were processed with 32×32 pixel correlation windows with 50% overlap, resulting in 79×59 vector fields containing the three velocity components. The drop-out rate was usually lower than 2%. Software written in C and partly based on routines published in the "Numerical Recipes" [22] was used for the first step of post-processing due to significantly higher performance compared to interpreted programming languages like Matlab. In the first stage, averages, fluctuation intensities, derivatives in cartesian and cylindrical coordinates, kinetic energies and correlations were computed. Derivatives were calculated from polynomials obtained by locally approximating the data in two dimensions with a least square algorithm. C-programs were used also for the demanding POD computations and conditional averaging. The final stage of post-processing was done in Matlab due to time-efficient programming in combination with the excellent graphical output. Matlab was used for the visualization of the results, in addition to Open-DX, Gnuplot and Tecplot.

Various physical quantities were analyzed to assess the spatial development of the coherent structures in the near wake. Averaged quantities were examined in cartesian as well as in cylindrical coordinates, in the coordinate system of the inclined cylinder and in the wind tunnel coordinate system.

It is advantageous to use cylinder coordinates in the central part of the near wake whereas in the outer parts that are dominated by the free stream cartesian coordinates are the better choice. Because of this mix, cartesian coordinates (native to the data acquired by PIV) are used throughout this thesis.

Other analyzed quantities include velocity gradients, the spanwise components of vorticity, Reynolds stresses, correlations of velocity fluctuations in different regions of the wake and kinetic energy. Helicity was found to be a suitable quantity for the investigation of flows past inclined cylinders (Degani [8]). But as it was not possible to compute this quantity due to the missing derivatives perpendicular to the laser light sheet, this quantity was not considered.

Although vorticity is the natural quantity to analyze and visualize vortices it is not the best choice for tracking and describing the vortex peel-off in most seen cases. This is due to the loss of coherence occurring outside of the shear layer region. Vorticity is computed from velocity derivatives and it is therefore very sensitive to noise. Additionally, vortical structures often consist of many vortex filaments rather than a single large vortex, as seen during the roll-up of a shear

layer. Due to this it can be difficult to obtain clear averages in regions with complex patterns of motion. In this case the averaged Ω_z was frequently relatively blurred outside the shear layer region, only few distinct coherent structures could be observed at $x/R > 2.5$.

It was found that the spanwise velocity component W and the Reynolds shear stress $\overline{u'v'}$ are better suited to describe the vortex peel-off and the development of coherent structures outside the shear layer region. Minima in W coincide well with the locations of the vortex cores. The maximum in shear stress does not represent the vortices themselves but instead the region of large velocity gradients between adjacent co-rotating vortices. This includes small ones that are present in the shear layer as well as the larger ones peeling-off.

Specific examples are presented as contour plots which are used for direct quantitative comparison of selected flow field data. For global comparison of the differently investigated cases integral quantities as circulation or flow rates through planes spanning the entire volume are presented. These two forms of representation are advantageous for the detailed analysis of selected data. But the amount and the complexity of the data requires a more general tool for a quick and simple evaluation of the acquired information. Therefore three-dimensional reconstructions (or pseudo-visualizations) were used to present most of the PIV data. This form is commonly considered to be well suited for visualizing and analyzing volumetric data, especially when used interactively.

3.4.1.1 3-D reconstructions

The individual data fields at every spanwise location were combined into volumetric data sets. Different types of visualization were available for further processing. Depending on the type of data up to seven different iso-surfaces were defined in these volumes, coded by color and opacity. These iso-surfaces mark the location of the boundary between regions of higher and lower values of a specific variable. The data sets are segmented accordingly.

The interpretation of three-dimensional iso-surfaces can be difficult if it is not possible to view them interactively from different viewing angles because the three-dimensional body has to be mapped onto a two-dimensional surface. To facilitate the interpretation one or two contour plots were added to the visualizations, as well as a model of the cylinder and part of the test section for better spatial orientation. The position of the iso-surfaces in space can be best assessed starting from a visualized plane such as the sides of the control volume or the additional contour plots and then following the structures along the spanwise direction. At the locations of the additional contour plots the position in space can be assessed immediately. Wherever the iso-surfaces intersect the surfaces of the control volume the otherwise closed surfaces are cut open, revealing the individual layers of the visualization. The inside surfaces are shaded to increase the contrast.

Figures 3.3 to 3.4 are presented to explain the contents and the correct interpretation of the three-dimensional reconstructions and to demonstrate the identification of coherent structures. The iso-surfaces of the dimensionless vorticity, $\frac{\Omega_z D}{U_\infty \cos \Lambda}$ in figure 3.3 show one elongated region containing vortical fluid on each side of the cylinder. It can hardly be observed that a vortex pair is peeling-off around $z/R = -5$. Individual vortices cannot be detected in these regions because data were sampled randomly when actuation was not applied i.e. in the baseline case. The decreasing coherence at $x/R > 2.5$ results in an even more blurred picture. The iso-surfaces are intersecting the side of the visualized volume at $z/R = 0$, the “body” is cut open and the individual levels are clearly visible. Additionally, the outer iso-surfaces are transparent so that the layering can be observed along the entire span as a lead to assess the gradients around the iso surfaces.

The two vertical contour plots facilitate the spatial orientation in the investigated volume – the control volume – that is marked by a frame of yellow lines passing through the corners of the contour plots. A second set of yellow lines around the control volume holds the coordinate system. The inclined cylinder itself and part of the tunnel are added to help visualize the orientation of the coherent structures with respect to the cylinder and the free stream, which is marked by the white arrows. Grids on the wall and the floor clarify additionally the perspective illustration of the 3-D reconstruction. Two legends with color bars are shown, the top left one with six distinct colors for the iso-surfaces and the continuous color bar on the bottom right for the two contour plots. This form of presentation is relatively complex compared to simple 2-D plots, but it describes the data in the control volume instead of just in a single plane. In figure 3.3 the distribution of vorticity can be examined in the spanwise direction as well as in the planes perpendicular to the cylinder.

In figure 3.4 iso-surfaces of the dimensionless spanwise velocity component, $\frac{W}{U_{\infty} \sin \Lambda}$, are shown. It is evident that this quantity is much more suitable for the examination of the three-dimensional structures in the near wake than the vorticity in spanwise direction. The peel-off process is clearly visible in this figure where the iso-surfaces intersect the side of the control volume that is bound by the ZY-plane at $x/R = 4$. The layered structure of the iso-surfaces is clearly visible and gradients can be estimated by the distance between the different iso-surfaces. The orientation of the iso-surfaces inside the control volume is clarified due to the shading of the inside surfaces. The low-speed regions of the spanwise velocity (iso-surfaces) coincide well with the location of the vortex cores (contour plots) as will be discussed in the next chapter.

By comparing figures 3.3 to 3.4 it becomes evident that the larger coherent structures in the near wake become more obvious when the spanwise velocity component, $\frac{W}{U_{\infty} \sin \Lambda}$ and the shear stress, $\frac{\overline{u'v'}}{\sqrt{\overline{u'^2}}\sqrt{\overline{v'^2}}}$ (see figure 3.5) are examined instead of the vorticity, $\frac{\Omega_z D}{U_{\infty} \cos \Lambda}$. In the vortex cores minima in $\frac{W}{U_{\infty} \sin \Lambda}$ can be observed whereas a maximum in $\frac{\overline{u'v'}}{\sqrt{\overline{u'^2}}\sqrt{\overline{v'^2}}}$ is found in the region between co-rotating vortices. In figure 3.5 the iso-surfaces are intersecting one contour plot as well as the sides of control volume, revealing their interior. At these locations the spatial orientation of the visualized coherent structures can be determined accurately by using the coordinate system established by the yellow axes. The three-dimensionality of the coherent structures in the near wake can be immediately assessed, consequently a visual comparison between different actuation cases is greatly facilitated.

Although for a detailed investigation of the flow, contour plots and 2-D profiles are necessary, the huge amount of volumetric data can best be evaluated by examining the three-dimensional reconstruction of the flow in the entire interrogated control volume. Observations based on the entire volume enable the selection of individual regions of interest for potential further analysis. The examination of data averaged over an entire sequence of events produces only static results – the entire volume is “frozen in time”. In contrast to this, analysis of the PIV data using Proper Orthogonal Decomposition (POD) enables a better understanding of the dynamics of the flow.

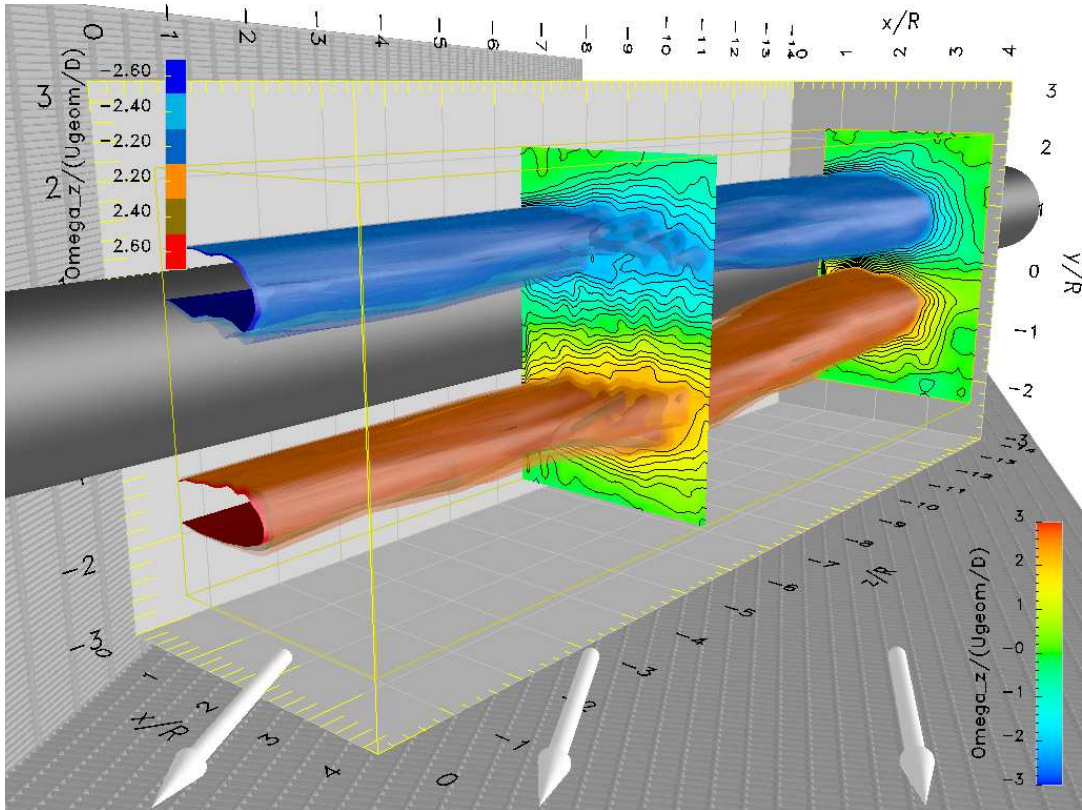


Fig. 3.3: Iso-surfaces of $\frac{\Omega_z D}{U_{\infty} \cos \Lambda}$, baseline, $\Lambda = 60^\circ$, $Re_n = 35000$

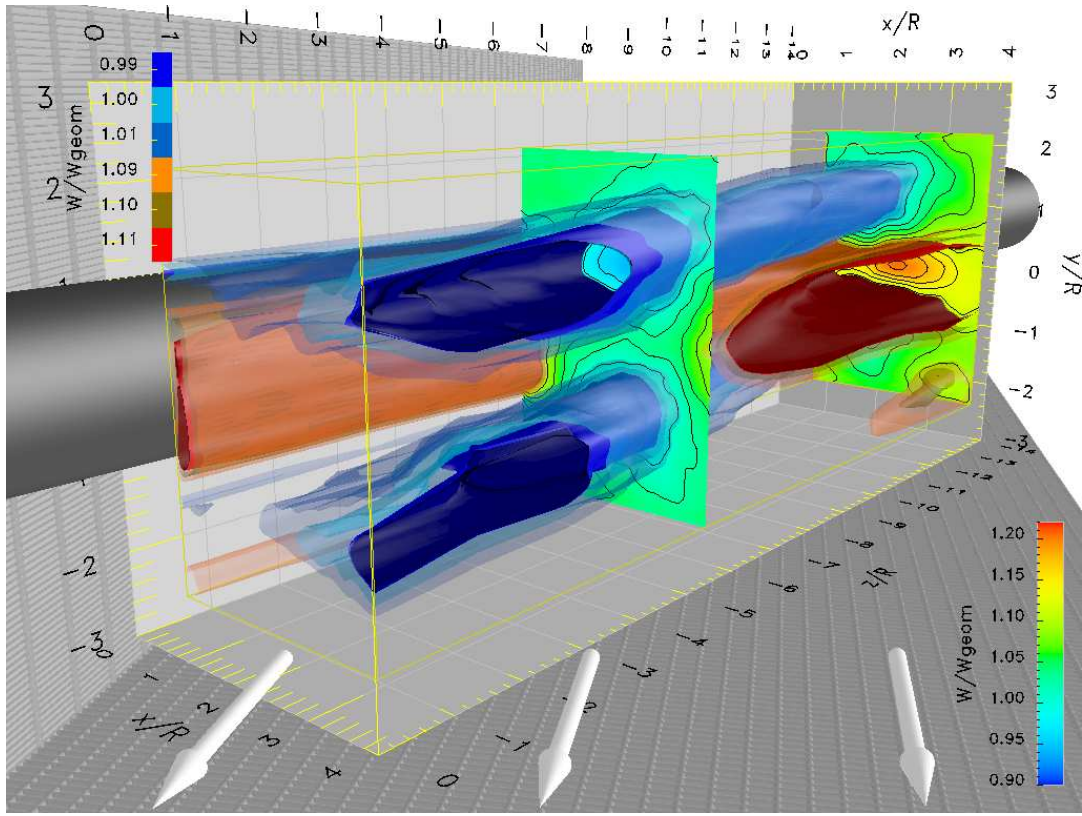


Fig. 3.4: Iso-surfaces of $\frac{W}{U_{\infty \sin \Lambda}}$, baseline, $\Lambda = 60^\circ$, $Re_n = 35000$

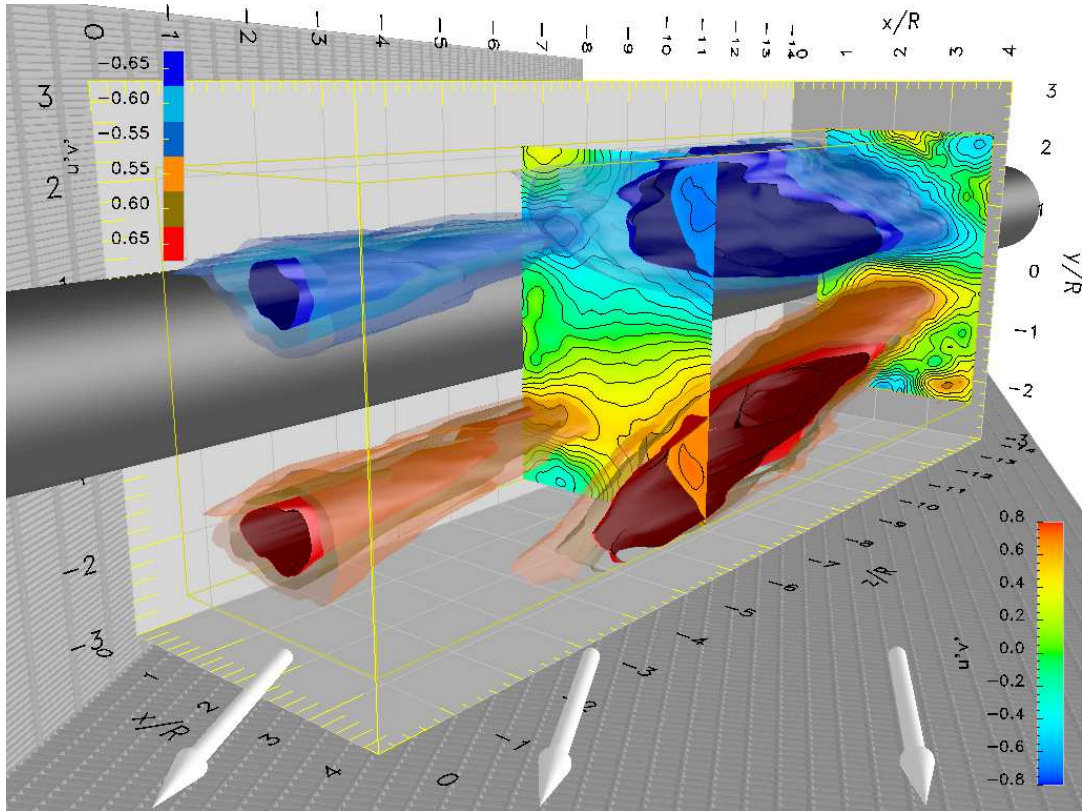


Fig. 3.5: Iso-surfaces of $\frac{\overline{u'v'}}{\sqrt{\overline{u'^2}}\sqrt{\overline{v'^2}}}$, baseline, $\Lambda = 60^\circ$, $Re_n = 35000$

3.4.2 Proper Orthogonal Decomposition

The Proper Orthogonal Decomposition (POD) is a general tool for analyzing multi-dimensional data. The result of a POD are modes forming a new orthogonal base that maximizes the projection of the input data onto the individual coordinate axes. The modes are ordered in a way that forces the first axis to correlate best with the input data, the following ones appear in declining order of significance. Therefore this new coordinate system is mathematically the optimal one to represent the input data. Orthogonality of the POD modes is equivalent to linear independence and therefore it is possible to superimpose individual modes for further analysis and processing. Apart from general data analysis and processing, POD is used widely for data compression.

A data set acquired (in fluid dynamic applications, see for example Kim & Rockwell [14]) as a number of time series taken at multiple locations can be decomposed by POD in a way that results in the maximum decrease (hence “proper”) of energy content with increasing mode number. The term “energy content” is used here strictly under the assumption that the POD is applied to velocity fluctuations.

The POD is a purely mathematical procedure in the way that no analytical base functions are introduced in contrast to, for example wavelet or Fourier transforms. The computed modes are determined solely by the input data, usually the fluctuations. This is considered as an advantage, but can result in POD modes that are difficult to interpret physically.

In the context of fluid dynamics a physical mode is here considered as being any characteristic structure that is non-stationary or unsteady and is thus represented by the fluctuations of the input quantity. Potential difficulties for the interpretation of POD modes are due to the fact that several physical modes can be (entirely or partly) represented by a single POD mode or that a single physical mode can be split into several POD modes. It depends entirely on the complexity of the input data. The POD is a linear operation, thus non-linear processes in the input are mapped onto the linear output.

The linearly independent POD modes can in the best case be directly used for identification and analysis of physical modes. In general, POD can be used for data reduction and analysis by considering only the modes that total a certain fraction of the energy content for the partial reconstruction of a flow field. Thus “noise” contained in higher modes is filtered out.

Basic Procedure

For the decomposition of data acquired by PIV each instantaneously acquired flow field is represented in the form of a single vector containing all velocity components at all spatial locations at a given time (Snapshot POD, see below). For an entire (temporal) data sequence the group of all spatial column vectors is combined into a matrix A .

The correlation matrix C is computed by

$$C = A^T \cdot A \quad (3.3)$$

It contains the cross-correlations between the instantaneously acquired flow fields for the entire data sequence. If velocity fluctuations of a flow field are taken as input to the POD, the unit of the quantities in this correlation matrix is $\frac{m^2}{s^2}$, being proportional to the kinetic energy content for the incompressible case.

A principal axis transformation is applied to this symmetric correlation matrix C to diagonalize it. This is done by solving the Eigenvalue problem

$$C \cdot e = \lambda \cdot e \quad (3.4)$$

For a symmetric, non-negative matrix, all Eigenvectors e are orthogonal, therefore the found modes are linearly independent. The Eigenvectors are ordered by decreasing magnitude of their respective Eigenvalues λ to ensure that lower modes have higher energy content.

Conventional and Snapshot POD

It depends on the type of data, or to be exact, on the dimensions of the matrix A , if a conventional POD or a Snapshot POD should be applied. Data obtained with Hotwire rakes is usually highly resolved in time (n samples) at a limited number of m locations ($n > m$) whereas PIV data is usually well resolved in space (m locations) for a limited number n of realizations in time ($n < m$). To minimize the computational effort the dimension of the correlation matrix should not

be unnecessarily large, thus the Snapshot POD was introduced to complement the conventional POD. The latter, applied to Hotwire data uses the columns of A for the time series, while the rows correspond to data acquired at different locations at the same instant, resulting in an $m \times m$ correlation matrix. In contrast to this the Snapshot POD uses the rows of A for the time series, resulting in a correlation matrix C of dimension $n \times n$.

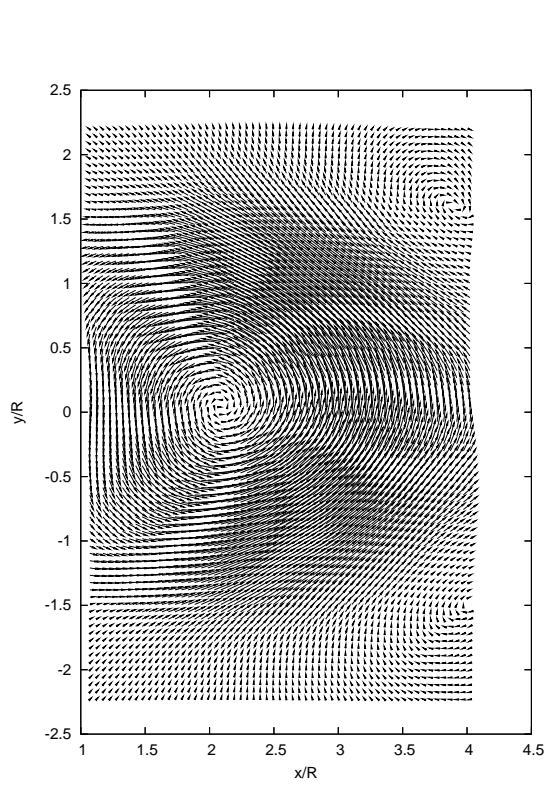


Fig. 3.6: Eigenflow, baseline, $z/R = -10.7$

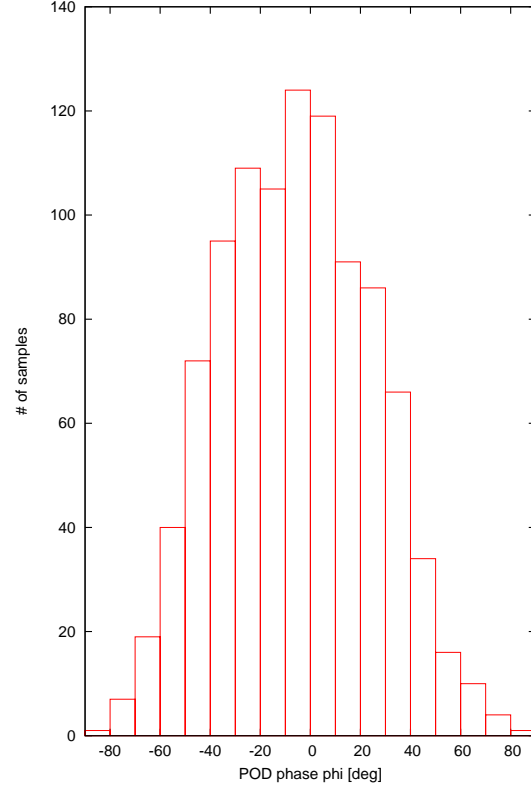


Fig. 3.7: POD phase histogram, baseline

Eigenflows, Modes and Reconstruction

For the Snapshot POD the elements of C represent cross-correlations of spatial vectors at different time delays, thus the Eigenvectors, or modes, are time dependent. By transforming the original data with the n^{th} mode e_n

$$A \cdot e_n = a_n \quad (3.5)$$

the so called Eigenflows a_n are obtained. They depend only on location and represent a pattern fixed in space that is characteristic of the n^{th} POD mode. In contrast to this the Eigenvectors e_n are space dependent for the conventional POD, therefore the coefficients a_n are time dependent in that case.

The Eigenflows are modulated in time by the dyadic product

$$a_n e_n = A_n \quad (3.6)$$

The result is the partial reconstruction of the flow field for the n^{th} mode which is varying in space and time, as does the original data. Reconstructions for different modes can be simply superimposed to obtain combinations of POD modes. Thus it is possible to obtain a flow field of lower dimension that contains a certain percentage of the total kinetic energy of the analyzed fluctuating quantity.

Dynamic Analysis of the Near Wake

The POD analysis of the PIV data yields some important dynamics of the near wake and enables the computation of conditional averages in the absence of any additional information about the processes in the wake that would enable direct conditional sampling or averaging.

The first POD mode of all analyzed data sequences can be interpreted clearly as meandering of the wake around the mean direction of the flow. In figure 3.6 a typical partial reconstruction of the baseline flow based on the first POD mode is presented. In this case the wake oscillates around the point $x/R = 2.1$, $y/R = 0$ and is deflected from its average orientation either up ($y/R > 0$) or down ($y/R < 0$).

The first POD mode contains the most energy of all POD modes, therefore the meandering of the wake is considered the dominant physical mode in the wake of an inclined cylinder. A procedure was developed to compute conditional averages with respect to the meandering of the wake to analyze the dynamics of the wake. It is based on the POD modes determined from the fluctuations of all three velocity components (u' , v' and w') and uses the Eigenflows determined for u and v (see figure 3.6) to determine the classification of the data to enable computing of conditional averages.

In analogy to harmonic oscillations of a pendulum, a phase angle φ is defined based on the maximum deflections of the wake. The phase angle φ is a mathematical interpretation of the first Eigenflows and does not measure the geometric deflection of the wake directly. This choice was necessary because in this study each complete PIV data set consists of several individual series taken at different spanwise positions. The correct (global) interpretation of the data requires a common parameter. This requirement is satisfied by the phase angle, which is independent of individual geometric properties like the local amplitude or the location of the center of rotation of the meandering motion. As the phase angle is based on the extrema of the meandering motion of the wake, the conditional average for $\varphi = 0$ is not necessarily equal to the simple average, depending on the characteristics of the oscillation.

The results of the partial reconstructions are velocity fields and not displacements because the input quantities to the POD are velocities. Nevertheless the sideways deflection of the wake can be deducted directly from the reconstructed velocity fields. The larger the deflection of the wake, the larger is the deviation of the individual velocity field from the mean flow. Thus the deviation is related to the velocities computed during the partial reconstruction.

In the first step of the process the extrema of the sideways deflection of the wake were identified for each data set, based on the reconstructions of the flow field computed with the first POD mode. Depending on the direction of the deflection, the phase angles of $\pm 90^\circ$ were assigned to these extrema. The results of the direction-detecting algorithm were checked for consistency by verifying the continuity of the spanwise flow. Based on this continuity the sign of the phase angle had to be corrected in a small number of cases. This necessity is due to the fact that the wake is not a rigid body, rotating around a single pivot point. Instead two “pivot points” can be found in some of the data sets, corresponding to a shorter wavelength of the meandering. The phase angle at the spanwise station $z/R = 0$ was taken as a reference.

In the second step the phase angle φ was determined for each individual realization from the deflections computed from the individual Eigenflows. According to this phase angle the original data were divided into classes of constant φ . The conditional averages were afterwards computed for each φ from the data sets included in the respective classes. An interval of 10° was considered as being the best compromise between angular resolution and the number of data sets available. A typical histogram for this distribution is shown in figure 3.7. Representative results of the conditional averaging show clearly (figure 3.8) the meandering of the wake around $y/R = 0$. They are similar to the structures observed in individual realizations by Lin et al. [17] on a 2-D cylinder.

The phase angle is based on the extrema of the meandering motion of the wake, thus the conditional average for $\varphi = 0$ is not necessarily equal to the simple average, depending on the characteristics of the oscillation.

This POD based method uses the energy content to determine the characteristic modes of the input data. It enables the direct segmentation of the PIV data into different classes to compute conditional averages of the original, unaltered data. It is advantageous that the procedure is defined purely mathematically and that neither assumptions concerning base functions nor data

manipulation like filtering or spatial shifting of the data fields are required during the process. The main disadvantage for general application is the sometimes problematic interpretation of the computed POD modes. Thus the results have to be carefully checked to ensure the physical relevance. The physical validity of the process was verified with independent experiments, see page 94.

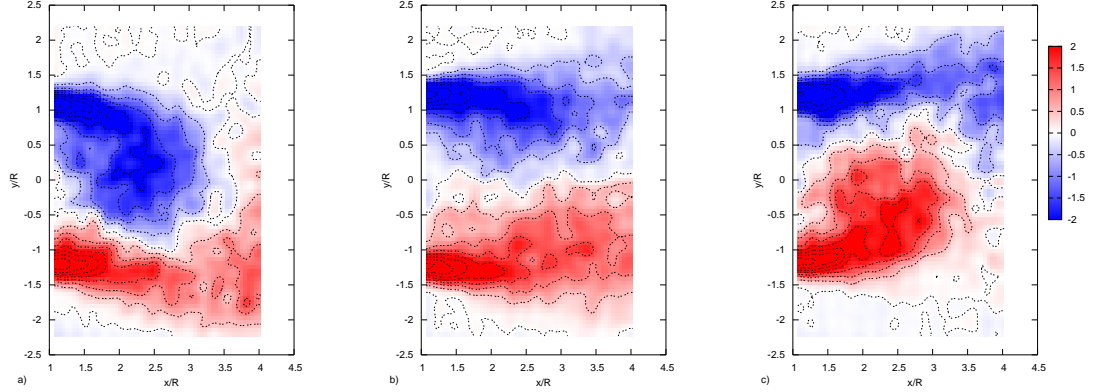


Fig. 3.8: POD phases, Ω_z , baseline, a) $\phi = 40^\circ$ (left), b) $\phi = 0^\circ$ (center), c) $\phi = -40^\circ$ (right), $\Lambda = 60^\circ$, $Re_n = 35000$, $z/R = -6.7$

In contrast to this, Fourier based methods extract the scales in space and time that are contained in the data. Bandpass filtering enables the detailed investigation of preset scales and thus structures of selected sizes. After extracting structures with predefined properties (i.e. size) the data has to be post-processed, in general by correlation and pattern-recognition techniques. The data is modified during the process depending on the chosen parameters. Therefore the results have to be checked carefully to avoid inadvertent data manipulations. The success of the post-processing depends on the complexity of the input data and requires individual adaptation of the process to the investigated problem.

Pattern recognition techniques are problematic in the investigated wake behind an inclined cylinder. Individual small vortices are rolling up into larger coherent structures, their numbers and arrangements change significantly between even consecutive individual realizations because the PIV data is not time resolved. The wake is meandering and thus the vortex patterns are stretched, rotated and sheared. Thus conventional correlation techniques can focus on specific points in the flow field to investigate the coherent structures in detail at exactly those locations, but not necessarily the global dynamics.

3.4.3 Data Acquisition

PIV data were acquired at eleven spanwise stations by positioning the laser light sheet in the middle of each slot, beginning at $z/R = 0$ marked as the “slot number one” closest to the downstream end of the cylinder in figure 2.2. A series of image pairs was recorded, then the laser light sheet was moved to the next slot to take the next data series. The process was repeated along the span of the cylinder up to slot number eleven, at a distance of 22” to the first station. The investigated volume spanned across the center of the test section.

The number of image pairs necessary to obtain stable averages was checked prior to the experiments. A large set of data was acquired and averages were computed over different numbers of vector fields. The convergence of the different averages was analyzed. For the test case a minimum of 300 image pairs was required to obtain stable value for the Reynolds stresses. Based on this result a total of 1000 image pairs was acquired per spanwise station as a compromise to enable the POD based conditional averaging of the data. This resulted in a number of 44000 individual images or approximately 50GB recorded per complete data set.

Baseline data (in the absence of periodic excitation) was acquired randomly. Due to limited storage capacity all other data were phase-locked relative to the excitation signal. In contrast to randomly sampled data the vortices in the shear layer region can be resolved more clearly in this way.

For most of the data points outside of the shear layers the difference computed from data acquired at a single phase (here shown only for 0°) and data averaged locally over 4 different phases (0° , 90° , 180° and 270°) was less than 2.5% for the spanwise velocity component (see figure 3.9). For the horizontal component perpendicular to the cylinder the difference was less than 5% (see figure 3.10) of the corresponding average velocity component. For data points outside the shear layers the difference computed in this way for the vertical velocity component was less than 10% (see figure 3.12) of the maximum of the locally averaged vertical velocity component.

Other acquired phase-locked data rendered similar errors when compared to the average, thus the data set taken at 0° (beginning of the blowing phase) is considered sufficiently representative for all four data sets. Larger differences were observed mostly only in the shear layers that separated from the cylinder. The differences in $\frac{W}{U_\infty \sin \Lambda}$ between data taken phase-locked at a single phase and data averaged over four different phases are distributed relatively homogeneously in spanwise direction.

The spanwise average of this difference is smaller than 1.5% of the local velocity in the outer region of the wake. In this region the vortex peel-off is primarily investigated. Thus the phase-locked data acquisition is considered sufficiently accurate to detect larger coherent structures based on a minimum in the spanwise velocity. Because of the large differences in the number of samples used to form an average (1200 when averaged over four phases compared to only 300 for a single phase $\neq 0^\circ$), the differences in the perceived peel-off of coherent vortices might be caused by an insufficient amount of data used. This is demonstrated in figures 3.13 to 3.15. The first two data sets averaged 1000 and 1200 samples respectively while the third contained only 300 samples. The contours look qualitatively identical. The first two data sets were taken independently over a time interval that spanned several months.

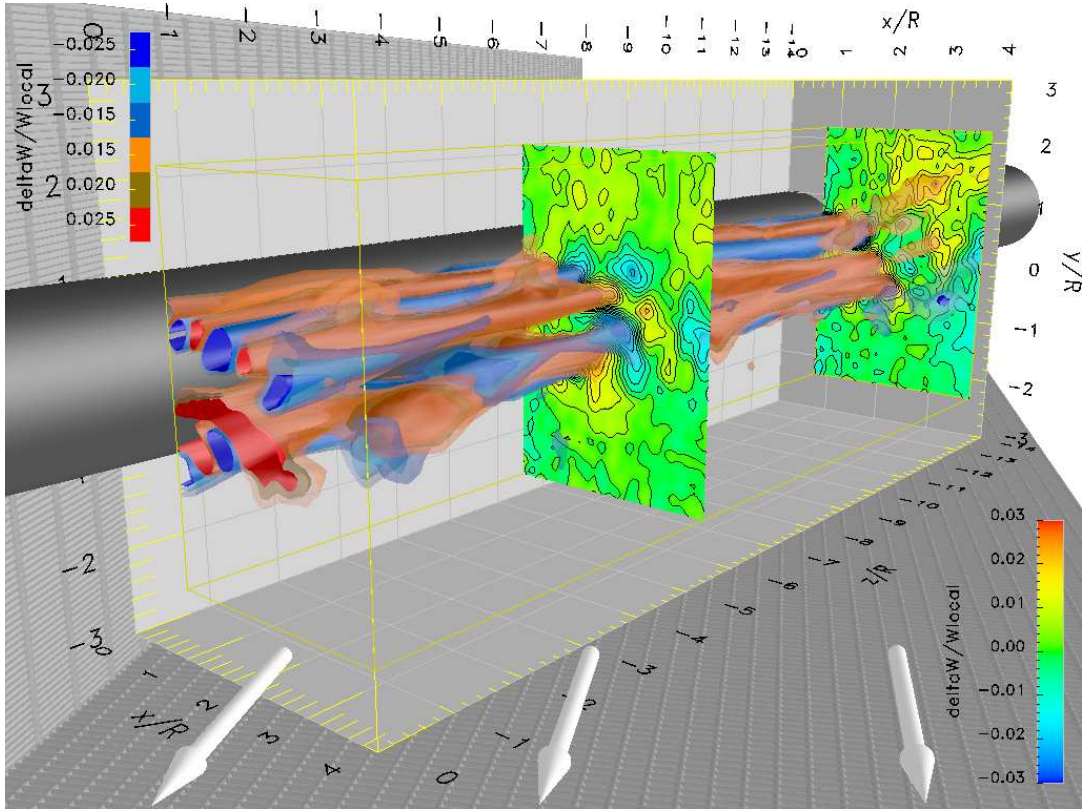


Fig. 3.9: Iso-surfaces of $\frac{W_{90^\circ} - W_{4ph.}}{W_{4ph.}}$, $F_n^+ = 1.52$, $C_{\mu,n} = 7\%$, sym., $\Lambda = 60^\circ$, $Re_n = 35000$

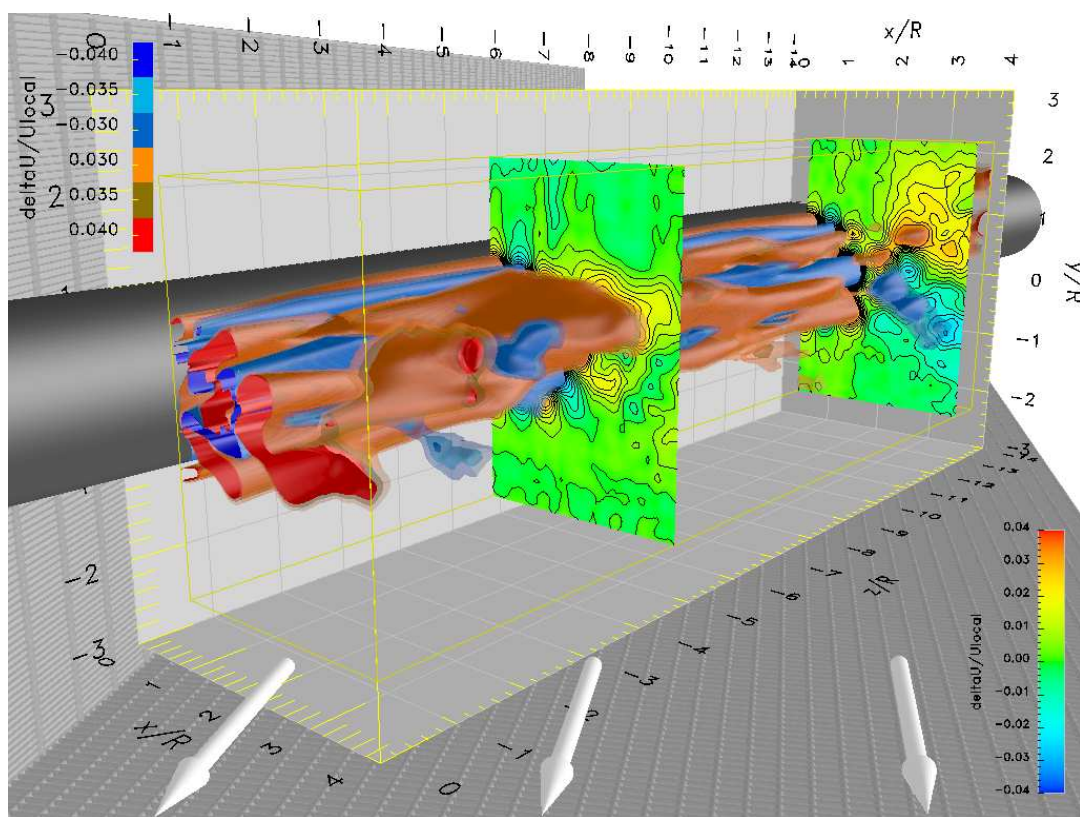


Fig. 3.10: Iso-surfaces of $\frac{U_{90^\circ} - U_{4ph.}}{U_{4ph.}}$, $F_n^+ = 1.52$, $C_{\mu,n} = 7\%$, sym., $\Lambda = 60^\circ$, $Re_n = 35000$

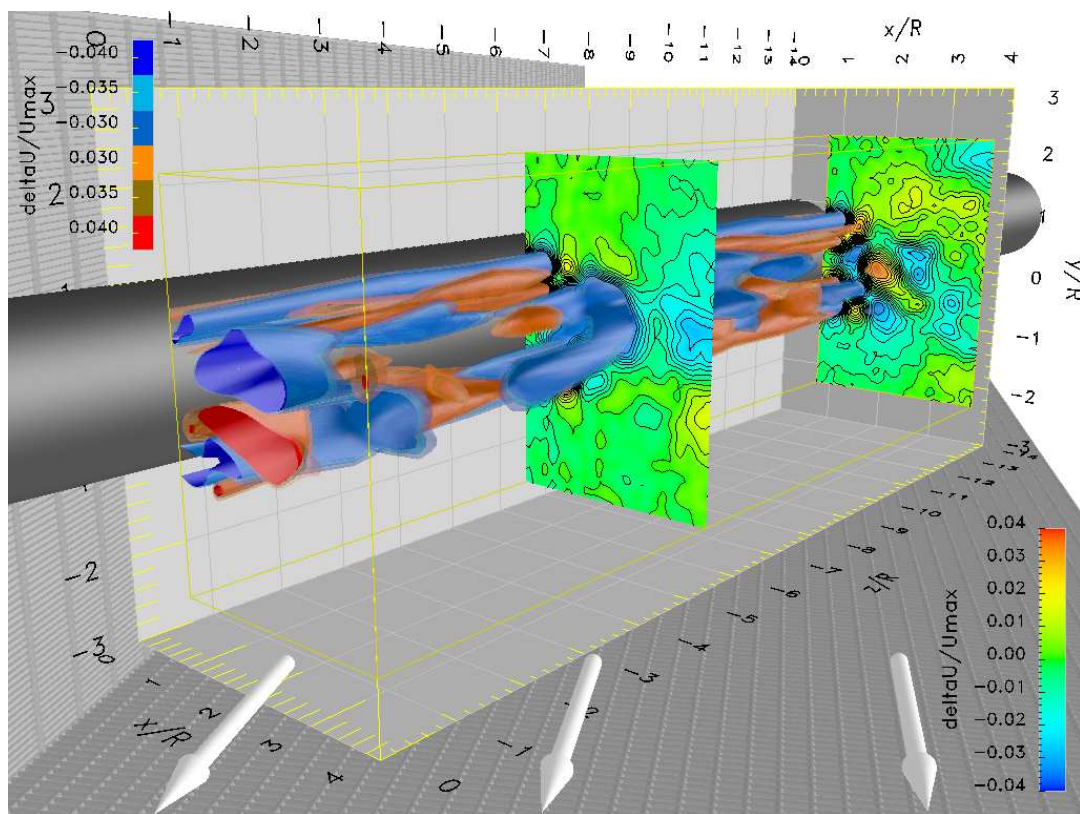


Fig. 3.11: Iso-surfaces of $\frac{U_{90^\circ} - U_{4ph.}}{\max(U_{4ph.})}$, $F_n^+ = 1.52$, $C_{\mu,n} = 7\%$, sym., $\Lambda = 60^\circ$, $Re_n = 35000$

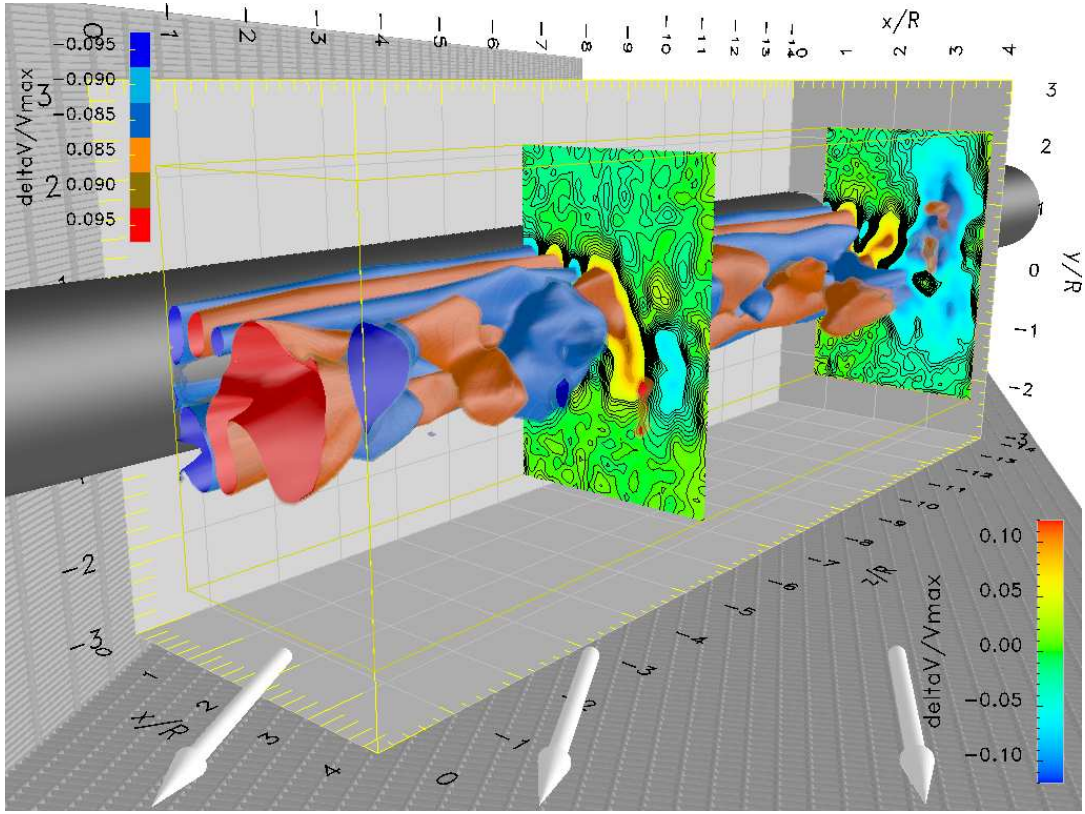


Fig. 3.12: Iso-surfaces of $\frac{V_{90^\circ} - V_{4ph.}}{\max(V_{4ph.})}$, $F_n^+ = 1.52$, $C_{\mu,n} = 7\%$, sym., $\Lambda = 60^\circ$, $Re_n = 35000$

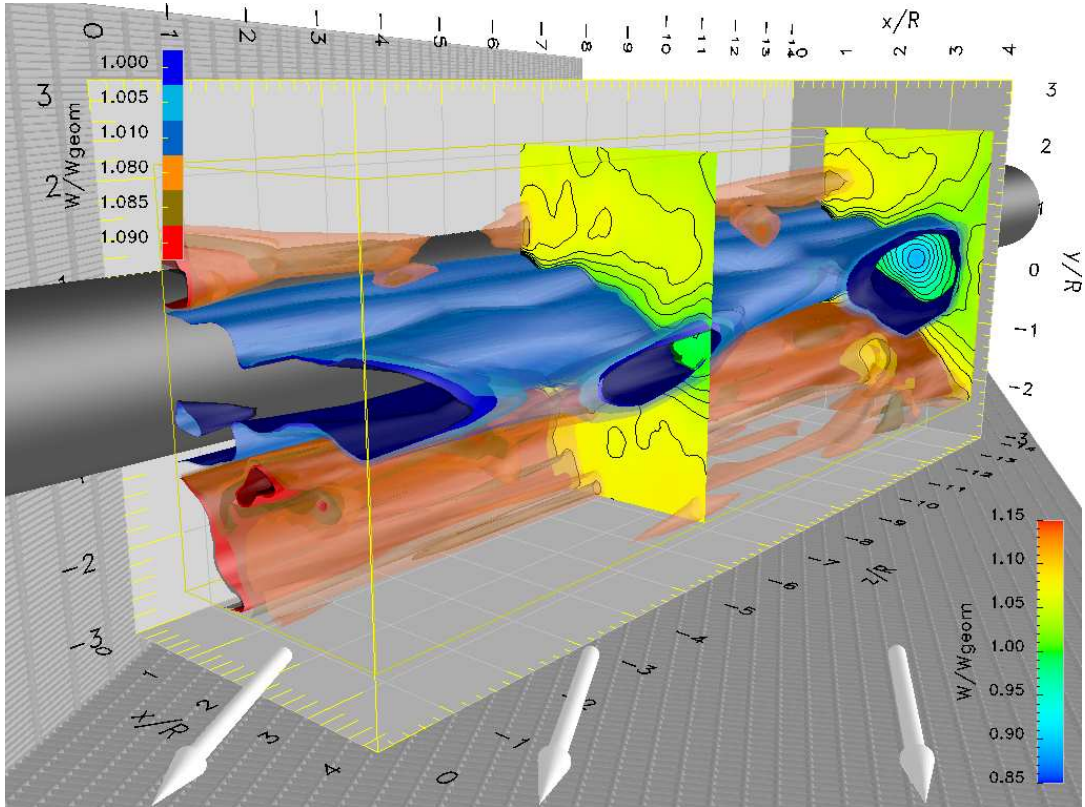


Fig. 3.13: Iso-surfaces of $\frac{W}{U_{\infty} \sin \Lambda}$, $F_n^+ = 1.52$, $C_{\mu,n} = 7\%$, sym., $\Lambda = 60^\circ$, $Re_n = 35000$ phase locked at 0° , 1000 samples

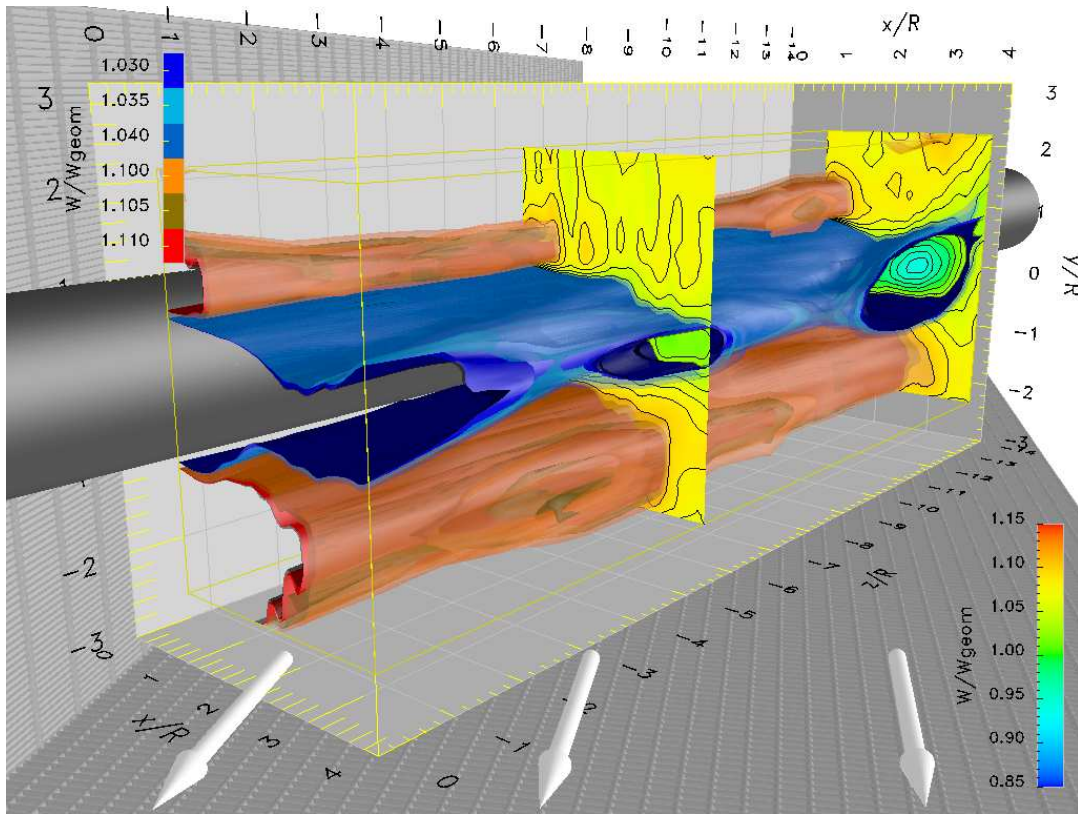


Fig. 3.14: Iso-surfaces of $\frac{W}{U_{\infty} \sin \Lambda}$, $F_n^+ = 1.52$, $C_{\mu,n} = 7\%$, sym., $\Lambda = 60^\circ$, $Re_n = 35000$ averaged over 4 phases, 1200 samples

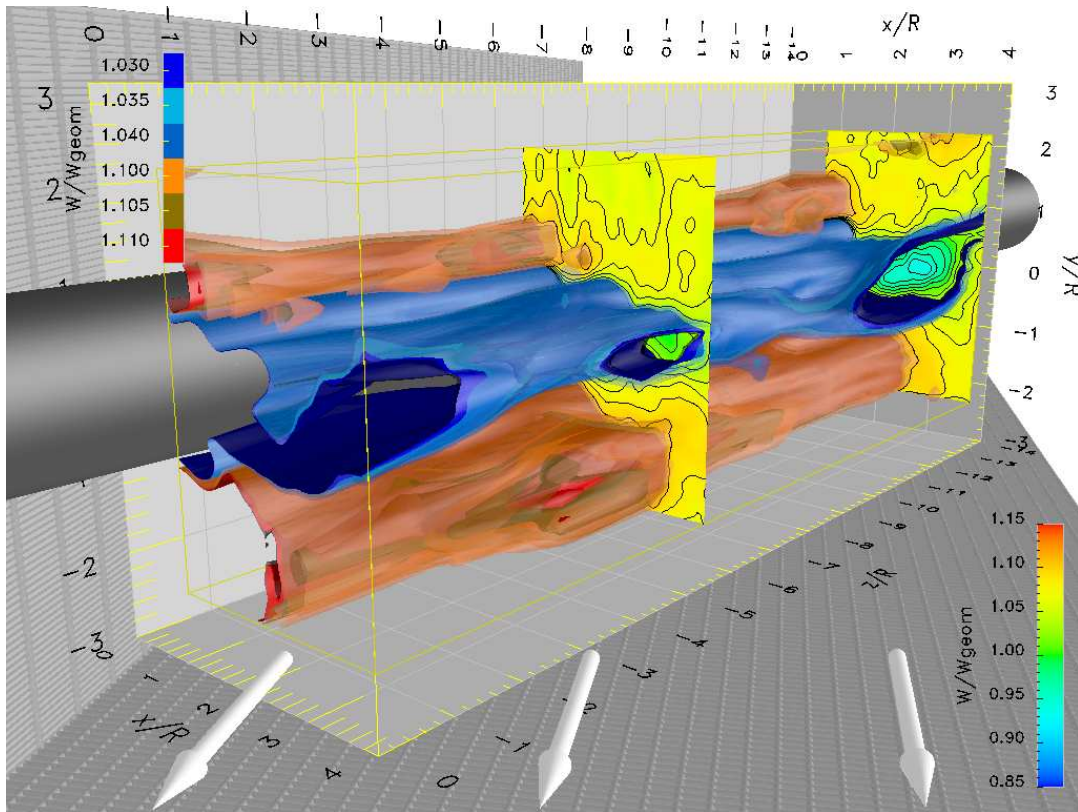


Fig. 3.15: Iso-surfaces of $\frac{W}{U_{\infty} \sin \Lambda}$, $F_n^+ = 1.52$, $C_{\mu,n} = 7\%$, sym., $\Lambda = 60^\circ$, $Re_n = 35000$, phase locked at 180° , 300 samples

Chapter 4

Results and Discussions

4.1 The Experiments – Overview

Active flow control was applied successfully for controlling the yaw angle of a “swiveling cylinder” proportionally to the level of actuation. For this proof-of-concept demonstration a cylinder was mounted on a low-friction bearing on the floor of a wind tunnel and the cylinder was allowed to swivel freely around the vertical axis.

Following these initial experiments a fundamental study of the flow around an inclined cylinder was carried out to investigate in detail the physics governing the flow when actuation is applied. It focussed mainly on a cylinder with a sweep-back angle of $\Lambda = 60^\circ$. At this angle the vortices forming in lee of the cylinder do not shed as observed for smaller sweep-back angles, but instead peel-off along the span. The peel-off locations are stationary, with a spanwise spacing of several diameters. Supplemental data were taken at $\Lambda = 45^\circ$. At this reduced sweep-back angle the vortices separate periodically from the cylinder in a low-frequent oscillation. Data taken at a sweep-back angle of 0° taken on a different setup (2-D cylinder, single slot) are presented in order to compare the complex three-dimensional flow around an inclined cylinder with its two-dimensional analog.

Oscillatory zero-mass-flux actuation was applied through either a single slot or a pair of symmetrically positioned slots to manipulate the flow around the cylinder. Lift and drag forces were controlled and the alterations of the coherent structures in the near wake were studied in detail.

Most runs were carried out at a free stream velocity of 15m/s, corresponding to a normal Reynolds number Re_n of approximately 35000, based on diameter and velocity normal to the cylinder. Further experiments were performed at 20m/s for the $\Lambda = 60^\circ$ case to vary the Reynolds number within a range suitable for the used actuation system. For $\Lambda = 45^\circ$ data were taken at 15m/s and 10.6m/s in a comparable Re range, and at 7m/s for the 2-D case to obtain a similar cross flow Re_n number.

The inclined cylinder was investigated in an “infinite” configuration, spanning the test section from wall to wall, and a finite one with the cylinder ending at 150mm (6”) distance from the wall. Pressure measurements were taken in all cases to determine the forces on the cylinder and the velocity deficit in the far wake. The near wake was investigated in detail for $\Lambda = 60^\circ$ by Particle Image Velocimetry (PIV). The limitation to a single sweep-back angle was necessary due to the available data storage and processing capacity. Finally, the stability of the flow in spanwise direction was investigated by examining the temporal and spatial development of disturbances introduced behind the cylinder using Hotwire and PIV, but no conclusive results were obtained due to the complexity of the flow.

4.2 The Swiveling Cylinder

Two configurations of the swiveling cylinder were investigated. The majority of the experiments were carried out on a cylinder that was pointing downstream, allowed to freely rotate around the vertical axis of its bearing. By actively controlling the side force with zero-mass-flux actuation the yaw angle obtained in equilibrium changed proportionally to the excitation level. Experiments

were carried out successfully at speeds varying from 7m/s up to 120m/s ($Ma=0.4$). The angle between the vertical axis of rotation and the cylinder was 45° and 60° . In a second configuration the cylinder was pointing upstream, held in place by piano wires connected to a rubber suspension. During these low-speed-only experiments the cylinder was only slightly deflected to the side by the actuation. It returned to its initial position aligned to the free stream whenever the excitation signal was turned off. All experiments were recorded on video and were mostly targeted at the visual demonstration of the capabilities to control the yaw angle of the inclined cylinder.

The first experiments were carried out at 7m/s in the open return wind tunnel in the AeroLab. It turned out that tripping of the flow was essential for a successful proportional control of the yaw angle. The flow had to be pre-conditioned to suppress the threshold for C_μ observed in untripped cases. This enabled a smooth operation and proportional control of the yaw angle starting from 0° . The tripping had to be absolutely identical on the opposite sides of the cylinder, otherwise the cylinder would have swung around and one branch of the necklace vortex would have attached to the base of the cylinder. Once this happened the cylinder would rest stable at a yaw angle of $\gamma = 20^\circ$ or more to the free stream. This situation was bistable. When the cylinder was forced (mechanically) to rotate to a yaw angle γ of opposite sign, the new orientation remained stable after removing the external torque. The optimum tripping device for this configuration was found to be an unwound guitar string, stretched along the cylinder and attached to it with double back tape. Only the ends of this three-dimensionally “wavy” wire were taped over to hold it securely in place.

The control of the yaw angle at 7m/s was proportional to the input and the cylinder followed changes in the excitation signal smoothly. It rested in the baseline case (no actuation applied) at $\gamma = -5^\circ$ yaw angle. This was likely caused by the asymmetry of the cylinder due to the single slot. Two internal actuators were mounted close to the tip of the cylinder, each of which was 2” wide. A sectional excitation level of $C_\mu = 1.4\%$ (based on diameter and U_∞ , $f = 250Hz$) resulted in a deflection of $\gamma = 13^\circ$ from the neutral position (-5°) of the cylinder. At $C_\mu = 3.3\%$ the deflection was $\gamma = 25^\circ$.

After the low-speed experiments were finished successfully, a modified setup with actuators mounted internally along the entire span of the cylinder was tested at higher speeds up to 120m/s. The actuation frequencies were adjusted for the individual cases to obtain the maximal performance at all free stream velocities. Some of the results obtained at 25m/s are shown in figure 4.1. An excitation voltage $U = 10V$ corresponded to $C_\mu = 0.3\%$ at 250Hz. The cylinder was deflected to $\gamma > 20^\circ$ (with respect to the free stream) at this relatively low level of forcing. Only proper tripping enabled smooth operation at this Reynolds number, as can be seen at the red curve marked with squares in figure 4.1. Irregularities in the other, untripped cases are likely to be caused by spanwise non-uniformities and a total separation of the flow on the unforced side. In particular the characteristics found for the last two experiments indicate a “lock-in” of the cylinder into one of the bi-stable positions, i.e. the necklace vortex attached entirely to one side of the cylinder.

The bi-stability of the swiveling cylinder was more evident at higher speeds. The cylinder oscillated around a mean resting position of considerable yaw angle γ_1 , but it was possible to move it manually to a stable position with $\gamma_2 = -\gamma_1$ in most cases. The bi-stable characteristics became evident several times during the experiments when hysteresis was observed.

For safety reasons the model was mounted for the high speed experiments in a way that the angle γ was increased with actuation to avoid triggering of the bi-stability by forcing it to yaw

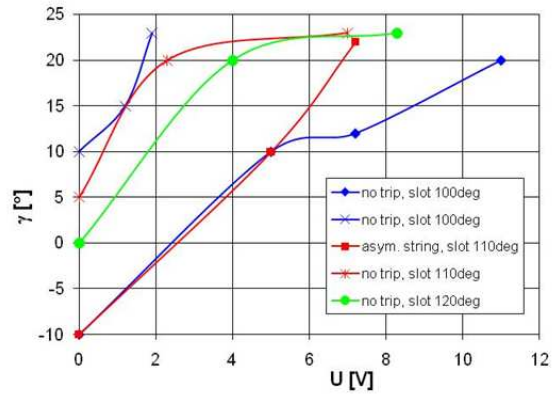


Fig. 4.1: Swiveling cylinder, 25m/s, $f = 250Hz$
 φ vs. excitation voltage, $\Lambda = 60^\circ$,
 untripped and tripped with guitar string

angles too close to the plane of symmetry at $\gamma = 0^\circ$. On the other hand the cylinder overshoot $\gamma = 0$ if the actuation level was reduced too quickly in some cases and the oscillations of the cylinder grew large during the reduction phase in other cases. The result of such an overshoot is presented in figure 4.2 (red curve). Starting from a stable position at $\gamma = 12^\circ$ the level of excitation is increased and the cylinder is forced to larger yaw angles. Reducing the forcing level to quickly resulted in a swing-over to a different stable position at $\gamma = -8^\circ$. Repeating the cycle with a slower decrease of C_μ returned the cylinder to the original position at $\gamma = 12^\circ$.

The actuation performs excellent at $100m/s$, taken into account the very low excitation level of $C_\mu = 0.045\%$ at $400Hz$. Even at this high velocity the yaw angle can be altered by up to 8° . A possibly more significant benefit is the reductions of oscillations of γ by using active flow control. The spanwise uniform excitation stabilizes the flow and reduces spanwise fluctuations considerably.

The experiments on the cylinder pointing upstream demonstrated successfully that the effectiveness of zero-mass-flux actuation is relatively independent of the orientation of the inclined cylinder to the flow.

In a first step into the detailed analysis of the flow around an inclined “infinite” cylinder with active flow control was mounted statically in a wind tunnel, spanning the test section from wall to wall. The cylinder was mounted at a preset yaw angle and the pressure distribution at mid span was measured.

The yaw moment with respect to the (in this case virtual) axis of rotation was computed from the pressure distribution around the cylinder. Only a single row of pressure taps was used due to the limitations caused by the internally mounted actuators. Therefore it had to be assumed that the pressure distribution was uniform along its span. Due to the preset yaw angle the corresponding branch of the necklace vortex was forced to attach to the base of the cylinder. This strong asymmetry stabilized the flow. The three-dimensionality of the flow was thus reduced significantly and the assumption concerning spanwise uniformity can be considered justified.

The results for forcing at various frequencies with $C_\mu = 1\%$ are shown in figure 4.3. A positive yaw moment C_m indicates that the yaw angle would increase on a freely rotating cylinder. Accordingly a negative yaw moment would deflect such a cylinder towards $\gamma = 0^\circ$. The different graphs are for different preset yaw angles and angles of rotation of the cylinder around it’s axis. Computed from both angles is the effective slot location with respect to the free stream, indicated in the legend.

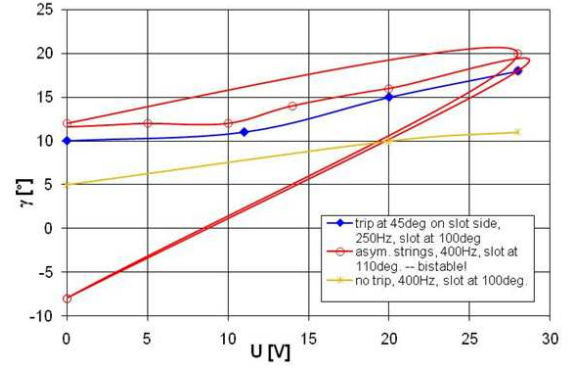


Fig. 4.2: Swiveling cylinder, $100m/s$, φ vs. excitation voltage, $\Lambda = 60^\circ$

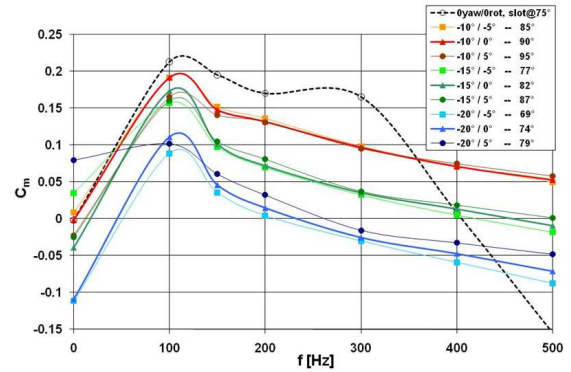


Fig. 4.3: Swiveling cylinder, yaw moment C_m , $\Theta_0 = 110^\circ$, $15m/s$, $C_\mu = 1\%$

4.3 Preliminary Experiments

Experiments on the swiveling cylinder were based on results obtained in earlier experiments on a 2-D cylinder. These results are presented for comparison with the complex three-dimensional flow behind the inclined cylinder.

A fence for preventing the wall boundary layer from disturbing the flow in lee of the inclined cylinder was installed after the initial experiments on the swept-back cylinder. The uniformity of the flow along the span was examined with surface flow visualization.

4.3.1 The Wall Boundary Layer Shedding Fence

Boundary layers on the wind tunnel wall contain spanwise vorticity that accumulates with increasing distance from the contraction. Any object protruding from the tunnel wall will disturb the predominantly two-dimensional boundary layer and force the vorticity to wrap itself around the protrusion like a necklace, hence the term necklace vortex.

The distorted vortices become reoriented in the streamwise direction downstream of the body. They are counter rotating and induce between them a velocity component directed to the wall. For a large obstacle protruding beyond the wall boundary layer the low base pressure may suck these vortices away from the wall. The situation is more conducive to the lifting of the vortices when the bluff body is inclined to the wall at a shallow angle, as is in this case the inclined cylinder at $\Lambda = 60^\circ$. The low pressure region behind the cylinder causes the necklace vortex to lift off the wall. The vortex pair then attaches to the rear of the cylinder, contaminating the natural distribution of vorticity in lee of the model.

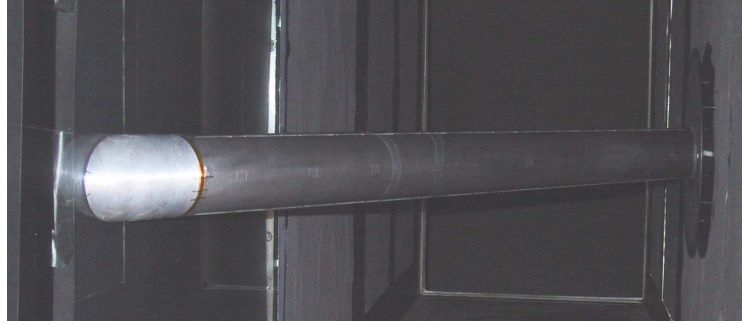


Fig. 4.4: Cylinder with boundary layer shedding fence on right, both slots visible, infinite configuration

The investigated flow was found to be very susceptible to disturbances in the initial conditions that cause a strong asymmetry of the flow field by single-sided attachment of only one branch of the necklace vortex. To prevent the necklace vortex from attaching itself to the base of the cylinder, a round plate having an elliptical cutout was mounted on the inclined cylinder (see figure 4.4). The distance to the tunnel wall was approximately 25mm, so it was outside the wall boundary layer. The plate served as an oversized boundary layer fence that prevented the necklace vortex from lifting off the wall.

It turned out that the very precise adjustment of this fence was of great importance. Due to this a first version of the fence mounted fix in the test section was replaced by one with standoffs that were adjustable from outside the test section during the experiments. A deviation of a few $\frac{1}{10}$ mm from the optimum position resulted immediately in a clearly detectable asymmetry of the flow on the cylinder. With the fence being approximately 0.3 mm out of alignment, the asymmetric pressure profile measured is presented in figure 4.5. The resulting lift coefficient was $C_l = -0.05$. This asymmetry is not necessarily caused by a globally different strength of the vortices on both sides of the cylinder. Instead it can be due to a staggered peel-off of the counter rotating vortices in lee of the cylinder, resulting in spanwise periodic fluctuations of the forces on the cylinder.

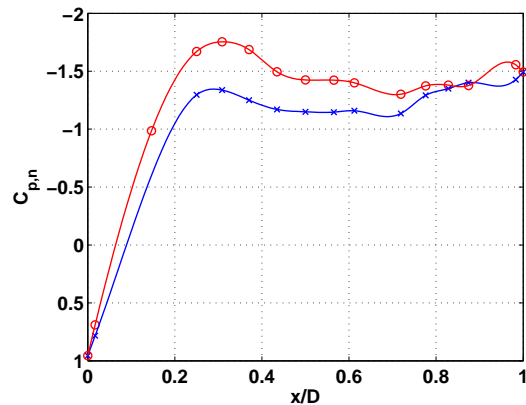


Fig. 4.5: $C_{p,n}$ vs. x/D , baseline, $Re_n = 35000$, $\Lambda = 60^\circ$, red: top, blue: bottom half, fence mis-aligned by 0.3 mm

Vortices on both sides of the cylinder accumulate vorticity generated in its boundary layers. Concurrently that vorticity is convected along the span at a rate depending on the sweep-back angle. The spanwise location where a vortex peels off the cylinder is determined by the accumulation of the vorticity along the span. Once the size of a vortex exceeds a critical value it starts to peel-off. The strengthening of a vortex on one side of the cylinder due to asymmetric boundary conditions will therefore result in its premature peel-off. The undisturbed vortex on the opposite side will have to accumulate vorticity over a longer period to grow to the same strength and size, therefore it is separating from the cylinder at a different, more downstream location. Thus the symmetry of the flow can be assured only by carefully adjusting the inflow conditions at the upstream end of an inclined cylinder.

4.3.2 Flow visualizations

Some of the first experiments carried out were surface flow visualizations with a suspension of Titanium Dioxide (“china clay method”) to assess the location and potential spanwise variation of the flow separation. A dummy model with taped pressure taps and slots was used. This was necessary to prevent any fluid from entering the inside of the cylinder. The model was painted black to enhance the contrast between the white Titanium Dioxide and the surface. The cylinder was mounted on a fixture that enabled contiguous adjustment of the sweep-back angle in the interval $60^\circ \leq \Lambda \leq 75^\circ$ so that several different sweep-back angles could be investigated easily. The end of the cylinder was kept blunt to allow for simple adjustment over the entire range of sweep-back angles and end effects were of no concern at this point of the investigation. For the “infinite” case the cylinder was just touching the wall. As presented in figures 4.6 and 4.7 for the

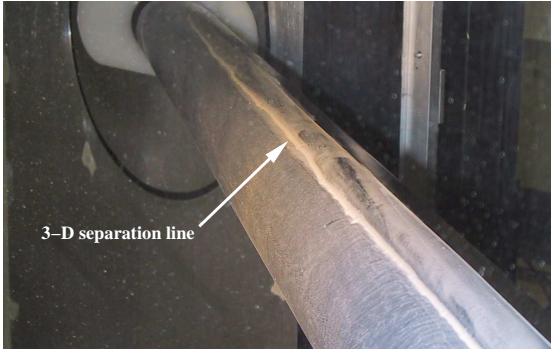


Fig. 4.6: Visualization, $\Lambda = 60^\circ$, $Re_n = 35000$

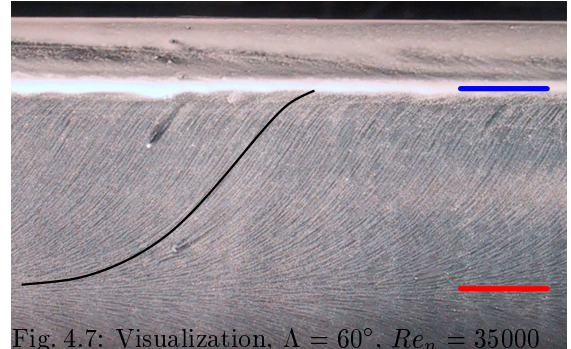


Fig. 4.7: Visualization, $\Lambda = 60^\circ$, $Re_n = 35000$

black: wall stream line
blue: 3-D separation line
red: 3-D “stagnation” line

infinite configuration the flow was uniform along the span, showing a 3-D separation line (marked in blue in figure 4.7) that is aligned with the axis of the cylinder. Only the last 0.25 D (approx. 20mm) were non-uniform (see figure 4.9) due to end effects. The end effects were comparable for all investigated sweep-back angles. The three-dimensional front “stagnation” line (marked in red) where the azimuthal velocity component vanishes is clearly visible in figure 4.7. Below and above this line of purely spanwise motion the flow was deflected around the cylinder. The azimuthal velocity of a fluid element traveling around the cylinder increases due to the favorable pressure gradient in azimuthal direction. After the pressure minimum is reached upstream of the 3-D separation line, the azimuthal motion is decelerated and the particles on the surface follow a more spanwise direction. The fluid element travels on an “S-shaped” path. This effect is marked by a black line on figure 4.7 between stagnation and separation line. Similar results were obtained for a finite configuration at a sweep back angle of $\Lambda = 64^\circ$ with a distance of 100 mm (4”) between the end of the cylinder and the wall. The spanwise uniformity of the flow was again excellent, as presented in figures 4.8 to 4.10). The cross flow Reynolds number was $Re_n = 35000$ in all presented cases.

Fig. 4.8: Visualization (detail), $\Lambda = 64^\circ$ Fig. 4.9: Visualization (end effect), $\Lambda = 64^\circ$ Fig. 4.10: China clay visualization, $\Lambda = 64^\circ$, $Re_n = 35000$

4.4 Asymmetric Forcing

The yaw angle of the swiveling cylinder was controlled proportionally to the forcing level by generating an asymmetric pressure distribution using active flow control through a single slot. Only cumulative effects were determined on this simple demonstration setup by measuring the equilibrium yaw angle.

For a detailed investigation of three-dimensional effects around an inclined circular cylinder a model was mounted statically in a wind tunnel at zero yaw. Due to the internal actuation the space inside the cylinder was limited, thus only a single row of pressure taps was used. The inability to determine potential spanwise variations of the flow by pressure measurements was compensated by using Particle Image Velocimetry (PIV) in the near wake at several spanwise stations distributed over 50% of the span of the cylinder. This enabled a detailed analysis of the flow structure in lee of the inclined cylinder. The cylindrical model was used for symmetric and asymmetric zero-mass-flux actuation, in the latter case the unused slot was taped to avoid interference on the unforced side of the cylinder. Prior to any experiments using excitation on the cylinder the boundary layer shedding fence was carefully adjusted to obtain a symmetric baseline pressure distribution. This symmetry was verified before and after each series of experiments.

Experiments were mostly carried out in an “infinite” configuration, with the cylinder spanning the wind tunnel test section from wall to wall, at sweep-back angles of $\Lambda = 60^\circ$ and $\Lambda = 45^\circ$. During the experiments the determination of the total drag proved to be difficult due to wall interference at the downstream end of the cylinder. Thus a finite configuration of an inclined cylinder was used to determine the effect of asymmetric actuation on the total drag, C_d .

4.4.1 The Infinite Cylinder

PIV data taken in the near wake of the infinite inclined cylinder with asymmetric actuation provided detailed information about the three-dimensional effects that were identified during the initial analysis of the pressure distributions. These pressure measurements provided conclusive lift and drag measurements despite the limitation to a single spanwise location.

4.4.1.1 Forces on the Cylinder

On the 2-D cylinder the effect of the excitation on lift and drag is mainly dependent on the location and the level of actuation, expressed by the momentum coefficient $C_\mu = \frac{2b}{D} \left(\frac{\sqrt{u_s^2}}{U_\infty} \right)^2$ and

only secondly on the frequency to which the flow is sensitive for $C_\mu < 6\%$ (see figures 4.11 and 4.12). Three regions can be distinguished in these figures: Below the first critical value of C_μ the lift varies little with the level of excitation. In this first region the flow is reattaching only downstream of the slot, thus the main effect is the reduction of the total drag, C_{dp} . Beyond this first critical value C_l and C_{dp} both vary strongly with C_μ up to the second critical value of the momentum coefficient. In this second region of the curves the flow is reattaching upstream of the slot until the 2-D separation bubble is eliminated and a “saturated” state is reached. The rate of variation is reduced when the second critical value of C_μ is exceeded and the flow is forced to reattach further downstream of the slot. For the two-dimensional cylinder the first critical value of C_μ decreased by 50% and the second by 30% when the dimensionless frequency was doubled from $F^+ = 1$ to $F^+ = 2$ (figure 4.11). This is due to the sensitivity to the actuation frequency of the shear layer upstream of the slot.

The form drag does not decrease significantly beyond the second critical value of C_μ whereas the lift increases throughout the entire investigated range of C_μ . This is due to the fact that the flow is attached upstream of the slot once the second critical value is exceeded. Increasing the level of actuation above this value lowered the minimum pressure, but the major characteristics of the pressure distribution remain unaltered as described by Taubert & Wygnanski [27]. Therefore the circulation and thus the lift increase substantially but the drag does not change significantly because the pressure difference between the front and aft sectors of the cylinder remains almost constant.

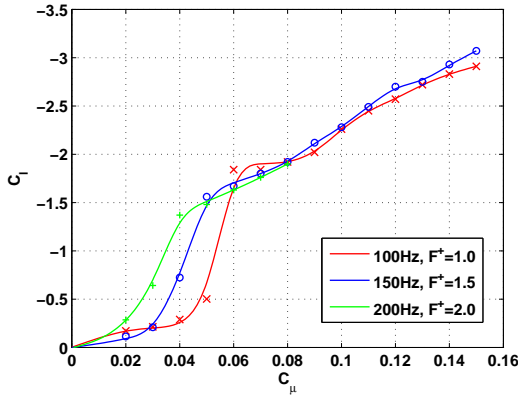


Fig. 4.11: C_l vs. C_μ , single slot, $\Theta = 110^\circ$, $\Lambda = 0^\circ$, $Re_n = 35000$

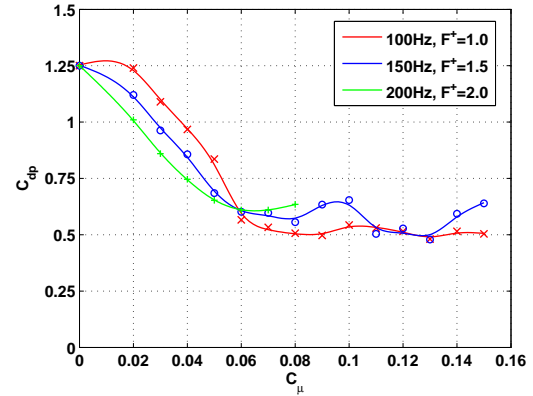


Fig. 4.12: C_{dp} vs. C_μ , single slot, $\Theta = 110^\circ$, $\Lambda = 0^\circ$, $Re_n = 35000$

The two critical values for C_μ exist as well at $\Lambda = 60^\circ$ $\Theta > 105^\circ$, but still the characteristics of the flow differ from the 2-D case (see figures 4.13 and 4.14). At $\Theta = 110^\circ$ the form drag is increased over the entire investigated range of frequencies when forcing below the first critical value of $C_{\mu,n}$. This is due to the increased distance in streamwise direction between the separation location and the slot in the inclined cases.

Increasing $C_{\mu,n}$ beyond the second critical value results again only in marginal increase of lift. Interesting is the difference in the dependence of C_l on the excitation frequency between $\Lambda = 0$ and $\Lambda = 60^\circ$. For the latter the effect can be neglected for $C_{\mu,n} < C_{\mu,n,crit2}$, whereas for larger levels of forcing C_l clearly depends on the excitation frequency. This is most likely due to the shallow 3-D separation bubble, observed by Wu et al. [34], forming upstream of the slot on the inclined cylinder. The largest values of C_l were obtained for excitation frequencies of $1.3 < F_n^+ < 1.8$, depending on the level of forcing (see figure 4.15).

In spite of three-dimensional flow and its variations the surface pressure measurements taken at a single spanwise location are considered conclusive after careful evaluation of the spanwise non-uniformities. Spanwise variations were estimated by comparing the results obtained on the infinite and finite configurations (see page 64) with the pressure taps being located at different spanwise positions. For forcing at low C_μ and at larger slot angles three-dimensional effects dominate the

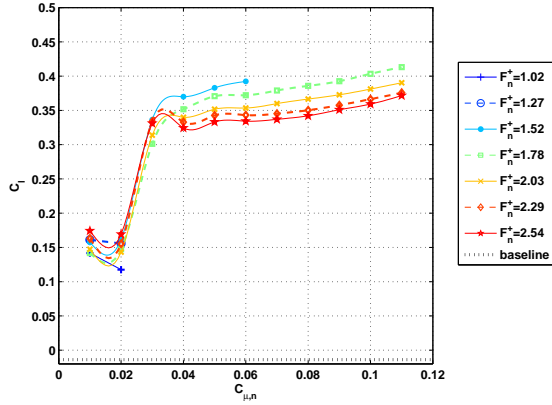


Fig. 4.13: C_l vs. $C_{\mu,n}$, $\Theta = 110^\circ$, asym.,
 $\Lambda = 60^\circ$, $Re_n = 35000$

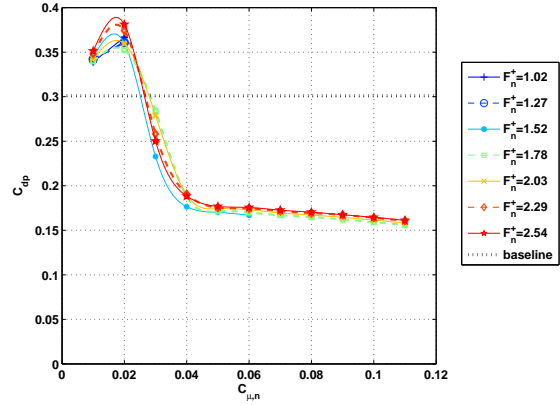


Fig. 4.14: C_{dp} vs. $C_{\mu,n}$, $\Theta = 110^\circ$, asym.,
 $\Lambda = 60^\circ$, $Re_n = 35000$

flow, therefore no valid estimate could be obtained for the spanwise variation of the pressure distributions and thus C_l and C_{dp} . Results for various frequencies emanating from a single slot location are shown in figures 4.13 and 4.14 while the effect of changing the slot location is presented in figures 4.16 and 4.17 for the representative excitation frequency of $F_n^+ = 1.78$ ($f = 175\text{ Hz}$, curves smoothed). The boundary layer shedding fence was adjusted carefully to obtain symmetry in the baseline cases in spite of changes in the flow caused by the varying slot location. This caused slight variations of the distance between the large coherent structures and the surface of the cylinder (see pages 64 ff) and thus differences in C_{dp} for the baseline cases.

Interesting is the discontinuity in the slope of the lift curves shown in figure 4.16 for slot angles larger than $\Theta = 110^\circ$. In particular for slot angles from $\Theta = 115^\circ$ to $\Theta = 125^\circ$ a plateau of moderate slope is enclosed between two regions with relatively large increase of C_l with $C_{\mu,n}$. For larger angles the plateau is less pronounced due to the reduced initial slope. This plateau was not observed on the 2-D cylinder (figure 4.11) and therefore is attributed to three-dimensional effects. The control of the yaw angle on the swiveling cylinder at slot angles between $\Theta = 100^\circ$ and $\Theta = 120^\circ$ was proportional to the excitation level, no discontinuities were found. Thus the observed plateaus have to indicate spanwise inhomogeneities in the generation of lift. The potential stimulation of spanwise variations in the coherent structures by asymmetric actuation was confirmed by PIV as described below.

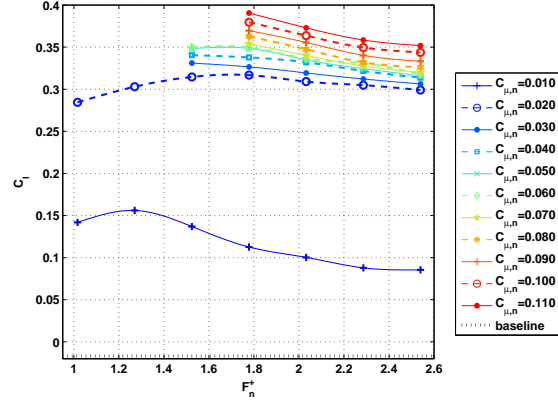


Fig. 4.15: C_l vs. F_n^+ , $\Theta = 105^\circ$, asym.,
 $\Lambda = 60^\circ$, $Re_n = 35000$

The form drag C_{dp} is initially increasing with $C_{\mu,n}$ before reaching a critical value and dropping sharply. This again differs from the situation found on the 2-D cylinder (figure 4.12), where the form drag decreases uniformly with increasing $C_{\mu,n}$. The maximum (see figures 4.14 and 4.17) coincides with the second step increase of C_l presented in figures 4.13 and 4.16. The position of the maximum in C_{dp} depends strongly on the slot position. These significant differences between the 2-D results and the results obtained at $\Lambda = 60^\circ$ suggest that a closer look at individual pressure distributions is desirable. (see page 34). For a slot position of $\Theta = 110^\circ$ the form drag is reduced by a factor of approximately two for the maximum $C_{\mu,n}$ used during the investigation.

The lift and the form drag curves obtained for different slot locations can be collapsed by a procedure based on a two stage curve fit. The second critical value for $C_{\mu,n}$ (sharp decrease in C_{dp}) likely depends on the slot location, in particular on the distance between slot and shear layer.

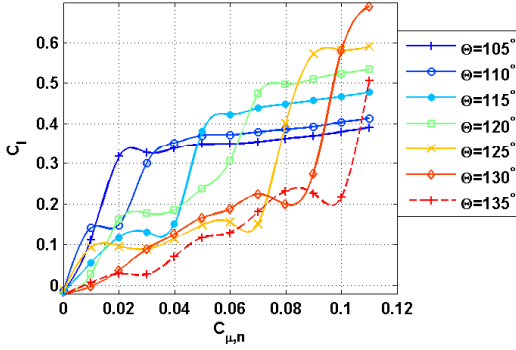


Fig. 4.16: C_l vs. $C_{\mu,n}$, $F_n^+ = 1.78$, asym.,
 $\Lambda = 60^\circ$, $Re_n = 35000$

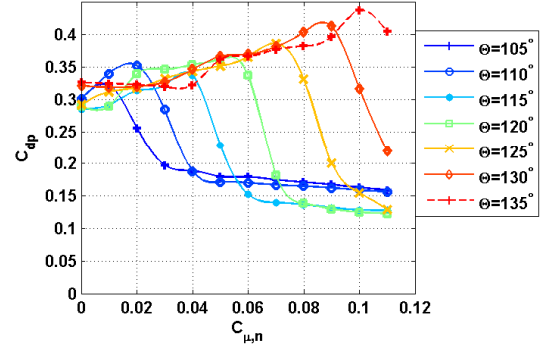


Fig. 4.17: C_{dp} vs. $C_{\mu,n}$, $F_n^+ = 1.78$, asym.,
 $\Lambda = 60^\circ$, $Re_n = 35000$

The momentum coefficient $C_{\mu,n}$ was scaled under this assumption by fitting the data with

$$C_l(C_{\mu,n,crit2}) = a \left[1 - \cos \left(\Theta - \frac{\pi}{2} \right) \right] \quad (4.1)$$

with $1 - \cos(\Theta - \frac{\pi}{2})$ being the vertical distance between the slot and a point at $\Theta = 90^\circ$ on the cylinder and a fitting coefficient a determined to $a = 0.36$. This scaling was applied to the C_l curves as well as to the C_{dp} graphs. In a second step C_l was scaled with the results of the curve fit

$$C_l(C_{\mu,n,crit2}) = \left\{ b \left[1 + \sin \left(\Theta - \frac{\pi}{2} - c \right) \right] + d \right\} \left(\Theta - \frac{\pi}{2} \right) \quad (4.2)$$

and C_{dp} was scaled with the coefficients obtained from the fit

$$C_{dp}(C_{\mu,n,crit2}) = e \left[1 - \cos \left(\Theta - \frac{\pi}{2} \right) \right] + f \quad (4.3)$$

The Ansätze for the curve fitting were determined empirically from geometric considerations. The form drag is scaled with the vertical distance between slot and a point at $\Theta = 90^\circ$, in combination with the offset f . For proper scaling of the lift a combined linear/trigonometric Ansatz proved to be most suitable. The term $[1 + \sin(\Theta - \frac{\pi}{2} - c)]$ corresponds to the horizontal distance between leading edge and slot. It is complemented by the linear term $(\Theta - \frac{\pi}{2})$ and the fitting coefficients b , c and d .

The results are presented in figures 4.18 and 4.19. The data collapse reasonable, with the exception of slot locations $\Theta < 115^\circ$ for C_{dp} and low levels of excitation for C_l . For the lift this is attributed to 3-D effects. A curve averaged over all Θ converges against their 2-D counterpart, although $\frac{dC_l}{dC_\mu}$ is reduced.

The deviation of the form drag curves for smaller Θ from the average is most likely due to the slot geometry. The straight slot is inclined at 30° to the surface of the cylinder and the oscillating jet emerging from the slot attaches to the surface of the cylinder due to the Coanda effect. Nevertheless perturbations can be observed at some distance to the surface of the cylinder. Therefore the excitation potentially disturbs the flow at smaller Θ when forcing at a low $C_{\mu,n}$ that is not suitable to fully reattach the flow upstream of the slot.

The pressure distributions are presented in two projections to facilitate analysis of the flow. The first one is given in a horizontal direction (parallel to U_∞) and described in airfoil-type coordinates with the origin at the leading edge, allowing one to assess easily the lift visually. The second is a projection onto a vertical axis (perpendicular to U_∞ and normal to the cylinder's axis) for analyzing form drag, in particular it facilitates greatly the identification of changes in the base pressure caused by stationary vortices that are close to the cylinder's surface.

Figures 4.20 and 4.21 demonstrate clearly the generation of lift resulting from the asymmetric flow induced by actuation. The pressure distributions were transformed to a cylindrical cross-section, as described on page 96. Interesting is the small plateau (figure 4.21) around $x/D = 0.5$ that is found in many of the acquired pressure distributions. The flow separates upstream of 90° ,

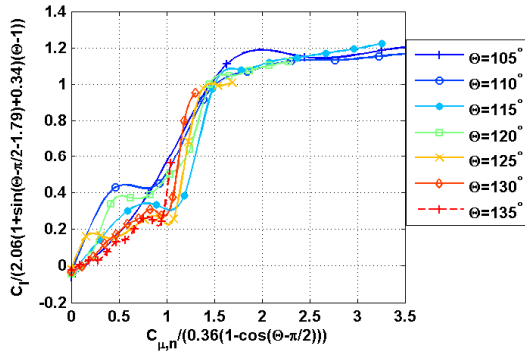


Fig. 4.18: Collapsed lift, $F_n^+ = 1.78$, asym.,
 $\Lambda = 60^\circ$, $Re_n = 35000$

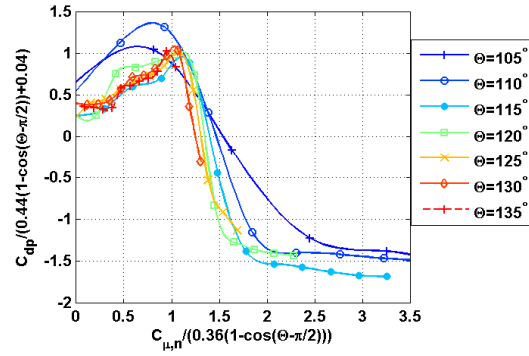


Fig. 4.19: Collapsed form drag, $F_n^+ = 1.78$, asym.,
 $\Lambda = 60^\circ$, $Re_n = 35000$

forming a separation bubble before reattaching upstream of the slot. For a slot angle of $\Theta = 110^\circ$ this separation bubble is shallow and reattachment occurs at some distance upstream of the slot. For the larger angle of $\Theta = 130^\circ$ two separation bubbles may exist (figure 4.25): a shallow one similar to the one found at $\Theta = 110^\circ$ and a second larger one directly upstream of the slot. The slope of the pressure coefficient around $x/D = 0.6$ is less pronounced than for the slot location of $\Theta = 110^\circ$, suggesting that the flow is intermittently reattaching in this region. The flow reattaches completely at the slot located at $\Theta = 130^\circ$.

The two different levels of actuation from a slot located at $\Theta = 130^\circ$ that are presented in figures 4.24 to 4.27 are characteristic for two different states of the actuated flow (see figure 4.16). With the single slot located at $\Theta = 130^\circ$, actuation at $C_{\mu,n} = 4\%$ causes asymmetry, but the change in lift is moderate. Actuation at $C_{\mu,n} = 11\%$ generates maximum lift at the beginning of the saturated region indicated by the plateau at larger values of $C_{\mu,n}$. The pressure distribution at the lower actuation level of $C_{\mu,n} = 4\%$ is presented in figure 4.24. The flow is already clearly asymmetric and the minimum pressure is reduced to $C_{p,n} = -2.2$ with the suction peak still located in the interval $0.25 < x/D < 0.3$. The distribution of the base pressure shown in figure 4.26 is now asymmetric with a local pressure minimum at $y/R = 0$, suggesting that a single strong vortex is located around $y/R = 0$.

The pressure distributions in figures 4.20 to 4.23 illustrate the effects of asymmetric actuation compared to the baseline. The slot was located at $\Theta = 110^\circ$, $x_s/D = 0.67$, forcing was applied at $F_n^+ = 1.78$, $C_{\mu,n} = 11\%$. The flow structure is relatively simple for a slot angle of $\Theta = 110^\circ$ (figures 4.21 and 4.23). The minimum pressure of $C_{p,n} = -4.3$ is found around $x/D = 0.5$, and with exception of the shallow separation bubble discussed above the flow is attached to approximately $x/D = 0.75$, $y/R = 0.85$ ($\approx 120^\circ$). Downstream of this point the slope of the pressure coefficient decreases (figure 4.21), indicating intermittent separation. Upstream of the slot the pressure distribution resembles the one of a cylinder at $\Lambda = 0^\circ$ but is slightly modified by the shallow separation bubble. Significant differences to the pressure distribution on a 2-D cylinder with asymmetric forcing are found for $x/D > 0.8$ where the curves from top and underside cross over (figure 4.21). Stationary vortices close to the cylinder cause a distortion of the base pressure profile (figure 4.23) with a local pressure maximum at approximately $y/R = 0.5$ (150°) and a local minimum located at $y/R = -0.7$ (-135°).

Forcing at $C_{\mu,n} = 11\%$ from the larger slot angle of $\Theta = 130^\circ$ (see figure 4.27) changes the characteristics of the flow considerably. The minimum pressure is now $C_{p,n} = -5.2$ and is still located around $x/D = 0.45$. The flow separates on the suction side at $x/D = 0.65$, reattaches only directly upstream of the slot ($x/D = 0.82$) and starts to separate at approximately $x/D = 0.9$, $y/R = 0.6$ ($\approx 145^\circ$). Except for the slot region no significant distortions of the base pressure can be observed, a single dominant stationary vortex is located close to -145° ($y/R = -0.6$).

Transforming the pressure distributions (and force coefficients) to a plane normal the cylinder requires re-normalization by the geometric velocity component perpendicular to the axis of the

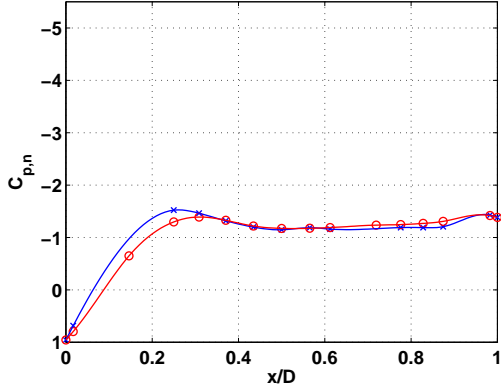


Fig. 4.20: $C_{p,n}$ distribution, $\Theta = 110^\circ$, asym., $x_s/D = 0.67$, baseline, $\Lambda = 0^\circ$, $Re_n = 35000$

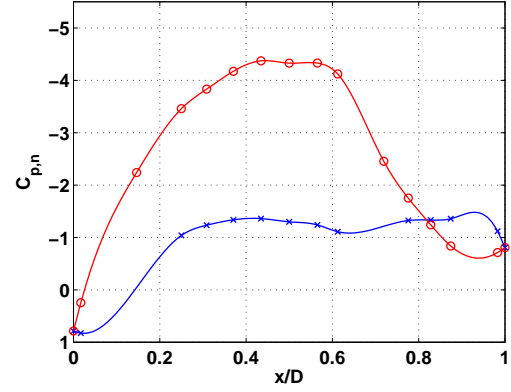


Fig. 4.21: $C_{p,n}$ distribution, $\Theta = 110^\circ$, asym., $x_s/D = 0.67$, $F_n^+ = 1.78$, $C_{\mu,n} = 11\%$, $\Lambda = 0^\circ$, $Re_n = 35000$

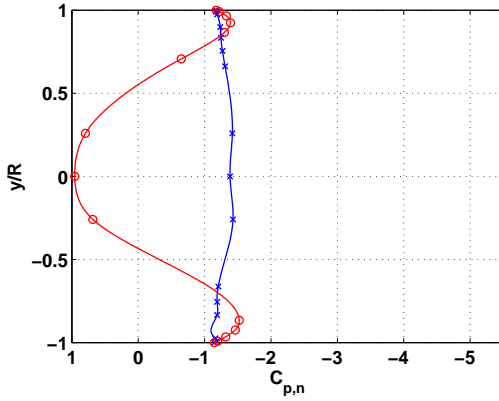


Fig. 4.22: $C_{p,n}$ distribution, $\Theta = 110^\circ$, asym., $y_s/R = 0.94$, baseline, $\Lambda = 0^\circ$, $Re_n = 35000$

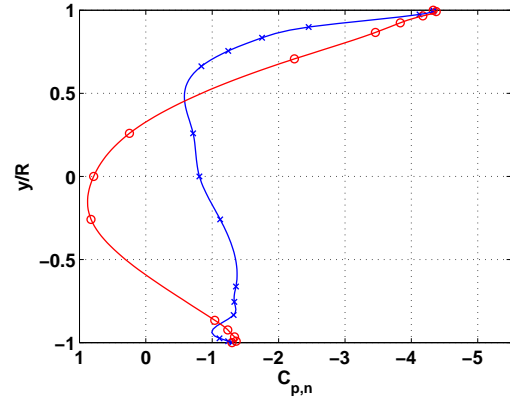


Fig. 4.23: $C_{p,n}$ distribution, $\Theta = 110^\circ$, asym., $y_s/R = 0.94$, $F_n^+ = 1.78$, $C_{\mu,n} = 11\%$, $\Lambda = 0^\circ$, $Re_n = 35000$

cylinder (see equation 4.5). The direct transformation of the pressure coefficients is given by

$$C_{p,n} = \frac{C_p}{(\cos \Lambda)^2} \quad (4.4)$$

For the sweep-back angle of 60° this equates to a multiplication of the C_p values by a factor of four.

The front stagnation pressure decreases noticeable for both slot positions when actuation at $C_{\mu,n} = 11\%$ is applied. In contrast to this no change in stagnation pressure was observed in the 2-D case. The difference to the expected value $C_{p,n,max} = 1$ is partly caused by the limited number of pressure taps, preventing the proper determination of the pressure maximum when the location of the 3-D stagnation line is altered due to the lift generation. This change in azimuthal position forces the stagnation streamline to curve close to the wall towards the cylinder in order to end perpendicular to the wall (see figure 4.28, left).

For a cylinder this change in direction of the stagnation streamline is equal to the angle at which the stagnation line is shifted. In the 2-D case this does not change the reference velocity, but for an inclined cylinder an additional step in the transformation of U_∞ to the normal reference velocity U_n is required. Compared to the simple geometric transformation

$$U_n = U_\infty \cos \Lambda \quad (4.5)$$

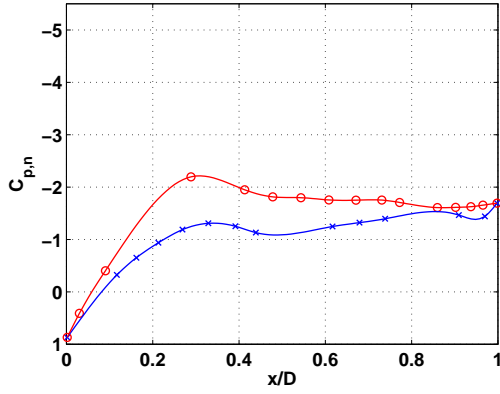


Fig. 4.24: $C_{p,n}$ distribution, $\Theta = 130^\circ$, asym.,
 $x_s/D = 0.82$, $C_\mu = 1.0\%$,
 $\Lambda = 0^\circ$, $Re_n = 35000$

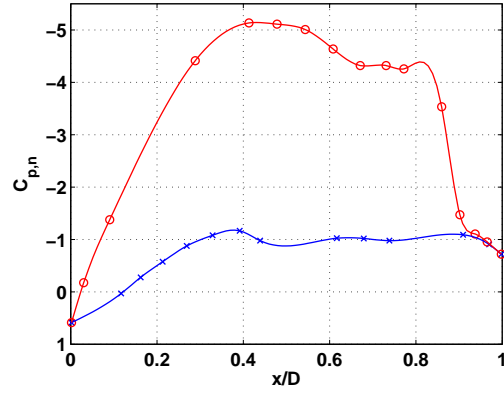


Fig. 4.25: $C_{p,n}$ distribution, $\Theta = 130^\circ$, asym.,
 $x_s/D = 0.82$, $F_n^+ = 1.78$, $C_\mu = 2.75\%$,
 $\Lambda = 0^\circ$, $Re_n = 35000$

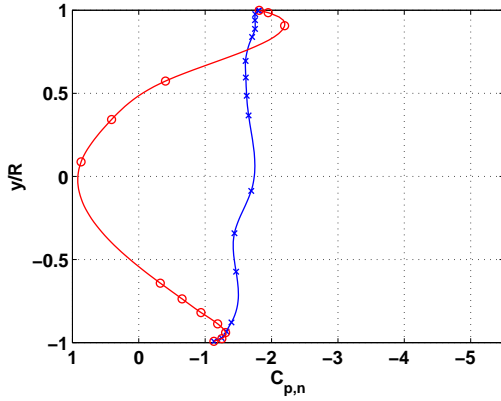


Fig. 4.26: $C_{p,n}$ distribution, $\Theta = 130^\circ$, asym.,
 $y_s/R = 0.77$, $F_n^+ = 1.78$, $C_{\mu,n} = 4\%$,
 $\Lambda = 0^\circ$, $Re_n = 35000$

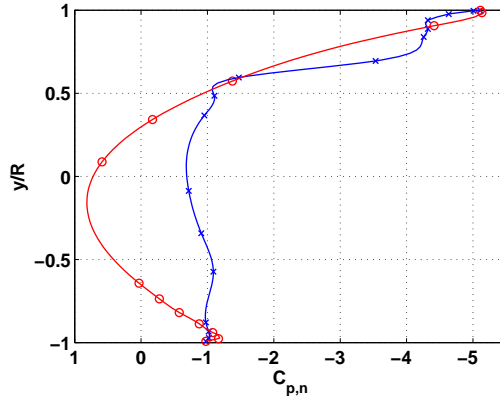


Fig. 4.27: $C_{p,n}$ distribution, $\Theta = 130^\circ$ asym.,
 $y_s/R = 0.77$, $F_n^+ = 1.78$, $C_{\mu,n} = 11\%$,
 $\Lambda = 0^\circ$, $Re_n = 35000$

the transformation of the reference velocity corrected for the shift of the stagnation line by the angle δ is

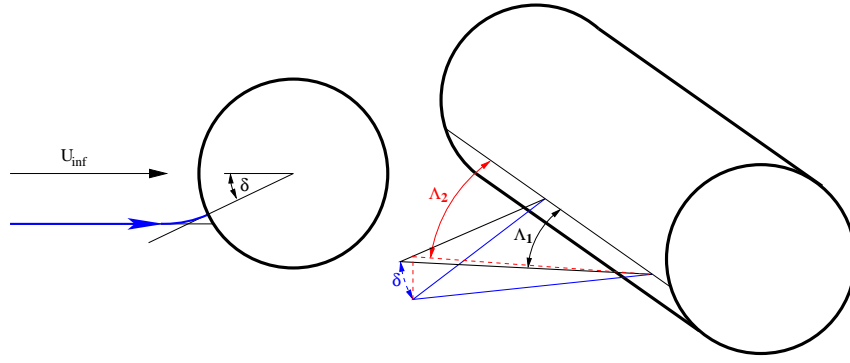
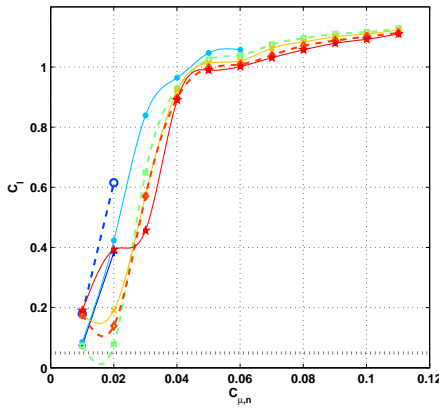
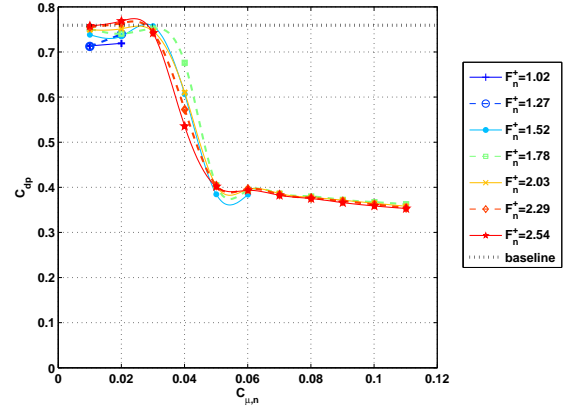
$$U_{n,c} = U_\infty \cos(\operatorname{acotan}(\cotan \Lambda \cos \delta)) \quad (4.6)$$

due to the projection of the sweep-back angle given by (see figure 4.28)

$$\Lambda = \operatorname{acotan}(\cotan \Lambda \cos \delta) \quad (4.7)$$

For the shift of $\delta = 10^\circ$ estimated from the interpolated curve in figure 4.27 the resulting difference in $C_{p,max}$ is approximately 2.5%. This error is considered negligible for the investigated range of C_μ , particularly when the limited azimuthal resolution of the pressure distributions is taken into account.

The characteristics of the C_l and C_{dp} curves (see figures 4.29 and 4.30) determined for an inclined cylinder at $\Lambda = 45^\circ$ with asymmetric excitation show more resemblance to the 2-D case (see figures 4.11 and 4.12 on page 31), but still include clearly three-dimensional effects. The plateau in the C_l curves is less pronounced and particularly the maximum in drag at low C_μ is reduced. This indicates that at low C_μ the lift coefficient alternates much weaker in spanwise direction or is even constant at this sweep angle.

Fig. 4.28: Correction for U_n due to shift of stagnation lineFig. 4.29: C_l vs. $C_{\mu,n}$, $\Theta = 110^\circ$, asym.,
 $\Lambda = 45^\circ$, $Re_n = 35000$ Fig. 4.30: C_{dp} vs. $C_{\mu,n}$, $\Theta = 110^\circ$, asym.,
 $\Lambda = 45^\circ$, $Re_n = 35000$

This effect can be explained by the natural oscillations (see figure 4.151 on page 99) of the spanwise peel-off location occurring for a sweep-back angle of $\Lambda = 45^\circ$. These oscillations in spanwise direction reduce the direct interaction between the individual vortices that peel-off at $\Lambda = 60^\circ$ in an almost stationary fashion. In contrast to $\Lambda = 60^\circ$ and similar to the 2-D configuration the dependence of C_l and C_{dp} on the frequency is noticeable for $\Lambda = 45^\circ$ for $C_{\mu,n} < 4\%$.

The lift and drag coefficients with respect to a circular cross section are compared in figures 4.31 and 4.32 for the three sweep-back angles of 0° , 45° and 60° . For $\Lambda = 0^\circ$, three regimes can be distinguished in the C_l curves: Initially the lift increases only slightly with $C_{\mu,n}$ and the flow is entirely separated upstream of the slot. The gradient $\frac{dC_l}{dC_{\mu,n}}$ is large above a certain frequency dependent threshold of $C_{\mu,n}$ and the flow reattaches gradually upstream of the slot until the separation bubble is eliminated. Further increase of the excitation level generates increased lift by keeping the flow attached downstream of the slot. In this saturated region the efficiency of the excitation is low.

Related characteristics are found for the lift and drag curves at $\Lambda = 45^\circ$ and $\Lambda = 60^\circ$. In the saturated region only a minor augmentation of the lift was achieved. Due to the stationarity of the vortices in the lee of the cylinder that cause reversed flow close to the surface, the potential of reattaching the flow downstream of the slot is limited and the force coefficients are almost constant, being insensitive to the increase of $C_{\mu,n}$. For a sweep-back angle of 60° the additional plateau at $4\% < C_{\mu,n} < 8\%$ (figure 4.31) and the initial increase in drag (figure 4.32) can only be explained by three-dimensional effects and the interaction between the vortices on both sides of the cylinder. These effects were investigated in detail by using PIV in the near wake.

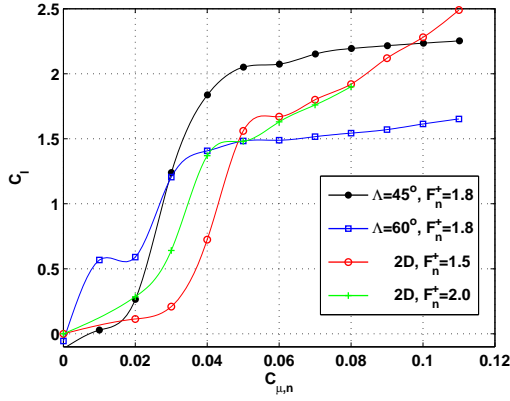


Fig. 4.31: C_l vs. $C_{\mu,n}$, $\Theta = 110^\circ$, asym., $Re_n = 35000$

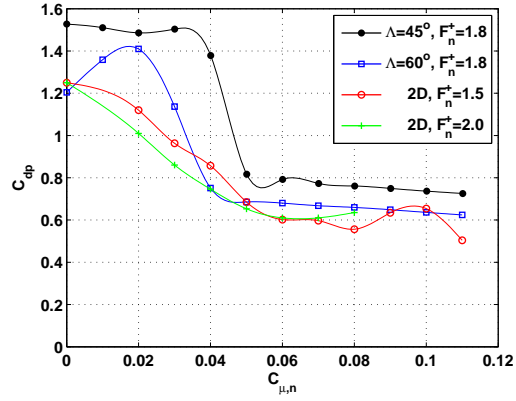


Fig. 4.32: C_{dp} vs. $C_{\mu,n}$, $\Theta = 110^\circ$, asym., $Re_n = 35000$

4.4.1.2 The Near Wake

The pressure distributions described in the last section suggest that the structure of the near wake downstream of an inclined cylinder with asymmetric forcing is highly three-dimensional. Quasi-stationary spanwise vortices close to the cylinder modify the base pressure distribution and therefore the form drag significantly. For identification and analysis of these coherent structures located close to the cylinder PIV data were acquired at several spanwise locations in the near wake. Forcing was applied in all cases from the slot located on the topside of the cylinder, $y/R > 0$.

The flow field represented by $\frac{\Omega_z D}{U_\infty \cos \Lambda}$ at the location of the pressure taps is presented in figure 4.33 to verify the position of the large vortices that contribute to the vortex drag by altering the base pressure profile. When forcing at $C_{\mu,n} = 11\%$ from a slot located at 110° (figure 4.33 a)), two stationary vortices are formed close to the cylinder. One clockwise rotating (blue) at $y/R = 0.6$ and a counterclockwise rotating vortex (red) at $y/R = -0.9$. These positions almost coincide with the locations ($y/R = 0.5$ and $y/R = -0.7$) estimated from the base pressure distribution shown in figure 4.23. The small differences in y/R might be caused by the combined effect of all vortices in lee of the cylinder. Forcing from a slot located at 130° with $C_{\mu,n} = 4\%$ resulted in similar consistency between the locations of the vortices gathered from two independent measurements: the center of the dominant negative vorticity (blue) is located at $y/R = 0.2$ and the center of positive vorticity (red) at $y/R = -1.2$. Based on the base pressure distribution (figure 4.26) the location of the dominant vortex was estimated to be $y/R = 0$. For excitation at $C_{\mu,n} = 11\%$ from a slot located at $\Theta = 130^\circ$, the vortex location determined from the base pressure profile (figure 4.27, $y/R = -0.6$) differs slightly from the true location of the vortex core ($y/R = -0.8$). It was not possible to locate the center of the negative vortex in figure 4.27 because no distinct local pressure minimum exists for $y/R > 0$.

The two different states of the flow identified in the pressure distributions can be distinguished clearly in the vorticity distributions (figure 4.33 b) and c)) at this spanwise position. At the lower level of actuation presented in figure 4.33 b) the wake is clearly asymmetric, but some characteristics of the baseline flow are preserved. The wake at this spanwise position is still formed by two smaller vortices close to the cylinder and two larger ones that started peeling-off further upstream. The smaller vortices are positioned almost symmetrically at $y/R = \pm 1.2$, the larger ones are positioned asymmetrically. Due to the asymmetric forcing the vortices that separated from the topside ($y/R > 0$) are enhanced, therefore they accumulate vorticity at a higher rate than the ones on the opposite side of the cylinder. On the other hand the wake is deflected downwards, thus the vortices on the unforced side are displaced into regions with higher streamwise velocity. Therefore the first peel-off occurs on the unforced underside, as can be confirmed in figure 4.36 at the upstream end of the cylinder (positive vorticity, marked in red). The alternate separation of vortices causes strong variations of the flow along the span (see figure 4.38). The analysis of the flow at a single spanwise position cannot necessarily provide representative information about

the entire span, therefore three-dimensional pseudo-visualizations of the flow are considered to be a more adequate means for analyzing this three-dimensional flow. Nevertheless selected contour plots allow for a more detailed “point” analysis.

The basic structure of the wake was altered for both slot locations at the higher forcing level of $C_{\mu,n} = 11\%$ shown in figure 4.33 a) and c). Instead of large individual vortices peeling-off an elongated vortex “sheet” consisting of individual vortices is formed and is deflected downwards. The origin of this elongated region is at the boundary of the investigated volume ($x/R = 1$) with $y/R = 0.6$ for the slot located at $\Theta = 110^\circ$ and $y/R = 0.5$ for the one located at $\Theta = 130^\circ$. This is consistent with the larger deflection of the vortices for the more downstream slot positions.

The distributions of the dimensionless velocity component $\frac{W}{U_{\infty} \sin \Lambda}$ is presented in figures 4.34 for the cases discussed above. The equivalence between minima in $\frac{W}{U_{\infty} \sin \Lambda}$ (blue) and extrema in $\frac{\Omega_z D}{U_{\infty} \cos \Lambda}$ (red & blue) is excellent for the slot located at 110° but less good for a slot location of $\Theta = 130^\circ$. This is due to the significant entrainment of fluid in this case. When forcing at $C_{\mu,n} = 4\%$ (figure 4.34 b)) a dominant vortex (blue) is formed, entraining fluid between itself and the two accumulations of positive vorticity (red). This fluid is forced to flow along the cylinder, increasing the local spanwise velocity and therefore disturbing the minima of $\frac{W}{U_{\infty} \sin \Lambda}$ in the vortex cores located close to the cylinder. Forcing at $C_{\mu,n} = 11\%$ reduces the distance between the counter rotating vortices and thus reduces the entrainment of fluid into the region next to the cylinder. Therefore the disturbance of $\frac{W}{U_{\infty} \sin \Lambda}$ is less developed although it is still present. Important is the difference in spanwise velocity between $y/R > 0$ (forced side) and $y/R < 0$. Due to the excitation the flow separates earlier on the unforced bottom side of the cylinder. Thus the flow is not deflected as much in the azimuthal direction as on the forced side (see discussion of the flow visualization on page 29) and the spanwise velocity is higher on the bottom side of the cylinder than on the topside. Therefore the convection of vorticity is decreased on the topside. This results in an increased rate of accumulation of vorticity on the forced side whereas the vortices on the opposite side are weakened relative to the baseline.

In figures 4.35 the distribution of $\frac{U}{U_{\infty} \cos \Lambda}$ is shown for the same combination of slot angle and excitation level as above. The minimum of $\frac{U}{U_{\infty} \cos \Lambda}$ for every x/R position occurs at the center of the wake. Thus this quantity enables the qualitative estimate of the lift generated depending on the angle of deflection of the wake. This is used below in figures 4.39 and 4.41 to visualize the spanwise variation of C_l .

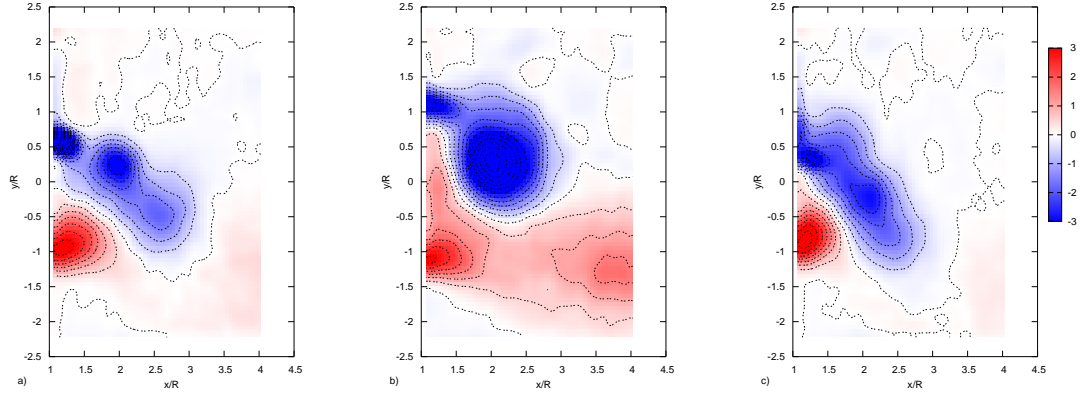


Fig. 4.33: asymmetric actuation, $\frac{\Omega_z D}{U_\infty}$, $Re_n = 35000$, $z/R = -12$, a) $\Theta = 110^\circ$, $F_n^+ = 1.78$, $C_{\mu,n} = 11\%$, b) $\Theta = 130^\circ$, $F_n^+ = 1.78$, $C_{\mu,n} = 4\%$, c) $\Theta = 130^\circ$, $F_n^+ = 1.78$, $C_{\mu,n} = 11\%$

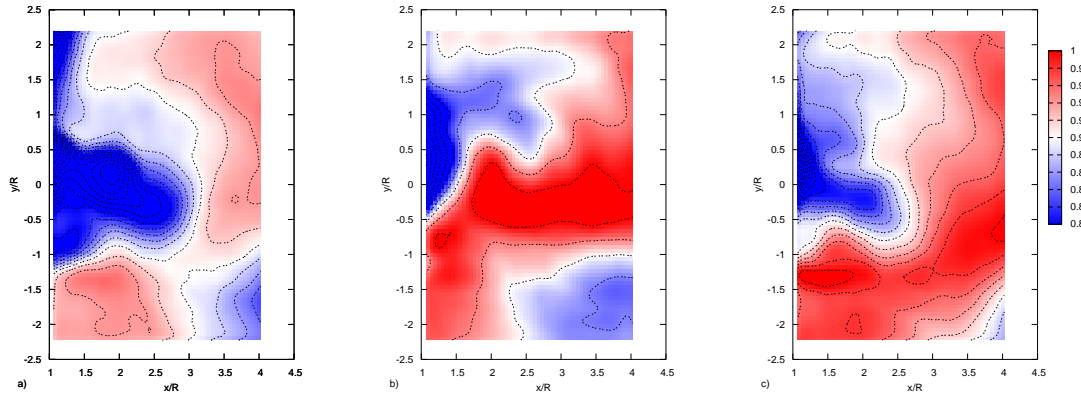


Fig. 4.34: asymmetric actuation, $\frac{W}{U_\infty \sin \Lambda}$, $Re_n = 35000$, $z/R = -12$, a) $\Theta = 110^\circ$, $F_n^+ = 1.78$, $C_{\mu,n} = 11\%$, b) $\Theta = 130^\circ$, $F_n^+ = 1.78$, $C_{\mu,n} = 4\%$, c) $\Theta = 130^\circ$, $F_n^+ = 1.78$, $C_{\mu,n} = 11\%$

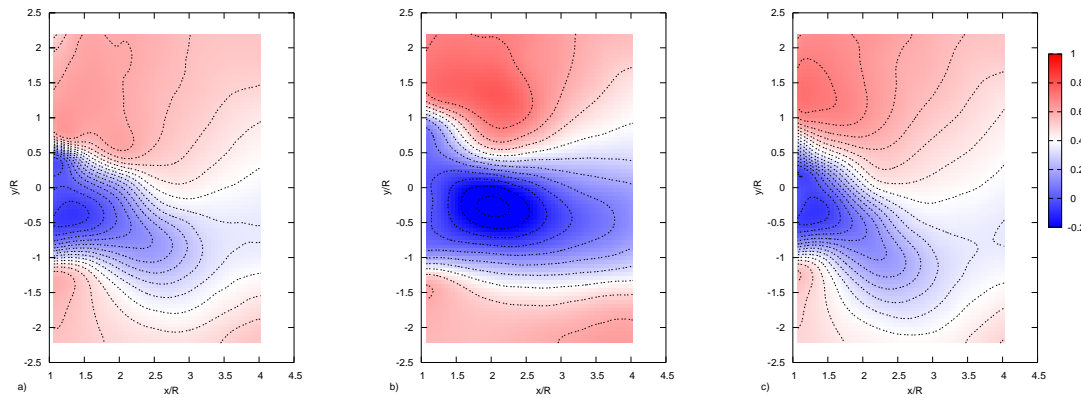


Fig. 4.35: asymmetric actuation, $\frac{U}{U_\infty \cos \Lambda}$, $Re_n = 35000$, $z/R = -12$, a) $\Theta = 110^\circ$, $F_n^+ = 1.78$, $C_{\mu,n} = 11\%$, b) $\Theta = 130^\circ$, $F_n^+ = 1.78$, $C_{\mu,n} = 4\%$, c) $\Theta = 130^\circ$, $F_n^+ = 1.78$, $C_{\mu,n} = 11\%$

Figures 4.36 and 4.37 visualize the flow downstream of an infinite cylinder inclined at $\Lambda = 60^\circ$ with asymmetric excitation emanating from a single slot located at $\Theta = 110^\circ$ on the topside of the model. The iso-surfaces of $\frac{\Omega_z D}{U_\infty \cos \Lambda}$ in figure 4.36 represent distinct levels of spanwise vorticity. Wherever the iso-surfaces are cut open by intersecting the boundaries of the interrogated control volume the darker interior of the otherwise closed “shells” is visible. Two additional contour plots facilitate orientation in the control volume. The legend for the iso-surfaces is shown on the upper left, the legend for the contour plots is at the lower right of the figure. The cylinder and part of the tunnel wall and floor were added to help visualize the orientation of the control volume in the test section. The direction of the free stream is indicated by three white arrows.

The strong two-dimensional excitation at $C_{\mu,n} = 11\%$ stabilizes the 2-D structures in the shear layers close to the cylinder and elongated vortical fluid “sheets”, consisting of vortices whose axes are parallel to the axis of the cylinder are formed in its lee. The formation of these vortex “sheets” by single sided actuation (figure 4.36) is clearly visible at the left side of the figure where the iso-surfaces of $\frac{\Omega_z D}{U_\infty \cos \Lambda}$ intersect the boundary of the investigated volume at $z/R = 0$. Both vortex “sheets” are deflected downwards, indicating that lift is generated. Vorticity is accumulated and at the same time convected along the span of the cylinder due to the strong spanwise velocity component. Thus the growth rate of a vortex is determined by the ratio between accumulation and convection. It therefore strongly depends on the sweep-back angle. Once a vortex reaches a critical size it is forced to separate from the vicinity of the cylinder and to change its orientation to be parallel to the free stream.

Due to the single sided forcing an imbalance is created between the two opposite sides of the cylinder. Thus the peel-off does not occur simultaneously on both sides, instead the vortices separate from the cylinder in alternating fashion. In figure 4.36 the strong vortex (blue) associated with the upper (forced) surface peels-off from the group of vortices that are parallel to the cylinder. Subsequently the bottom vortex (red), takes its position next to the solid surface (see contour plot at $z/R = -13.3$), increases in strength and thereafter peels-off the cylinder and intersects the boundary of the investigated volume at $x/R = 4$. Due to the strong 2-D forcing the vortex “sheets” are stabilized and become almost stationary along the span.

In figure 4.37 iso-contours of the spanwise velocity component reveal more details of the near wake than the spanwise vorticity. The comparison of figures 4.36 and 4.37 confirms that the vortex cores are represented well by minima in $\frac{W}{U_\infty \sin \Lambda}$. They are formed by vorticity generated in the 3-D boundary layers on the cylinder. Due to skin friction, fluid is decelerated near the surface of the cylinder, in azimuthal direction as well as in spanwise direction. This generates spanwise vorticity, at the same time causing a deficit in the spanwise velocity component. The formation of vortices is associated with the accumulation of $\frac{\Omega_z D}{U_\infty \cos \Lambda}$, thus fluid with a deficit in $\frac{W}{U_\infty \sin \Lambda}$ is accumulated in the vortex cores. Due to the asymmetric periodic excitation the location of flow separation is different on opposite sides of the cylinder. In this case the flow separates further downstream on the top side, where the forcing is applied. Therefore the velocity deficit on the upper side is more pronounced, increasing the difference in the deficit in $\frac{W}{U_\infty \sin \Lambda}$ between both sides. In spite of these differences in $\frac{W}{U_\infty \sin \Lambda}$, comparable levels of $\frac{\Omega_z D}{U_\infty \cos \Lambda}$ can be observed on both sides of the wake. Thus the analogy between the distributions of $\frac{\Omega_z D}{U_\infty \cos \Lambda}$ and $\frac{W}{U_\infty \sin \Lambda}$ is strictly qualitative.

Fluid is entrained between counter rotating vortices and is accelerated (marked in red) in spanwise direction. The vortices with a deficit in $\frac{W}{U_\infty \sin \Lambda}$ and the structures formed by entrained fluid that was accelerated in spanwise direction separate both from the cylinder during the peel-off process. They are re-oriented in streamwise direction with increasing distance from the cylinder, causing the spatial fluctuations in the streamwise velocity distribution that are detected in the far wake.

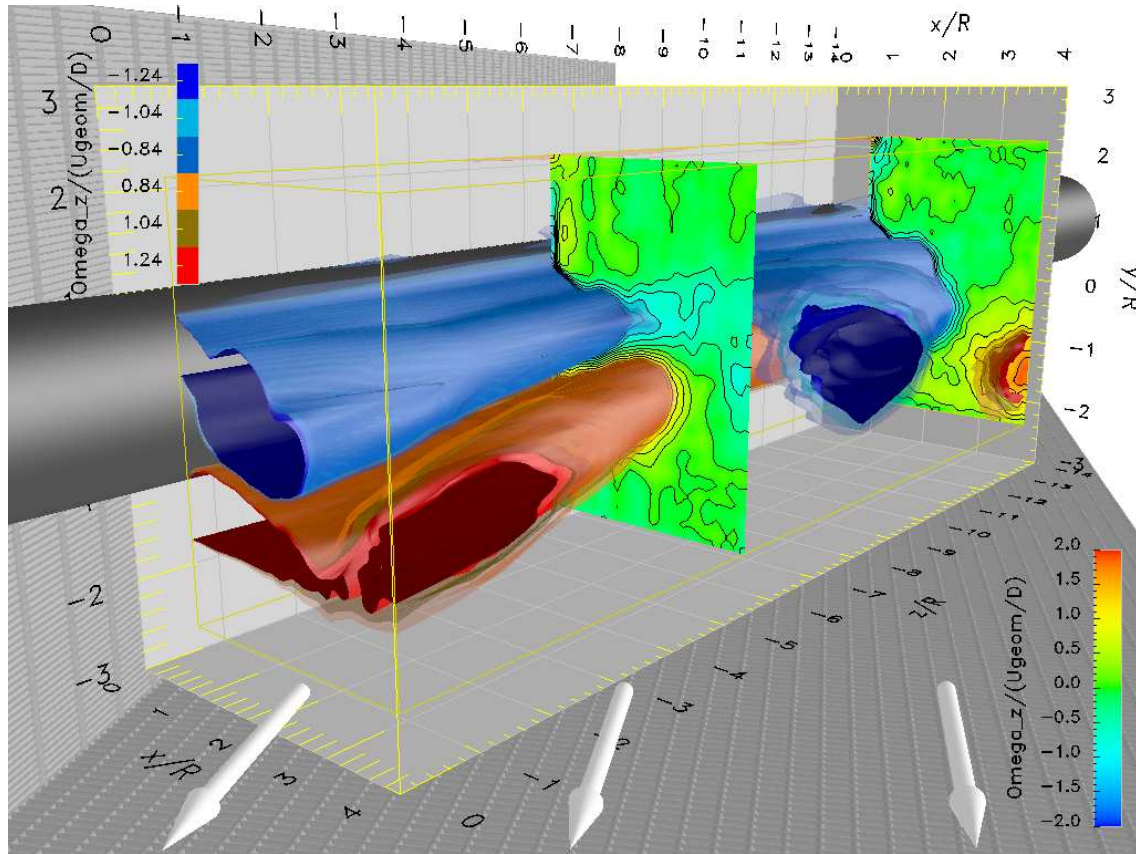


Fig. 4.36: Iso-surfaces of $\frac{\Omega_z D}{U_{\infty \cos \Lambda}}$, $\Theta = 110^\circ$, $F_n^+ = 1.78$, $C_{\mu,n} = 11\%$, asym., $\Lambda = 60^\circ$, $Re_n = 35000$

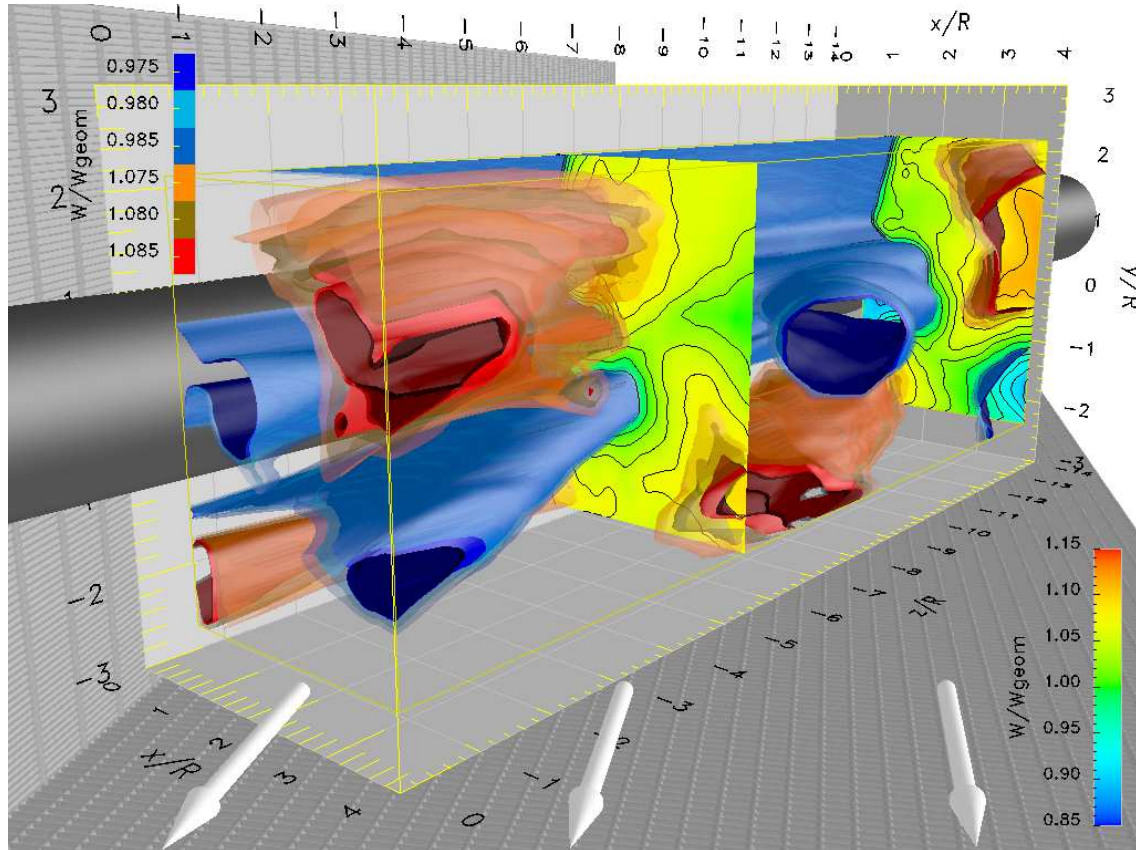


Fig. 4.37: Iso-surfaces of $\frac{W}{U_{\infty \sin \Lambda}}$, $\Theta = 110^\circ$, $F_n^+ = 1.78$, $C_{\mu,n} = 11\%$, asym., $\Lambda = 60^\circ$, $Re_n = 35000$

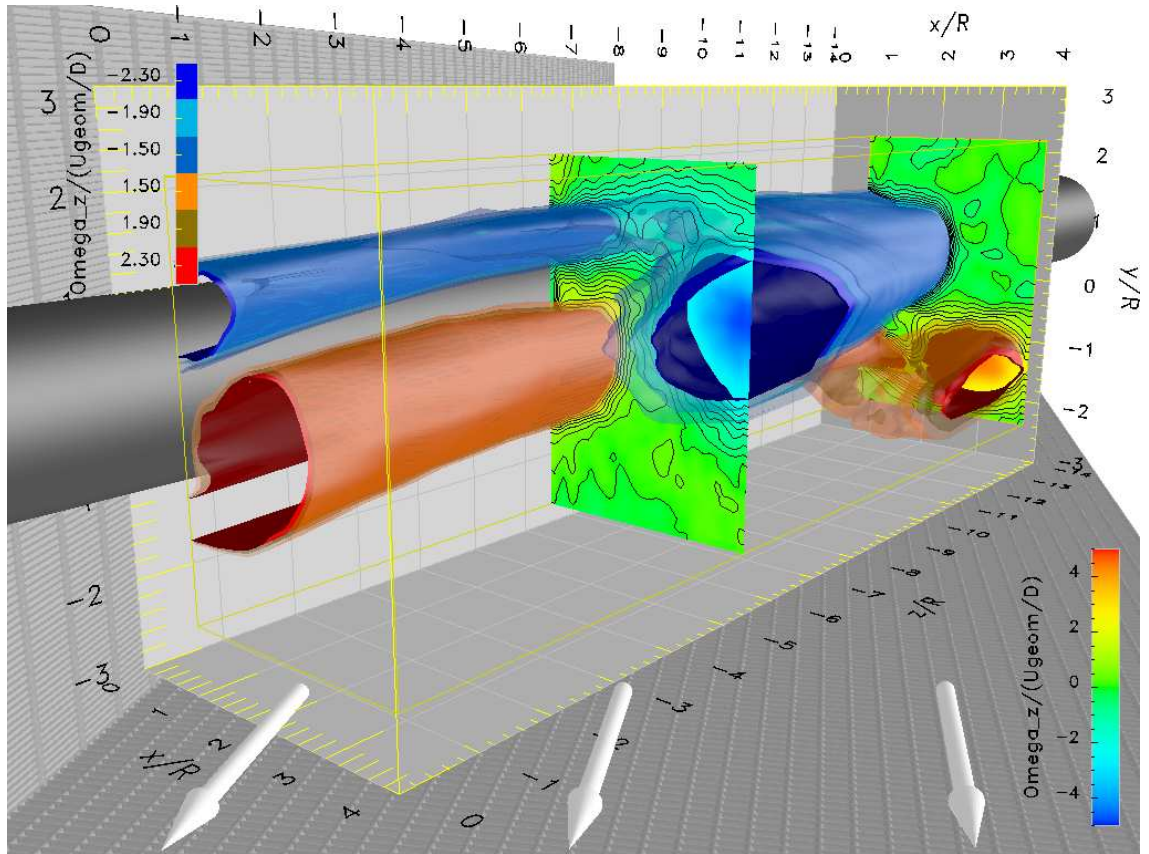


Fig. 4.38: Iso-surfaces of $\frac{\Omega_z D}{U_{\infty} \cos \Lambda}$, $\Theta = 130^\circ$, $F_n^+ = 1.78$, $C_{\mu,n} = 4\%$, asym., $\Lambda = 60^\circ$, $Re_n = 35000$

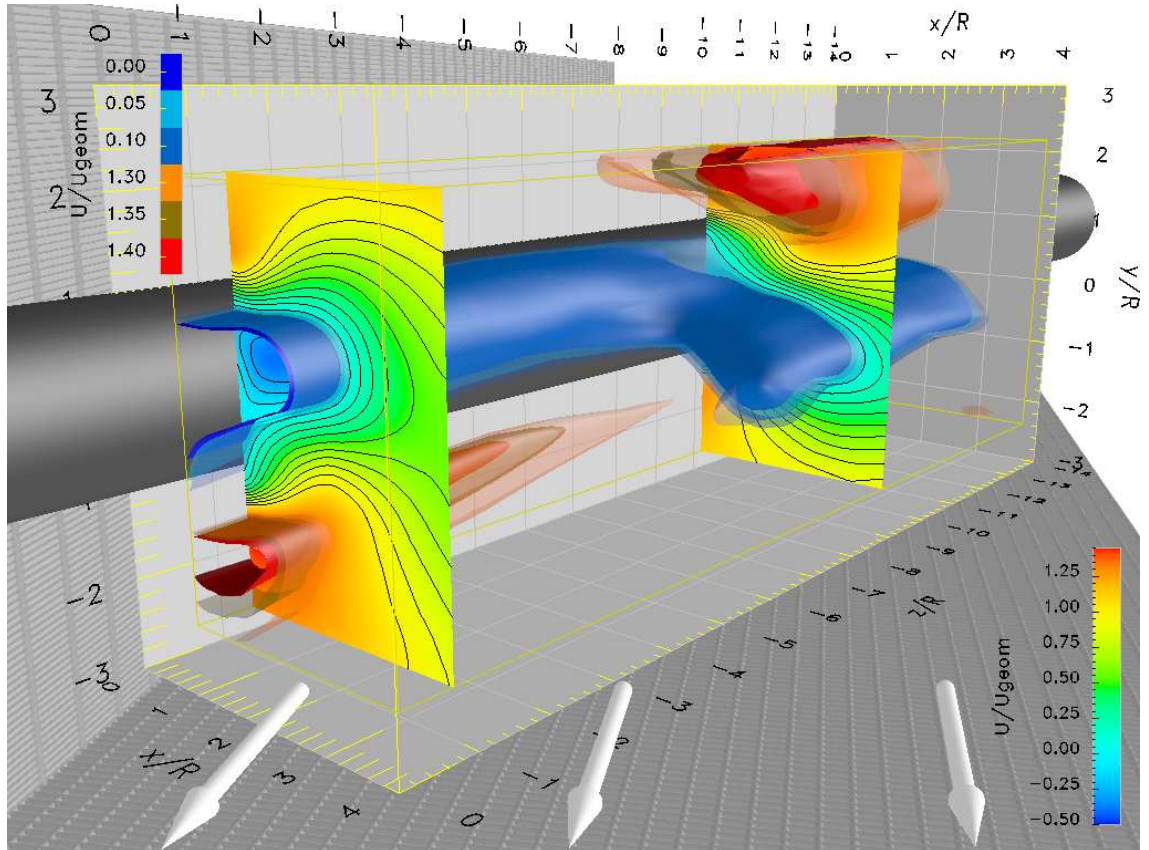


Fig. 4.39: Iso-surfaces of $\frac{U}{U_{\infty} \cos \Lambda}$, $\Theta = 130^\circ$, $F_n^+ = 1.78$, $C_{\mu,n} = 4\%$, asym., $\Lambda = 60^\circ$, $Re_n = 35000$

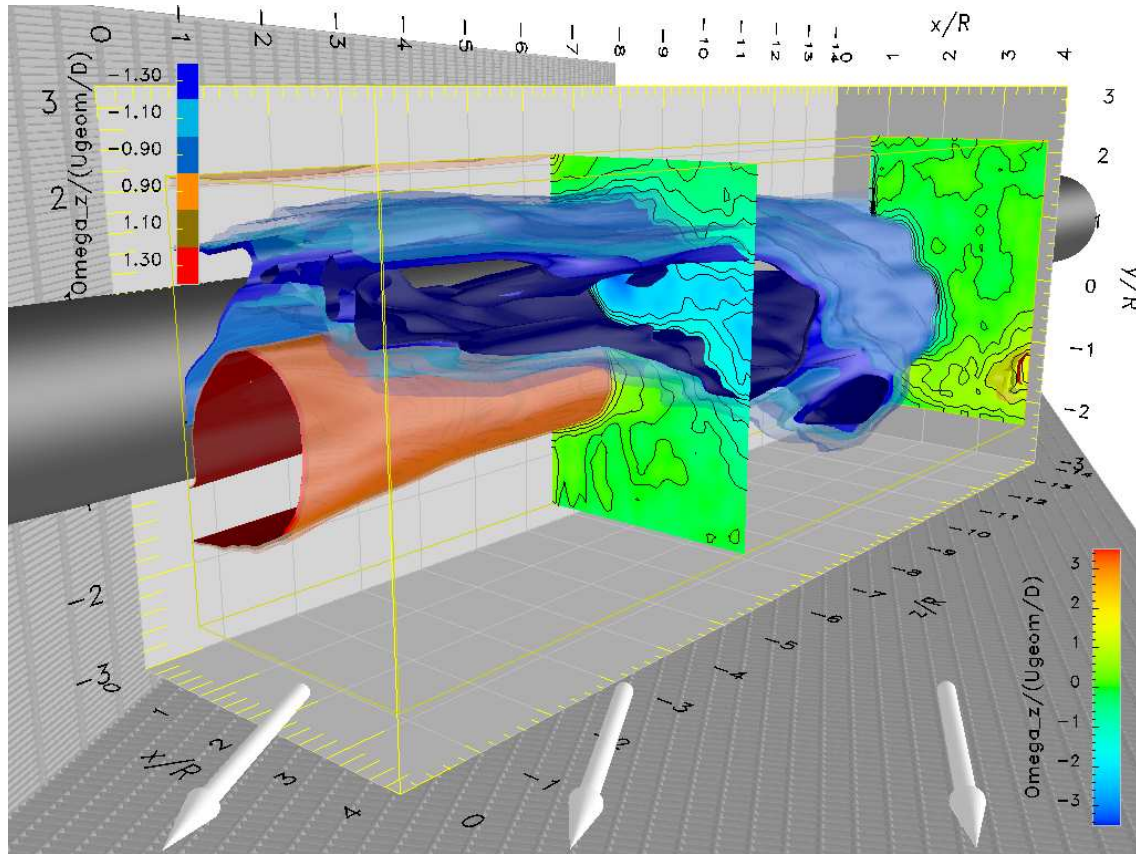


Fig. 4.40: Iso-surfaces of $\frac{\Omega_z D}{U_{\infty} \cos \Lambda}$, $\Theta = 130^\circ$, $F_n^+ = 1.78$, $C_{\mu,n} = 11\%$, asym., $\Lambda = 60^\circ$, $Re_n = 35000$

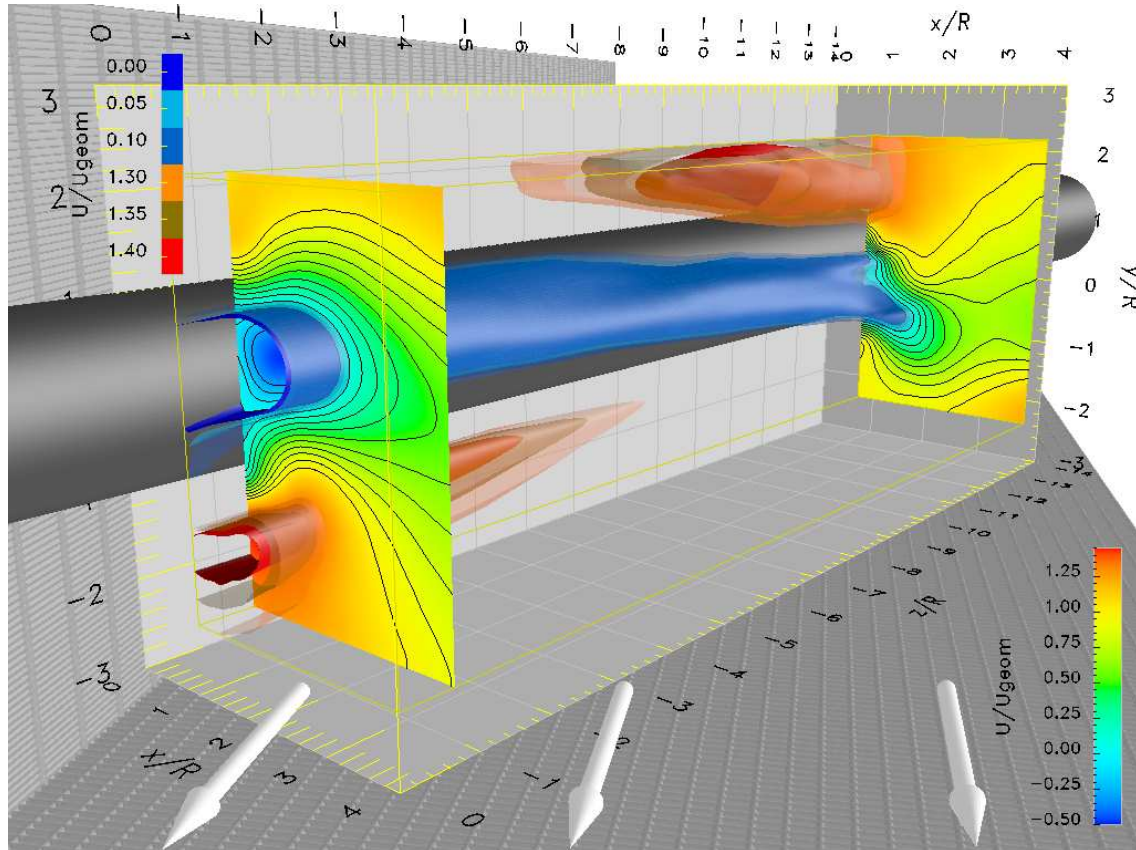


Fig. 4.41: Iso-surfaces of $\frac{U}{U_{\infty} \cos \Lambda}$, $\Theta = 130^\circ$, $F_n^+ = 1.78$, $C_{\mu,n} = 11\%$, asym., $\Lambda = 60^\circ$, $Re_n = 35000$

Moving the slot from $\Theta = 110^\circ$ to a location at $\Theta = 130^\circ$ (see figures 4.38 to 4.41) results in a more complex flow. The vorticity iso-surfaces corresponding to $C_{\mu,n} = 4\%$ and plotted in figure 4.38 show again clearly the vortex peel-off from the bottom side first ($z/R = -13.3$, red vortex) and then from the topside. At the first spanwise plane ($z/R = -13.3$) the concentration of $\frac{\Omega_z D}{U_\infty \cos \Lambda}$ splits in two with a large vortex (blue) already separating from the cylinder, while a smaller vortex on the topside remains parallel to the cylinder. This vortex continuously accumulates the vorticity shed along the entire span of the cylinder, comparable to the vortices forming on top of a delta wing that are described together with means of controlling it by Margalit et al. [18]. The angle between the separating vortex and the cylinder increases along the span until the vortex leaves the interrogated volume entirely at $z/R = -5.3$. Actuation at $C_{\mu,n} = 11\%$ generates a vortex sheet downstream of the slot that seems to peel-off as an entity. The flow varies noticeably along the span in both cases. This is due to the location of the slot which is relatively far downstream, thus a significantly higher C_μ may be required to reattach the flow entirely.

The flow around the cylinder is not entirely attached but contains a larger bubble upstream of the slot at both levels of actuation, as discussed for figures 4.24 to 4.27. Due to this bubble the azimuthal position of the stagnation line is less affected by the actuation and thus the influence of the actuation on the side opposite of the slot is reduced. Consequently, no vortex “sheet” is formed on this side at the higher level of excitation. The single vortex on the side opposite of the slot is instead forced towards larger y/R at reduced x/R by induction from the peeling-off vortex. This induction depends on the position of the individual vortices that is varying along the span. This variation of the vortex positions along the span results in significant fluctuations of the lift in spanwise direction for both excitation levels, as illustrated in figures 4.39 and 4.41 by iso-surface of $\frac{U}{U_\infty \cos \Lambda}$ marking the orientation of the wake.

The available maximum level of excitation is not sufficient for this downstream slot location to reattach the flow uniformly along the span. Although on the average lift should be generated the local lift alternates along the spanwise direction. Thus the pressure distributions acquired at a single spanwise position might not be representative at larger slot angles. In contrast to this the asymmetric excitation applied from a slot located at $\Theta = 110^\circ$ stabilized the flow and increased the spanwise uniformity close to the cylinder. In every case the alternating vortex peel-off introduces spanwise variations of the local lift, the differences lie in the amplitude of these fluctuations and are dependent on slot angle and level of excitation.

Increasing the slot angle from $\Theta = 110^\circ$ to $\Theta = 130^\circ$ results in an increase by 100% in the turbulent kinetic energy at an excitation level of $C_{\mu,n} = 11\%$. The iso-levels of turbulent kinetic energy, k in figures 4.42 and 4.43 were chosen in a way that iso-surfaces enclosing similar volumes are generated, enabling a simple comparison of the turbulent kinetic energy in the entire investigated control volume. The shape of the regions with high turbulent kinetic energy changes from a more horizontal orientation at $\Theta = 110^\circ$ to a more vertical one at $\Theta = 130^\circ$. This can be explained by the different structures of the wakes, as shown in figures 4.36 for $\Theta = 110^\circ$ and 4.40 for $\Theta = 130^\circ$. In the first case the vortical structures are elongated and extend through the entire control volume. The region between vortices of opposite sign with the highest shear is horizontally elongated. In the second case the coherent structures of $\frac{\Omega_z D}{U_\infty \cos \Lambda}$ are more compact and restricted to a region close to the cylinder, with the exception of the peeling-off vortices at $z/R = -7$ (blue) and $z/R = -13.3$ (red). Thus the regions with the highest shear are located close to the cylinder.

So far mostly qualitative results based on visual interpretation of the PIV data were discussed. Due to the complexity of the flow it would require advanced pattern recognition techniques to estimate the location of individual vortices reliably in a general procedure suitable for all acquired data series. The computation of integral quantities is a simpler way to obtain quantitative results, in particular for the characterization of the dynamics observed in the near wake.

The spanwise component of the circulation, Γ_z was determined for every PIV data sequence. The spanwise distribution of the dimensionless circulation $\frac{\Gamma_z}{U_\infty \cos \Lambda R}$ is presented in figures 4.44 and 4.45 for two different slot locations for the forced topside (blue) and bottom side (red, $-y/R$) of the cylinder. Vorticity is accumulated and the circulation increases until the vortex is separating from the cylinder and leaves the investigated volume, thus the circulation decreases in this phase

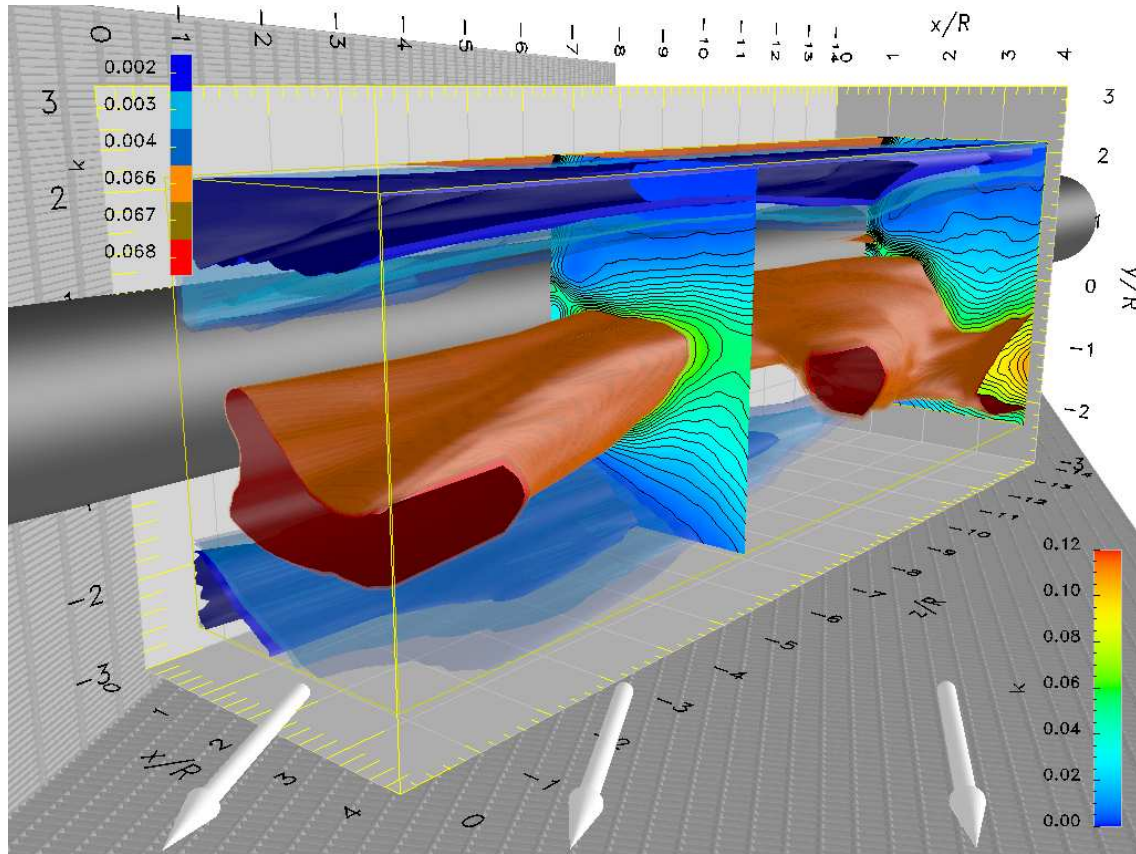


Fig. 4.42: Iso-surfaces of k , $\Theta = 110^\circ$, $F_n^+ = 1.78$, $C_{\mu,n} = 11\%$, asym., $\Lambda = 60^\circ$, $Re_n = 35000$

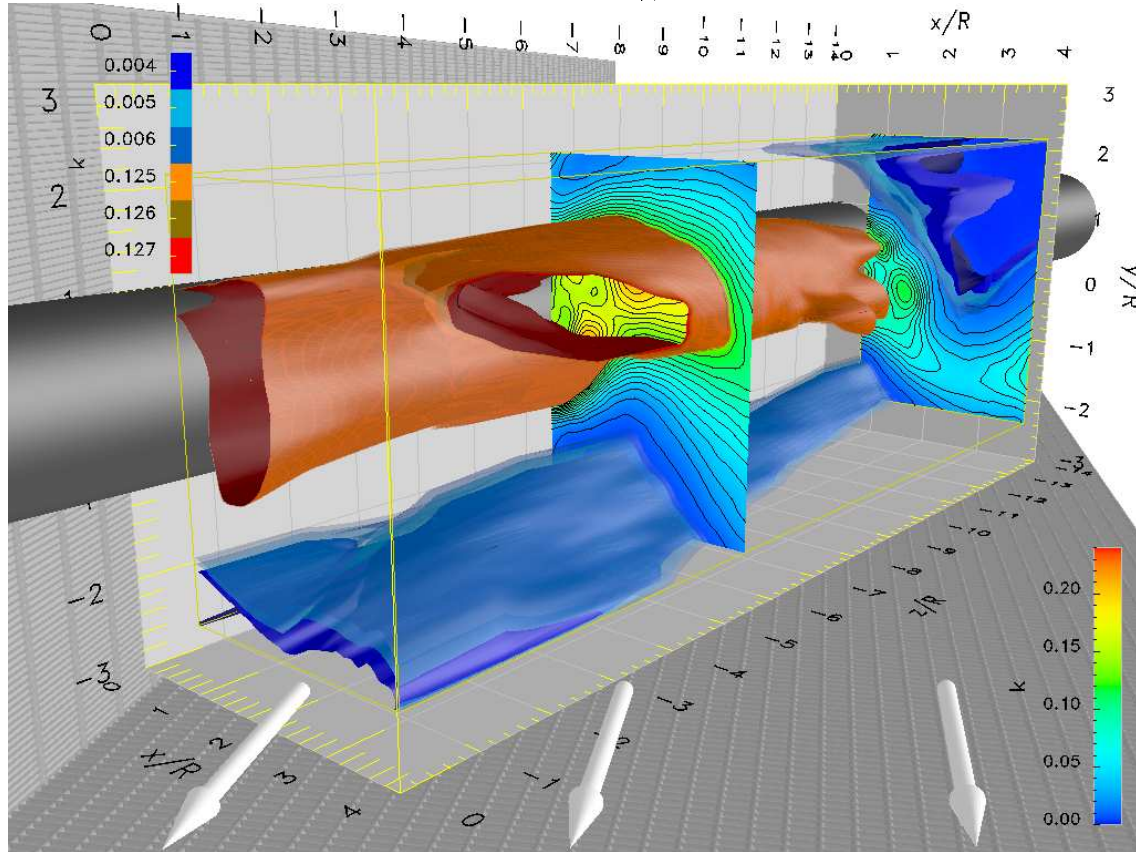


Fig. 4.43: Iso-surfaces of k , $\Theta = 130^\circ$, $F_n^+ = 1.78$, $C_{\mu,n} = 11\%$, asym., $\Lambda = 60^\circ$, $Re_n = 35000$

of the peel-off process. When the slot is located further downstream at $\Theta = 130^\circ$, the boundary layer separates from the forced side at a location further downstream and the vortices in lee of the cylinder are located at smaller y/R , provided that excitation is applied at a suitable level. Due to the difference in their position the critical size of the vortices is increased, thus more vorticity can be accumulated before the vortices are peeling-off the cylinder. Therefore the fluctuations in circulation are significantly increased at $\Theta = 130^\circ$.

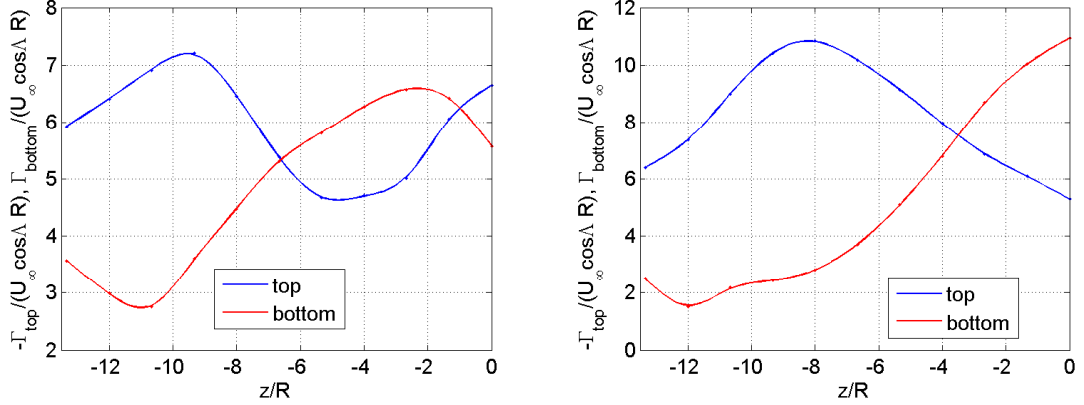


Fig. 4.44: $\frac{\Gamma_z}{U_\infty \cos \Lambda R}$, $\Theta = 110^\circ$, $F_n^+ = 1.78$, asym., $C_{\mu,n} = 11\%$, $\Lambda = 60^\circ$, $Re_n = 35000$, Fig. 4.45: $\frac{\Gamma_z}{U_\infty \cos \Lambda R}$, $\Theta = 130^\circ$, $F_n^+ = 1.78$, asym., $C_{\mu,n} = 11\%$, $\Lambda = 60^\circ$, $Re_n = 35000$

It was not possible to detect the centers of the large vortices directly without using advanced pattern recognition algorithms because of the complex structure of the wake. This is mostly due to the fact that the larger coherent structures are often formed by a number of smaller vortices that would be problematic to identify reliably. Instead of determining the location of the centers of individual vortices, an integral “center of vorticity” was determined analogous to the center of mass of an arbitrary body. This is a robust measure to quantify the distribution of vorticity even in complex flows. The X-, and Y-coordinates were computed by

$$x_\Omega = \frac{\sum_{i=1}^n \Omega_{z,i} x_i}{\sum_{i=1}^n \Omega_{z,i}}, \quad y_\Omega = \frac{\sum_{i=1}^n \Omega_{z,i} y_i}{\sum_{i=1}^n \Omega_{z,i}} \quad (4.8)$$

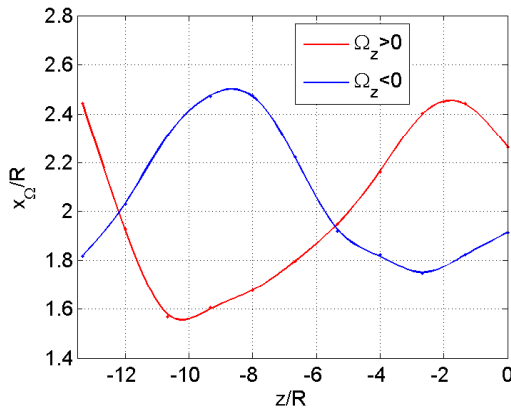


Fig. 4.46: x_Ω/R , $\Theta = 110^\circ$, $F_n^+ = 1.78$, asym., $C_{\mu,n} = 11\%$, $\Lambda = 60^\circ$, $Re_n = 35000$

The center of vorticity is considered only a limited approximation for the true location of the vortices. Nevertheless the trends of the change of location of the center of vorticity and of the estimated center of the dominating vortex seem to correlate in most cases. Figures 4.46 illustrates the increase of the X-component of the center of vorticity when vorticity is accumulated ($\frac{\Gamma_z}{U_\infty \cos \Lambda R}$ increases, see figures 4.44 and 4.45) and the size of the vortices increases.

4.4.1.3 Near Wake Dynamics

Spatial variations of the flow in the near wake were detected directly by analyzing the averaged PIV data at different spanwise locations. The spatial resolution of PIV in the XY-plane is well suited for the investigated configuration and the resolution in spanwise direction can be adapted

to any requirement, but the resolution in time is very limited. In this case the maximum sampling frequency is limited by the NdYAG laser to 10Hz. Correlations computed for the baseline (see page 104) revealed that the coherent structures in the near wake fluctuate in spanwise direction. These dynamics of the wake were examined by processing the PIV data by Proper Orthogonal

Decomposition (POD see page 17). Fluctuations found for the cases with a slot angle of $\Theta = 130^\circ$ were extremely complex, as was expected due to the significant variations of C_l in spanwise direction. Therefore only results for the slot located at $\Theta = 110^\circ$ are presented below.

The data were analyzed by POD and divided into different classes of “POD phase angles” to obtain conditional averages, as is described on page 19. Although the flow was stabilized by strong asymmetric forcing, significant oscillations were found. Presented in figures 4.48 to 4.49 are iso-surfaces of the $\frac{U}{U_{\infty \cos \Lambda}}$ velocity component. The minima of $\frac{U}{U_{\infty \cos \Lambda}}$ in any given YZ-plane represent the center of the wake, therefore the iso-contours of $\frac{U}{U_{\infty \cos \Lambda}}$ illustrate the orientation of the wake accurately.

The POD phases (see pages 19 ff for details) are based on the first POD Eigenflow describing the meandering of the wake. The maximum deflections of the wake detected in the partial reconstructions were assigned to a phase angle of $\pm 90^\circ$ and the phases of all individual data sets in the sequence were determined based on these reference points. The POD phase 0° is the average of the two extrema. Therefore the conditional average of the original for 0° is close to the mean flow, provided the oscillations of the wake are approximately symmetric. The other two phases shown in figures 4.48 and 4.49 represent upward deflections (40° , mathematical positive sense of rotation) or downward deflections for -40° .

The minima in $\frac{U}{U_{\infty \cos \Lambda}}$ are found at $y < 0$ for the POD phase of 0° and the maximum in $\frac{U}{U_{\infty \cos \Lambda}}$ is found above the cylinder, according to the generated lift. This is consistent with the analysis of the pressure distributions. The spanwise variations can be neglected in this case ($F_n^+ = 1.78$, $C_{\mu,n} = 11\%$), therefore the pressure profile measured at the single spanwise location is representative for the entire span. At a POD phase of -40° (figure 4.48) the flow is deflected downwards from the average direction and lift is increased. For the POD phase of 40° shown in figure 4.49 this is reversed and the wake is partially deflected upwards, potentially generating negative lift.

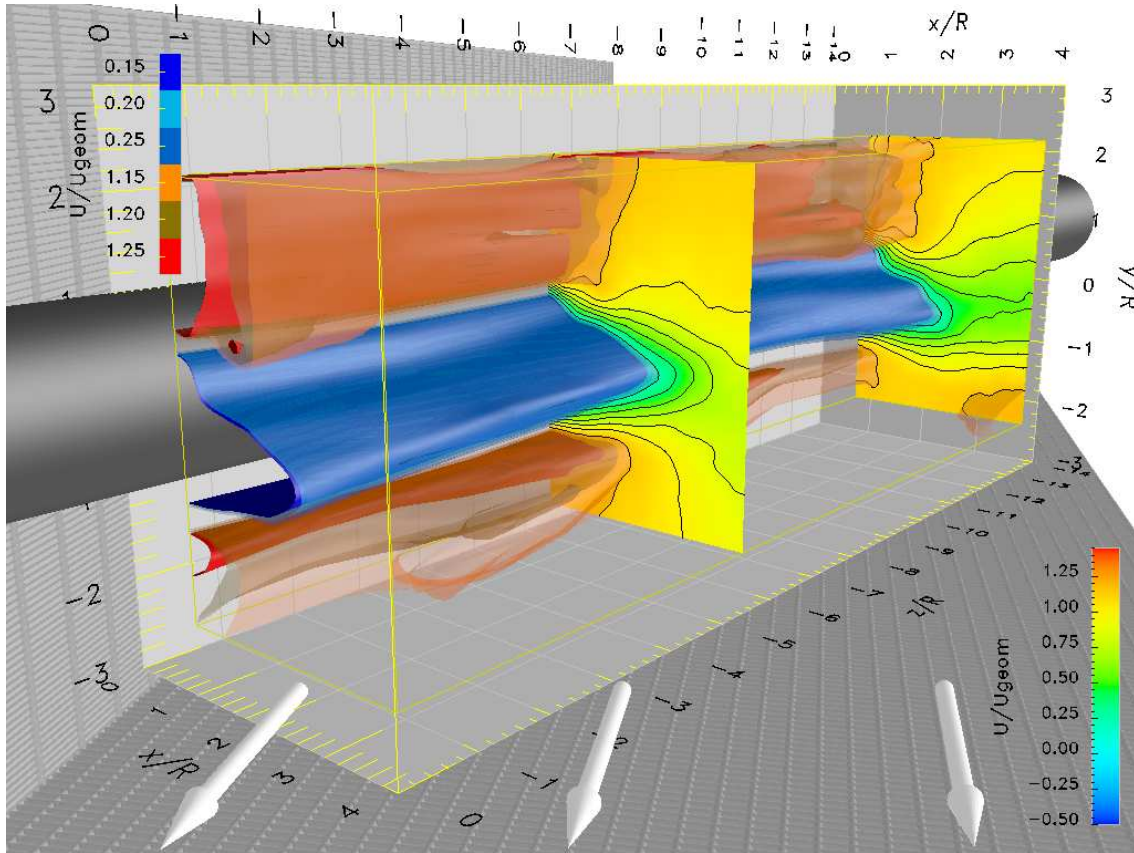


Fig. 4.47: $\frac{U}{U_{\infty \cos \Lambda}}$, POD $\varphi = 0^\circ$, $\Theta = 110^\circ$, $F_n^+ = 1.78$, $C_{\mu,n} = 11\%$, asym., $\Lambda = 60^\circ$, $Re_n = 35000$

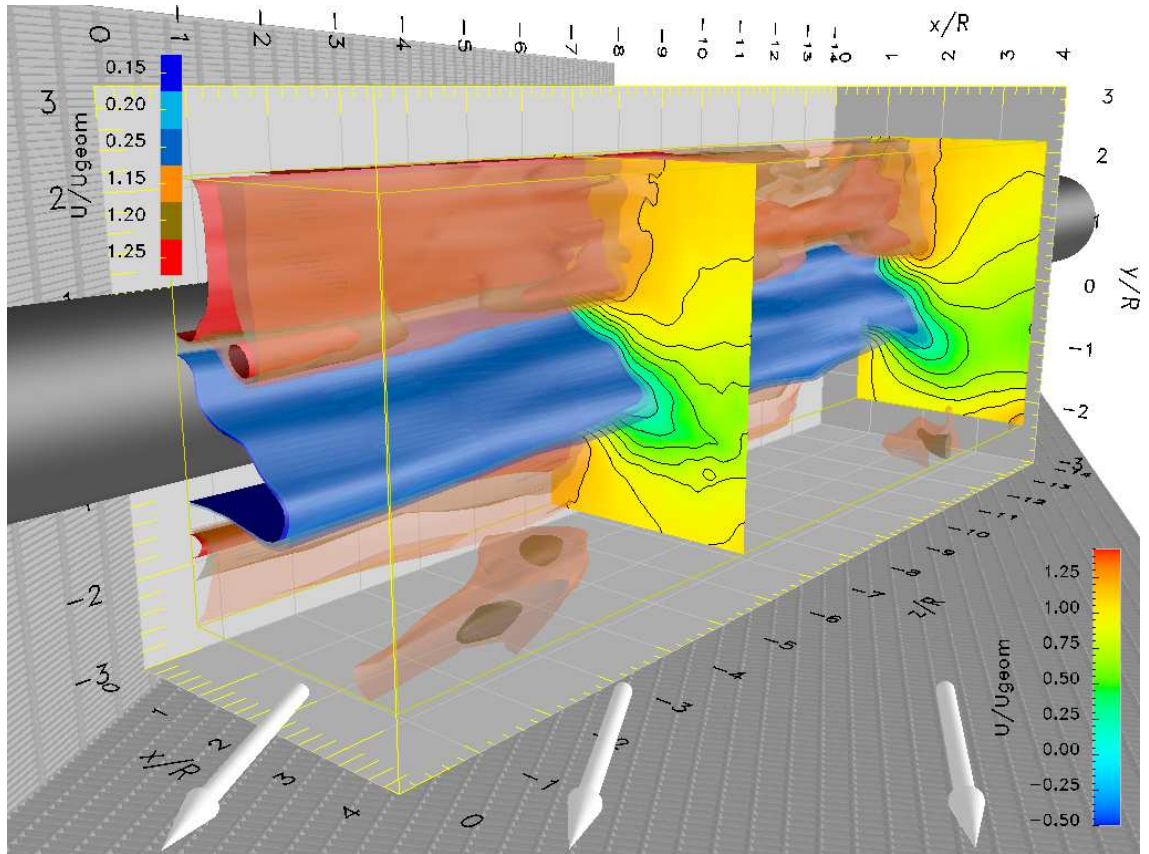


Fig. 4.48: $\frac{U}{U_{\infty \cos \Lambda}}$, POD $\varphi = -40^\circ$, $\Theta = 110^\circ$, $F_n^+ = 1.78$, $C_{\mu,n} = 11\%$, asym., $\Lambda = 60^\circ$, $Re_n = 35000$

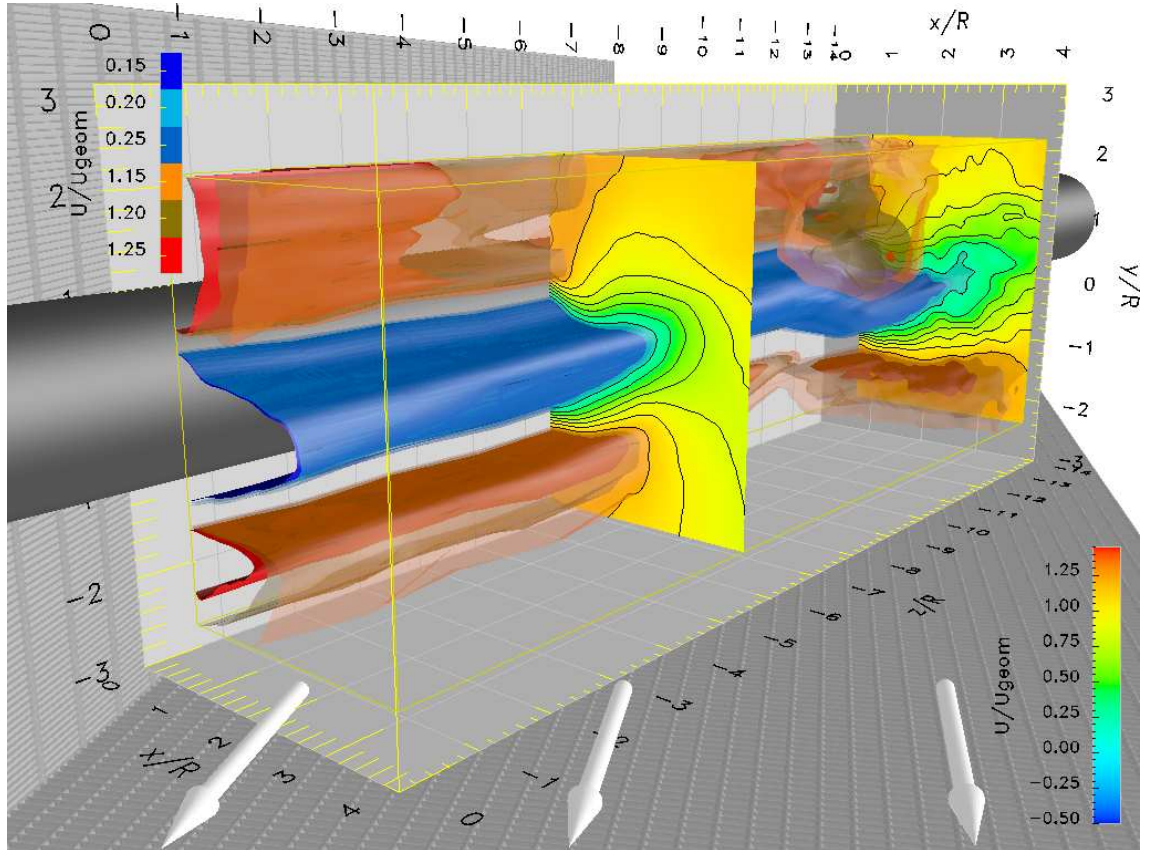


Fig. 4.49: $\frac{U}{U_{\infty \cos \Lambda}}$, POD $\varphi = 40^\circ$, $\Theta = 110^\circ$, $F_n^+ = 1.78$, $C_{\mu,n} = 11\%$, asym., $\Lambda = 60^\circ$, $Re_n = 35000$

The dynamics of the wake with asymmetric excitation are visualized by iso-surfaces of $\frac{\Omega_z D}{U_\infty}$ in figures 4.51 to 4.58 for three different cases of slot angle and excitation level. Three different sets of three figures each (for three POD phase angles) and two additional visualizations of streamlines are presented. In this case vorticity is the preferred quantity for the 3-D visualization because vortices with different sense of rotation cannot be distinguished when using minima of $\frac{W}{U_\infty \sin \Lambda}$ for identification of vortex cores. The coherence of the vorticity is considerably increased due to the conditional averaging, although the number of samples entering the averages is reduced significantly. The magnitude of the averaged vorticity is approximately doubled, as can be seen by comparing the iso-levels of figure 4.51 to the levels of figure 4.36.

The relation between the peel-off process and the meandering of the wake can be clearly observed by comparing the wake at different POD phase angles for each set of three figures. The wake oscillates around a center position (figure 4.50, $\Theta = 110^\circ$, $C_{\mu,n} = 11\%$). This mid position does not necessarily correspond to the averaged flow field, it is the position between the two extreme deflections of the wake, as described above on pages 19 ff. When the wake is deflected downwards (figure 4.51) the negative vorticity (blue) is aligned parallel to the cylinder in three individual vortices and no peel-off can be observed on this side. The downward deflection of the wake forces the positive vorticity (red) into a region of higher streamwise velocity and a vortex containing positive vorticity is peeling-off around $z/R = -2$. This process could be considered as a forced shearing-off of the positive vorticity. The vortex does not grow into a region of higher streamwise velocity but is rather displaced into it by the global deflection of the wake, followed by a separation from the cylinder. Accordingly, an accumulation of negative vorticity (blue) is peeling-

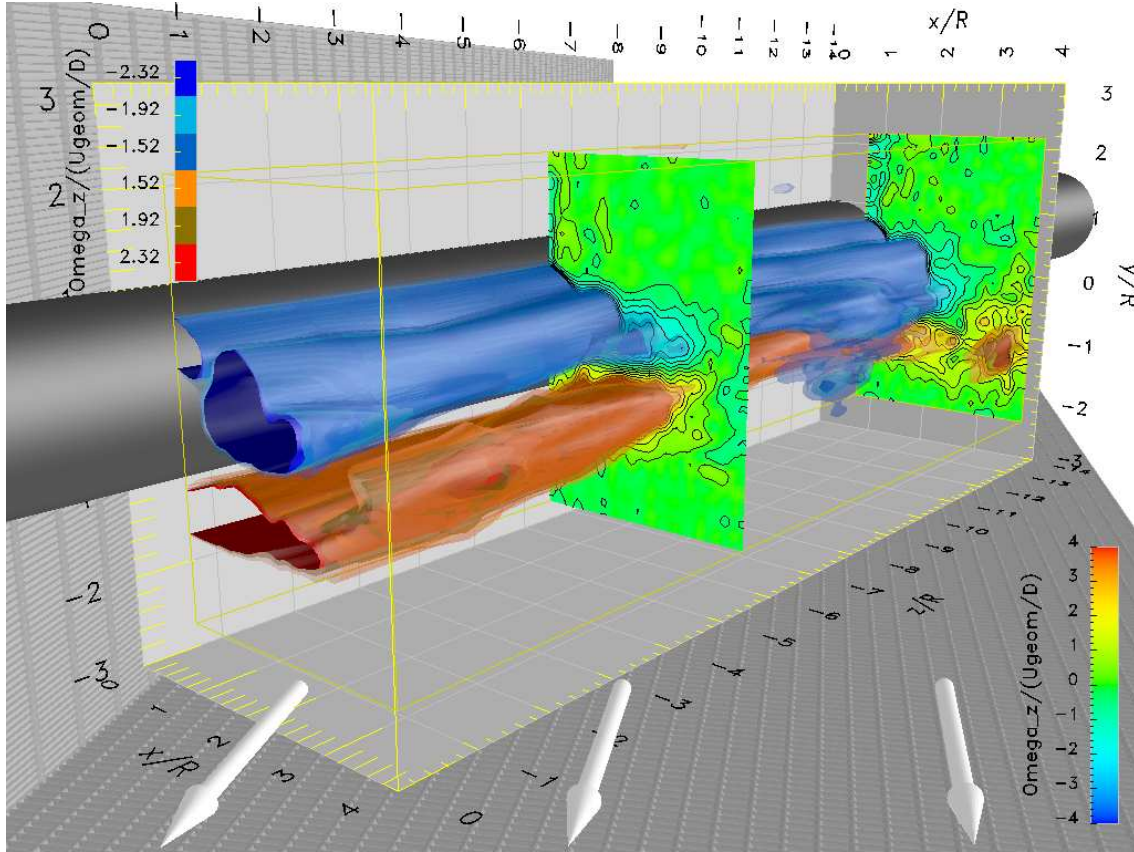


Fig. 4.50: $\frac{\Omega_z D}{U_\infty}$, $\Theta = 110^\circ$, $F_n^+ = 1.78$, $C_{\mu,n} = 11\%$, asym., POD $\varphi = 0^\circ$, $\Lambda = 60^\circ$, $Re_n = 35000$

off around $z/R = -12$ when the wake is deflected upwards and the vortices on the topside of the wake are displaced towards higher streamwise velocity (figure 4.52). The relation between the vortex peel-off and the meandering of the wake generates a fluctuation of the separating vortices. The spanwise peel-off location of the vortices seems to vary only little in spanwise direction for excitation at $\Theta = 110^\circ$ and higher levels of C_μ , although the peel-off process varies in time. This results in a quasi-stationary position of the vortices.

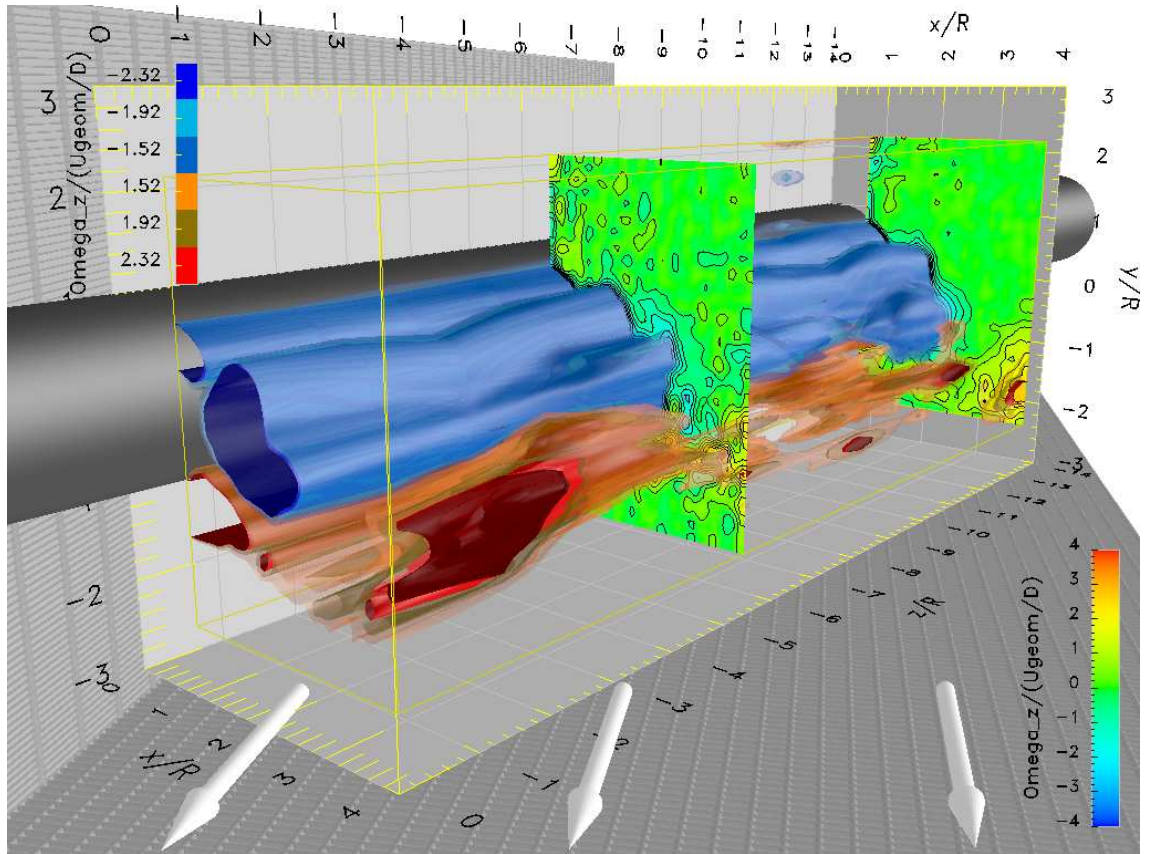


Fig. 4.51: $\frac{\Omega_z D}{U_\infty}$, $\Theta = 110^\circ$, $F_n^+ = 1.78$, $C_{\mu,n} = 11\%$, asym., POD $\varphi = -40^\circ$, $\Lambda = 60^\circ$, $Re_n = 35000$

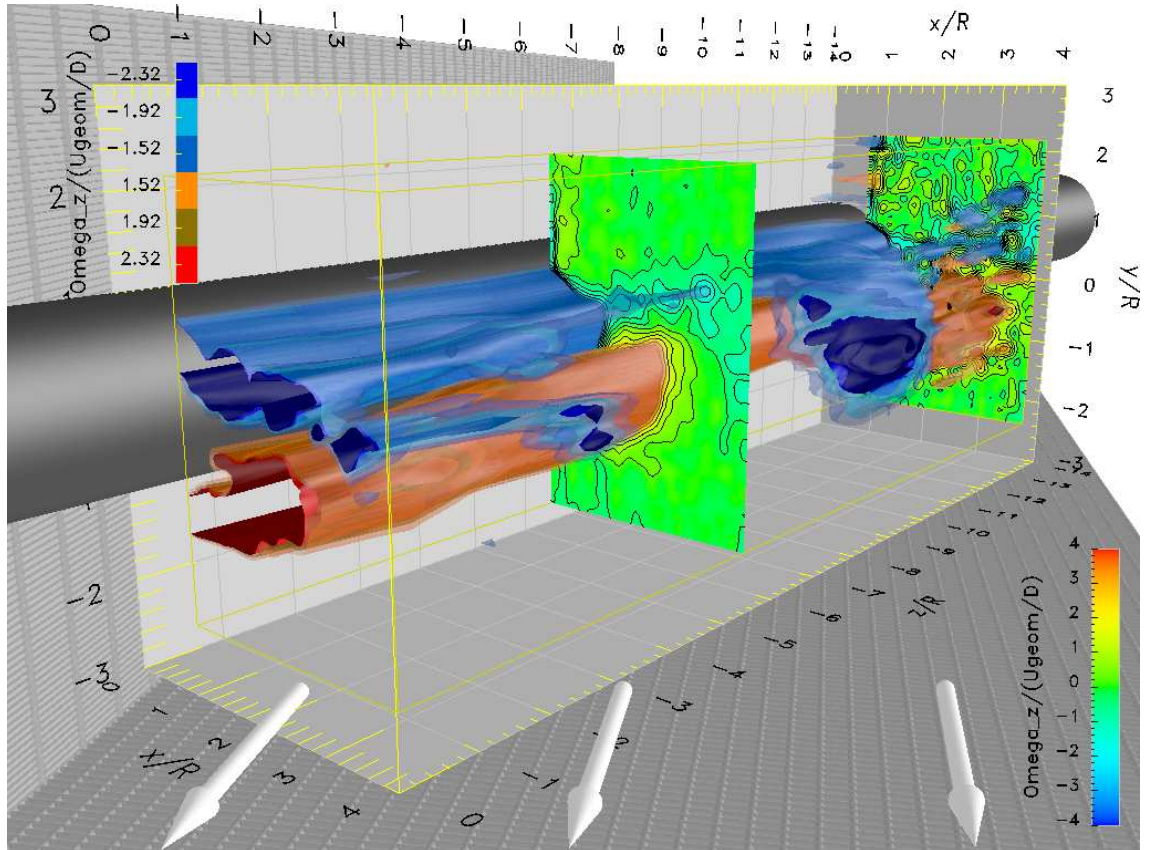


Fig. 4.52: $\frac{\Omega_z D}{U_\infty}$, $\Theta = 110^\circ$, $F_n^+ = 1.78$, $C_{\mu,n} = 11\%$, asym., POD $\varphi = 40^\circ$, $\Lambda = 60^\circ$, $Re_n = 35000$

The stationarity of the vortex peel-off is decreased considerably when forcing is applied from a slot located further downstream at $\Theta = 130^\circ$, as presented in figures 4.53 to 4.58. The iso-values of $\frac{\Omega_z D}{U_\infty}$ in these figures were increased in comparison to figures 4.51 to 4.52 for better identification of the coherent structures close to the cylinder. Compared to the simple average shown in figure 4.40 the iso-levels are approximately doubled.

At $C_{\mu,n} = 11\%$ an elongated accumulation of negative vorticity consisting of several individual vortices extends along the entire investigated spanwise region when the wake is deflected downwards ($\varphi = -40^\circ$, figure 4.53). A vortex is peeling-off at $z/R = -13.3$, losing coherence quickly in spanwise direction for $z/R > -11$. On the unforced side a single large vortex is oriented parallel to the cylinder's axis, growing in size along the span.

At a POD phase of $\varphi = 0^\circ$ (figure 4.54) the vorticity concentrations on both sides are still relatively compact and located close to the cylinder. The positive vortex moves towards $y/R = 0$ and thus the accumulation of negative vorticity is displaced towards $y/R > 0$. The start of the peel-off process can be observed on the contour plot at $z/R = -5.3$ and for $z/R > -2$. At the latter location the coherence found for $\varphi = -40^\circ$ is reduced and it can be observed on the contour plot how the negative vorticity is displaced towards larger x/R and y/R . It seems that the positive vorticity pushes aside the negative vortex, forcing a large accumulation of negative vorticity to separate from the cylinder.

This process is continued at $\varphi = 40^\circ$ (figure 4.55). The positive vorticity bulges further towards $y/R > 0$ around $z/R = 6$ and the negative vorticity is further displaced into the free stream. The coherence of the negative vorticity is decreasing more and more at the downstream end of the cylinder due to the peel-off. At $\varphi = 40^\circ$ a large accumulation of negative vorticity (blue) is clearly separating from the cylinder around $z/R = -12$.

The peel-off process for forcing at $C_{\mu,n} = 11\%$ from a slot located at $\Theta = 130^\circ$ can be envisioned as a modulation of the negative vorticity by the vertical oscillations of the positive vortex. This causes a fluctuating separation of large accumulations of negative vorticity that are "chopped off" the cylinder. The vertical motion towards $y/R > 0$ of the positive vortex itself is enhanced by induction from the separated negative vorticity.

Two weak vortices remain along the entire span close and almost parallel to the cylinder on both sides of the cylinder, accumulating constantly the vorticity generated in the two boundary layers. Interesting is the elongated accumulation of positive (red and yellow) vorticity at the upstream end (contour plot at $z/R = -13.3$ of the investigated volume, indicating a vortex sheet connecting the small positive vortex located close to the cylinder to a vortex that peeled-off further upstream (in spanwise direction), similar to the weaker one visible (yellow-green in the contour plot) at the same spanwise position in figure 4.56.

For a reduced level of excitation of $C_{\mu,n} = 4\%$ the two-dimensionality of the two vortices close to the cylinder is diminished when the wake is deflected (figures 4.56 and 4.58). This destabilizing effect of a low-level excitation causes strong spanwise variations of the flow. The increase in the spanwise variations are the result of a more pronounced peel-off process, visible in the less blurred vorticity distributions in figures 4.57 and 4.58. The vortex peeling-off at $\varphi = 40^\circ$ (blue, around $z/R = -13.3$ in figure 4.58) is clearly more coherent than the one observed when forcing at a higher level (figure 4.55). The comparison of the contour plots located at $z/R = -5.3$ does not yield a considerable variation of the vortex location for the three presented POD phases. Nevertheless the strength of the separating vortex fluctuates significantly. As seen before it is strongest when the wake is deflected upwards (figure 4.58, $\varphi = 40^\circ$). It almost vanishes in the plane of the contour plot ($z/R = -5.3$) for $\varphi = 40^\circ$.

Thus the peel-off process differs largely between the two different excitation levels. The peeling-off vortex seems to be quasi-stationary but unsteady when forcing is applied at a low level whereas at the higher level of forcing the separating vortex seems to be quasi-steady but instationary. The importance of minimizing these fluctuations for any technical application is given by the potentially powerful oscillations in lift and drag that might be generated by strong temporal variations of the vortex peel-off.

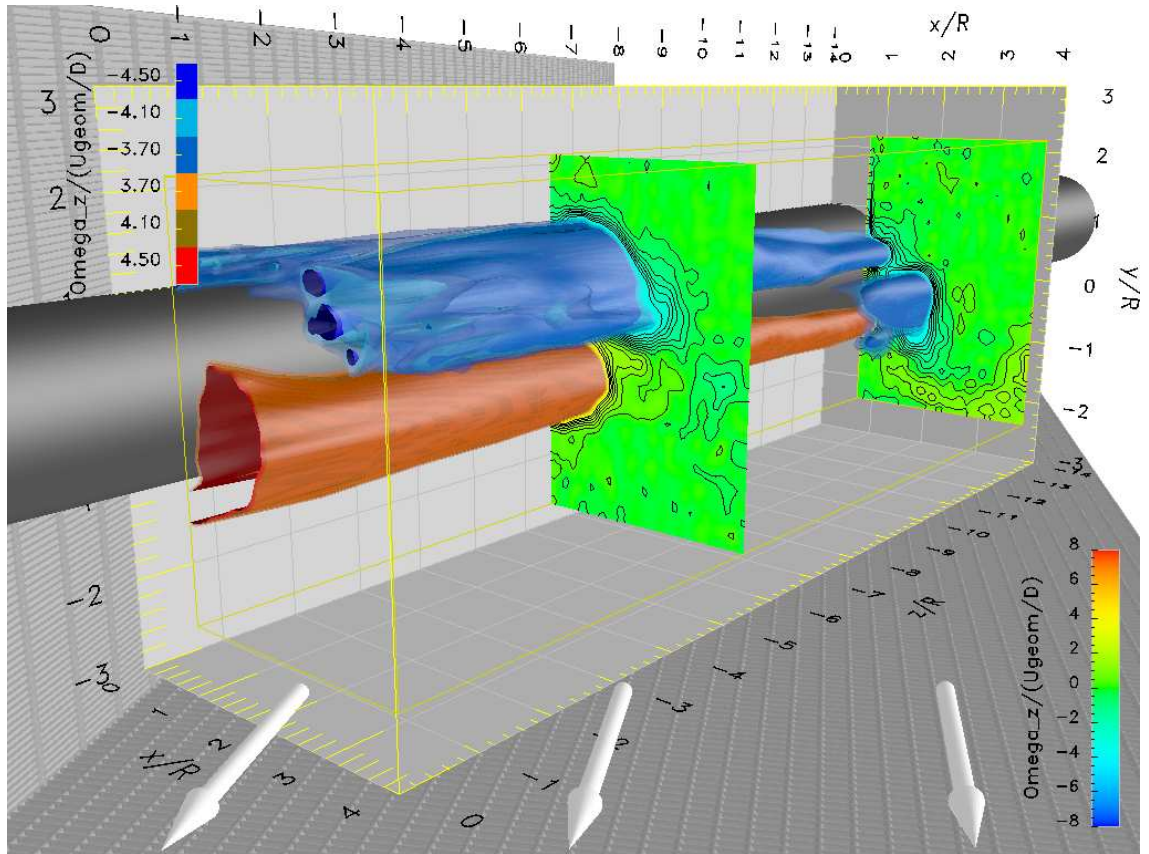


Fig. 4.53: $\frac{\Omega_z D}{U_\infty}$, $\Theta = 130^\circ$, $F_n^+ = 1.78$, $C_{\mu,n} = 11\%$, asym., POD $\varphi = -40^\circ$, $\Lambda = 60^\circ$, $Re_n = 35000$

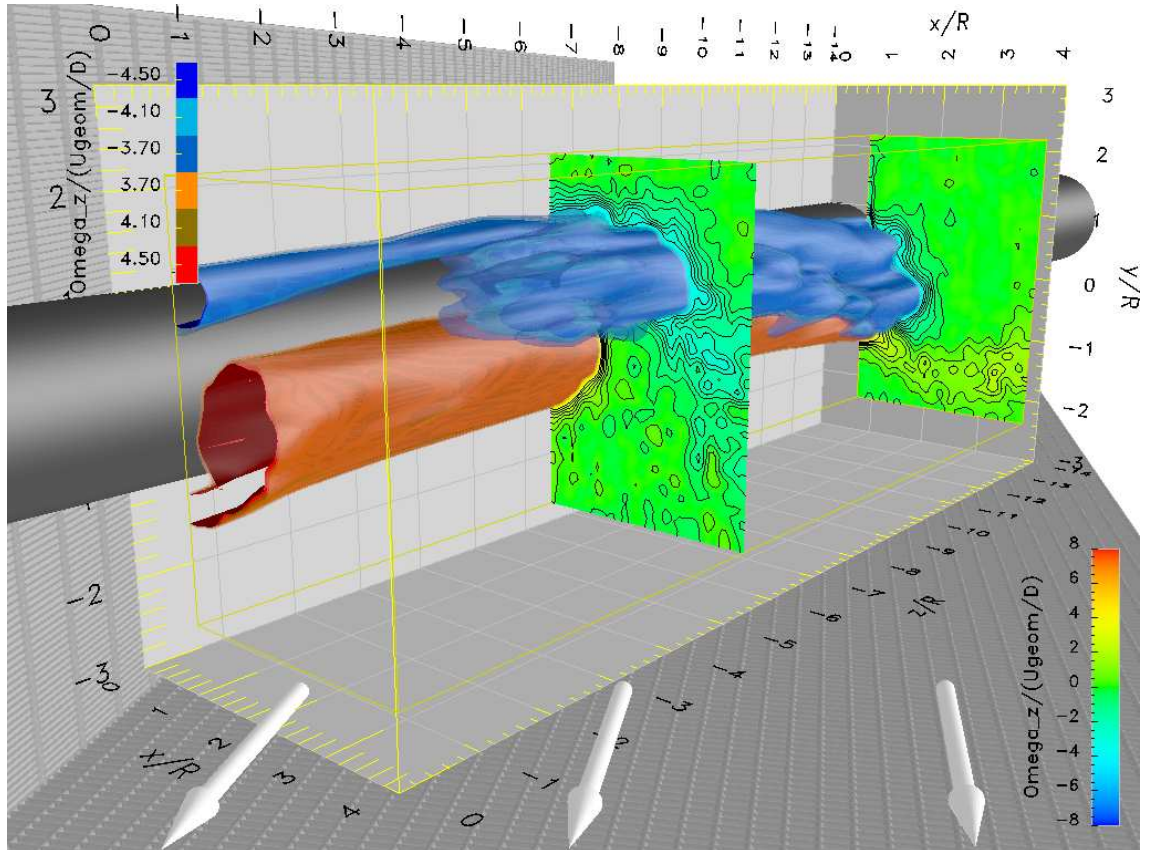


Fig. 4.54: $\frac{\Omega_z D}{U_\infty}$, $\Theta = 130^\circ$, $F_n^+ = 1.78$, $C_{\mu,n} = 11\%$, asym., POD $\varphi = 0^\circ$, $\Lambda = 60^\circ$, $Re_n = 35000$

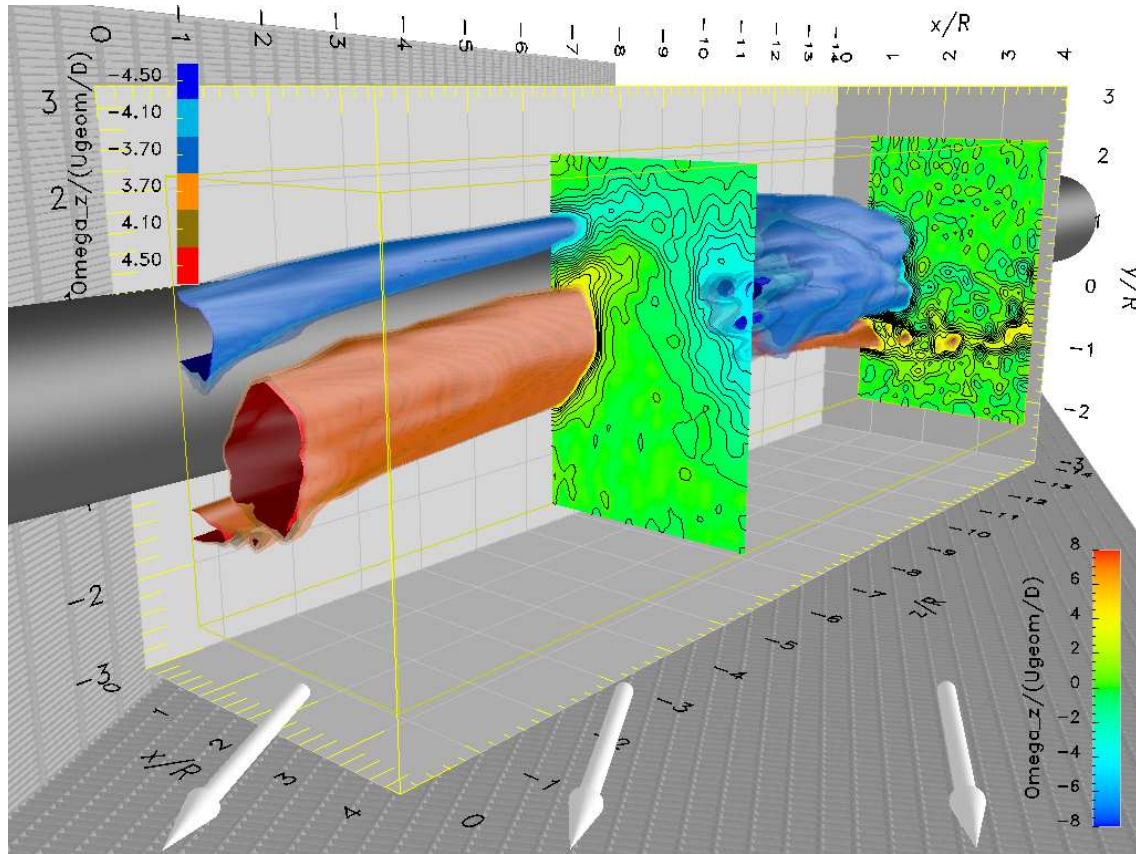


Fig. 4.55: $\frac{\Omega_z D}{U_\infty D}$, $\Theta = 130^\circ$, $F_n^+ = 1.78$, $C_{\mu,n} = 11\%$, asym., POD $\varphi = 40^\circ$, $\Lambda = 60^\circ$, $Re_n = 35000$

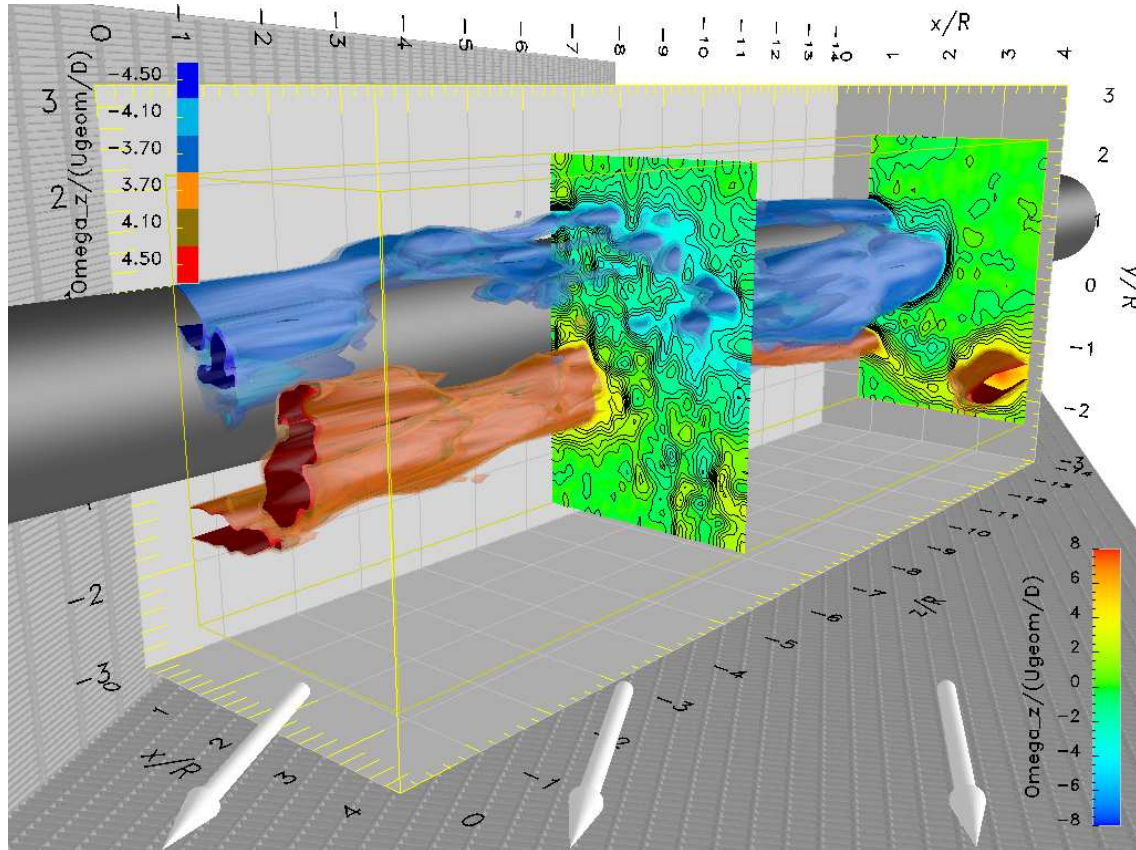


Fig. 4.56: $\frac{\Omega_z D}{U_\infty D}$, $\Theta = 130^\circ$, $F_n^+ = 1.78$, $C_{\mu,n} = 4\%$, asym., POD $\varphi = -40^\circ$, $\Lambda = 60^\circ$, $Re_n = 35000$

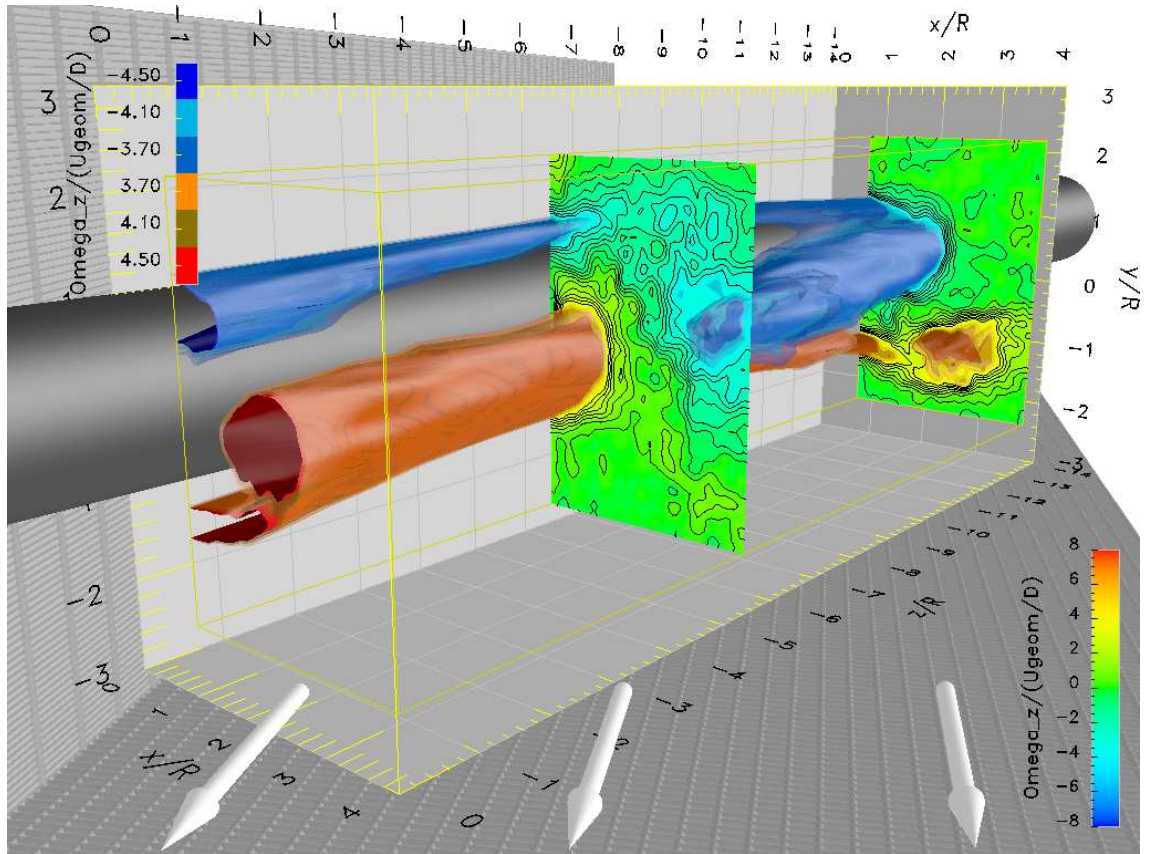


Fig. 4.57: $\frac{\Omega_z D}{U_\infty}$, $\Theta = 130^\circ$, $F_n^+ = 1.78$, $C_{\mu,n} = 4\%$, asym., POD $\varphi = 0^\circ$, $\Lambda = 60^\circ$, $Re_n = 35000$

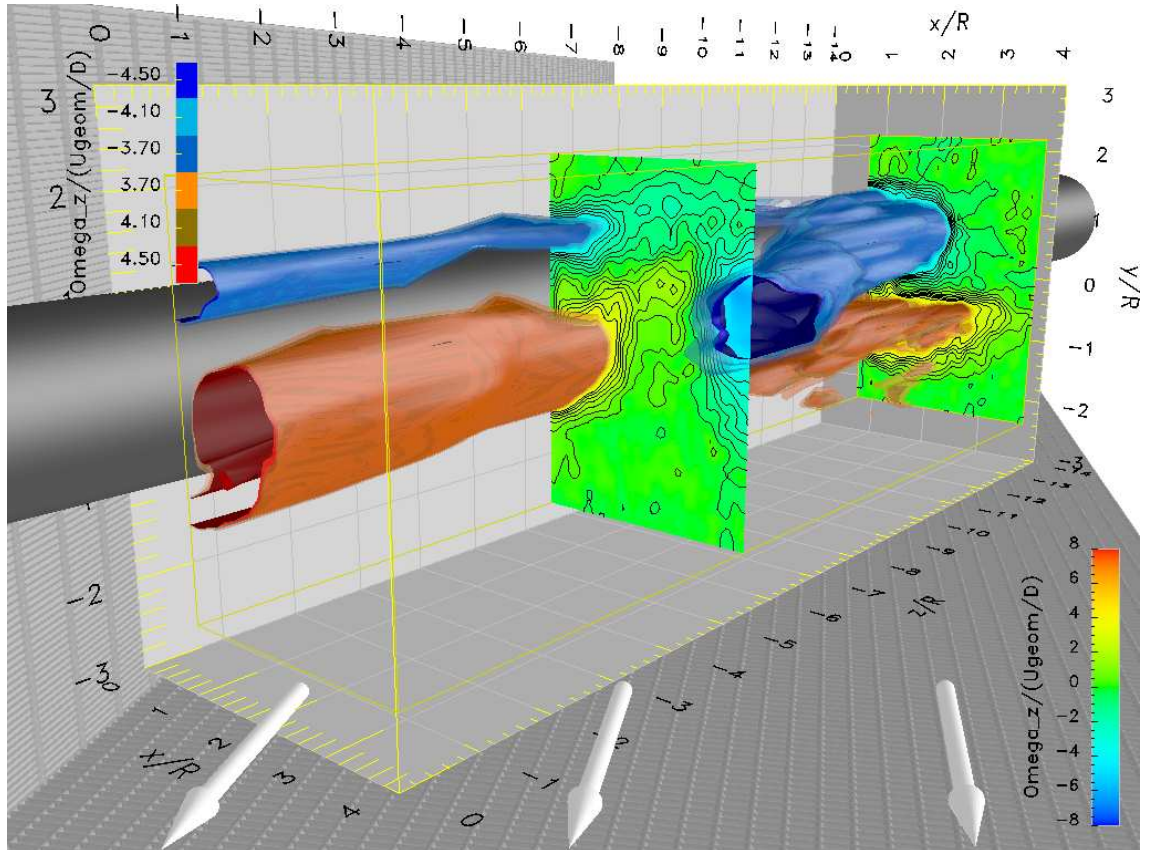


Fig. 4.58: $\frac{\Omega_z D}{U_\infty}$, $\Theta = 130^\circ$, $F_n^+ = 1.78$, $C_{\mu,n} = 4\%$, asym., POD $\varphi = 40^\circ$, $\Lambda = 60^\circ$, $Re_n = 35000$

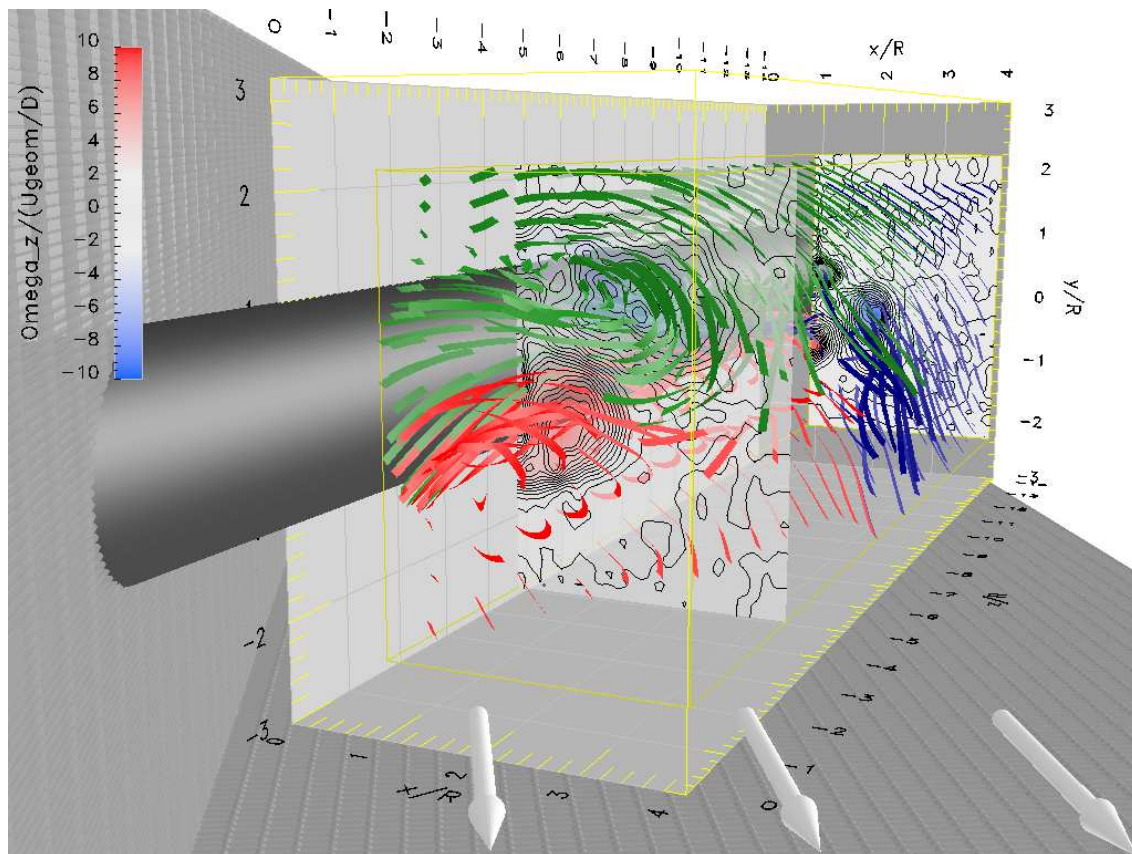


Fig. 4.59: Streamlines and $\frac{\Omega_z D}{U_\infty}$, $\Theta = 130^\circ$, $F_n^+ = 1.78$, $C_{\mu,n} = 11\%$, asym.,
POD $\varphi = -40^\circ$, $\Lambda = 60^\circ$, $Re_n = 35000$

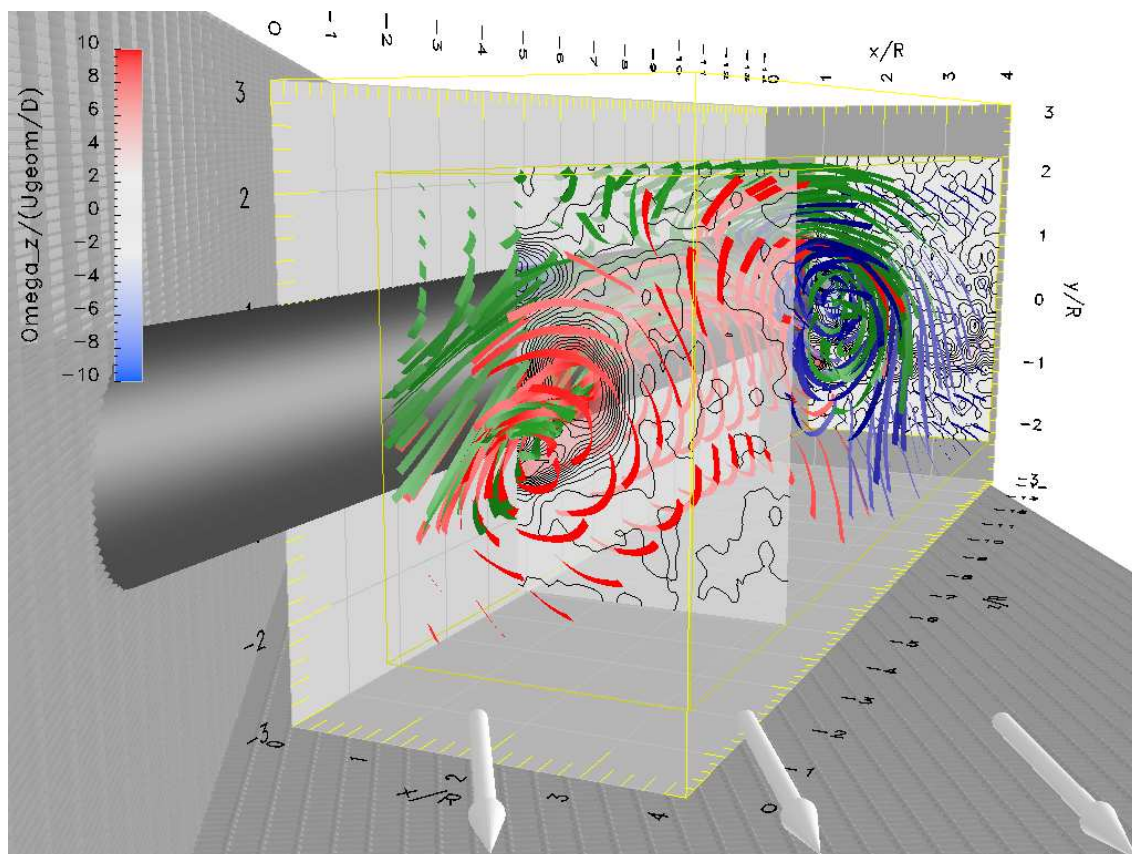


Fig. 4.60: Streamlines and $\frac{\Omega_z D}{U_\infty}$, $\Theta = 130^\circ$, $F_n^+ = 1.78$, $C_{\mu,n} = 11\%$, asym.,
POD $\varphi = 40^\circ$, $\Lambda = 60^\circ$, $Re_n = 35000$

Streamlines are very suitable to visualize vortex dynamics, especially when a time (resolved) series or phase-locked averages are available. In this case streamlines are computed from the conditional averages of different POD phases (figures 4.59 and 4.60). They are color coded, based on their origin at the boundaries of the control volume. Streamline originating at the XY-plane at $z/R = -13.3$ ('upstream end') are marked in blue, green streamlines start at the YZ-plane at $x/R = 1$, $y/R > 0$ and red ones at the YZ-plane at $x/R = 1$, $y/R < 0$. The curl of the "stream-ribbons" indicates the local vorticity. Contour plots of vorticity were added at two spanwise positions to facilitate orientation in the control volume, the corresponding legend is shown on the upper left.

In figure 4.59 (see corresponding vorticity iso-surfaces in figure 4.56) the wake is relatively compact and the flow around the inclined cylinder is relatively smooth. The streamlines at the YZ-plane at $x/R = 4$ ("downstream side") are all deflected downwards. This indicates the generation of positive lift along the entire span. The "red" and the "green" vortices visible at the downstream end ($z/R = 0$) of the control volume are of comparable size although the presented POD phase $\varphi = -40^\circ$ is deflected downwards and forcing is applied from the top half of the cylinder.

Figure 4.60 shows (see iso-surfaces in figure 4.58) a wake that is deflected upwards (POD $\varphi = 40^\circ$). Two large vortices are peeling-off the cylinder. One is formed mainly by streamlines originating at the upstream end (blue) and $y/R > 0$ (green). This vortex is peeling off the cylinder around $z/R = -12$, as discussed for figure 4.55. The second vortex is formed mostly by streamlines originating in the YZ-plane for $y/R < 0$ (red) with entrainment of some streamlines starting at $y/R > 0$ (green). It is separating from the cylinder and pushing the fluid marked in green up into the free stream, causing the peel-off of the "blue" vortex. This confirms the observations discussed for figures 4.53 to 4.55.

During the separation process the vortices increase in size and are disturbing the flow around the cylinder, causing temporal and spanwise fluctuations of lift and drag, in particular when the wake is deflected upwards with $\varphi > 0$.

The dynamics of the wake could be described quantitatively by determining the locations of all individual vortices and tracking their positions over the entire time series. Instead of trying to analyse the position every single vortex an integral approach was considered better suitable to characterize the state of the wake. The center of vorticity as defined in equations 4.8 (page 47) was computed for all POD phases and spanwise positions to quantify the vortex dynamics in the near wake.

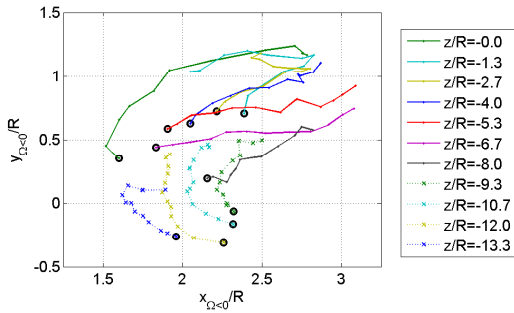


Fig. 4.61: Center of $\Omega_z < 0$, $\Theta = 130^\circ$,
 $F_n^+ = 1.78$, $C_{\mu,n} = 11\%$, asym.

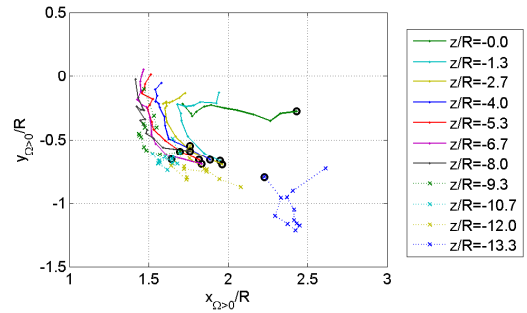


Fig. 4.62: Center of $\Omega_z > 0$, $\Theta = 130^\circ$,
 $F_n^+ = 1.78$, $C_{\mu,n} = 11\%$, asym.

The location of the center of vorticity at various POD phases ($\Theta = 130^\circ$, $F_n^+ = 1.78$, $C_{\mu,n} = 11\%$) is presented for $\Omega < 0$ (forced side) in figure 4.61 and for $\Omega > 0$ in figure 4.62. The black circles mark the most negative phase equivalent to the largest downwards deflection of the wake. In general a displacement towards larger absolute values of y/R and therefore higher values of U increases the horizontal distance x/R of the vortices to the cylinder: the vortices are "swept away" by the free stream. The vertical motion of vortices on both sides of the cylinder is in phase.

On the unforced side ($\Omega_z > 0$) the trajectory of the vortices is relatively homogeneous along the span, with exception of the first two ($z/R = -13.3$ and $z/R = -12.0$) and last ($z/R = 0$) spanwise station. In all other cases the location center of positive vorticity fluctuates by approximately

$x/R = 0.5$ and $y/R = 0.5$ to $y/R = 0.7$. At the upstream end the investigated volume the flow is dominated by the large accumulation of negative vorticity peeling-off the cylinder. At its downstream end the vortex on the unforced side has grown to its maximum diameter and is starting to peel off, this explains the almost horizontal trajectory at this spanwise station.

On the forced side the situation is different with a horizontal fluctuation of approximately $x/R = 0.8$ to $x/R = 1.3$ for $z/R \geq -8$ (downstream region) in contrast to $x/R < 0.5$ for $z/R < -8$. In the upstream region the vortex just starting to peel-off the cylinder, therefore the position in X-direction is relatively constant. For $z/R \geq -8$ the vortex on the forced side separated from the cylinder, therefore the horizontal motion is less restricted.

4.4.1.4 The Far Wake

Data were acquired in the far wake of the cylinder with a vertical (perpendicular to the cylinder) rake of Pitot tubes that was traversed horizontally across the test section of the wind tunnel. The wake rake was located $10D$ downstream of the downstream end of the cylinder when the latter was at its maximum sweep-back angle of 60° . The minimum distance between wake rake and tunnel walls was to 4" (100mm). The data are presented by contour plots (individually scaled for best resolution) in combination with 3-D surface plots (all of which retain a constant range of scales) to facilitate comparison between different data sets.

Due to wall interference at the downstream end of the cylinder it was not possible to accurately determine the total drag in the "infinite" configuration by integrating the measured dynamic pressure over the entire area. The velocity deficit determined in the baseline case (see figure 4.63, inactive slot taped) the limitations of the measurements in the far wake. A disturbance can be observed near the tunnel wall to which the upstream end of the cylinder is connected ($z_T/R = -5.3$ in figures 4.63). It was caused by the necklace vortex shed from the cylinder at the intersection with the fence mounted at a distance of 1" (2.5cm) to the wall. Because the main necklace vortex was successfully prevented from attaching to the base of the cylinder it remained located close to the side wall of the test section. It was in this position detected by the wake rake in most of the measurements. The velocity gradient in this vortex pair normal to the wall is significant compared to the maximum velocity deficit caused by the cylinder. Therefore already minor changes in location of the necklace vortex result in large variations at the right boundary of the wake. These changes in location could be caused by changes in the low pressure region in lee of the cylinder altering the pressure gradient perpendicular to the wall.

The spanwise flow generated in lee of the cylinder impinges on the opposite side of the test section at an angle of 30° on the wall, thus the velocity deficit fans out as shown for $z_T/R > 4.5$ in figures 4.63 a) and b). Additionally, the impinging vortices will interact with the necklace vortex that forms at the downstream end of the cylinder, therefore measurements in the region close to the side walls are problematic. It is not possible to determine the minimum velocity on this side because this extremum is located clearly outside the scanned area and too close to the wall to obtain accurate data.

Travel of the wake rake traverse was determined by the length of the linear bearings holding the traverse and the open area of the frame stabilizing the top of the test section. The limited travel of the traverse is not considered to be problematic because the end effects described above prevented the acquisition of accurate and undisturbed data close to the side walls of the test section in all investigated cases. Despite these shortcomings the velocity distribution across the test section enabled a detailed analysis of the three-dimensional processes in the wake of an inclined cylinder. The combination of the data obtained in the far wake with the PIV data acquired in the near wake together with the pressure distributions taken on the cylinder enabled the clear identification of the relevant vortical structures and analysis of the flow in the far wake. The data taken on the "finite" cylinder that is discussed below and eliminated the interference between the downstream end and the side wall provided more accurate results for the total drag.

The series of wake measurements presented in figures 4.63 to 4.66 covered the range of C_μ in which the wake changed from a highly distorted state to an undisturbed one. The distortions were caused by vortices in lee of the cylinder that impinged on the wall at the downstream end. Actuation frequency was $F_n^+ = 1.78$ (175Hz) in all cases considered presently.

For an excitation level of $C_{\mu,n} = 2\%$ the wake is pulled towards the center of the test section

(figure 4.64) when compared to the baseline (figure 4.63). The shift is sufficient to estimate the magnitude of the velocity minimum but the wake remains highly distorted. This shift of the wake can be caused either by an altered vortex peel-off location or by a change in the pressure in lee of the cylinder that would modify the reorientation of the peeled-off vortices in the streamwise direction.

The structure of the wake changes drastically when forcing at a higher level of $C_{\mu,n} = 4\%$ (figure 4.65). Several minima are distributed across the test section instead of the single large velocity deficit close to the side wall. The transition to an undisturbed state of the wake without any wall interference is not complete, as can be seen at the residual disturbances still fanning out at the wall. At $C_{\mu,n} = 11\%$ the wall interference is negligible on both sides (figure 4.66), the slight increase of the disturbances caused by the necklace vortex is due to its interaction with the peeled-off vortices. The total drag C_d can be determined accurately with the existing setup only for an undisturbed wake.

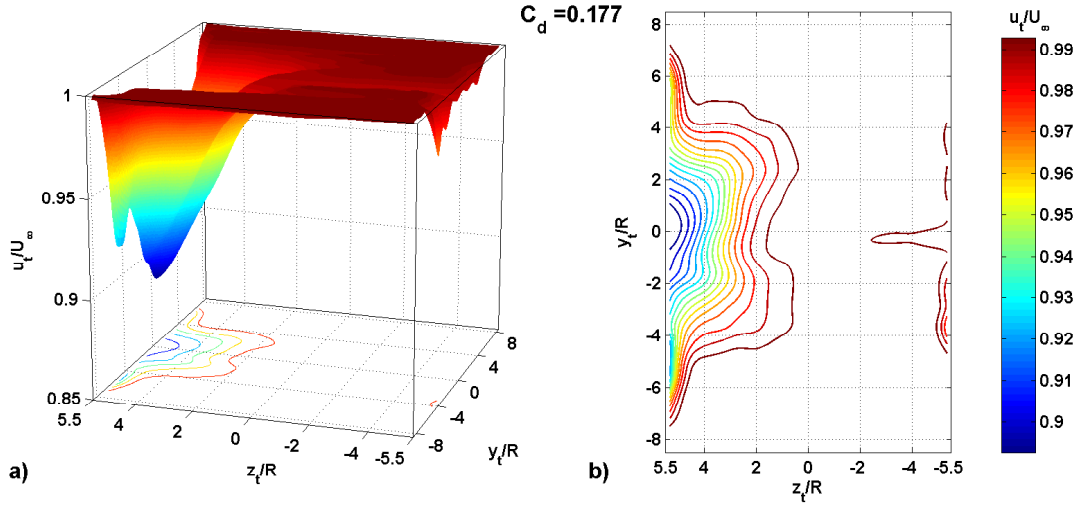


Fig. 4.63: Far wake, $\frac{U_T}{U_\infty}$, $\Theta = 110^\circ$, baseline, $\Lambda = 60^\circ$, $Re_n = 35000$

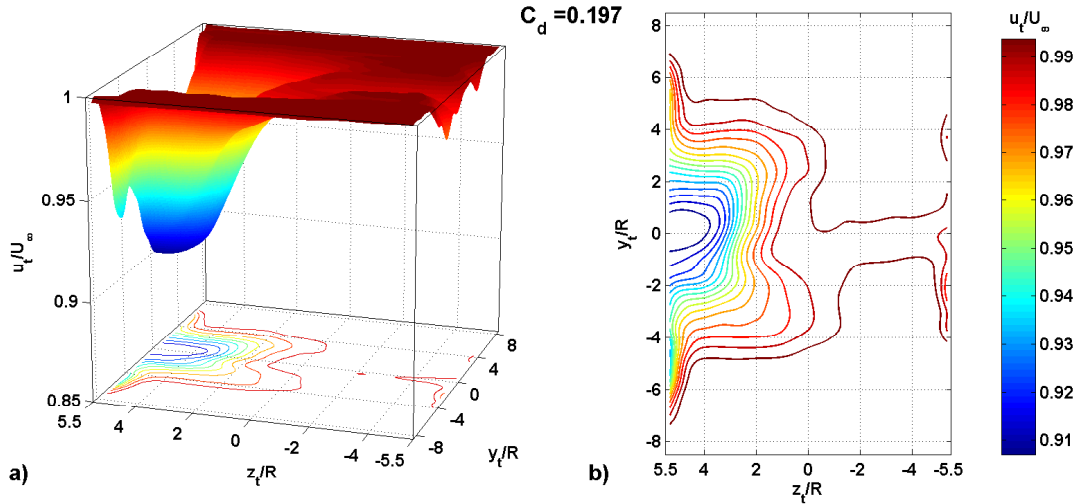


Fig. 4.64: Far wake, $\frac{U_T}{U_\infty}$, $\Theta = 110^\circ$, $F_n^+ = 1.78$, $C_{\mu,n} = 2\%$, asym., $\Lambda = 60^\circ$, $Re_n = 35000$

Three distinct velocity minima can be identified in figure 4.66. Two vortices can be observed in figure 4.50, peeling-off inside the investigated volume and at the upstream end a third vortex is still visible within the data volume. Because these three vortices are all visible inside the region investigated by PIV (figure 4.36), they have to be located at $z_T/R > -3.5$ based on the boundaries

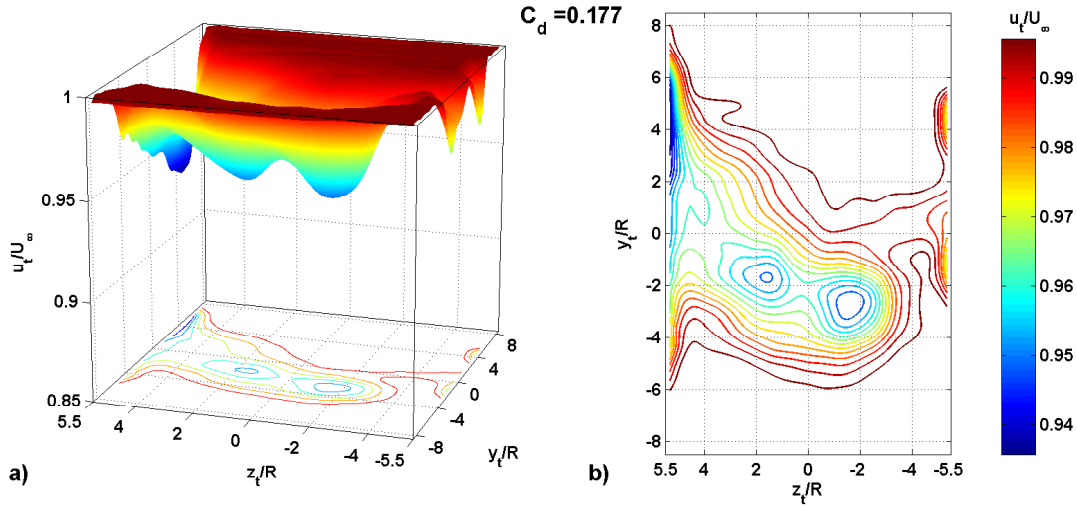


Fig. 4.65: Far wake, $\frac{U_T}{U_\infty}$, $\Theta = 110^\circ$, $F_n^+ = 1.78$, $C_{\mu,n} = 4\%$, asym., $\Lambda = 60^\circ$, $Re_n = 35000$

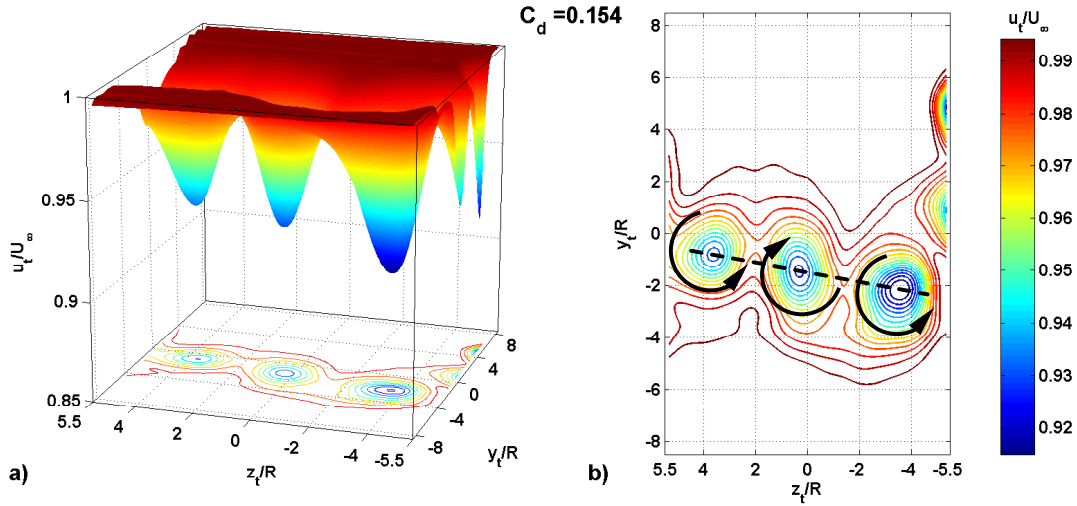


Fig. 4.66: Far wake, $\frac{U_T}{U_\infty}$, $\Theta = 110^\circ$, $F_n^+ = 1.78$, $C_{\mu,n} = 11\%$, asym., $\Lambda = 60^\circ$, $Re_n = 35000$

of the region investigated by PIV. The two that are actually peeling-off from the cylinder in the observed volume have to be located at $z_T/R > 0$. This matches the locations of the vortices found in the far wake. It proves that the velocity deficits in streamwise direction found in the far wake are caused by the spanwise velocity deficits in the cores of the peeled-off vortices that were reoriented in streamwise direction downstream of the cylinder. Their sense of rotation can therefore be derived directly from the PIV data acquired in the near wake. It is marked by the black arrows in figure 4.66.

The distance between the velocity minima and the plane of symmetry at $y/R = 0$ varies for $C_{\mu,n} = 11\%$ linearly with z/R (marked by a black line in figure 4.66). It is caused by induction between the three vortices. The induction of the left and right vortices on the middle one cancel out, therefore it likely stays in place. In contrast to this the outer vortices are displaced by induction from the middle vortex.

The differences in magnitude between the individual minima are less than 2% of U_∞ , possibly caused by a gradient of the spanwise velocity due to wall effects. Such a gradient would not only affect the velocity deficit directly but also the rate of convection of vorticity along the span and therefore the peel-off process. The necklace vortex visible at the right boundary of the figure is deflected to positive y/R due to induction by the first separated vortex, implying that the first peeled off vortex comes from the bottom side of the cylinder (“red vorticity” at $z/R = -13.3$ in figure 4.36). This is consistent with the discussion associated with figures 4.36 to 4.38.

The velocity deficit in figure 4.66 have an approximate cross sectional diameter of $2.5/R - 3R$. The necklace vortex at this streamwise location should be of comparable diameter. The extent of the velocity deficit caused by the necklace vortex can be detected at $z_T/R = -4.5$ to $z_T/R = -5$. The distance between this coordinate and the side wall ($z_{T,wall}/R = -8$) determines the diameter of the necklace vortex of approximately $3/R$. This confirms that the necklace vortex is completely shed from the cylinder by the plate mounted at its upstream end.

As already observed in the pressure distributions around the cylinder and the PIV results in the near wake, actuation from a slot position of $\Theta = 130^\circ$ changes the structure of the wake significantly. The point of actuation at $C_{\mu,n} = 4\%$ is located on the lower part of the lift curve for $\Theta = 130^\circ$ shown in figure 4.17. At this level of excitation the lift is alternating along the span (see figure 4.39). The resulting vortex forming at the jump in C_l can be identified clearly in the far wake as a velocity deficit of large magnitude (see figure 4.67). The minimum located at $y_T/R = -3$, $z_T/R = 0$ is caused by the first vortex peeling-off the cylinder (positive vorticity (red) at $z_T/R = -12$ in figure 4.38). The jump in C_l occurs within $1-2D$ downstream of this peel-off location (see large blue vortex in figures 4.38 and 4.39), generating the second velocity minimum at $y_T/R = 1$, $z/R = 3$. It is deflected upwards due to the locally negative lift generated downstream of the peel-off location of this second vortex (see figures 4.38 and 4.39). This effect is complemented by the self induction of this vortex in wall proximity.

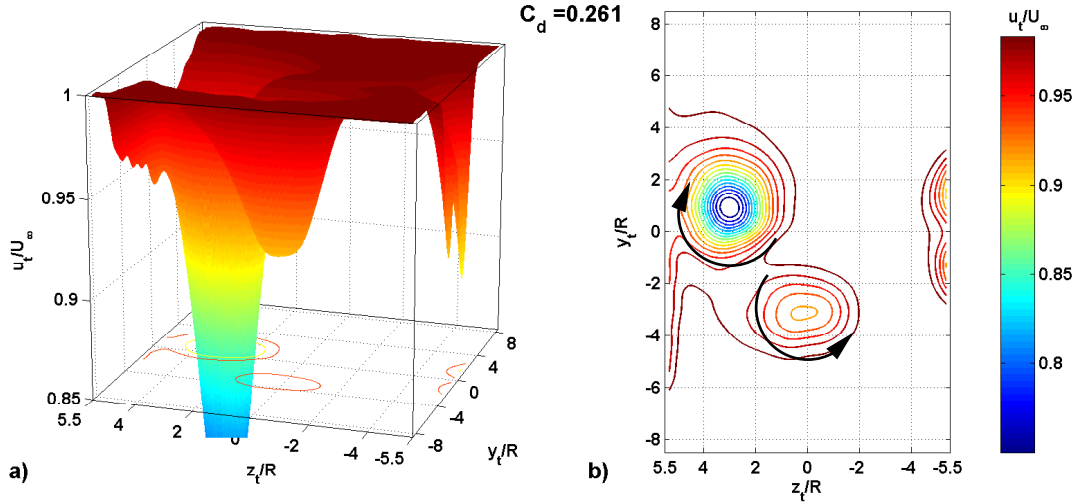


Fig. 4.67: Far wake, $\frac{U_T}{U_\infty}$, $\Theta = 130^\circ$, $F_n^+ = 1.78$, $C_{\mu,n} = 4\%$, asym., $\Lambda = 60^\circ$, $Re_n = 35000$

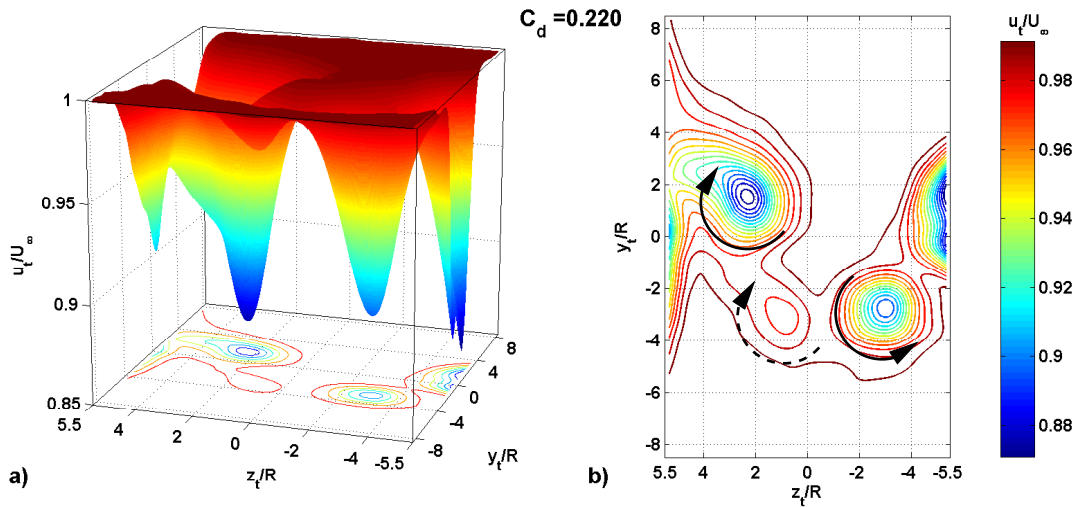


Fig. 4.68: Far wake, $\frac{U_T}{U_\infty}$, $\Theta = 130^\circ$, $F_n^+ = 1.78$, $C_{\mu,n} = 11\%$, asym., $\Lambda = 60^\circ$, $Re_n = 35000$

The weak vortex marked by the dashed arrow in figure 4.68 might be caused by a vertical motion of the negative vortex that peeled of the cylinder. It can be observed the contour plot located at $z/R = -5.3$ in figures 4.53 to 4.55 that the separating vortex is actually moving away from the cylinder and is concurrently deflected downwards. Because this is a dynamic phenomenon it might occur only over short periods of time and thus generate an averaging artifact.

The far wake of a cylinder inclined at 45°

Reducing the sweep-back angle alters the characteristics of the wake significantly. A single dominant velocity deficit exists in the baseline case at $z_T/R = 2$, a second minimum is found close to the wall at $z_T/R = 5.2$ and two side-minima are located at $y_T/R = \pm 4$, $z_T/R = 0$, as can be seen in figure 4.69. The disturbances caused by the necklace vortex ($z_T/R = -5.3$) are distinct, but the necklace vortex is clearly shed from the cylinder and located close to the sidewall of the test section.

The magnitudes and the geometric extent of the velocity deficits are noticeably increased by excitation compared to the sweep-back angle of $\Lambda = 60^\circ$. The increased size can be explained by the oscillations of the peeling-off vortices described on page 97 for the baseline case. The velocity distribution measured in the far wake is therefore considered to be the time average of two vortices periodically changing location.

The necklace vortex is pulled away from the side wall by induction from the first peeled-off vortex. Due to the smaller sweep back angle and the thus altered position of the peeled-off vortices this effect is more pronounced than for $\Lambda = 60^\circ$.

Asymmetric actuation at $C_{\mu,n} = 2\%$ (see figure 4.70) reduces the spanwise periodical fluctuations of the peel-off location and the velocity deficit is less smeared out than in the baseline case. It generates lift alternating along the span, as described above for a sweep-back angle of $\Lambda = 60^\circ$. The first vortex peeling-off the cylinder causes the velocity minimum found at $y_T/R = -4$, $z_T/R = -1.5$, thus lift is generated on the upstream section of the cylinder. The velocity minimum is still smeared out, thus spanwise fluctuations of the peel-off location are still likely to exist. The dominant velocity deficit observed in the baseline case is located at $y_T/R = 1$. As the vortex might be displaced due to self-induction, it is not conclusive if lift is generated in the downstream section of the cylinder, past the first peel-off.

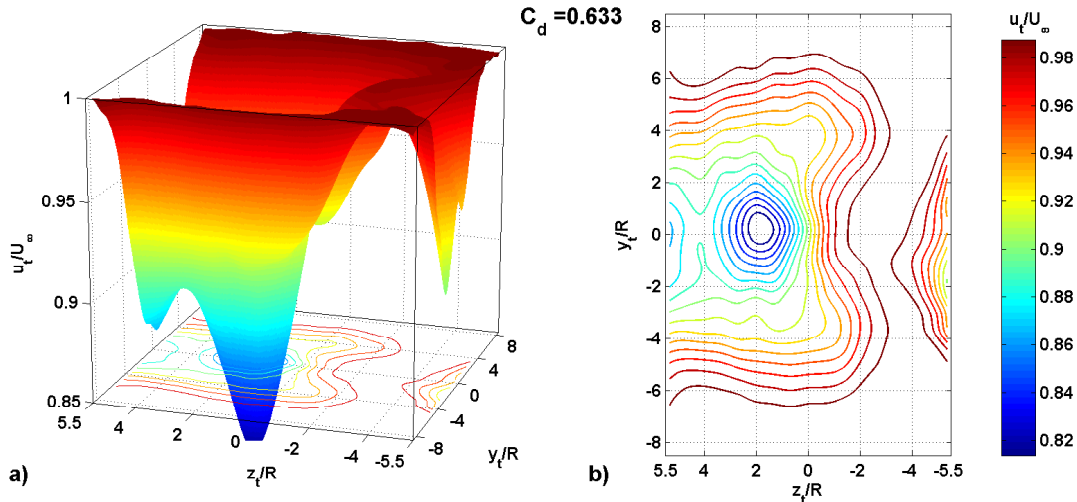


Fig. 4.69: Far wake, $\frac{U_T}{U_\infty}$, $\Theta = 110^\circ$, baseline, $\Lambda = 45^\circ$, $Re_n = 35000$

The spanwise variations of lift are reduced by forcing at $C_{\mu,n} = 5.3\%$ (see figure 4.71). The first two velocity deficits ($z_T/R = -4$ and $z_T/R = -1$) are located at $y_T/R < 0$, the second set ($z_T/R = 2$ and $z_T/R > 5.3$) is located around $y_T/R = 0$, thus lift is generated. The vertically elongated shape of the second velocity minimum at $z_T/R = -1$ indicates a strong vertical oscillation of the second peeled-off vortex. Therefore it is likely that the observed third (weak) velocity minimum at $z_T/R = 1.5$ is actually an artifact due to averaging. It is possible that it results from an additional horizontal movement of the vertically elongated vortex, indicated by the black

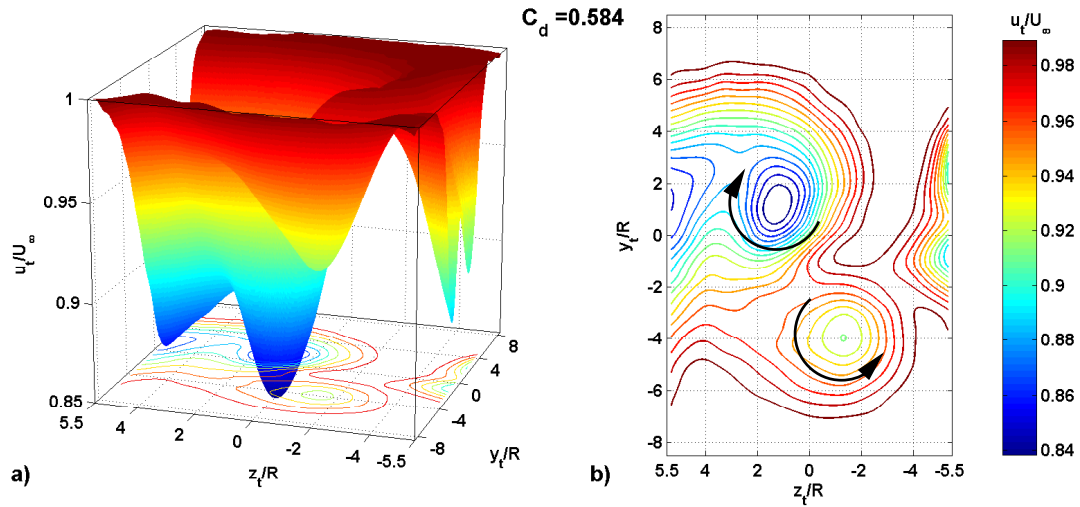


Fig. 4.70: Far wake, $\frac{U_T}{U_\infty}$, $\Theta = 110^\circ$, $F_n^+ = 1.78$, $C_{\mu,n} = 4\%$, asym., $\Lambda = 45^\circ$, $Re_n = 35000$

arrows. This is the most probable explanation for the large difference in strength between the velocity deficits located at $z_T/R = -1$ and $z_T = 2$ because in all other investigated cases the naturally peeled-off vortices are of approximately equal strength, provided that no merging took place and that the velocity minima are not smeared out due to fluctuations. Vortices that were forced by the wall (or the endplate in the finite case) to separate from the cylinder at its downstream end were significantly weaker.

Distortions of the wake due to wall interference are still present at the highest level of excitation ($z_T/R = 5.3$ in figure 4.71), therefore the total drag (figure 4.72) can be determined only with limited accuracy. The strong reduction in C_d between the two plateaus in figure 4.72 are caused by the suppression of the spanwise fluctuation of the peel-off location. This reduces the velocity deficit at $z_T/R > 0$ drastically and generates a wake structure comparable to the one observed at $\Lambda = 60^\circ$.

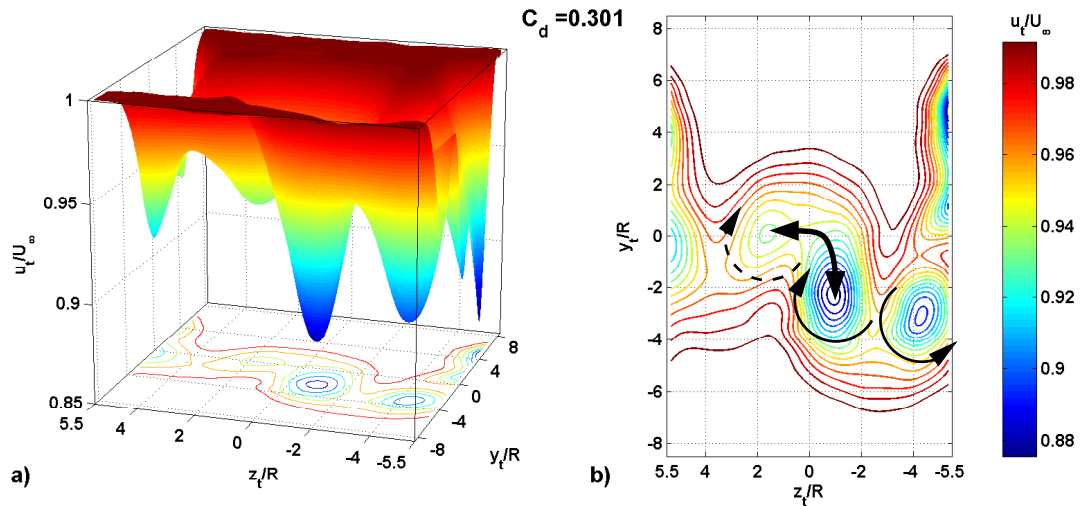


Fig. 4.71: Far wake, $\frac{U_T}{U_\infty}$, $\Theta = 110^\circ$, $F_n^+ = 1.78$, $C_{\mu,n} = 11\%$, asym., $\Lambda = 45^\circ$, $Re_n = 35000$

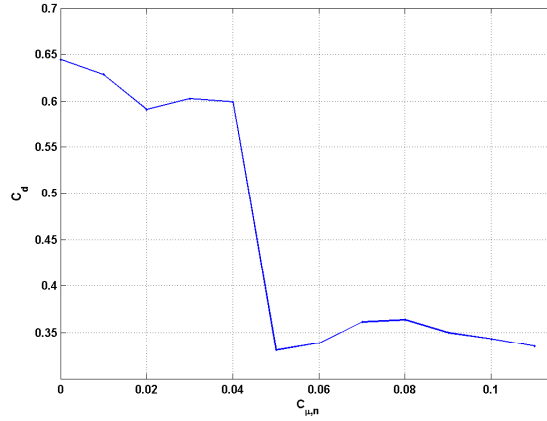


Fig. 4.72: Far wake, C_d , $\Theta = 110^\circ$, asym.,
 $\Lambda = 45^\circ$, $Re_n = 35000$

4.4.2 The Finite Cylinder

The interaction between the downstream end of the cylinder and the side wall is avoided in the “finite” configuration of an inclined cylinder. An elliptic endplate was mounted parallel to the freestream to the end of the cylinder to reduce changes of the spanwise pressure gradient. Additionally, it forces the vortices in lee of the cylinder to separate from the model at a defined spanwise location and distance to the side wall. Eliminating the side wall interference enabled an accurate determination of the total drag for the finite configuration of the inclined cylinder.

The cylinder ($\Lambda = 60^\circ$) was retracted by 12” (30.5cm) from the test section, resulting in a gap of 6” (15cm) between the tip of the cylinder and the wall. Moving the cylinder caused the row of pressure taps (used before in the infinite configuration) to be relocated closer to the wall, thus into a different spanwise region (see figure 4.74).

Figure 4.73 presents iso-surfaces of $\frac{W}{U_\infty \sin \Lambda}$ computed in the entire volume. The PIV data were taken in the infinite configuration and are viewed from the top, thus the XZ plane of the control volume is parallel to the paper plane. The endplate mounted in the finite configuration is shown as black dashed line.

It is assumed that the distances of the peel-off locations to the upstream end of the cylinder would not be altered in the finite configuration provided the spanwise pressure gradient is constant. Potentially the peel-off location of the rightmost vortex shown in figure 4.73 is slightly changed due to interference with the endplate. For all other vortices peeling-off the cylinder the effect of the endplate is assumed to be negligible for asymmetric excitation above the critical value of C_μ . The angle between the peeling-off vortices and the cylinder computes for asymmetric excitation from a slot location of $\Theta = 110^\circ$ to approximately 28.5° . The distance between the vortices measured perpendicular to their cores is in this case $3.5R$.

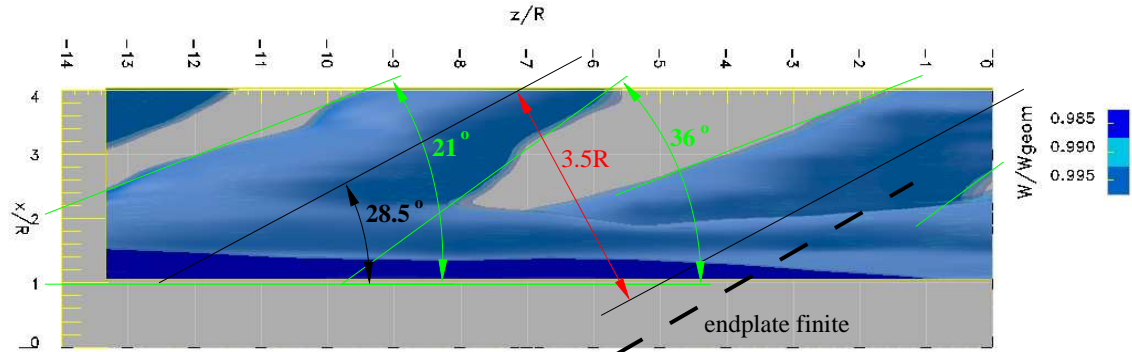


Fig. 4.73: Vortex spacing, $\frac{U_T}{U_\infty}$, $\Theta = 110^\circ$, $F_n^+ = 1.78$, $C_{\mu,n} = 11\%$, asym., $\Lambda = 60^\circ$, $Re_n = 35000$

4.4.2.1 Forces on the Cylinder

The pressure distribution for the baseline of the finite cylinder is presented in figure 4.181 on page 114, in comparison to results obtained for the infinite configuration. The relocation of the cylinder moved the pressure taps to a different spanwise position and well outside the region that could have been investigated with PIV. Due to the endplate obstructing the view, no PIV data were acquired in the finite configuration. Even without the endplate the limited optical reach of the PIV system would have prevented the data acquisition at the relocated pressure taps. Provided that the peel-off process was not altered significantly by retracting the cylinder and adding the endplate, it can be safely assumed that in the finite configuration the stationary vortices in lee of the cylinder are located closer (see figure 4.74 to the surface of the cylinder. The distance between the vortex core to the cylinder at the location of the pressure taps changes from $x/R = 1.15$ (infinite) to $x/R = 0.7$ (finite), according to the extrapolation of the vortex core (red line).

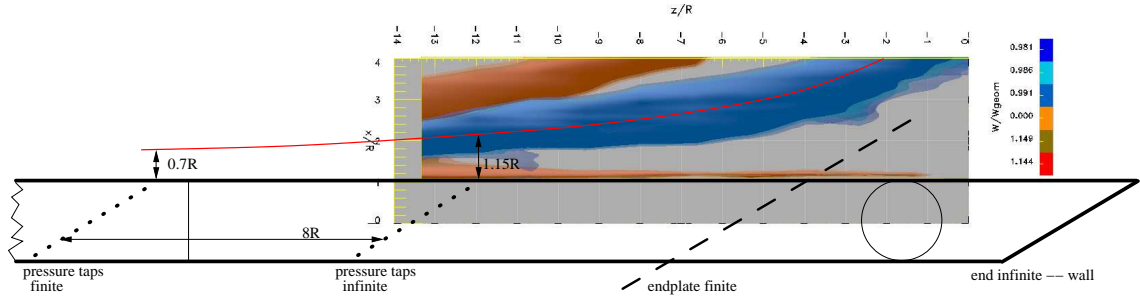


Fig. 4.74: Location of vortex cores, baseline, finite & infinite configuration

The base pressure distribution depends strongly on the location and strength of the stationary vortices (see figure 4.152 on page 99) aft of the cylinder. Significant differences between the pressure distributions measured on the finite and the infinite configuration are caused by the spanwise variations in the distance of the vortex cores to the surface of the cylinder described above. Under the assumption that the vortex peel-off is periodic along the span, PIV data taken in the infinite configuration one full spanwise period downstream of the location of the pressure taps were used for a more detailed analysis. The spanwise period was estimated for asymmetric forcing at $C_{\mu,n} = 11\%$ from the minima in $\frac{W}{U_{\infty} \sin \Lambda}$ marking the vortex cores presented in figure 4.75. The vortices peel-off alternately, therefore the two distances marked in the figure add up to a full spanwise period of approximately $14R$. The distance between the velocity minima in the far wake (figure 4.68) was determined to be $14.5R$. The average of both results, $14.25R$, was taken as the best estimate for the spanwise period of the vortex peel-off. In the infinite configuration the pressure taps are located close to $z/R = -12$. PIV data are available at this spanwise position. In the finite case the pressure taps are relocated to $z/R = -20$ (figure 4.74). Shifting this spanwise position by an entire period results in a new position of $z/R = -5.75$ with PIV data available at $z/R = -5.3$.

The PIV data for $z/R = -5.3$ (figure 4.76, considered representative for the finite case) and $z/R = -12$ (figure 4.77, infinite case) illustrate clearly the differences between the spanwise locations of the pressure taps in the finite and infinite configuration. At $z/R = -5.3$ (figure 4.76), assumed to be representative for the finite configuration, the vorticity accumulated on the underside of the cylinder (red) is peeling-off and is therefore located at a larger distance to the cylinder. The vortex on the opposite side is compact and located close to the surface of the cylinder. Therefore vortex induction reduces the base pressure on the upper part of the cylinder and lift is increased. At $z/R = -12$ the situation is reversed: the vortex at $y/R = -1$ (red) is very compact and located close to the cylinder due to induction from the vortices (blue) peeling-off from the top side. This strong vortex close to the surface of the cylinder generates a more negative base pressure on the underside of the cylinder, thus lift is reduced.

It is assumed that these two states of the flow mark approximately the extrema of C_l because they correspond to the extrema in the peel-off process. This can be observed in figure 4.75 at the size (marked by green arrows) of the vortex oriented parallel to the cylinder. Thus the maximum

spanwise variation of the lift (figure 4.78) is estimated to be $\pm 25\%$ of the average value. A comparable spanwise variation of $\pm 30\%$ of the average value is obtained for the drag, as presented in figure 4.79.

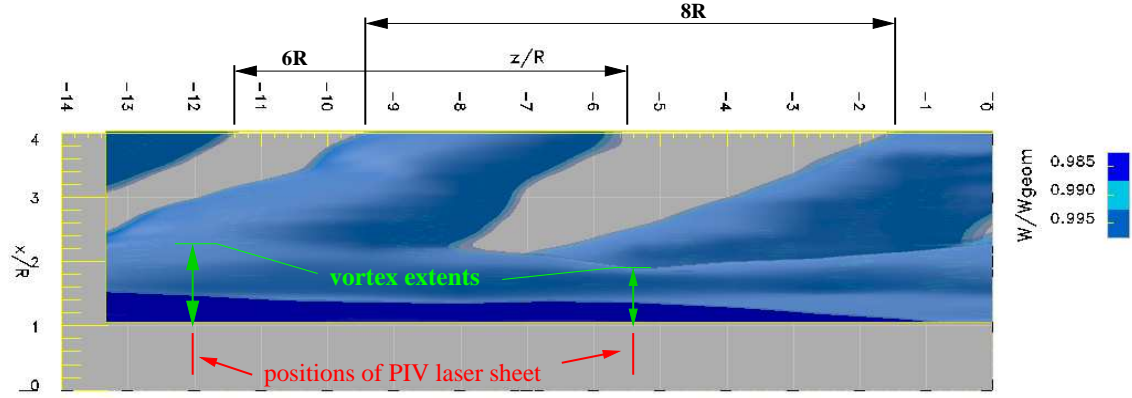


Fig. 4.75: Location of vortex cores, asymmetric forcing, finite & infinite configuration

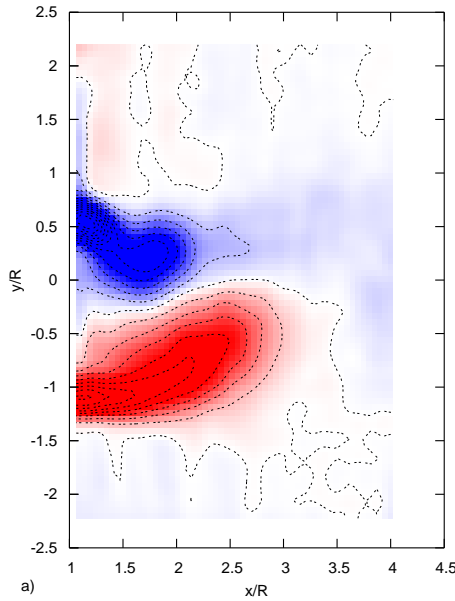


Fig. 4.76: $\frac{\Omega_z D}{U_\infty}$, $z/R = -5.3$, $F_n^+ = 1.78$,
 $C_{\mu,n} = 11\%$, “finite”, $C_l = 0.68$,
 $\Lambda = 60^\circ$, $Re_n = 35000$

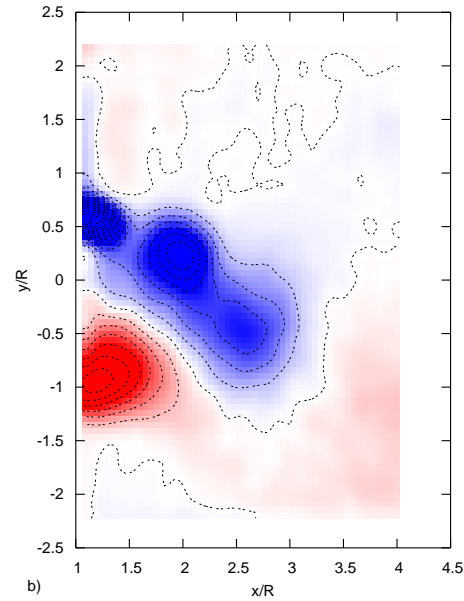


Fig. 4.77: $\frac{\Omega_z D}{U_\infty}$, $z/R = -12.0$, $F_n^+ = 1.78$,
 $C_{\mu,n} = 11\%$, “infinite”, $C_l = 0.41$,
 $\Lambda = 60^\circ$, $Re_n = 35000$

4.4.2.2 The Far Wake

The finite configuration was investigated at the representative frequency of $F_n^+ = 1.78$ and a slot location of $\Theta = 110^\circ$ for different actuation levels. The velocity deficits observed in the infinite configuration at baseline and low levels of forcing are also present in the finite configuration, shifted by approximately $3R$ towards the center of the tunnel. The central velocity deficit is enclosed by two side minima. The distortion of the wake at the downstream end is significantly reduced, as shown in figure 4.80 and the disturbances caused by the necklace vortex are moderate. The two outer velocity minima are caused by the vortices peeling-off symmetrically when no actuation is

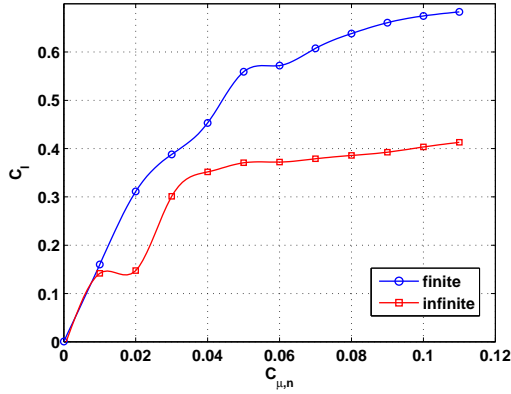


Fig. 4.78: C_l , $\Lambda = 60^\circ$, $\Theta = 110^\circ$, $Re_n = 35000$
 $F_n^+ = 1.78$, asym., finite & infinite

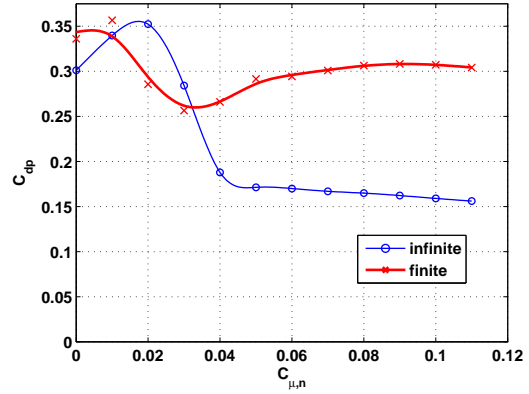


Fig. 4.79: C_{dp} , $\Lambda = 60^\circ$, $\Theta = 110^\circ$, $Re_n = 35000$
 $F_n^+ = 1.78$, asym., finite & infinite

applied, the large minimum at $y_T/R = 0$ represents all vortices that were forced to separate from the cylinder by the endplate, thus the vorticity merged and the velocity deficits accumulated.

Compared to the infinite cylinder (figure 4.64) the far wake is less distorted when forcing at low C_μ (see figure 4.81). The wake is slightly shifted towards $y/R > 0$, thus negative lift is created for forcing at $C_{\mu,n} = 2\%$. When the excitation level is increased already forcing at $C_{\mu,n} = 4\%$ (figure 4.82) generates an undisturbed wake. The vertical location of the three velocity minima caused by peeled-off vortices varies linearly with the spanwise position. This displacement is caused by induction, as discussed before. The necklace vortex was pulled away from the wall by induction. For $C_{\mu,n} > 2\%$ the disturbance caused by the necklace vortex is of the same magnitude than the other velocity minima but still located close to the wall.

Further increase of the excitation level increases the lift and the velocity minima are deflected more towards negative y_T/R . For $C_{\mu,n} \geq 6\%$ (figures 4.83 and 4.84) additional but small velocity minima are located at the downstream end of the cylinder. These structures are caused by the vortices oriented parallel to the cylinder that are strengthened by the forcing as seen in the PIV data for the infinite case. These vortices do not peel-off naturally because they did not grow to the critical size necessary for the natural peel-off process, thus they are forced by the endplate to separate from the cylinder. The differences in the far wake at $C_{\mu,n} = 6\%$ and $C_{\mu,n} = 11\%$ are negligible, thus the effectivity of the excitation is reduced for high forcing levels. The red arrow and the dashed black arrow mark a potential artifact due to averaging. The red arrow joins to weak vortices that are connected by a blurred region of lower velocity. It is likely that this is in fact a single vortex that peels-off only temporarily and therefore oscillates between the two indicated locations. This would agree best with the existing vortex pattern and the connected induction.

The difference between the total drag C_d computed from the velocity measured in the far wake of the finite configuration (figure 4.85) and the form drag determined at midspan for the corresponding infinite case is significant, with a maximum of 18% of the average value. A much better agreement between C_d and C_{dp} can be obtained by averaging the two curves shown in figure 4.79 which are estimates for the extrema of the spanwise variation in C_{dp} . The standard deviation of the difference between the total drag in the finite configuration and the averaged form drag is $\sigma = 0.014$ (figure 4.85). Therefore the estimates for the spanwise variations are considered to be accurate. The lift generated at lower excitation levels is alternating in spanwise direction (see page 43). This explains the initial increase in the averaged C_{dp} for $C_{\mu,n} < 3\%$. The lift coefficient averaged between both spanwise positions is presented in figure 4.86. Instead of the two distinct zones of a strong increase of C_l with C_μ and the saturated region the slope of the averaged C_l curve reduces gradually with increasing C_μ . Taking into account the strong spanwise variations this is considered an averaging artifact. The begin of the saturated region (marked by the green line in figure 4.86) can be determined to $4\% < C_{\mu,n,crit} < 5\%$ by comparing the characteristics of C_l and C_{dp} .

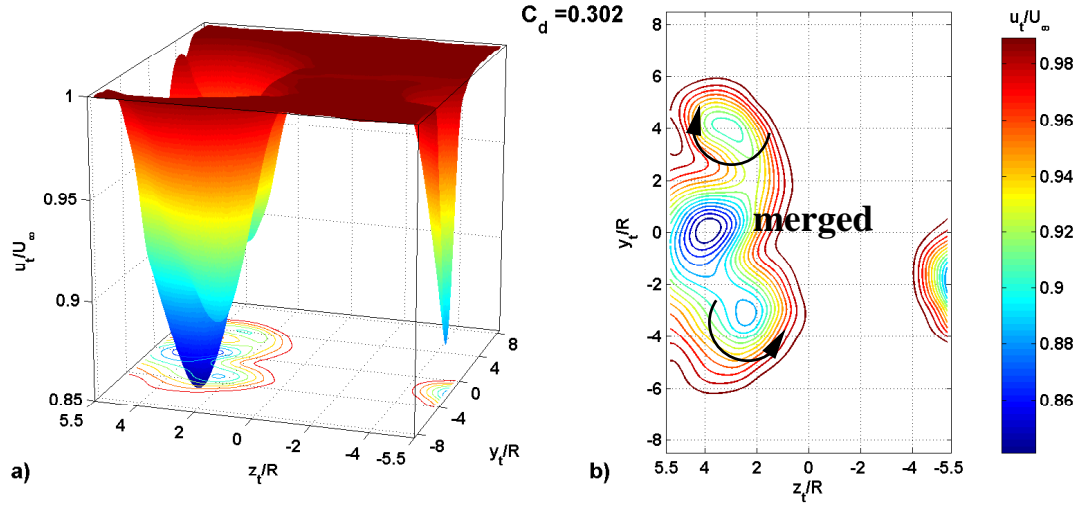


Fig. 4.80: Far wake, $\frac{U_T}{U_\infty}$, $\Theta = 110^\circ$, baseline, finite, $\Lambda = 60^\circ$, $Re_n = 35000$

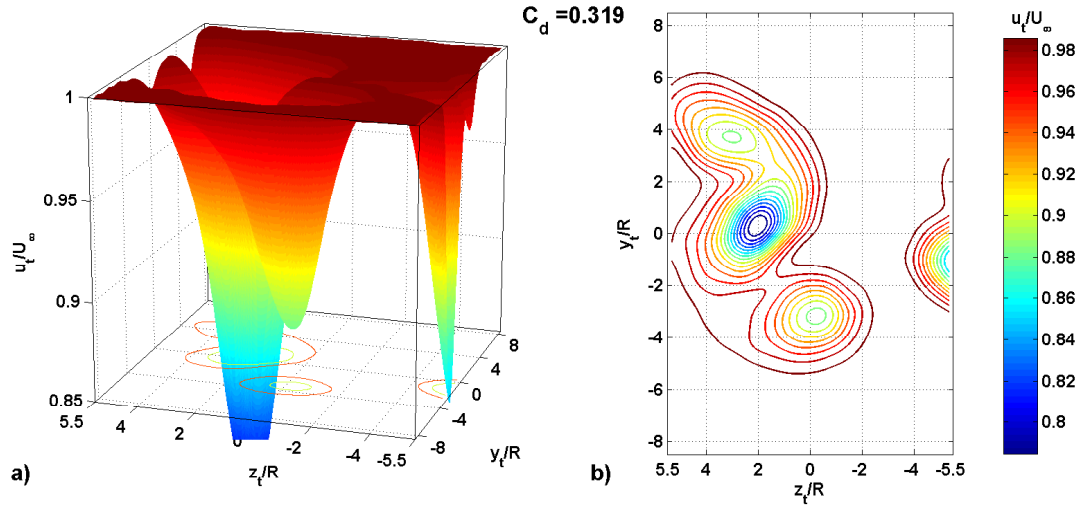


Fig. 4.81: Far wake, $\frac{U_T}{U_\infty}$, $\Theta = 110^\circ$, $F_n^+ = 1.78$, $C_{\mu,n} = 2\%$, asym., finite, $\Lambda = 60^\circ$, $Re_n = 35000$

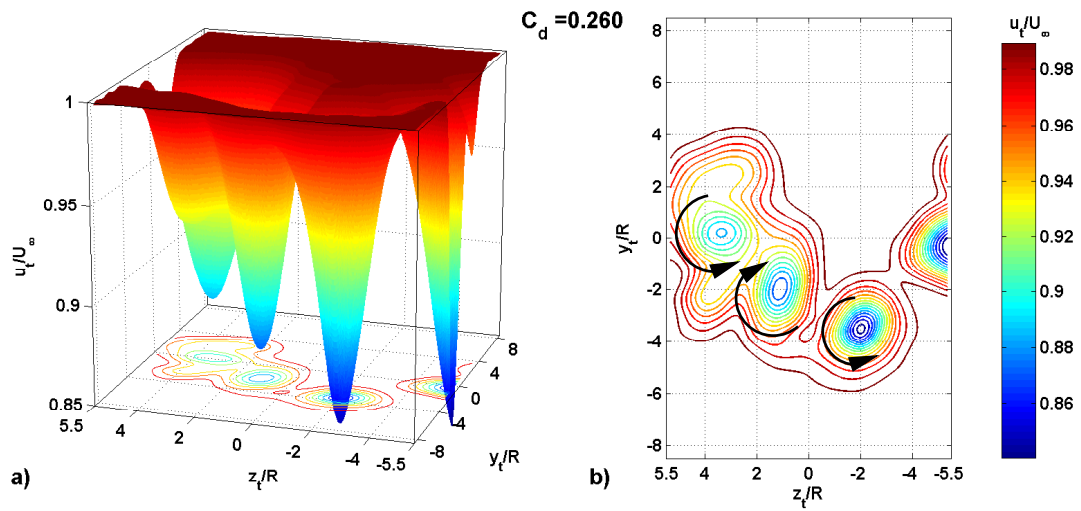


Fig. 4.82: Far wake, $\frac{U_T}{U_\infty}$, $\Theta = 110^\circ$, $F_n^+ = 1.78$, $C_{\mu,n} = 4\%$, asym., finite, $\Lambda = 60^\circ$, $Re_n = 35000$

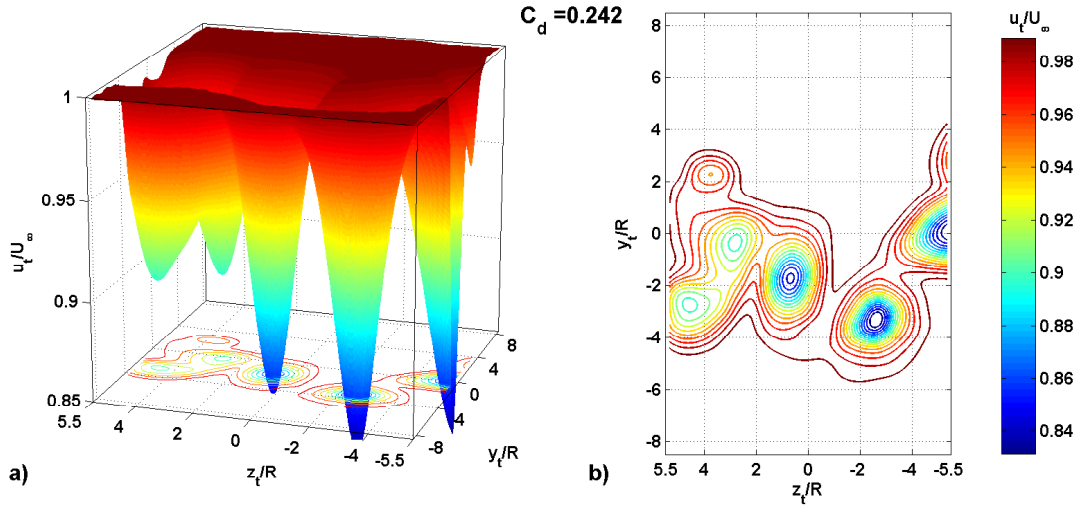


Fig. 4.83: Far wake, $\frac{U_T}{U_\infty}$, $\Theta = 110^\circ$, $F_n^+ = 1.78$, $C_{\mu,n} = 6\%$, asym., finite, $\Lambda = 60^\circ$, $Re_n = 35000$

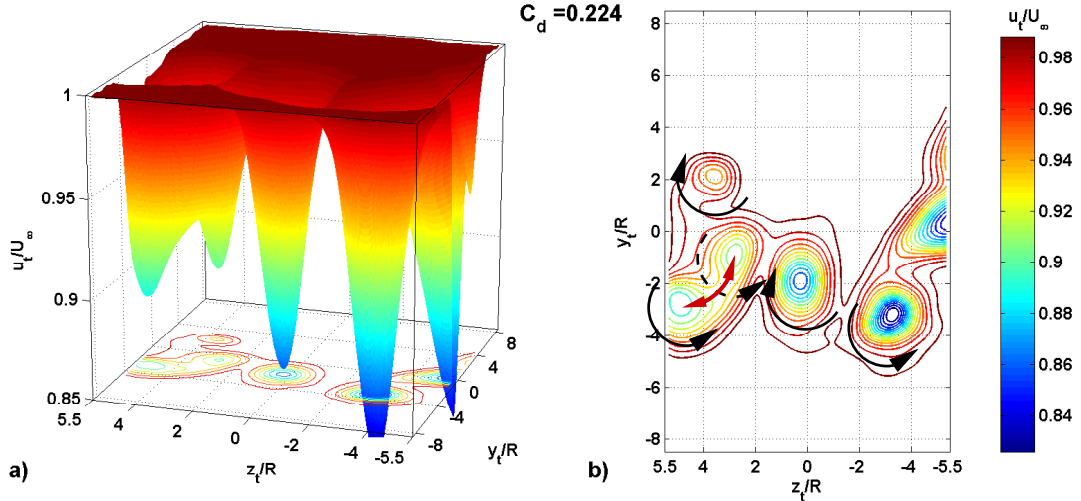


Fig. 4.84: Far wake, $\frac{U_T}{U_\infty}$, $\Theta = 110^\circ$, $F_n^+ = 1.78$, $C_{\mu,n} = 11\%$, asym., finite, $\Lambda = 60^\circ$, $Re_n = 35000$

In spite of the spanwise variations of the flow, lift and drag of an inclined cylinder can be investigated accurately by measuring the pressure distribution at two spanwise positions. This is possible by estimating the variations along the span by combining pressure data and PIV results as demonstrated. The averaged values of C_{dp} agree well with results obtained in the far wake, provided the pressure distributions are acquired in the extrema of the peel-off process, i.e. at the location of a vortex peel-off and inbetween two such events.

4.5 Symmetric Forcing

The effects of active flow control on an inclined cylinder using zero-mass-flux excitation from two slots located symmetrically on the circumference were investigated in detail. Various frequencies and amplitudes were tested in an infinite configuration with the cylinder spanning the entire test section and a finite configuration to avoid interaction between the flow and the tunnel side wall at the downstream end of the model. The momentum coefficient is given per slot to allow for a better comparison of the figures based on the critical values of $C_{\mu,n}$ described above for asymmetric actuation.

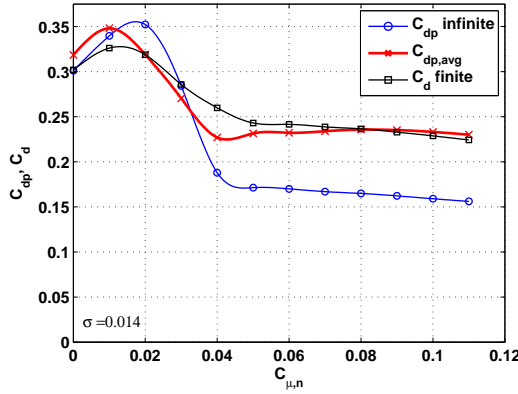


Fig. 4.85: C_d & C_{dp} , $\Theta = 110^\circ$, $F_n^+ = 1.78$,
asym., $\Lambda = 60^\circ$, $Re_n = 35000$,
 $\sigma_{C_{dp}-C_d} = 0.014$

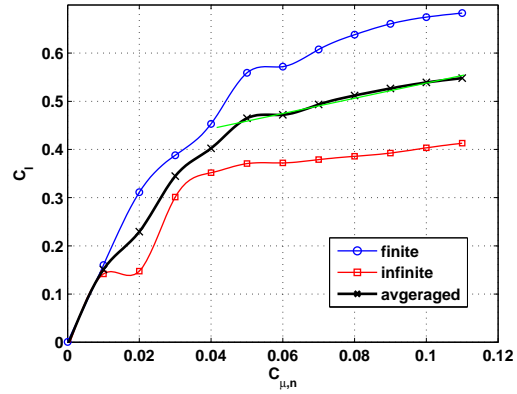


Fig. 4.86: Averaged C_l , $\Theta = 110^\circ$, $F_n^+ = 1.78$,
asym., $\Lambda = 60^\circ$, $Re_n = 35000$

4.5.1 The Infinite Cylinder

The infinite configuration was investigated to obtain the maximum possible length to diameter ratio. Due to the internal actuation requiring a minimum diameter of 3" this ratio was limited to $L/D = 16$ in the infinite configuration at the maximum investigated sweep-back angle of $\Lambda = 60^\circ$. Several vortices peeled-off the cylinder within the available span, therefore the three-dimensionality of the flow was considered to be fully developed in the investigated volume. The potential effect of the upstream side wall on the peel-off process due to restriction of the spanwise flow was examined by introducing pressurized air at the boundary layer shedding fence, blowing axially along the base of the cylinder.

4.5.1.1 Forces on the Cylinder

The baseline pressure distribution with taped and untaped slots (figure 4.87) is almost identical to the pressure distribution acquired with axial blowing to compensate the deficit in spanwise velocity at the upstream end. The slight distortion around $x/D = 0.7$ for the case with axial blowing (see figure 4.88) is due to the taping of the slots causing interference between the tape and the pressure taps located close to it. The base pressure is reduced by approximately 10% but the characteristics (compare figure 4.150 on page 99) of the base pressure profile are unaltered. Therefore the peel-off process at midspan is unaffected by the initial deficit in spanwise velocity at the upstream end of the cylinder. Therefore axial blowing was not applied during experiments using AFC.

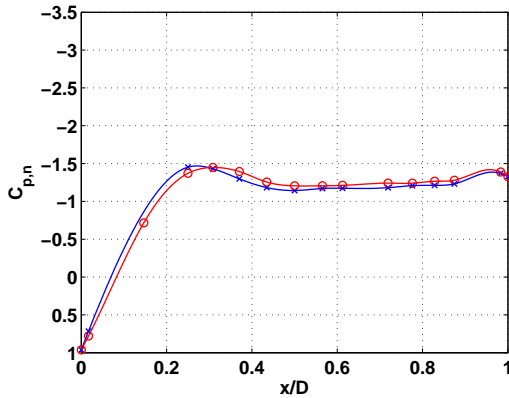


Fig. 4.87: C_p vs. x/D , baseline,
slots at $x_s = 0.67$ untaped,
 $\Theta = \pm 110^\circ$, $\Lambda = 60^\circ$, $Re_n = 35000$

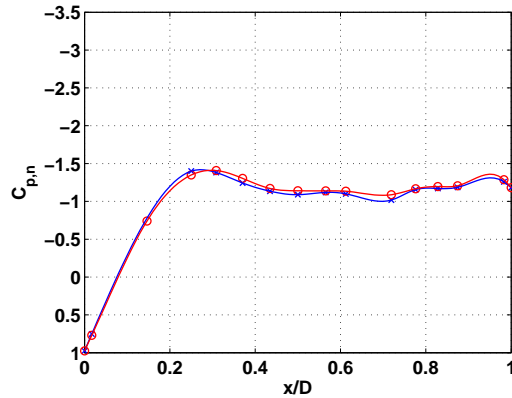


Fig. 4.88: C_p vs. x/D , slots at $x_s = 0.67$ taped,
baseline with axial blowing,
 $\Theta = \pm 110^\circ$, $\Lambda = 60^\circ$, $Re_n = 35000$

The suction peaks on both sides of the cylinder are enhanced compared to the unforced case when excitation is applied. The minimum pressure coefficient $C_{p,n,min}$ (figure 4.89) converges for higher $C_{\mu,n}$ towards the value $C_{p,min} = -3$ for potential flow. This value cannot be exceeded because no circulation is generated in the symmetrically forced case, in contrast to cases with asymmetric excitation where $C_{p,n} < -3$ can be observed. The pressure distribution remains symmetric (figure 4.89) at all frequencies for values of $C_{\mu,n}$ above the threshold necessary to reattach both sides simultaneously. Around $x/D = 0.5$ small and shallow separation bubbles are found on both sides of the cylinder, as was observed in the asymmetrically forced cases. The center part of the base pressure profile (see figure 4.90) remains almost undisturbed, indicating that the strength of stationary vortices and their distance to the surface of the cylinder are not altered as significantly as in the asymmetrically forced cases (see figure 4.26).

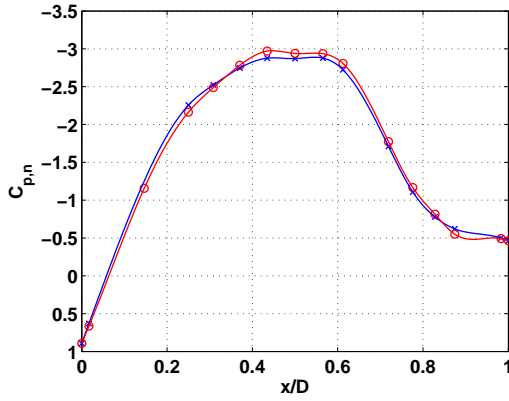


Fig. 4.89: C_p vs. x/R , $F_n^+ = 1.78$,
 $C_{\mu,n} = 7\%$ per slot, sym., $\Theta = \pm 110^\circ$,
 $\Lambda = 60^\circ$, $Re_n = 35000$

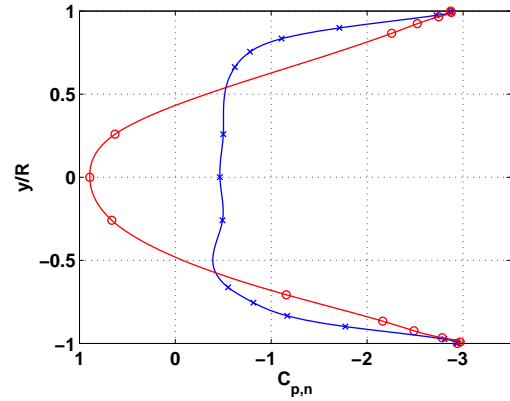


Fig. 4.90: y/R vs. C_p , $F_n^+ = 1.78$,
 $C_{\mu,n} = 7\%$ per slot, sym., $\Theta = \pm 110^\circ$,
 $\Lambda = 60^\circ$, $Re_n = 35000$

The effects of symmetric actuation on C_l and C_{dp} at a cross flow Reynolds number of $Re_n = 35000$ ($U_\infty = 15m/s$) are presented in figures 4.91 and 4.92. As in the case of asymmetric excitation the flow becomes highly three-dimensional when forcing at low $C_{\mu,n}$. The flow reattaches once the threshold in C_μ is exceeded. In most cases this occurs only on one side of the cylinder, due to small asymmetries and fluctuations in the separated flow and the excitation. This can be best observed at the lift curves shown in figure 4.91 for $Re_n = 35000$ and for an increased Reynolds number of $Re_n = 47000$ in figure 4.93. For symmetric excitation at $C_{\mu,n} < 5\%$ ($C_{\mu,n} > 7\%$ for $F_n^+ = 3.05$) the lift generated at mid-span is unpredictable and can be randomly positive or negative. For a controlled flow ($C_{\mu,n} > 5\%$) the generated lift is close to $C_l = 0$, due to the symmetry of the setup.

The effects of symmetric excitation on the form drag are presented for two different Reynolds numbers in figures 4.92 and 4.94. An increase in form drag can be observed at $\Lambda = 60^\circ$ for excitation levels below a frequency dependent threshold. This value varies between $C_{\mu,n} = 2.5\%$ for higher frequencies and 3% for lower frequencies. At these levels of excitation no reattachment can be achieved, the flow is mainly disturbed by the forcing and thus the form drag increases.

Large variations of form drag with C_μ can be observed for $C_{\mu,n} > 5\%$. This is again caused by the local reattachment of the flow on only one side of the cylinder discussed above. The dependence of the form drag on the excitation frequency is negligible for $C_{\mu,n} > 5\%$ in all investigated cases, with the exception of $F_n^+ = 3.05$ with an increased critical value of $C_{\mu,n} = 7\%$. After reaching the saturated region at the critical value of $C_{\mu,n} = 5\%$ the further reduction of C_{dp} is limited. The form drag was reduced by a factor of six when excitation was applied at the maximum value of C_μ .

At a sweep-back angle of $\Lambda = 45^\circ$ the lift coefficient oscillates for $C_{\mu,n} < 4.5\%$ (see figure 4.95). For $C_{\mu,n} > 5\%$ the oscillations are limited to higher frequencies with $F_n^+ > 2.54$ that are less effective in reattaching the flow. Beyond $C_{\mu,n} = 6\%$ the lift is close to zero for all forcing

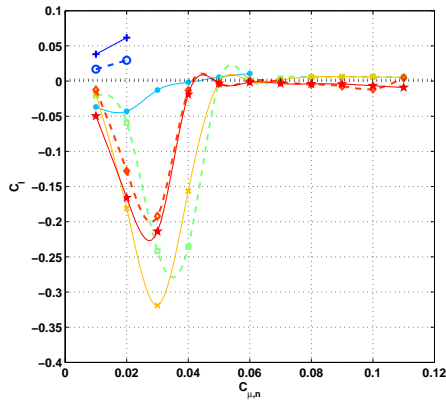


Fig. 4.91: C_l vs. $C_{\mu,n}$ per slot, sym.,
 $\Theta = \pm 110^\circ$, $\Lambda = 60^\circ$, $Re_n = 35000$

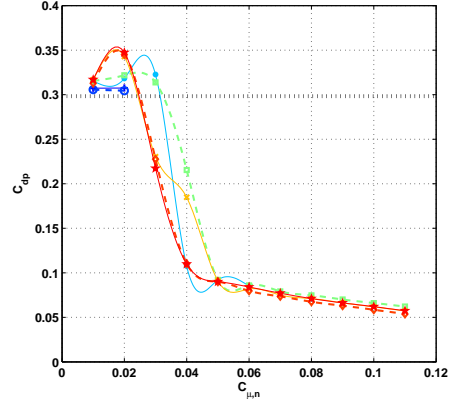


Fig. 4.92: C_{dp} vs. $C_{\mu,n}$ per slot, sym.,
 $\Theta = \pm 110^\circ$, $\Lambda = 60^\circ$, $Re_n = 35000$

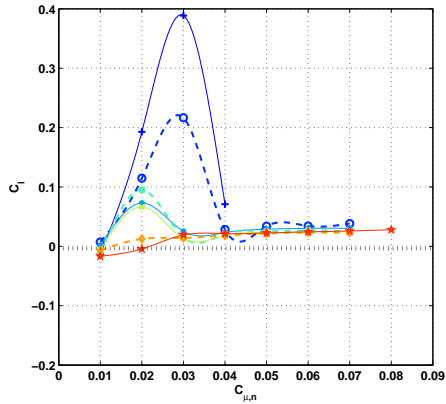


Fig. 4.93: C_l vs. $C_{\mu,n}$ per slot, sym.,
 $\Theta = \pm 110^\circ$, $\Lambda = 60^\circ$, $Re_n = 47000$

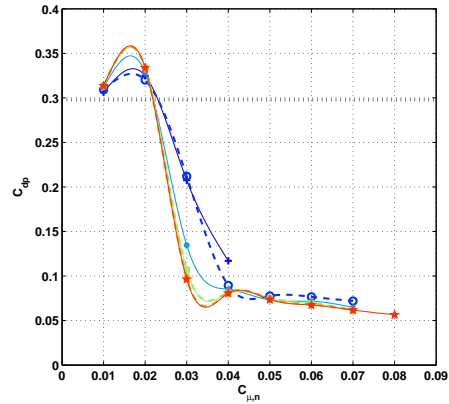


Fig. 4.94: C_{dp} vs. $C_{\mu,n}$ per slot, sym.,
 $\Theta = \pm 110^\circ$, $\Lambda = 60^\circ$, $Re_n = 47000$

frequencies. Above the critical value of $C_{\mu,n} = 5\%$ the form drag is independent of the forcing frequency up to $F_n^+ = 2.54$ (figure 4.96). A reduction of performance occurs above this critical value. Below the critical value the local form drag depends not only on the excitation level but also on the excitation frequency. The effectiveness of the drag reduction increases gradually with the frequency until it drops sharply above $F_n^+ = 2.54$ ($f = 250Hz$). For $\Lambda = 45^\circ$ the form drag is reduced by a factor of 4.5 in the investigated range of C_μ , compared to a factor of six for $\Lambda = 60^\circ$. The performance of active flow control for drag reduction is therefore clearly dependent on the sweep-back angle.

4.5.1.2 The Near Wake

The surface pressure measurements showed that the flow is at least locally asymmetric when forcing at $C_{\mu,n} < 6\%$ (per slot), depending on the frequency. The iso-surfaces of $\frac{W}{U_\infty \sin \Lambda}$ shown in figure 4.97 confirm this asymmetry throughout the investigated control volume for excitation at $F_n^+ = 1.78$, $C_{\mu,n} = 3\%$ (per slot). The coherent structures forming aft of the cylinder are distinct in the sense that only one large vortex (minimum in $\frac{W}{U_\infty \sin \Lambda}$, blue) peels off the cylinder (figure 4.97) within the control volume around $z/R = -1$ and $y/R = -1.5$. Because of this single peel-off two different regions with $\frac{W}{U_\infty \sin \Lambda} > 1.1$ (red) are located at $y/R < 0$, $z/R < -5$ and $y/R > 0$, $z/R > -5$. These regions of increased spanwise velocity are at least partly caused by the entrainment of fluid by the large separating vortices. The entrainment process accelerates the entrained fluid in spanwise direction by “squeezing” it between two adjacent vortices or between a vortex and the cylinder’s surface. The asymmetry of the wake is significant although the flow is forced symmetrically. This confirms the results obtained by surface pressure measurements.

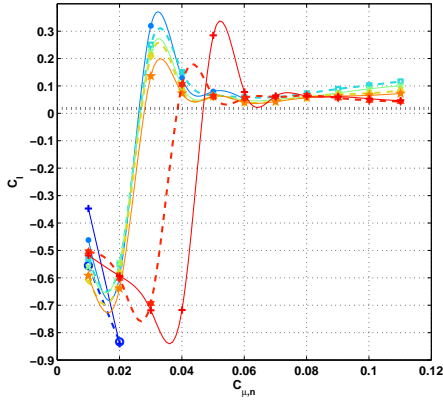


Fig. 4.95: C_l vs. $C_{\mu,n}$ per slot, sym.,
 $\Theta = \pm 110^\circ$, $\Lambda = 45^\circ$, $Re_n = 47000$

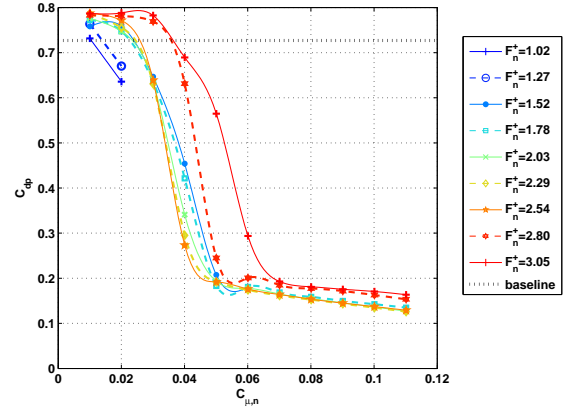


Fig. 4.96: C_d vs. $C_{\mu,n}$ per slot, sym.,
 $\Theta = \pm 110^\circ$, $\Lambda = 45^\circ$, $Re_n = 47000$

The wake changes significantly when excitation is applied at a lower frequency, $F_n^+ = 1.52$ with an increased forcing level of $C_{\mu,n} = 4\%$ (see figure 4.98). Deficits (blue) in spanwise velocity are found mostly in the top half ($y/R > 0$) of the control volume whereas regions with $\frac{W}{U_\infty \sin \Lambda} > 1.1$ (red) are dominating the bottom half. The wake is deflected upwards although symmetric forcing is applied. Additionally, the coherent structures in the wake are relatively irregular, the peel-off process observed for the baseline (see figure 4.154 on 101) and for other cases excited symmetrically at a higher level (see below) seems to be disturbed. Most of the vortical structures (blue) extend along most of the span and are oriented only slightly inclined with respect to the cylinder's axis.

At the same level of excitation ($C_{\mu,n} = 4\%$) but with increased forcing frequency $F_n^+ = 2.29$ the structures in the near wake shows entirely different characteristics, as can be seen in figure 4.99. The wake is symmetric and a regular peel-off pattern is visible in the plane of symmetry, $y/R = 0$ along the span. The flow is visualized by iso-contours of $\frac{W}{U_\infty \sin \Lambda}$ due to the better coherence compared to Ω_z . Thus vortices of different sense of rotation cannot be distinguished, but iso-contours of $\frac{\Omega_z D}{U_\infty \cos \Lambda}$ (see discussion for figure 4.102 below) show that vortices from the top and bottom side of the cylinder peel-off in an alternating fashion, visible best at their intersection with the boundaries of the interrogated control volume. Due to the symmetric actuation drag is reduced and the shear layers separating from both sides of the cylinder are forced towards the plane of symmetry. Thus the peeling-off vortices are located approximately in this plane.

The asymmetry of the flow forced with $C_{\mu,n} = 3\%$ at $F_n^+ = 1.78$ (figure 4.97) is more pronounced than for forcing with $C_{\mu,n} = 4\%$ at $F_n^+ = 2.29$ (figure 4.99). Nevertheless it seems that in the former case the characteristics of the vortex peel-off, in particular the angle between separating vortex and cylinder, are closer to the symmetric cases presented in figures 4.99 and 4.100. Thus it seems that for symmetric forcing at low $C_{\mu,n}$ several different modes of vortex peel-off exist, depending on small differences in forcing frequency and level of actuation. This is due to the interaction between the flow reattachment on both sides of the cylinder. Once the flow reattaches (temporarily) on one side of the cylinder the wake becomes (locally) asymmetric and the shear layer on the opposite side is forced away from the surface. This increases the level of excitation necessary to reattach the flow on the opposite side. This situation might be stable or not, depending on the free stream turbulence, frequency and level of forcing. Thus the wake is in general relatively complex and is possibly switching between different peel-off modes when forcing is applied at low $C_{\mu,n}$.

The characteristics of the wake resemble the ones presented in figure 4.99 for excitation at an increased level of $C_{\mu,n} = 7\%$ and at the same frequency ($F_n^+ = 1.52$) than in figure 4.98. In this case the wake is more coherent, this is visible at the downstream end ($z/R = 0$) where the vortical structures (blue) extend to $x/R = 4$. Three vortices are peeling-off the cylinder approximately equidistantly, separating from the compact region of vortical fluid (blue in figure 4.100) formed by the shear layers. Three large coherent vortices can be observed in each shear layer, oriented parallel to the cylinder's axis and running along the model in the entire investigated control volume.

Similar characteristics are found when forcing at $F_n^+ = 1.78$ with $C_{\mu,n} = 11\%$ (figure 4.101),

but the individual vortices in the shear layers cannot be distinguished in this case. The regions with $\frac{W}{U_{\infty} \sin \Lambda} > 1.1$ are reduced in size. The comparison of figures 4.99, 4.100 and 4.101 show clearly that the characteristics of the wake are alike for symmetric excitation above the threshold required for spanwise uniform reattachment. As shown before, three vortices are peeling-off in the investigated control volume, but the estimated peel-off frequency in spanwise direction decreases from $\frac{1}{6.5R}$ (figure 4.99) to $\frac{1}{5.5R}$ (figure 4.101). For this case of forcing at the highest considered level of $C_{\mu,n} = 11\%$ the extent of the wake in Y-direction is the smallest of all discussed cases, as is the drag.

The iso-contours of $\frac{\Omega_z D}{U_{\infty} \cos \Lambda}$ in figure 4.102 illustrate that the vortices identified in figures 4.97 to 4.101 are indeed peeling-off in an alternating fashion. The vortex located around $z/R = -12$ is separating from the top shear layer (negative vorticity, marked in blue in the contour plot at $z/R = -13.3$) and the one located around $z/R = -7$ is peeling-off the bottom shear layer (positive vorticity, marked in red in the contour plot at $z/R = -5.6$). The vortex peeling off at the downstream end of the control volume is directly visible in the iso-surfaces of $\frac{\Omega_z D}{U_{\infty} \cos \Lambda}$ at $z/R = -1$. Nevertheless vorticity is not considered to be the optimum quantity for visualizing coherent structures in the near wake, as can be verified easily when comparing figures 4.101 ($\frac{W}{U_{\infty} \sin \Lambda}$) and 4.102 ($\frac{\Omega_z D}{U_{\infty} \cos \Lambda}$).

Figures 4.103 to 4.105 present streamlines computed in the investigated control volume for different levels of excitation at $F_n^+ = 1.78$. Additionally, two contour plots (light grey planes) of $\frac{\Omega_z D}{U_{\infty} \cos \Lambda}$ are added at $z/R = -4$ and $z/R = -13.3$. Because the flow field is averaged and can thus be considered to be steady, streamlines and streaklines coincide. The following terminology describing the color coding of the streamlines depending on their origin is valid only under this assumption. The blue streamlines are formed by fluid that entered the control volume through the upstream XY-plane at $z/R = -13.3$ and the green streamlines consist of fluid that entered through the YZ-plane at $x/R = 1$ with $y/R > 0$. The origin of the streamlines marked in red is the YZ-plane at $x/R = 1$ with $y/R < 0$.

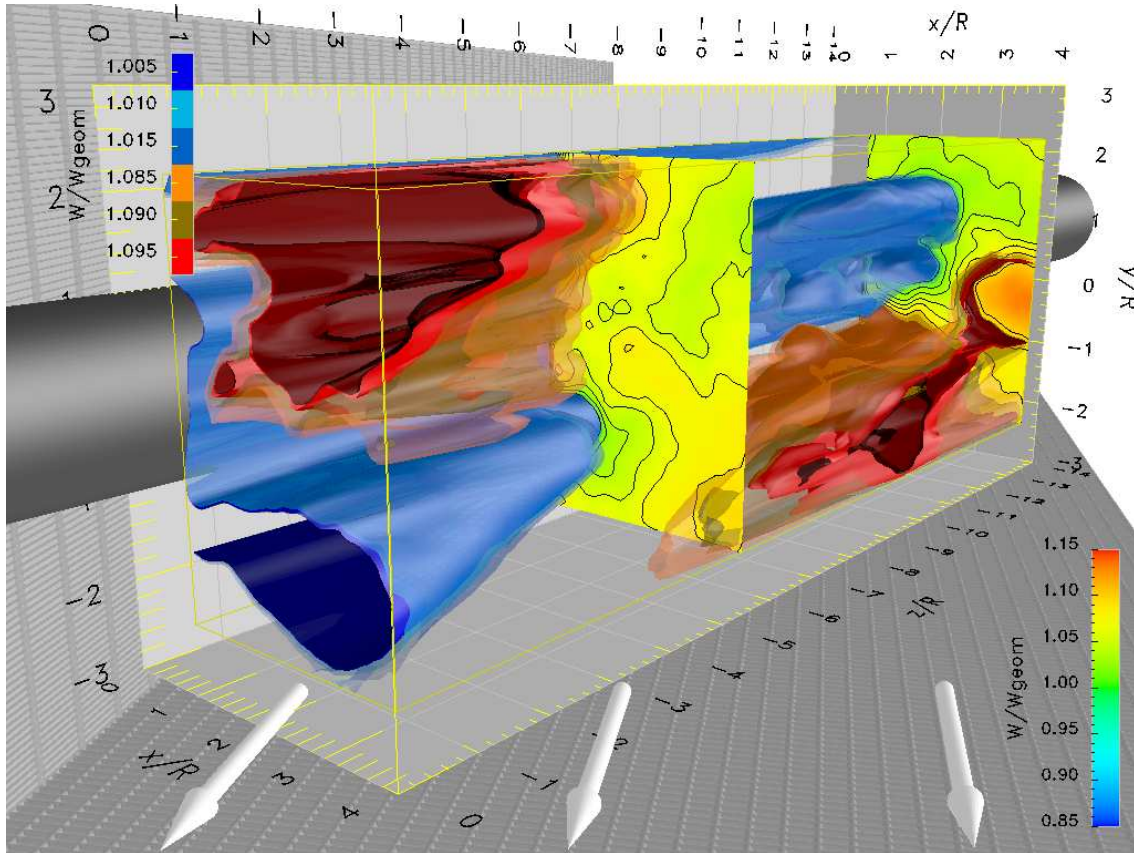


Fig. 4.97: $\frac{W}{U_{\infty} \sin \Lambda}$, $F_n^+ = 1.78$, $C_{\mu,n} = 3\%$ per slot, sym., $\Theta = \pm 110^\circ$, $\Lambda = 60^\circ$, $Re_n = 35000$

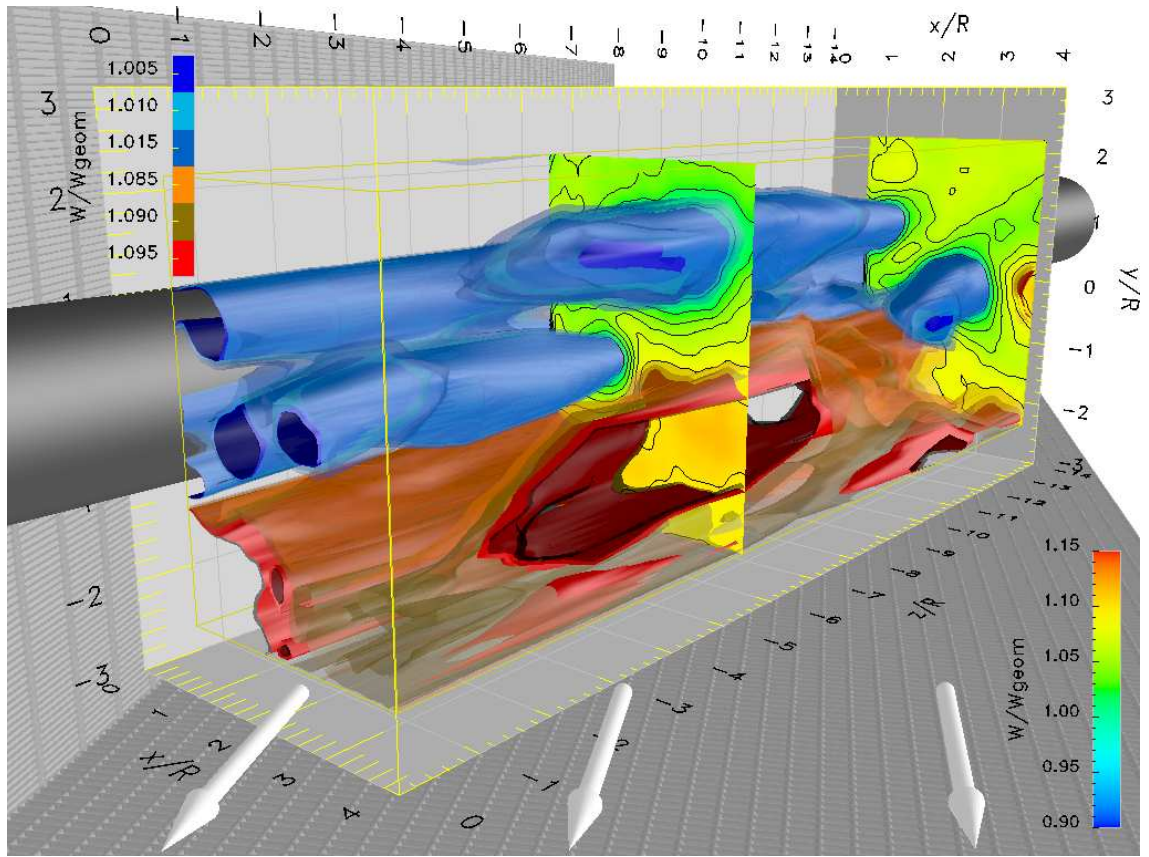


Fig. 4.98: $\frac{W}{U_\infty \sin \Lambda}$, $F_n^+ = 1.52$, $C_{\mu,n} = 4\%$ per slot, sym., $\Theta = \pm 110^\circ$, $\Lambda = 60^\circ$, $Re_n = 35000$

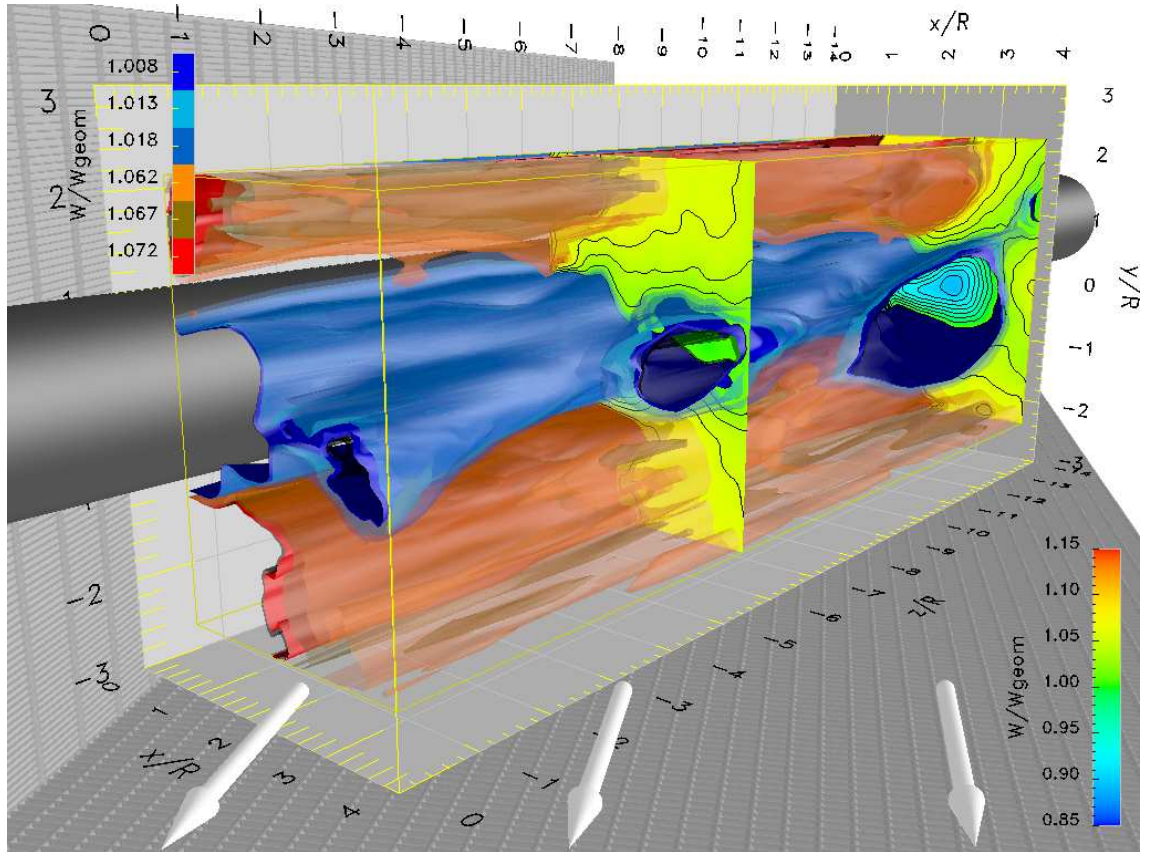


Fig. 4.99: $\frac{W}{U_\infty \sin \Lambda}$, $F_n^+ = 2.29$, $C_{\mu,n} = 4\%$ per slot, sym., $\Theta = \pm 110^\circ$, $\Lambda = 60^\circ$, $Re_n = 35000$

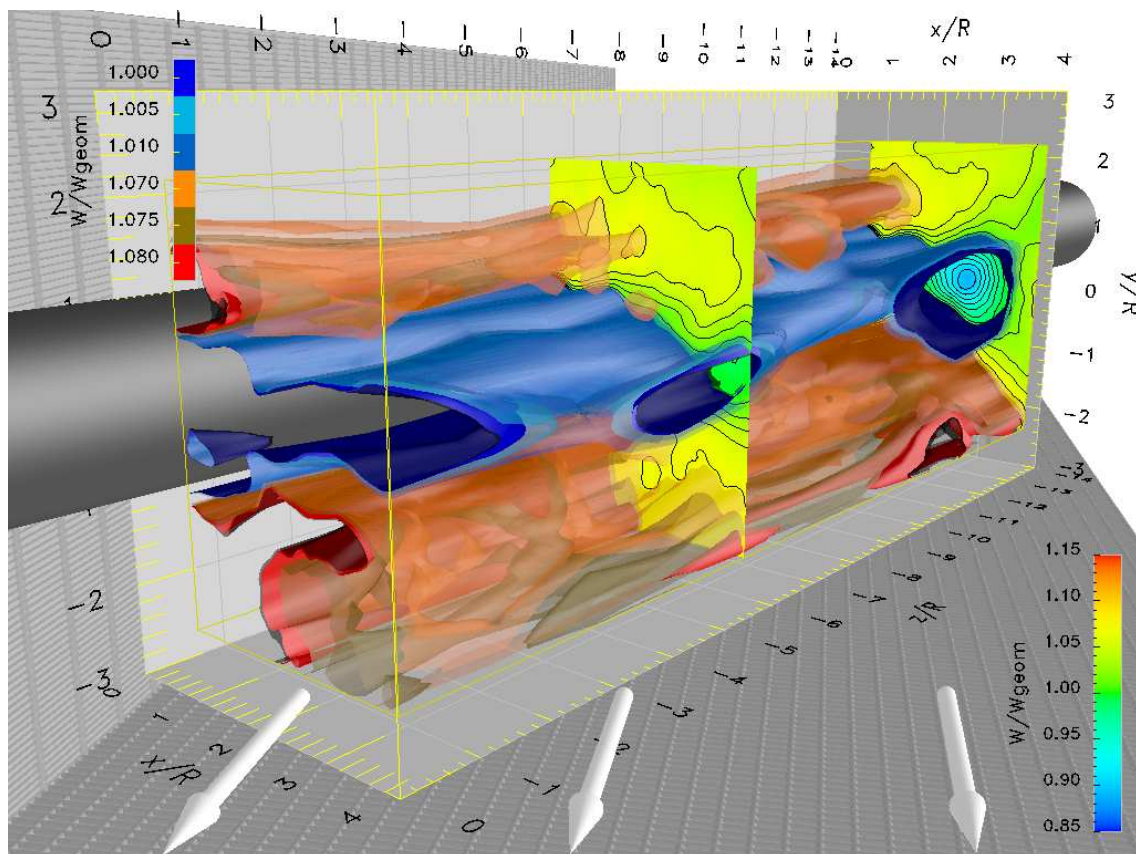


Fig. 4.100: $\frac{W}{U_{\infty} \sin \Lambda}$, $F_n^+ = 1.52$, $C_{\mu,n} = 7\%$ per slot, sym., $\Theta = \pm 110^\circ$, $\Lambda = 60^\circ$, $Re_n = 35000$

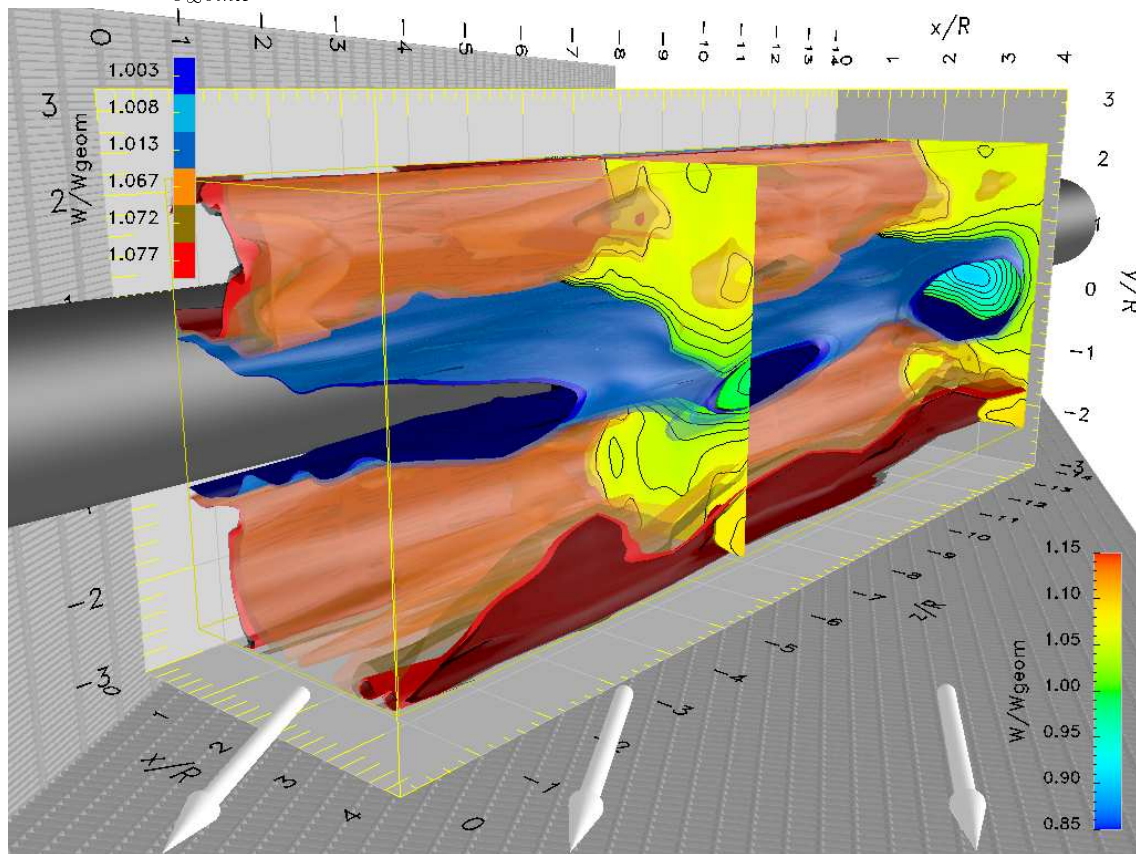


Fig. 4.101: $\frac{W}{U_{\infty} \sin \Lambda}$, $F_n^+ = 1.78$, $C_{\mu,n} = 11\%$ per slot, sym., $\Theta = \pm 110^\circ$, $\Lambda = 60^\circ$, $Re_n = 35000$

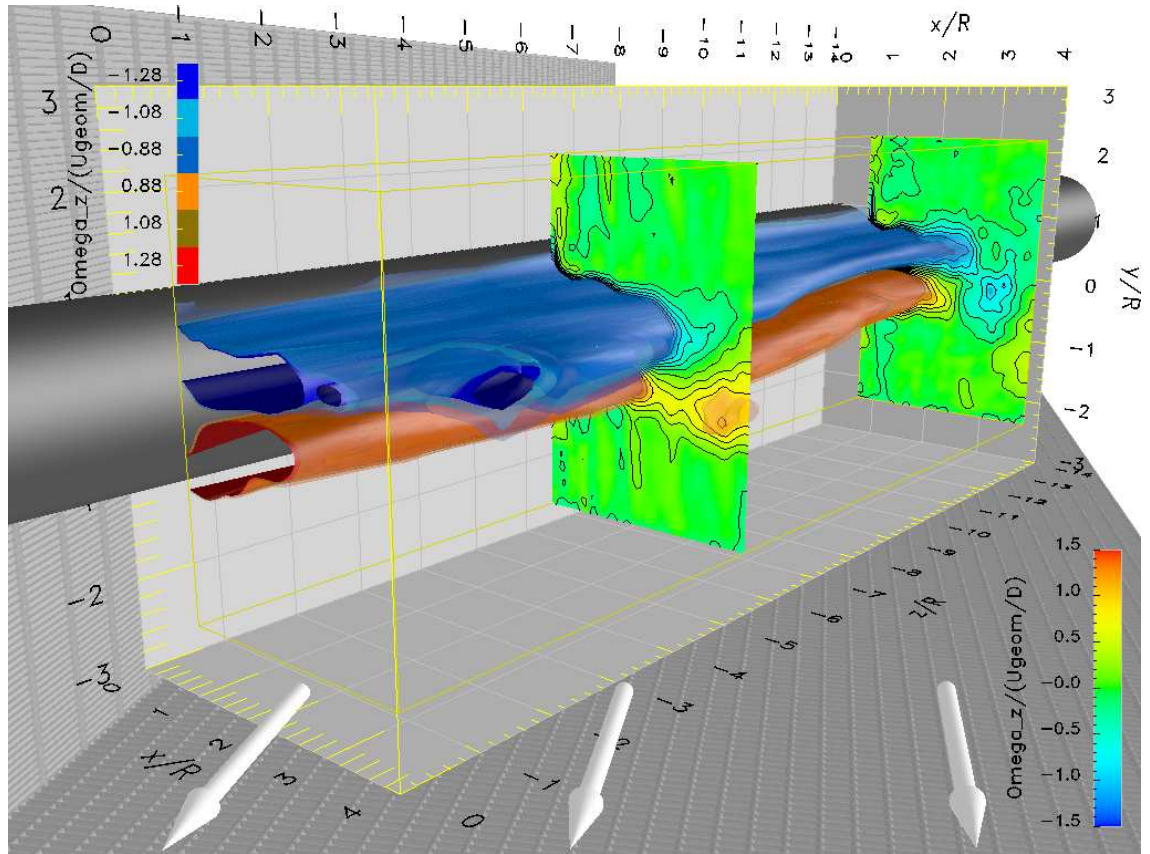


Fig. 4.102: $\frac{\Omega_z D}{U_\infty \cos \Lambda}$, $F_n^+ = 1.78$, $C_{\mu,n} = 11\%$ per slot, sym., $\Theta = \pm 110^\circ$, $\Lambda = 60^\circ$, $Re_n = 35000$

At the lowest level with $C_{\mu,n} = 3\%$ the region with flow in spanwise direction is relatively large, visible at the bundle of red, green and some blue streamlines exiting the control volume through the XY-plane at $z/R = 0$. This region is enclosed between the shear layers separating from the cylinder, thus the wake is relatively wide and the streamlines are parallel to the top edge of the upstream contour plot at $z/R = -13.3$. The downstream contour plot shows the local asymmetry of the wake, a single negative vortex (faint blue) in the top half and two positive vortices (faint red) in the bottom half. The small bundle of green streamlines intersecting the contour plot between the two positive vortices indicates the entrainment of fluid between these two vortices. It seems that due to this entrainment fluid is crossing the centerline of the wake from $y/R > 0$ to $y/R < 0$.

The region of spanwise flow is considerably reduced in size by increasing the level of excitation from $C_{\mu,n} = 3\%$ to $C_{\mu,n} = 4\%$ (figure 4.104). The asymmetry of the wake is decreased and the entrainment of fluid originating from $y/R > 0$ between the positive vortices is reduced but still present. The wake is more compact, indicating a reduced drag.

Further increase to $C_{\mu,n} = 11\%$ (figure 4.105) results in a relatively small region of spanwise flow between the now symmetrically located vortices. The shear layer are forced together until contact, as can be observed in the downstream contour plot. This very compact wake indicates a significant reduction of the drag. The two-dimensionality of the flow is increased considerably, as can be seen in the now relatively smooth flow around the cylinder at this level of excitation. This can be seen in particular by comparing the green streamlines between figures 4.104 and 4.105. The two-dimensionality of the flow is increased considerably.

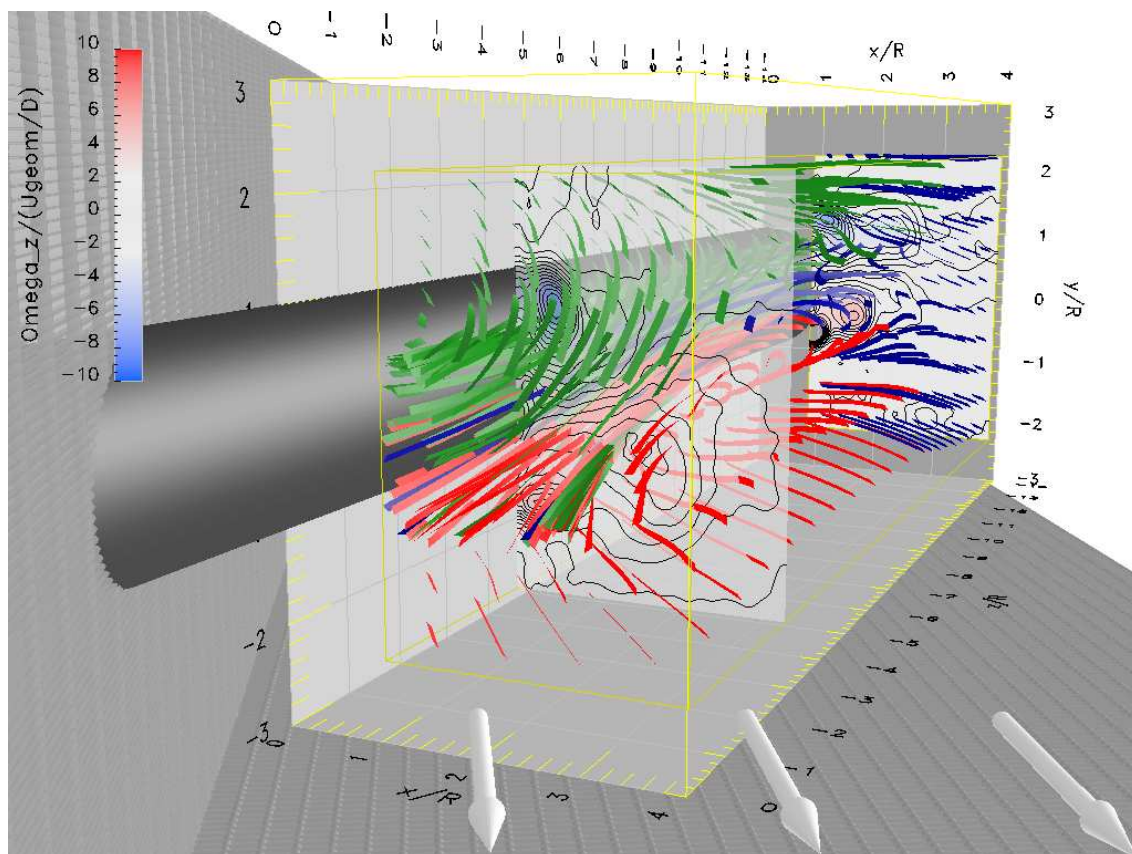


Fig. 4.103: Streamlines, $F_n^+ = 1.78$, $C_{\mu,n} = 3\%$ per slot, sym., $\Theta = \pm 110^\circ$, $\Lambda = 60^\circ$, $Re_n = 35000$

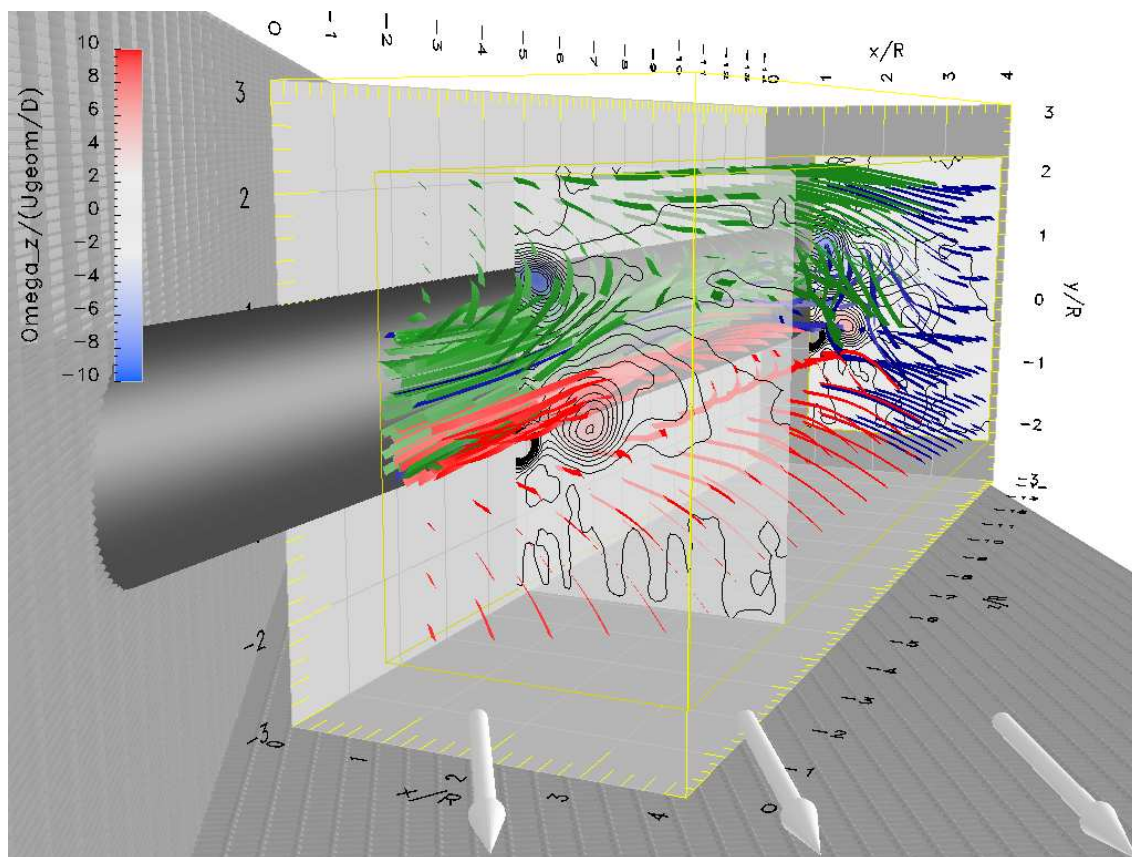


Fig. 4.104: Streamlines, $F_n^+ = 1.78$, $C_{\mu,n} = 4\%$ per slot, sym., $\Theta = \pm 110^\circ$, $\Lambda = 60^\circ$, $Re_n = 35000$

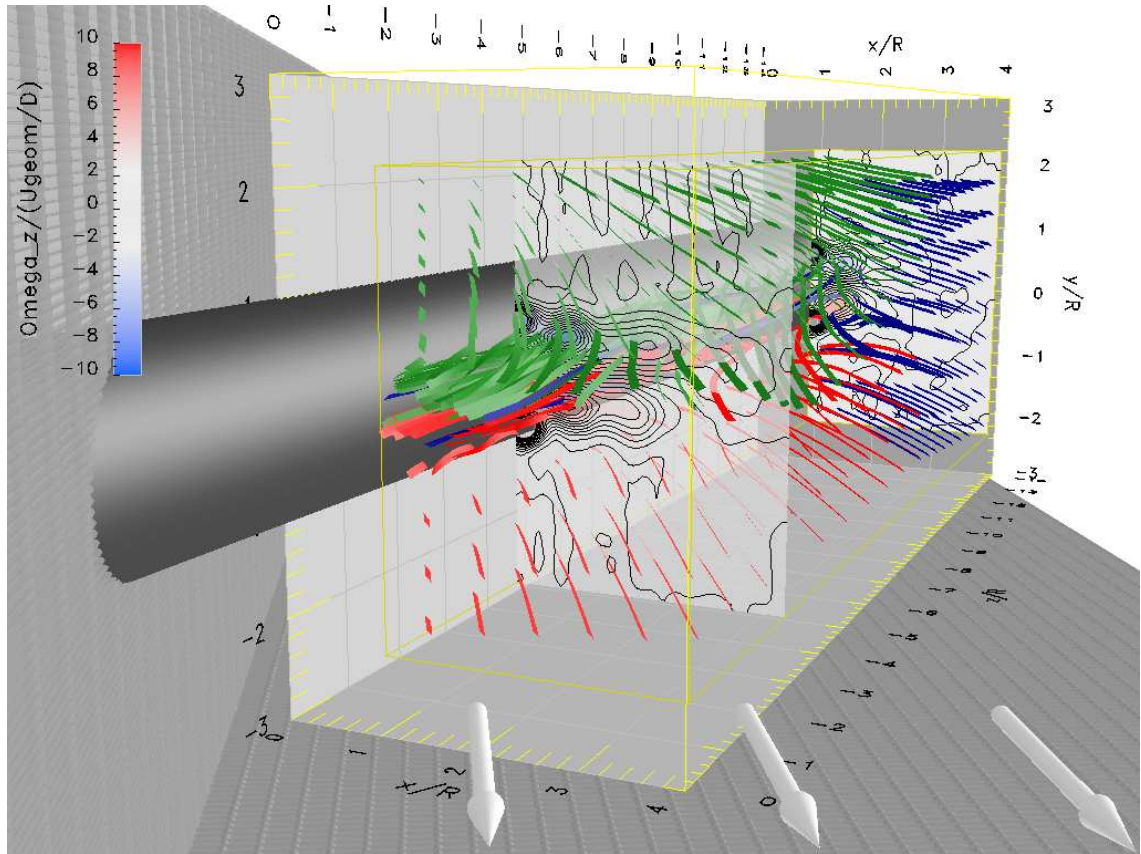


Fig. 4.105: Streamlines, $F_n^+ = 1.78$, $C_{\mu,n} = 11\%$ per slot, sym., $\Theta = \pm 110^\circ$, $\Lambda = 60^\circ$, $Re_n = 35000$

4.5.1.3 Near Wake Dynamics

Symmetric forcing stabilizes the 2-D characteristics of the flow and thus reduces the level of turbulent kinetic energy k with increasing C_μ . In the baseline case the maxima of $\frac{u'^2 + v'^2 + w'^2}{U_\infty^2}$ clearly coincide with the peeling-off vortices up to approximately $z/R = -4$, as visualized by iso-surfaces of k in figure 4.106. Downstream of this point $z/R > -4$ the maximum of turbulent kinetic energy lies in the region of the largest velocity gradients, between the vortex pair close to the cylinder and the second pair that peeled off the cylinder at approximately $z/R = -6$.

When symmetric excitation is applied at the low level of $C_{\mu,n} = 3\%$ the symmetry of the flow is destroyed and only a single large vortex peels off the cylinder (see figure 4.97) in the investigated volume. The maximum of turbulent kinetic energy (figure 4.107) is located above the vortex core and shifted towards the cylinder. The intensity of k is slightly increased compared to actuation at $C_{\mu,n} = 3\%$, visible at the larger cross sectional area of the “core” marked in red on the left side of the figure. This indicates that the location of the vortex is not stabilized by the cylinder any more once it peeled-off, thus the jitter in the position of the vortex increases with increased distance to the cylinder.

When the excitation level is increased to $C_{\mu,n} = 4\%$ (figure 4.108) the structure of the wake changes again greatly and the maximum of $\frac{u'^2 + v'^2 + w'^2}{U_\infty^2}$ is found between the vortices in lee of the cylinder. The distribution of k is almost two-dimensional in this case, visualized by iso-surfaces of turbulent kinetic energy in figure 4.108. Only the vortex peel-off around $z/R = -5$ indicates the three-dimensional nature of this flow. The maximum in k at this level of excitation is approximately 65% of the maximum turbulent kinetic energy in the baseline case. This indicates that the symmetric actuation enhances the two-dimensional characteristics of the wake and reduces the fluctuations of the coherent structures past the cylinder.

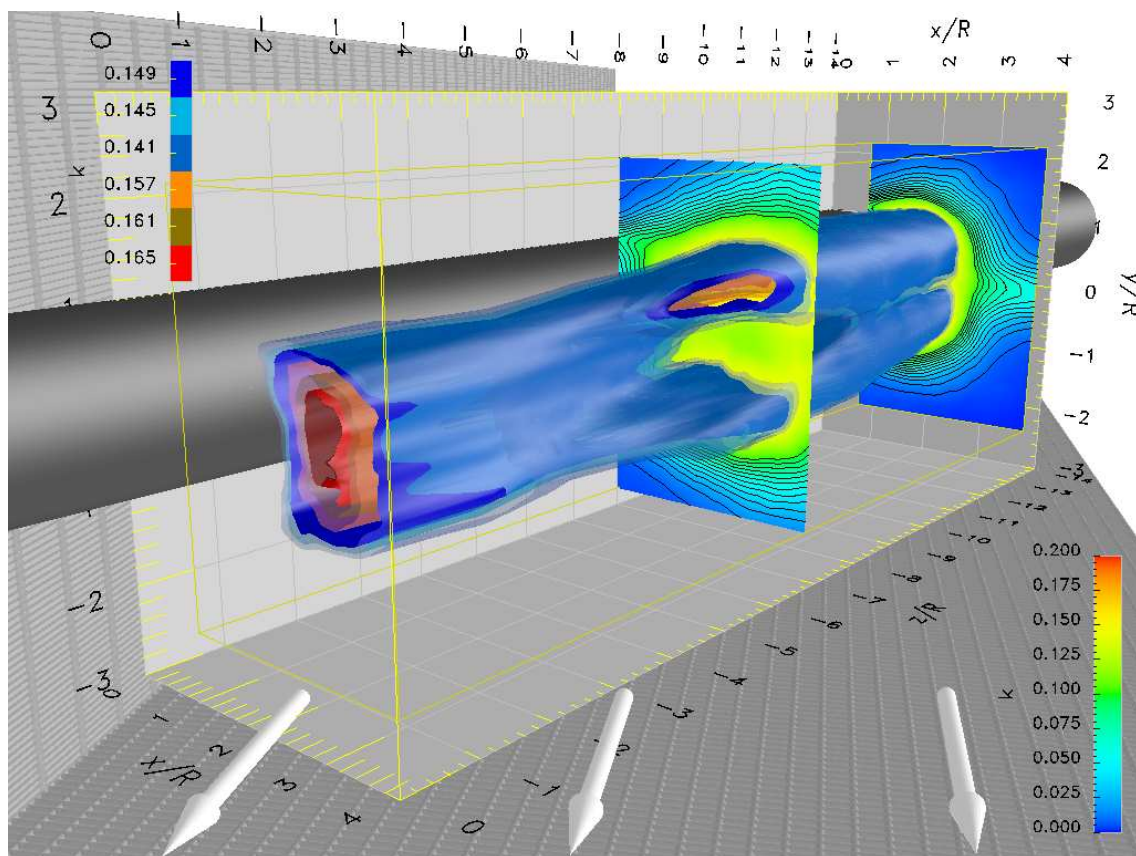


Fig. 4.106: Iso-surfaces of $\frac{\overline{u'^2 + v'^2 + w'^2}}{U_\infty^2}$, baseline, $\Theta = \pm 110^\circ$, $\Lambda = 60^\circ$, $Re_n = 35000$

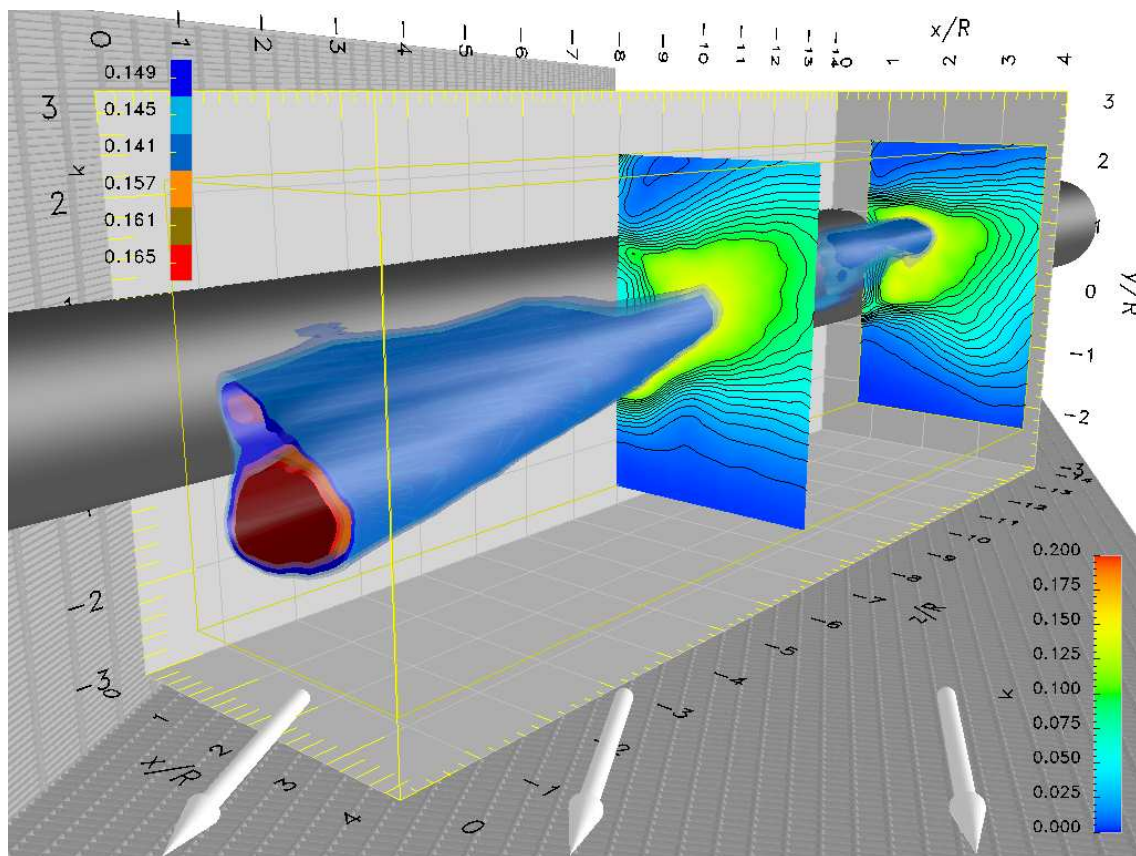


Fig. 4.107: $\frac{\overline{u'^2 + v'^2 + w'^2}}{U_\infty^2}$, $F_n^+ = 1.78$, $C_{\mu,n} = 3\%$, sym., $\Theta = \pm 110^\circ$, $\Lambda = 60^\circ$, $Re_n = 35000$

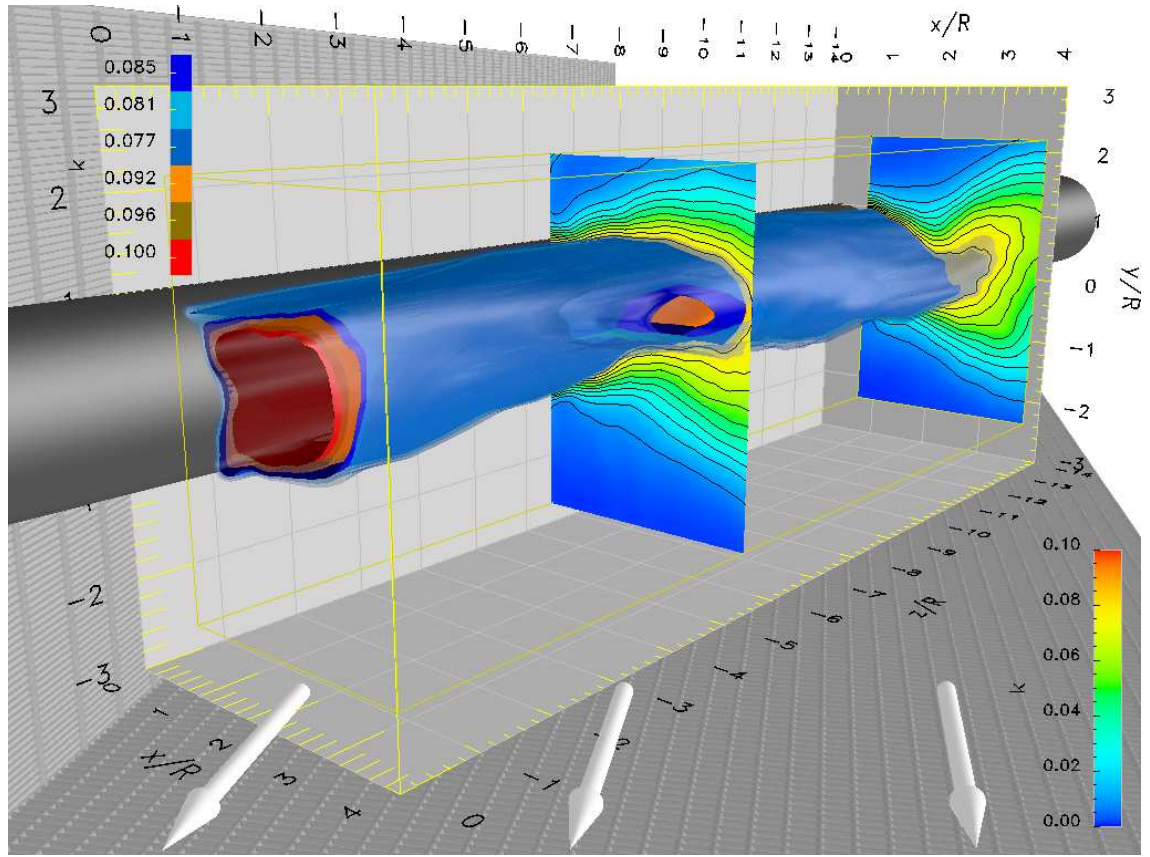


Fig. 4.108: $\frac{\overline{u'^2 + v'^2 + w'^2}}{U_\infty^2}$, $F_n^+ = 1.78$, $C_{\mu,n} = 4\%$, sym., $\Theta = \pm 110^\circ$, $\Lambda = 60^\circ$, $Re_n = 35000$

Further increase of $C_{\mu,n}$ (figure 4.109) results in another significant modification of the structure of the turbulent kinetic energy in the near wake. At this level of excitation the two-dimensional spanwise vortices in lee of the cylinder are stabilized even more. The width of the wake is reduced and the vortices formed on both sides of the cylinder are deflected strongly towards the plane of symmetry at $y/R = 0$. The maximum values of k are still found close to the vortex cores in an elongated zone around $y/R = 0$. The magnitude of k is reduced to 25% of the value found in the baseline case. The wake is stabilized considerably by the actuation and fluctuations of the vortices in strength and/or location are minimized. The maximum of k at the upstream side ($z/R = -13.3$) of the control volume in figure 4.109 indicates a strong vortex that is fluctuating considerably more than the other vortices peeling off. This vortex is the first one separating from the cylinder and therefore more susceptible for minor changes in the inflow conditions. As can be seen later in the far wake (figure 4.116 on 84) the location of this vortex is oscillating between two positions, confirming the above statement.

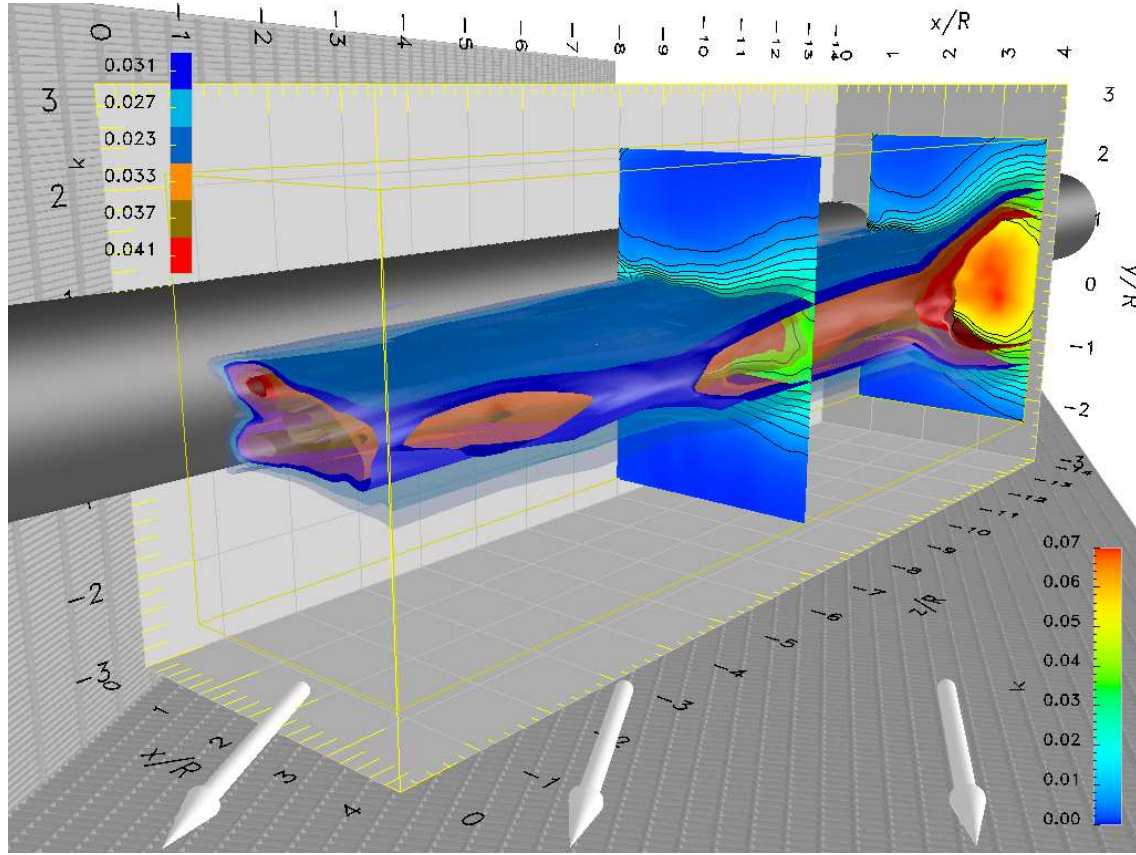


Fig. 4.109: $\frac{u'^2 + v'^2 + w'^2}{U_\infty^2}$, $F_n^+ = 1.78$, $C_{\mu,n} = 7\%$, sym., $\Theta = \pm 110^\circ$, $\Lambda = 60^\circ$, $Re_n = 35000$

The variation of the center of Ω_z (see equation 4.8 on page 47) with the POD phase (see pages 19 ff) is greatly reduced with increasing level of symmetric excitation, as illustrated in figures 4.110 to 4.112 for all spanwise stations. The smallest numerical value of the POD phase is marked for every spanwise position by a black circle. This point is equivalent to the beginning (phases with insufficient numbers of samples excluded) of the cycle describing the meandering of the wake. At a forcing level of $C_{\mu,n} = 3\%$ (see figure 4.110) the center of $\Omega_z < 0$ (top side, “blue vortices”) is moving approximately $1R$ in horizontal direction and $0.8R$ in vertical direction.

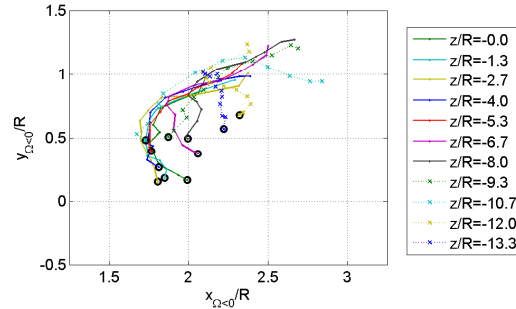


Fig. 4.110: Center of $\Omega_z < 0$, $\Theta = \pm 110^\circ$, $F_n^+ = 1.78$, $C_{\mu,n} = 3\%$, sym., $\Lambda = 60^\circ$, $Re_n = 35000$

When forcing is increased to $C_{\mu,n} = 4\%$ (figure 4.111) the horizontal displacement of the center of $\Omega_z < 0$ over the different POD phases remains to be approximately $1R$ and the vertical displacement is reduced to values between $0.3R$ and $0.8R$, depending on the spanwise position. A further increase of the excitation to $C_{\mu,n} = 7\%$ reduces the vertical motion to $0.3R$ at all spanwise positions (figure 4.112) and the horizontal motion is reduced to $0.75R$. Symmetric forcing reduces the periodic motion of the vortices significantly, in particular the vertical displacement caused by the meandering of the wake.

This confirms the observation discussed before that the symmetric forcing is stabilizing the wake by reducing the movement of the vortices, in particular the vertical motion corresponding to a meandering of the wake.

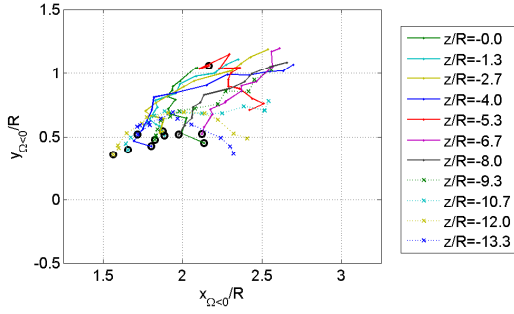


Fig. 4.111: Center of $\Omega_z < 0$, $\Theta = \pm 110^\circ$,
 $F_n^+ = 1.78$, $C_{\mu,n} = 4\%$, sym.,
 $\Lambda = 60^\circ$, $Re_n = 35000$

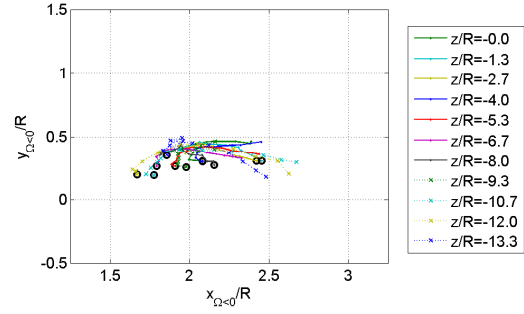


Fig. 4.112: Center of $\Omega_z < 0$, $\Theta = \pm 110^\circ$,
 $F_n^+ = 1.78$, $C_{\mu,n} = 7\%$, sym.,
 $\Lambda = 60^\circ$, $Re_n = 35000$

4.5.1.4 The Far Wake

The interference between the spanwise flow at the downstream end of the cylinder and the side wall of the test section prevents the accurate determination of C_d for the baseline (both slots open) and low levels of excitation in the infinite configuration. A single large velocity deficit is located close to the side wall of the tunnel (left side in figure 4.113). The necklace vortex that is shed from the cylinder by the fence mounted at its upstream end is just detected at the right side of the investigated area. Neither the location of the velocity minimum nor its magnitude can be determined properly due to its position close to the wall. The wake is symmetric around $y_T/R = 0$ and no lift is generated. When forcing is applied at $C_{\mu,n} = 2\%$ the velocity minimum is shifted only little away from the wall and its location as well as the magnitude could be estimated coarsely at best. The velocity distribution is slightly asymmetric. The total drag computed for these two cases has to be considered inaccurate due to the strong wall interference.

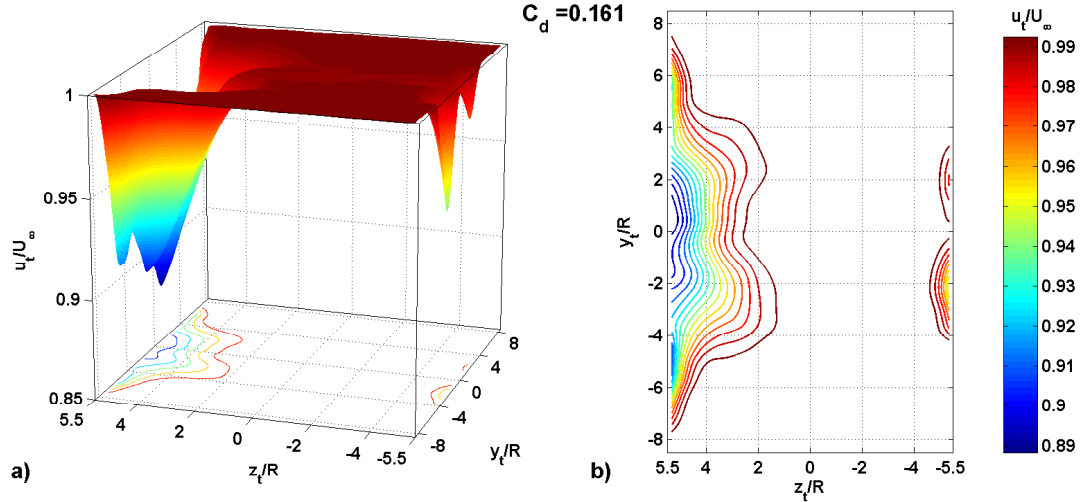


Fig. 4.113: Far wake, $\frac{u_T}{U_\infty}$, $\Theta = \pm 110^\circ$, baseline, sym., $\Lambda = 60^\circ$, $Re_n = 35000$

Increasing the level of excitation to $C_{\mu,n} = 4\%$ (figure 4.115) changes the characteristics of the far wake drastically. In this case several weak velocity minima are distributed along the span instead of the single velocity deficit close to the downstream end. The individual minima mark the cores of the vortices that peeled off the cylinder. Compared to asymmetric forcing the peeled-off vortices are significantly weaker. The velocity minima are centered around $y_T/R = -1$, therefore C_l has to be slightly positive.

At a level of excitation of $C_{\mu,n} = 7\%$ (figure 4.116) the wake is symmetric around $y_T/R = 0$, with exception of the first velocity deficit at $z_T/R = -1.5$. The vortex that causes this deficit is for short periods displaced to $y_T/R = -2.5$, $z_T/R = -3$ due to fluctuations in the peel-off process.

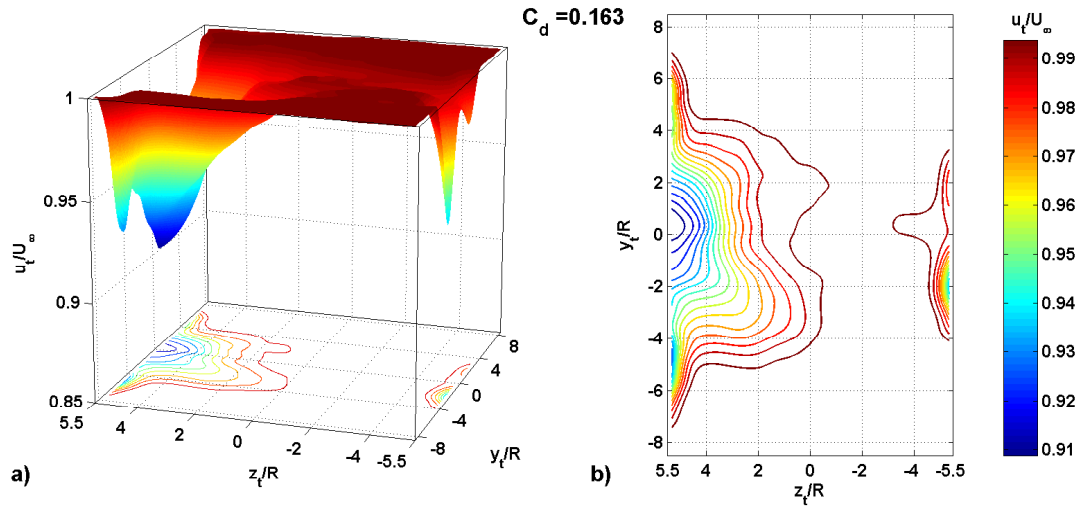


Fig. 4.114: Far wake, $\frac{u_T}{U_\infty}$, $\Theta = \pm 110^\circ$, $F_n^+ = 1.78$, $C_{\mu,n} = 2\%$, sym., $\Lambda = 60^\circ$, $Re_n = 35000$

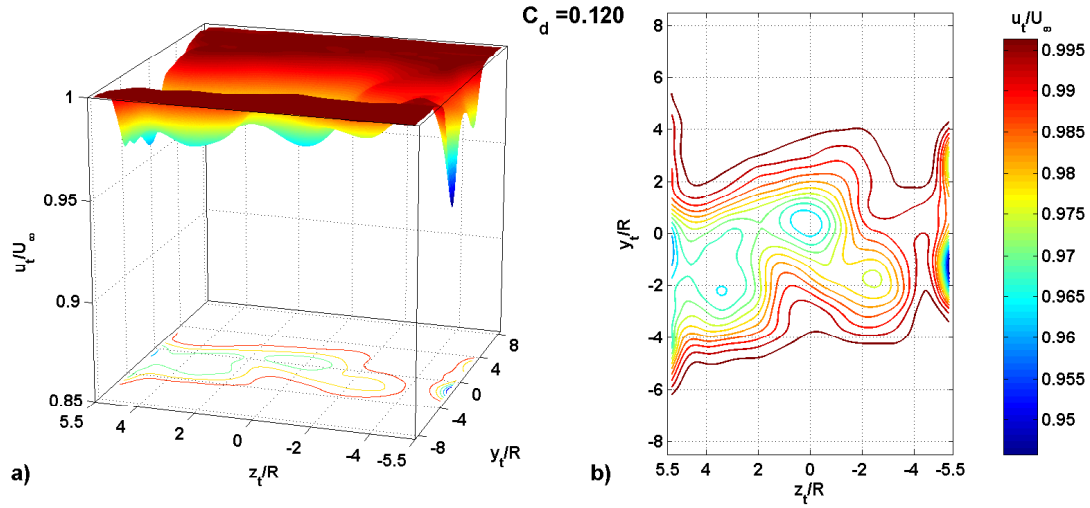


Fig. 4.115: Far wake, $\frac{u_T}{U_\infty}$, $\Theta = \pm 110^\circ$, $F_n^+ = 1.78$, $C_{\mu,n} = 4\%$, sym., $\Lambda = 60^\circ$, $Re_n = 35000$

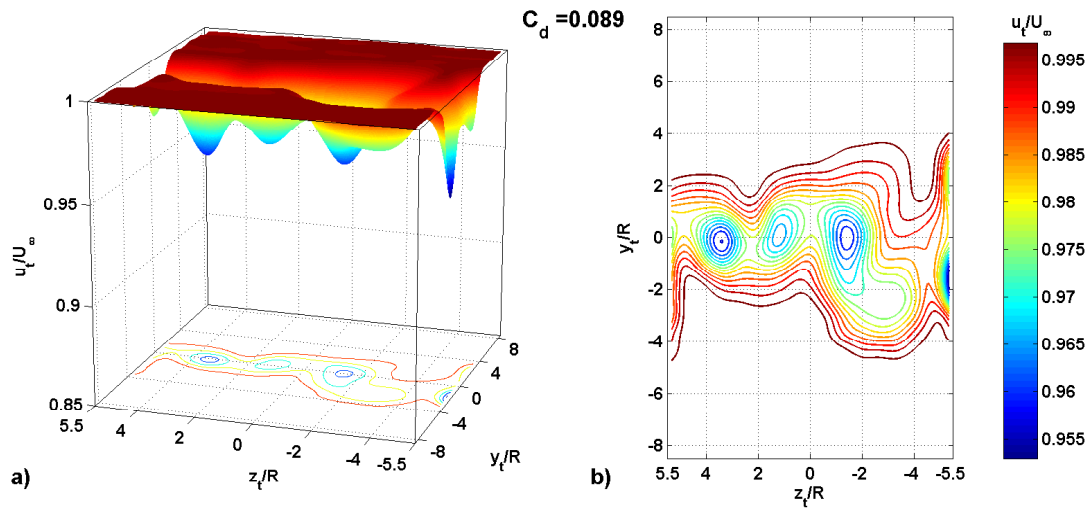


Fig. 4.116: Far wake, $\frac{u_T}{U_\infty}$, $\Theta = \pm 110^\circ$, $F_n^+ = 1.78$, $C_{\mu,n} = 7\%$, sym., $\Lambda = 60^\circ$, $Re_n = 35000$

The velocity minima are noticeably enhanced compared to excitation at $C_{\mu,n} = 4\%$. Further increase of C_μ causes only minor modifications of the wake (compare figure 4.117). A fourth velocity deficit is located close to the downstream end of the cylinder and just detected at the boundary of the investigated area.

The drag computed in the far wake of the infinite inclined cylinder with symmetric forcing at higher levels is problematic because only a fraction of the accumulated vorticity (and thus deficit in W) is peeling-off along the span. A large part is contained in the vortices oriented parallel to the cylinder, running along the entire span. Therefore the total drag computed from the data taken in the far wake of the infinite configuration has to be considered inaccurate for all levels of excitation.

Nevertheless, figure 4.117 shows correctly the three states of the flow with AFC identified earlier for the 2-D and $\Lambda = 60^\circ$ configurations. For low levels of excitation the drag increases by approximately 10% and it fluctuates. After a critical value is exceeded the total drag is reduced to an unrealistically low value of $C_d = 0.09$. Further increase in C_μ results only in minor additional reduction of C_d for the saturated flow

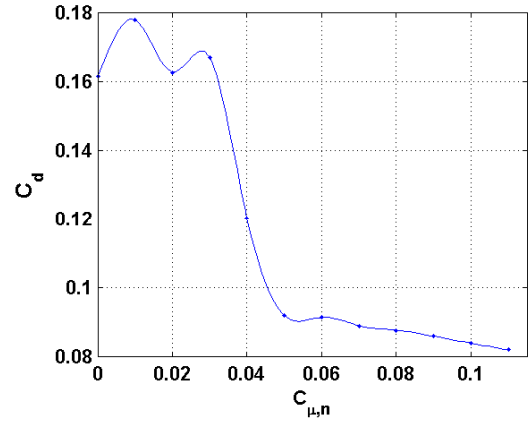


Fig. 4.117: C_d vs. $C_{\mu,n}$, $\Theta = \pm 110^\circ$, sym.,
 $F_n^+ = 1.78$, $\Lambda = 60^\circ$, $Re_n = 35000$

The far wake of a cylinder inclined at 45°

A large velocity deficit extending over more than half of the tunnel cross section (figure 4.118) is found at a sweep-back angle of $\Lambda = 45^\circ$. It consists mainly of two local minima adjacent to the side wall touched by the downstream end of the cylinder. The wake is symmetric with the two minima being aligned at $y_T/R = 0$. The wide wake indicates fluctuations of the vortices peeling-off, indicated by the black arrow in figure 4.118. This was confirmed by spectra computed from Hotwire data (see figure 4.151 on page 99) and is similar to the baseline for asymmetric forcing with one slot taped. Once a vortex starts to peel off the downstream end of the cylinder it will by induction push the opposite vortex closer to the cylinder. Concurrently, the separating vortex is pushed away from the plane of symmetry $y_T/R = 0$ by induction from the vortex that is still close to the cylinder. The result is the observed blurred velocity deficit caused by averaging of the two vortices of opposing vorticity. The upstream necklace vortex is detected for all excitation levels at the far right of the investigated area.

The symmetry of the wake is distorted severely (figures 4.119 and 4.120) at low levels of forcing. The resulting asymmetry is likely generated by asymmetric fluctuations of the peeling-off vortices, indicated in by the black arrow in figure 4.119. The lower vortex is prevented from peeling-off in a periodic fashion due to the symmetric excitation and peels off stationary instead. The upper keeps peeling-off along the span in an oscillating fashion as in the baseline case, as indicated. The lower velocity minimum is shifted to $y_T/R = -1$, $z_T/R = 2$ due to the imbalance between the two vortices and the magnitude of the velocity minima differ considerably due to the averaging.

At $C_{\mu,n} = 2\%$ (figure 4.120) the asymmetry of the wake is increased. In this case the upper vortex is kept attached to the cylinder along the entire span and fans out when contacting the side wall of the test section. It is displaced towards $y_T = 5$ due to self induction at the wall. The opposite vortex peels-off along the span and causes a weak velocity deficit at $y_T/R = -2.5$, $z_T/R = 2$.

When the level of excitation is increased to the critical value of $C_{\mu,n} = 3\%$ (figure 4.121) the characteristics of the wake are changed significantly. The velocity deficit is extending over an elongated region from $z_T/R = 5.3$ to $z_T/R = -3$ at $y_T/R = 0$, with its minimum close to the side wall. The wake is symmetric with respect to $y_T = 0$ except for the upstream necklace vortex just detected at the right side of the investigated area.

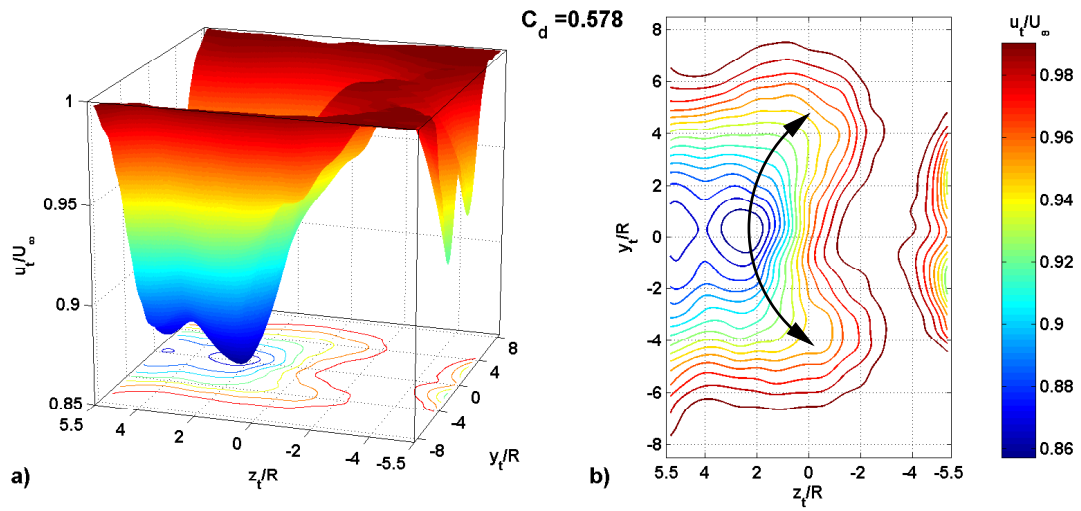


Fig. 4.118: Far wake, $\frac{u_T}{U_\infty}$, $\Theta = \pm 110^\circ$, $F_n^+ = 1.78$, baseline, sym., $\Lambda = 45^\circ$, $Re_n = 35000$

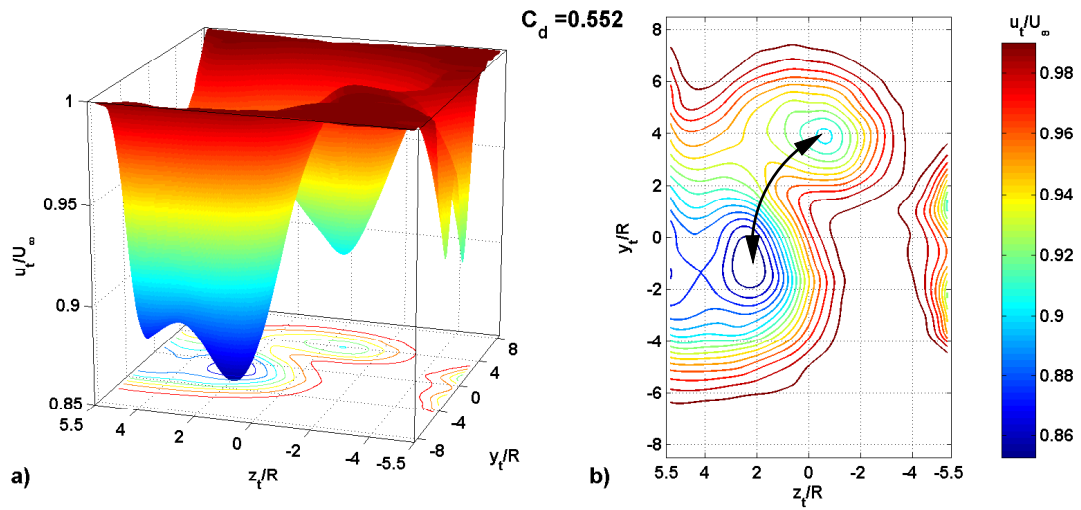


Fig. 4.119: Far wake, $\frac{u_T}{U_\infty}$, $\Theta = \pm 110^\circ$, $F_n^+ = 1.78$, $C_{\mu,n} = 1\%$, sym., $\Lambda = 45^\circ$, $Re_n = 35000$

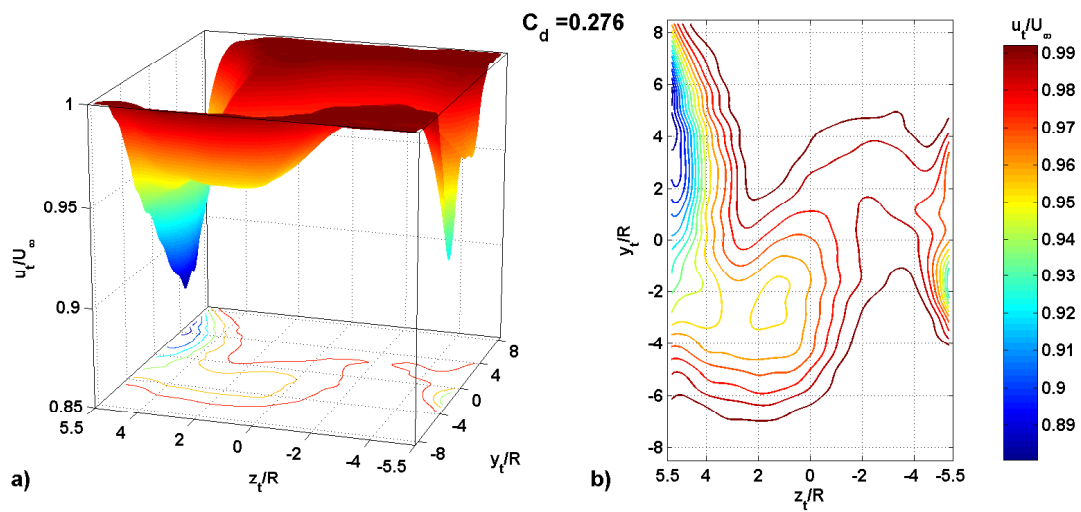


Fig. 4.120: Far wake, $\frac{u_T}{U_\infty}$, $\Theta = \pm 110^\circ$, $F_n^+ = 1.78$, $C_{\mu,n} = 2\%$, sym., $\Lambda = 45^\circ$, $Re_n = 35000$

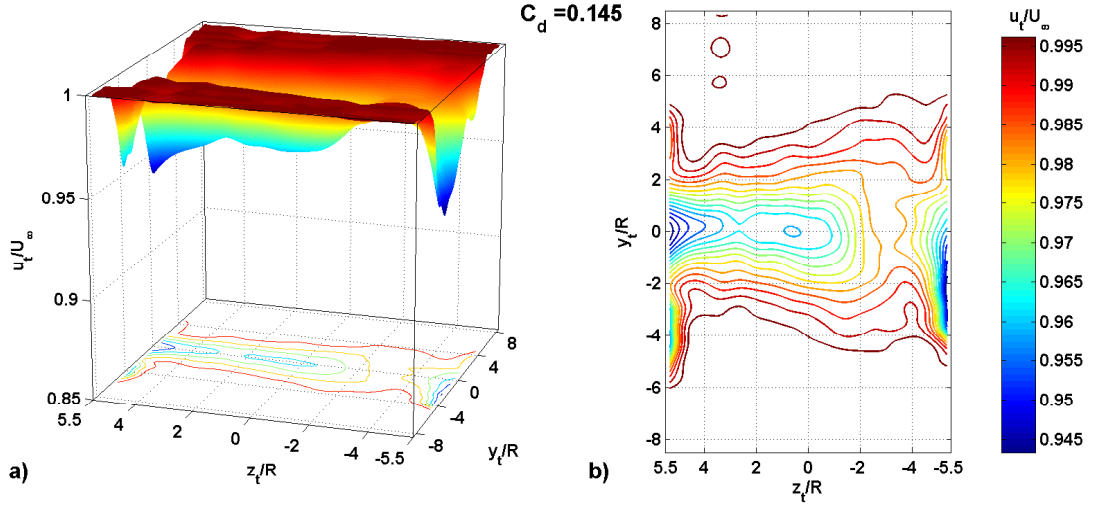


Fig. 4.121: Far wake, $\frac{u_t}{U_\infty}$, $\Theta = \pm 110^\circ$, $F_n^+ = 1.78$, $C_{\mu,n} = 3\%$, sym., $\Lambda = 45^\circ$, $Re_n = 35000$

The total drag determined for forcing at various $C_{\mu,n}$ with $F_n^+ = 1.78$ from a slot location of $\Theta = \pm 110^\circ$ in the infinite configuration at $\Lambda = 45^\circ$ is presented in figure 4.122. It follows the trend observed for the asymmetrically forced cases at $\Lambda = 0^\circ$ and $\Lambda = 60^\circ$. The total drag increases for low C_μ until reaching a critical value $1\% < C_{\mu,n,crit1} < 2\%$. Beyond this value it decreases until a second critical value $C_{\mu,n,crit2} = 5\%$ is reached and the flow is fully attached upstream of both slots (not taking into account the shallow separation bubble). The values of C_d determined for the infinite configuration have to be considered too low because the spanwise flow along the cylinder impinging on the wall cannot be included in the computation due to wall interference and the limitations in the travel of the wake rake traverse.

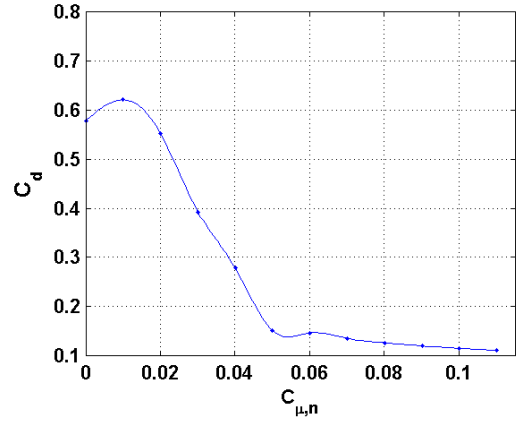


Fig. 4.122: C_d vs. $C_{\mu,n}$, $F_n^+ = 1.78$, $\Lambda = 45^\circ$, $Re_n = 35000$

4.5.2 The Finite Cylinder

The cylinder was retracted by 12" from the test section to investigate a finite configuration. This procedure relocated the pressure taps at a different spanwise position closer to the side wall of the test section. An elliptical endplate of 12.25" x 6.75" was mounted aligned to the free stream to the end of the cylinder to stabilize the spanwise pressure gradient and to minimize end effects. The distance between the tip of the cylinder and the side wall was 6".

Iso-surfaces of $\frac{W}{U_\infty \sin \Lambda}$ computed in the entire investigated control volume are presented in figure 4.123. The PIV data were acquired in the infinite configuration. The XZ-plane of the control volume is parallel to the paper plane, thus the data is presented in a "top view". The endplate mounted in the finite position is marked by the dashed black line. It is assumed that, for a properly adjusted system and identical excitation, the vortex peel-off locations are mainly dependent on the upstream conditions, in particular by the distance to the side wall at the upstream end of the cylinder. Provided the spanwise pressure gradient remains unaltered, the vortices peeling-off in the finite configuration with symmetric excitation would therefore interfere noticeably with the endplate, marked by the dashed black line in figure 4.123. Nevertheless, the endplate is necessary to minimize changes in the spanwise pressure gradient due to end effects and to provide a defined spanwise peel-off position.

The angle between the separating vortices and the cylinder is estimated to be 21° for symmetric excitation and undisturbed flow. It is noticeable smaller than the estimated 28.5° for asymmetric actuation (see figure 4.73 on page 64). The spacing between the vortices is approximately $2R$ measured perpendicular to the vortex axes. This is a decrease in spacing of 40% compared to asymmetric excitation.

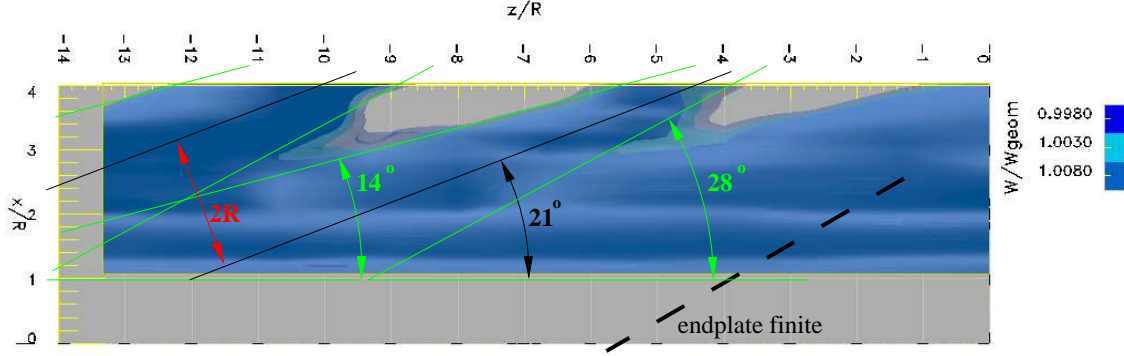


Fig. 4.123: Vortex spacing, $\frac{W}{U_\infty \sin \Lambda}$, $\Theta = \pm 110^\circ$, $F_n^+ = 1.78$, $C_{\mu,n} = 7\%$, sym., $\Lambda = 60^\circ$, $Re_n = 35000$

4.5.2.1 Forces on the Cylinder

As for the asymmetrically forced case the pressure distributions acquired at the spanwise position closer to the wall are altered by the stationary vortices located closer to the surface of the cylinder (see page 64 ff) for the baseline (figure 4.124) as well as the forced cases (see figure 4.125). The base pressure is lowered significantly, increasing the local form drag. As for the asymmetrically forced

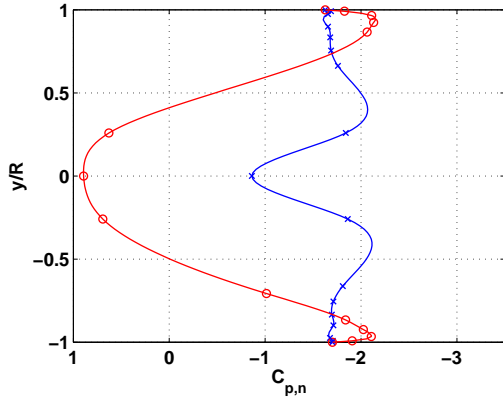


Fig. 4.124: y/R vs. $C_{p,n}$, $\Theta = \pm 110^\circ$, baseline, sym., $\Lambda = 60^\circ$, $Re_n = 35000$

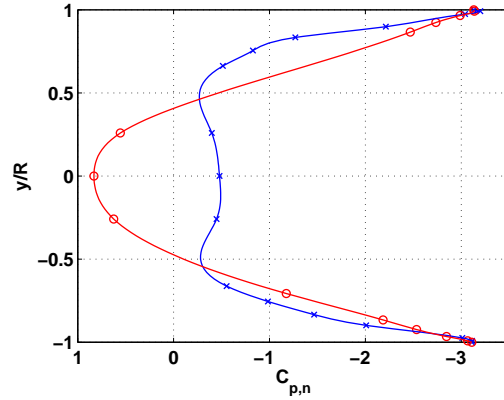


Fig. 4.125: y/R vs. $C_{p,n}$, $\Theta = \pm 110^\circ$, $F_n^+ = 1.78$, $C_{\mu,n} = 11\%$, sym., $\Lambda = 60^\circ$, $Re_n = 35000$

case, the pressure distributions acquired at the spanwise position closer to the wall are altered by the stationary vortices being located closer to the surface of the cylinder (see page 64 ff) for the baseline (figure 4.124) as well as the forced cases (see figure 4.125). The base pressure is lowered significantly, increasing the local form drag (see figure 4.144 on page 97 for comparison).

4.5.2.2 The Far Wake

Measurements of the velocity deficits in the far wake of the finite cylinder enable a more accurate determination of the total drag than in the infinite configuration. The velocity deficit in the far wake of a finite cylinder without actuation (figure 4.126) was determined with both slots being untaped. It hardly differs from the baseline data taken with one slot taped during the experiments with asymmetric forcing. The velocity minima are slightly wider and the upstream necklace vortex

is more symmetric than in the corresponding asymmetric case. The side minima are formed by the vortices naturally peeling off the cylinder and the large deficit located at $z_T/R = 4$ (location of the tip of the cylinder) is formed by the vortices forced to separate from the finite cylinder by the endplate. The wake is slightly asymmetric, in spite of the nominally symmetric configuration.

When forcing is applied at a low level with $C_{\mu,n} = 2\%$ (figure 4.127) the asymmetry is reversed and the wake is slightly displaced towards $y_T/R > 0$. The wake is more compact and the side minima are reduced considerably. Nevertheless, the main characteristic of the wake with one large central velocity deficit is preserved. The total drag is only little reduced by 6.5% from $C_d = 0.295$ to $C_d = 0.276$.

The shape of the wake changed noticeable at an increased forcing level of $C_{\mu,n} = 4\%$. The velocity deficit at the end of the cylinder is significantly reduced in size as well as in magnitude. Around $y_T/R = 0$, $z_T/R = -0.5$ a second but weaker velocity minimum occurs. It is caused by the first vortex that peels off the cylinder. The other vortices peeling off the cylinder (see figure 4.99 for the infinite case) are combined with the main velocity deficit. The total drag is reduced by 50% with respect to the baseline.

The velocity deficit at $z_T/R = 4$ is reduced in size and magnitude when forcing at $C_{\mu,n} = 7\%$ (figure 4.128). In this case two side-minima exist, probably formed by the peeled-off vortices. The second minimum was shifted slightly to $z_T/R = -1$. The total drag is reduced by 57% to $C_d = 0.126$.

The wake of the finite cylinder is in all cases undistorted and well captured within the investigated area. The necklace vortex is hardly affected by the symmetric forcing for all levels of excitation.

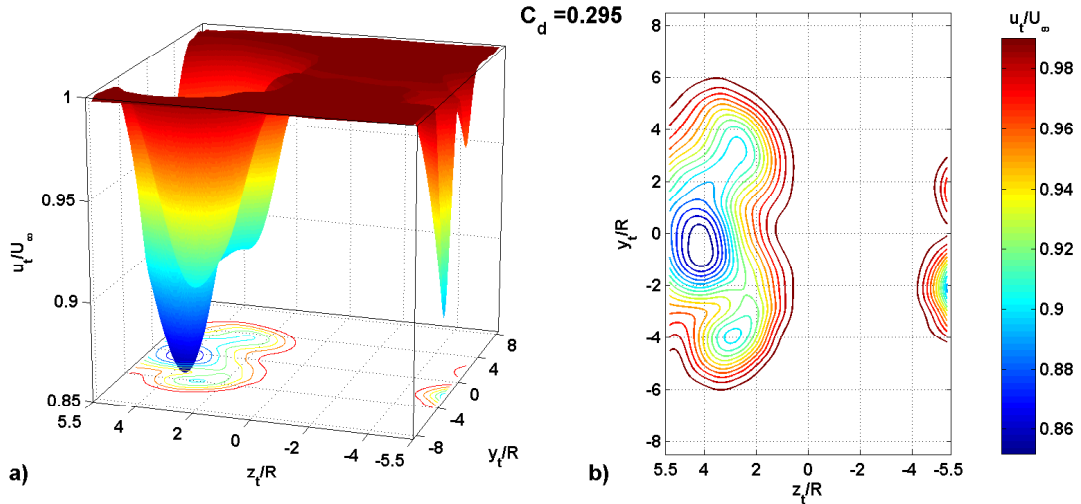


Fig. 4.126: Far wake, $\frac{u_T}{U_\infty}$, $\Theta = \pm 110^\circ$, baseline, sym., finite, $\Lambda = 60^\circ$, $Re_n = 35000$

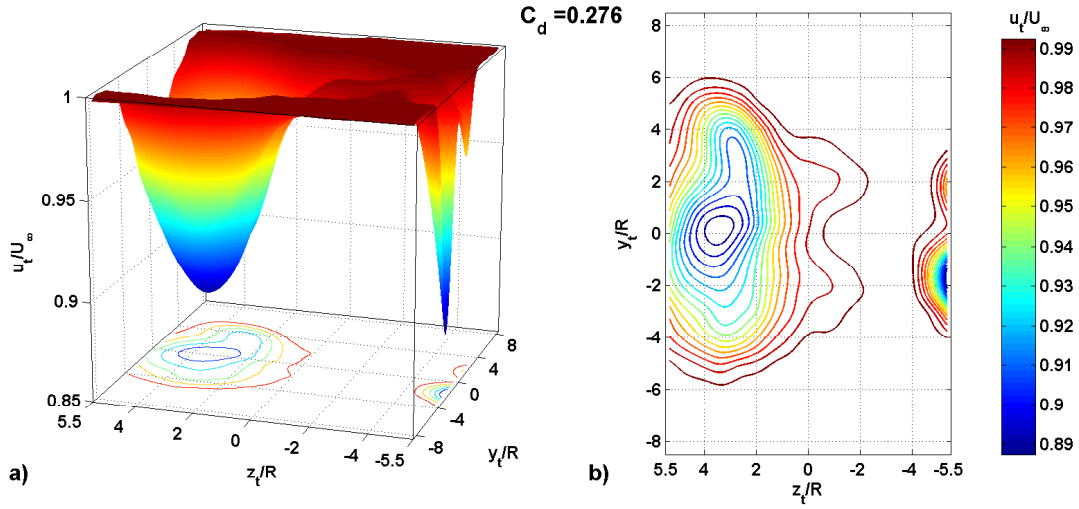


Fig. 4.127: Far wake, $\frac{u_T}{U_\infty}$, $\Theta = \pm 110^\circ$, $F_n^+ = 1.78$, $C_{\mu,n} = 2\%$, sym., finite, $\Lambda = 60^\circ$, $Re_n = 35000$

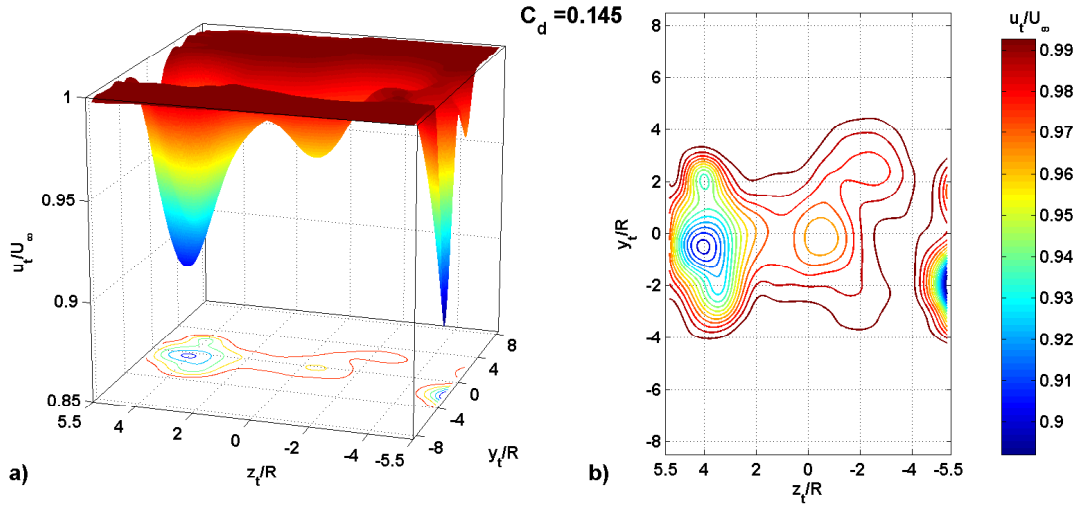


Fig. 4.128: Far wake, $\frac{u_T}{U_\infty}$, $\Theta = \pm 110^\circ$, $F_n^+ = 1.78$, $C_{\mu,n} = 4\%$, sym., finite, $\Lambda = 60^\circ$, $Re_n = 35000$

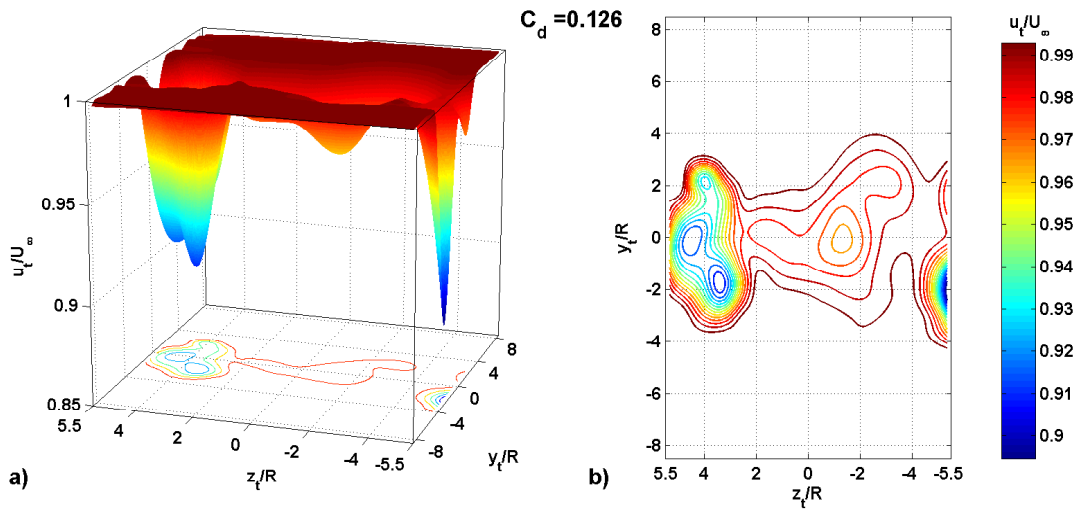


Fig. 4.129: Far wake, $\frac{u_T}{U_\infty}$, $\Theta = \pm 110^\circ$, $F_n^+ = 1.78$, $C_{\mu,n} = 7\%$, sym., finite, $\Lambda = 60^\circ$, $Re_n = 35000$

The total drag of the finite configuration with symmetric excitation is compared in figure 4.130 with the corresponding asymmetric case. Important to note is that the level of excitation is given “per slot” for both graphs because the critical values of $C_{\mu,n}$ depend on the properties at each individual slot. The total drag increases initially with the forcing level for both curves until it drops after exceeding $C_{\mu,n,crit1}$. The values for both cases are in the range $1\% < C_{\mu,n,crit1} < 2\%$. The rate of decrease of C_d is reduced once the flow fully reattaches upstream of the slot (not considering a potential shallow 3-D separation bubble). This second critical value is for the symmetric as well as for the asymmetric case approximately $C_{\mu,n,crit2} = 5\%$.

Both critical values of $C_{\mu,n}$ are similar for asymmetrical and symmetrical forcing together with the characteristics of the two presented graphs. The effect of the second slot on C_d when forcing symmetrically is therefore additive. A potential interference between the two slots in the symmetric configuration is thus minor.

The reduction

$$\Delta C_d = \frac{C_d - C_{d,0}}{C_{d,0}} \quad (4.9)$$

of the total drag for excitation at $C_{\mu,n,total} = 10\%$ is in the asymmetric case $\Delta C_d = 26\%$. The reduction for symmetric forcing at the same level of excitation $C_{\mu,n,total} = 10\%$ doubled with $\Delta C_d = 54\%$. Thus the effect of symmetric forcing from two slots on the total drag seems to be cumulative, provided actuation is applied above the critical value for reattaching the flow upstream of the slots.

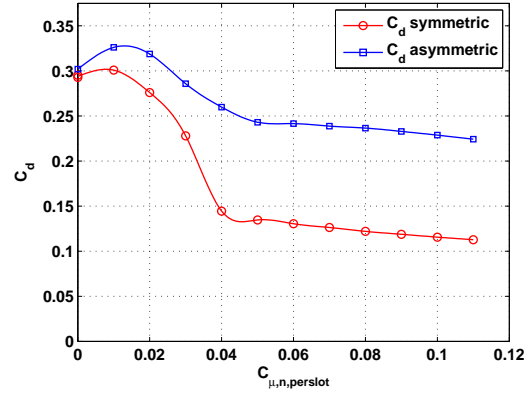


Fig. 4.130: C_d vs. $C_{\mu,n}$, $\Theta = \pm 110^\circ$, $F_n^+ = 1.78$, sym., finite, $\Lambda = 60^\circ$, $Re_n = 35000$

4.6 Generic Actuation

The cases of actuation described in the two last chapters dealt with actuation from a single slot and from both slots at identical frequencies and amplitude. Generalized cases of excitation include forcing from both slots at the same frequency but at different levels, phase delays between the two slots and forcing at two different frequencies but with the same C_μ .

4.6.1 Single-sided actuation with both Slots open

Experiments were carried out with asymmetric excitation from only one row of actuators but with both slots untaped to investigate the cross-talk between both slots. Due to the common back chamber of the actuators the membranes of the inactive row of actuators were driven by the oscillating pressure generated in this common chamber. This generated a weak forcing signal in the nominally inactive slot at a phase delay of approximately $\delta = 180^\circ$. The forcing level was not determined for the nominally inactive slot because the taped configuration was used for all other experiments with asymmetric forcing.

The configuration with untaped slots is equivalent to forcing at a single frequency with differing forcing levels at the two slots and the pressure on both sides of the cylinder is lowered (figure 4.131), reducing the asymmetry of the flow and thus C_l . Additionally, the oscillation of the stagnation “line” due to single sided actuation is reduced when the nominally inactive slot is not taped. The

lift is increased and the form drag reduced when the inactive slot is taped (figure 4.6.1). The comparison of the form drag is not considered conclusive due to the inconsistencies found for determining C_{dp} at one single spanwise location only. An increase of the forcing level to 12% reduced the form drag to $C_{dp} = 0.069$ for untaped slots whereas the reduction was only moderate for the taped case with $C_{dp} = 0.156$ at $C_{\mu,n} = 11\%$. The results obtained from symmetric forcing indicate that the effects on the total drag are cumulative. Thus it should be possible to adjust drag and lift independently by forcing with different amplitudes on opposing sides of the cylinder.

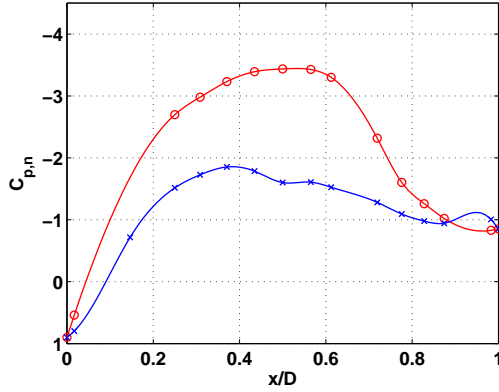


Fig. 4.131: $C_{p,n}$ distribution, both slots open, $\Theta = 110^\circ$, asym., $x_S/D = 0.67$, $F_n^+ = 1.78$, $C_{\mu,n} = 8\%$, $C_l = 0.247$, $C_{dp} = 0.173$, $\Lambda = 60^\circ$, $Re_n = 35000$

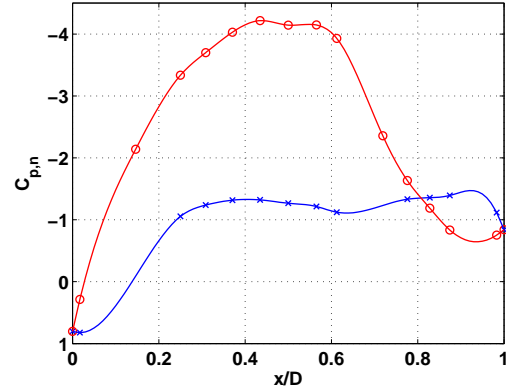


Fig. 4.132: $C_{p,n}$ distribution, inactive slot taped, $\Theta = 110^\circ$, asym., $x_S/D = 0.67$, $F_n^+ = 1.78$, $C_{\mu,n} = 8\%$, $C_l = 0.386$, $C_{dp} = 0.165$, $\Lambda = 60^\circ$, $Re_n = 35000$

4.6.2 Double-sided Actuation with Phase Delay

Most experiments were carried out with the excitation from the two slots being in phase, thus the velocity signals measured at every single slot were identical within the accuracy of the calibration. A potential dependence of lift and form drag on the phase delay, δ between the oscillations emanating from the two opposing slots was examined for a phase shift of $\delta = 90^\circ$ and $\delta = 180^\circ$, as presented in figures 4.133 to 4.136. No curve fit was applied to the data to avoid oscillations of the fitted curves due to scatter of the data and the strong variations in the slopes of the graphs.

The excitation system was calibrated individually for each phase delay to consider the coupling between the actuators through the common back chamber. The useful range of frequencies and forcing levels had to be adapted due to the differing back-pressure.

For a phase delay of $\delta = 90^\circ$ the characteristics of lift and form drag at mid-span indicate considerable three-dimensional effects and potential spanwise variations of the flow not only for low levels of excitation but also for $C_{\mu,n} > 6\%$. The lift is essentially unpredictable for $C_{\mu,n} < 4\%$. This is consistent with observations for $\delta = 0^\circ$ (page 72) and caused by the interaction between the coherent structures on the opposing sides of the cylinder. The frequency dependence of C_l for $C_{\mu,n} > 4\%$ is increased compared to $\delta = 0^\circ$. The characteristics of the form drag differ considerably from the results for $\delta = 0^\circ$. The frequency dependence of C_{dp} is significant at $\delta = 90^\circ$ (figure 4.133) over the entire investigated range of $C_{\mu,n}$.

The results obtained when driving the two slots with a phase delay of $\delta = 90^\circ$ are not fully consistent. This might be due to the internal coupling of all actuators through the common back chamber. The forcing signal at $\delta = 90^\circ$ is distorted compared the two other cases due to superposition of the forcing signals caused by the common back chamber. No correction of the input signals was available during the phase-delay experiments to minimize this effect, unlike for the later conducted experiments with two differing frequencies described below.

The form drag is independent of the forcing frequency over the entire range of $C_{\mu,n}$ when forcing is applied at a phase delay of $\delta = 180^\circ$. This could be caused by an external coupling of the opposing sides of the cylinder due to an azimuthal oscillation of the front stagnation line. Thus the signals of both slots would determine the reattachment of the flow, reducing potential variations

of the excitation signal between the two slots as well as in the spanwise direction. C_{dp} is reduced considerably when the forcing level is increased to the critical value of $C_{\mu,n} = 4\%$, forcing the flow to reattach upstream of the slot. In the saturated region beyond this value $\frac{C_{dp}}{C_{\mu,n}}$ is reduced. The lift is approximately zero for excitation above the critical level of $C_{\mu,n} = 4\%$. The results are consistent with the results for a phase delay of $\delta = 0^\circ$, including the performance.

Although the drag reduction is slightly enhanced for a phase delay of $\delta = 90^\circ$ (80% instead of 75% for $\delta = 180^\circ$ at $C_{\mu,n} = 6\%$) this benefit of running the excitation out-of-phase is not considered sufficient to accept the inconsistencies caused by the increased complexity of the flow.

This complexity is indicated by the strong variations of C_l and C_{dp} with C_μ as well as with F^+ . It shows clearly the limitations of the setup with a row of pressure taps at a single spanwise location only. Therefore already slight shifts of the coherent structures in spanwise direction can alter lift and form drag significantly, as seen in figures 4.133 and 4.134.

A phase delay of $\delta = 180^\circ$ forces the front stagnation line to oscillate, resulting in a coupling between both sides. The focus for this investigation was set on the (direct) interaction of the coherent structures in the wake, therefore this additional effect was undesirable. Additionally, the range of $C_{\mu,n}$ had to be limited for $\delta \neq 0$ to protect the actuators from mechanical damage. Thus all other experiments were carried out only at $\delta = 0^\circ$.

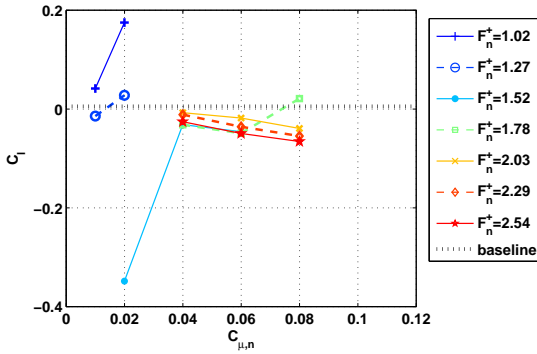


Fig. 4.133: C_l vs. $C_{\mu,n}$, $\delta = 90^\circ$, sym.,
 $\Theta = \pm 110^\circ$, $\Lambda = 60^\circ$, $Re_n = 35000$

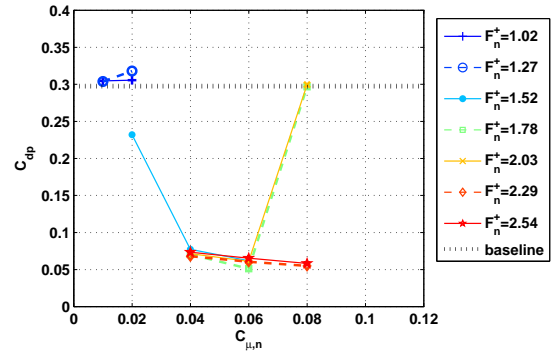


Fig. 4.134: C_{dp} vs. $C_{\mu,n}$, $\delta = 90^\circ$, sym.,
 $\Theta = \pm 110^\circ$, $\Lambda = 60^\circ$, $Re_n = 35000$

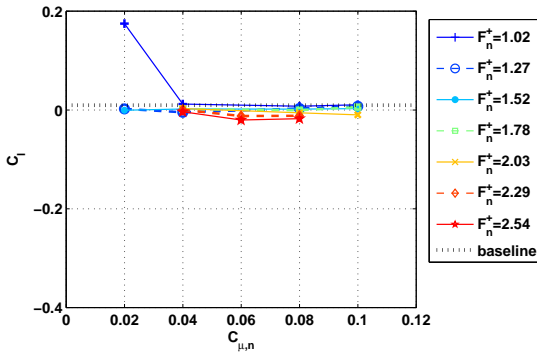


Fig. 4.135: C_l vs. $C_{\mu,n}$, $\delta = 180^\circ$, sym.,
 $\Theta = \pm 110^\circ$, $\Lambda = 60^\circ$, $Re_n = 35000$

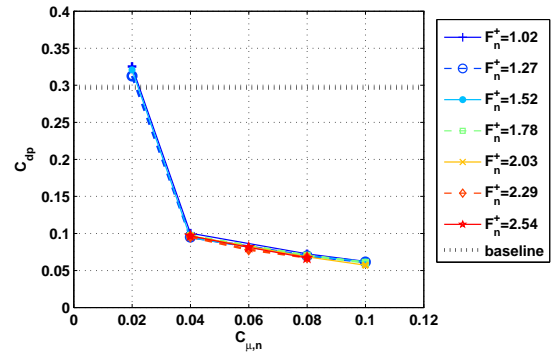


Fig. 4.136: C_{dp} vs. $C_{\mu,n}$, $\delta = 180^\circ$, sym.,
 $\Theta = \pm 110^\circ$, $\Lambda = 60^\circ$, $Re_n = 35000$

4.6.3 Double-sided Actuation with differing Frequencies

The effect of forcing with frequencies differing between both slots on the formation of the coherent structures in the near wake was investigated briefly. The difference in the frequency of the oscillating jets emanating from the slots generates a different number of vortices per unit time at the opposing slots. As these small vortices roll-up in the shear layers in lee of the cylinder the

difference in forcing frequency could affect the meandering of the wake, provided that suitable frequencies are chosen.

Both frequencies were chosen at the upper range of the investigated frequencies ($f_1 = 214\text{Hz}$, $F_n^+ = 2.19$ at the upper side and $f_s = 234\text{Hz}$, $F_n^+ = 2.38$ at the lower side) due to limitations of the computer controlled signal generation. The resulting beat frequency $f_b = f_2 - f_1$ was $F_b = 18\text{Hz}$, approximating the natural shedding frequency of a cylinder at $\Lambda = 0^\circ$ at the corresponding cross flow velocity. The dependence of C_l and C_{dp} on this small difference in frequency is negligible (see figures 4.91 and 4.92).

Because the actuators were coupled by a common back chamber potential distortions of the velocity oscillations emanating from the two slots were minimized by correcting the input signals to the amplifiers for this cross-talk. This was carefully checked by comparing the signals of the internal health-monitoring pressure sensors to the standard case with both rows of actuators operating at identical frequencies. Forcing at $C_{\mu,n} = 7\%$ at the two frequencies (figures 4.137 and 4.138) did not alter the pressure distribution around the cylinder compared to symmetric forcing at a single frequency ($F_n^+ = 1.78$, 175Hz , see figures 4.89 and 4.90) at the same level of excitation.

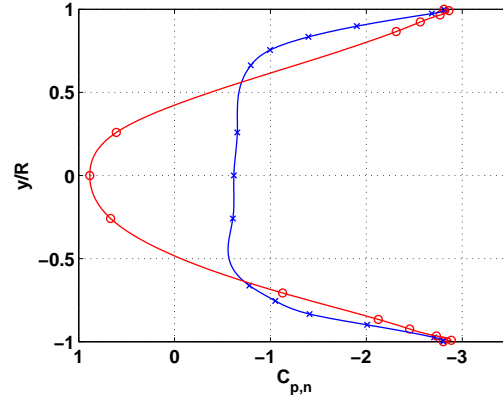
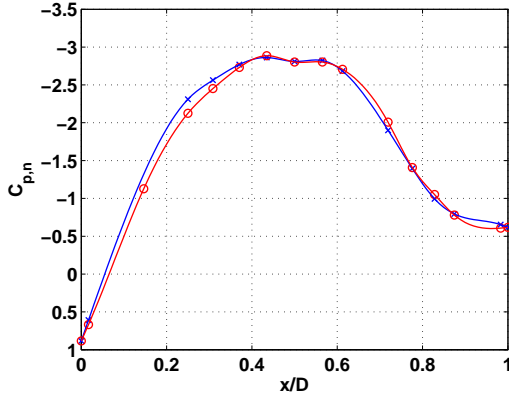


Fig. 4.137: $C_{p,n}$ vs. x/D , bi-frequent actuation, 216Hz & 234Hz, $C_{\mu,n} = 7\%$,
 $C_l = 0.014$, $C_{dp} = 0.118$,
 $\Theta = \pm 110^\circ$, $\Lambda = 60^\circ$, $Re_n = 35000$

Fig. 4.138: y/R vs. $C_{p,n}$, bi-frequent actuation, 216Hz & 234Hz, $C_{\mu,n} = 7\%$,
 $C_l = 0.014$, $C_{dp} = 0.118$,
 $\Theta = \pm 110^\circ$, $\Lambda = 60^\circ$, $Re_n = 35000$

PIV data were acquired phase-locked to the beat frequency. The iso contours of $\frac{\Omega_z D}{U_\infty \cos \Lambda}$ presented in figure 4.139 show a peeling-off vortex pattern similar to the one shown in figure 4.140 for a POD phase $\varphi = -50^\circ$ with forcing at $F_n^+ = 2.29$ and $C_{\mu,n} = 4\%$.

The long-time averaged pressure distribution in figure 4.137 is symmetric, thus the PIV data describes one phase of a meandering wake. This indicates that the similarity between the POD Eigenflow and the phase-locked data taken with forcing at two frequencies is based on the flow physics. It confirms the physical validity of the conditional averages obtained by the POD based analysis of the wake dynamics.

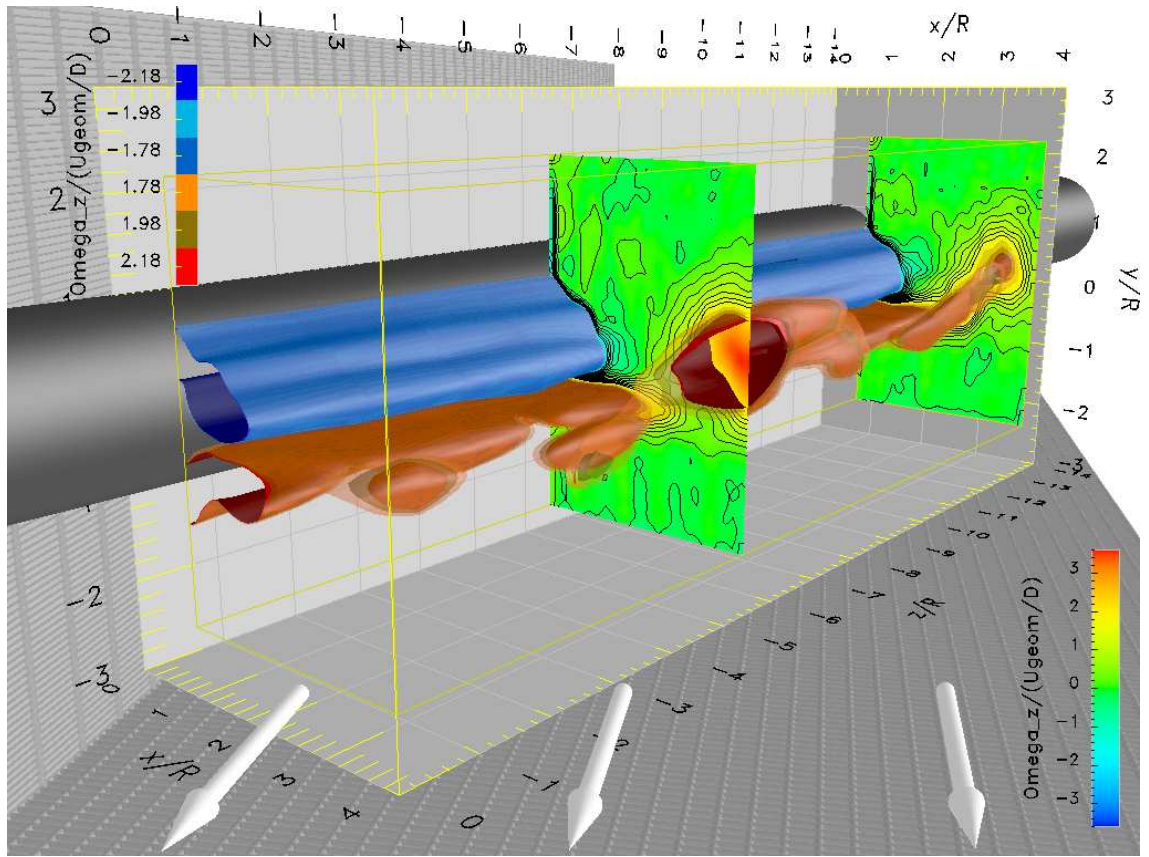


Fig. 4.139: $\frac{\Omega_z D}{U_{\infty} \cos \Lambda}$, bi-frequency @ 216Hz & 234Hz, $C_{\mu,n} = 7\%$, $\Theta = \pm 110^\circ$, $\Lambda = 60^\circ$, $Re_n = 35000$

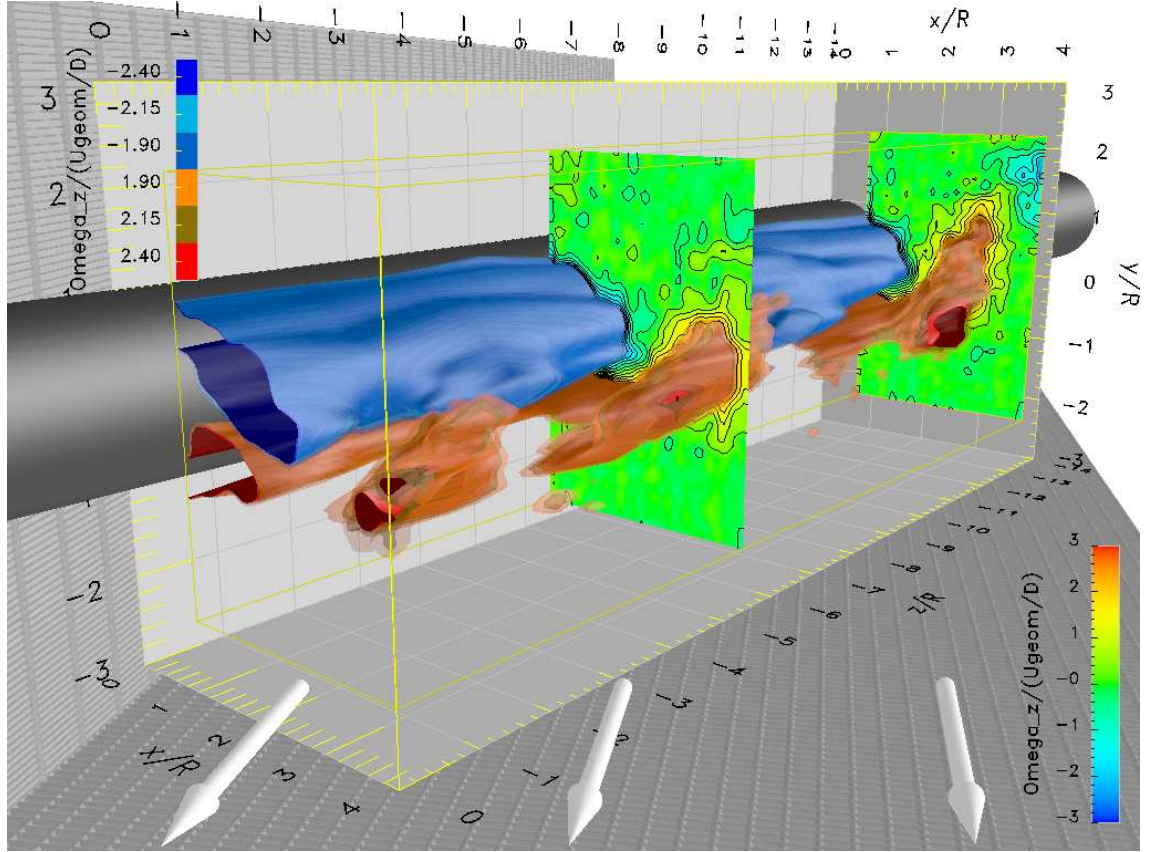


Fig. 4.140: $\frac{\Omega_z D}{U_{\infty} \cos \Lambda}$, $C_{\mu,n} = 4\%$, $\Theta = \pm 110^\circ$, sym., $F_n^+ = 2.29$, $C_{\mu,n} = 4\%$, $\Lambda = 60^\circ$, $Re_n = 35000$

4.7 Baseline

The cylinder was carefully adjusted to obtain a symmetric pressure distribution. Because only one row of pressure taps was available in midspan the symmetry was verified in subsequent experiments, using PIV data taken over 50% of the span of the cylinder. Due to the sensitivity of the adjustment symmetry was checked during the experiments whenever possible. The spanwise uniformity was checked initially with surface flow visualizations.

4.7.1 The Infinite Cylinder

4.7.1.1 Forces on the Cylinder

Baseline data were taken at the beginning and end of a series of experiments dedicated to a given topic of investigation for consistency checking. Therefore data without actuation was acquired with both slots open during all series of symmetric forcing, with one slot taped for asymmetric forcing and with both slots taped for dedicated baseline runs. Representative pressure distributions are shown for two sweep-back angles in figures 4.141 to 4.148. The pressure distributions are presented in two projections for better visual access to the forces on the cylinder. Due to the symmetric character of the baseline configuration lift was negligible in both cases. In the natural, streamwise projection (figures 4.143 and 4.144) it is immediately apparent that the form drag was more than doubled when the sweep-back angle was reduced. For both sweep-back angles the base pressure coefficient agrees well with the form drag C_{dp} .

The distributions are mostly symmetric, the observed asymmetries in the range $0 < x/D < 0.4$ in figure 4.141 might be due to small imperfections of the model. Other possible sources of asymmetry might be small misalignments of yaw or rotation angles and in particular of the wall boundary layer shedding fence. C_l at baseline is for all investigated nominally symmetric configurations negligible.

The form drag differs significantly between the two sweep-back angles. At $\Lambda = 45^\circ$ C_{dp} (determined at a single spanwise location) is increased to approximately 250% of the form drag at $\Lambda = 60^\circ$.

The original pressure distributions were transformed to the cylindrical cross section as presented in figures 4.145 to 4.148 for comparison of C_p distributions taken at different sweep-back angles. For a correct transformation of the pressure distributions to a plane normal to the cylinder, C_p , C_{dp} and C_l values have to be transformed as well to take into account the projection of the reference velocity given by equation 4.5. The transformation reduces the difference in form drag $C_{p,n}$ between $\Lambda = 45^\circ$ and $\Lambda = 60^\circ$ to only 20% due to the transformation of the reference velocities. In contrast to pressure distributions plotted in streamwise direction (elliptical cross section) the data plotted in a plane normal to the cylinder's axis does not allow to estimate the form drag coefficient from the base pressure coefficient.

The suction peak of $C_{p,n} = 1.4$ around $x/D = 0.3$ in figure 4.145 is comparable to the values for $\Lambda = 0^\circ$ (see figure 4.149, page 99) and $\Lambda = 60^\circ$ (figure 4.146). The pressure in the separated region $0.5 < x/D < 0.8$ show a similar trend of slowly dropping toward the trailing edge for both cases. Interesting is the difference in the interval $0.8 < x/D < 1.0$. The distinct pressure drop can be explained for the $\Lambda = 60^\circ$ case by the pair of vortices located aft of the cylinder. These vortices are mostly stationary at a given spanwise location, in contrast to the periodically shed vortices in the two-dimensional configuration. Although the differences seem to be minor in the standard projection of figures 4.145 and 4.146 their significance for the drag becomes clear in the vertical projection presented in figures 4.147 and 4.148. For better comparison the distributions of the different sweep-back angles and the 2-D case are combined in figure 4.150.

It turns out that the characteristics of the base pressure distributions can be predicted by placing two opposite vortices outside a cylinder in a uniform cross-flow and a second pair of opposite signs inside the cylinder. The analytical solution for this potential flow problem was presented by Bickley (in: Zdravkovich [35]). The emerging C_p values depend on the strength of the selected vortices and their location relative to the trailing edge. An example of such simple ideal flow model generated with [12] is shown in figure 4.152. The effect of the vortices on the pressure distribution may be

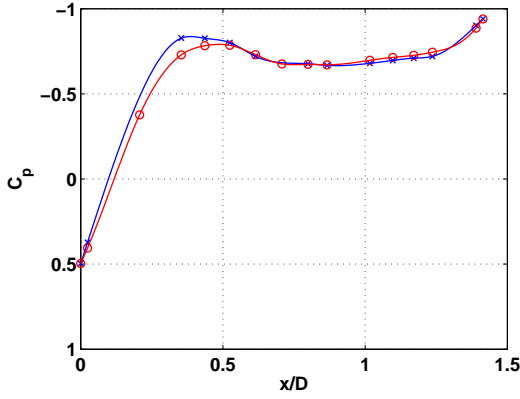


Fig. 4.141: C_p vs. x/D , $\Lambda = 45^\circ$, baseline, $Re_n = 35000$, $C_{dp} = 0.728$

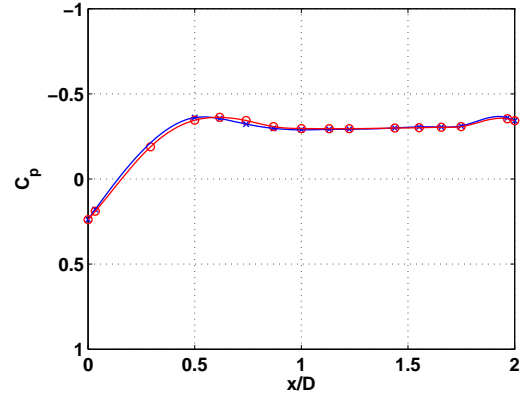


Fig. 4.142: C_p vs. x/D , $\Lambda = 60^\circ$, baseline, $C_{dp} = 0.299$

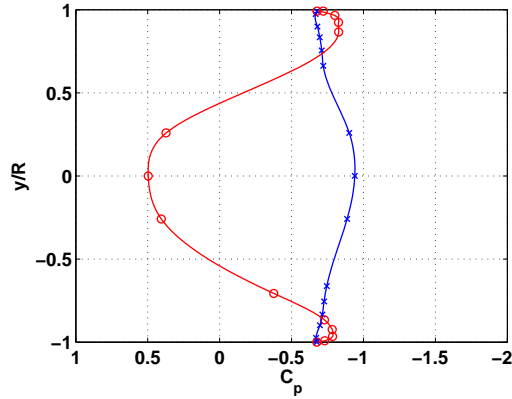


Fig. 4.143: y/R vs. C_p , $\Lambda = 45^\circ$, baseline, $Re_n = 35000$

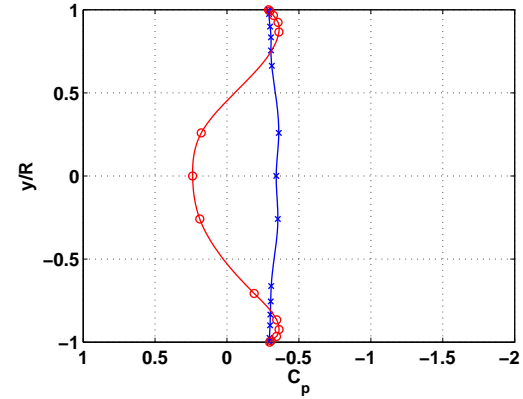


Fig. 4.144: y/R vs. C_p , $\Lambda = 60^\circ$, baseline, $Re_n = 35000$

obtained by subtracting the calculated pressure distribution on the front end of the cylinder from the rear of the cylinder. The so obtained base pressure distribution resembles the one shown in figure 4.150. This approach was used to predict the base pressure of bluff bodies.

Taking into account the differences between the models for the 2-D experiments ($\Lambda = 0$) and those for $\Lambda \neq 0$ it can be safely stated that the differences in $C_{dp,n}$ are acceptable between $\Lambda = 0^\circ$ and $\Lambda = 60^\circ$. The influence of the stationary vortices for $\Lambda = 60^\circ$ is evident, but does not contribute to C_{dp} . The pressure distribution on the lee side of the cylinders is only distorted but the average base pressure remains unaltered. Interesting is the increase in pressure at $y/R = 0$ for $\Lambda = 60^\circ$. This is caused by a (weak) 3-D “stagnation” of the fluid forced towards the cylinder between the stationary vortex pair. Spectra were taken in lee of the cylinder at $\Lambda = 60^\circ$ at the outer boundary of the shear layers but no characteristic frequency was found, supporting the interpretation that the location of the vortex pair is virtually steady.

In contrast to the $\Lambda = 60^\circ$ case a sweep-back angle of $\Lambda = 45^\circ$ caused a significantly increased vortex drag. The difference in drag was $\Delta C_{p,\Lambda} = 0.206$ or more than 16% of the C_{dp} of the 2-D configuration. An explanation for this considerable difference between $\Lambda = 45^\circ$ and the other two sweep-back angles can be found by analyzing the spectra taken aft of the cylinder, presented in figures 4.151. At $\Lambda = 45^\circ$ the vortices in lee of the cylinder are neither shedding nor virtually steady like at the larger sweep-back angle. The spanwise vortices oscillate at a low frequency of approximately 0.5 Hz (see in figure 4.151). This oscillation can only be the result of an unsteady separation of the vortices from the cylinder.

The ratio of Strouhal numbers for the configurations $\Lambda = 0^\circ$ and $\Lambda = 45^\circ$ is close to 40 whereas the drag only varies by a factor of 2.5. This is interesting because for a 2-D circular cylinder the drag is proportional to the inverse of the shedding frequency, the excessive increase can therefore

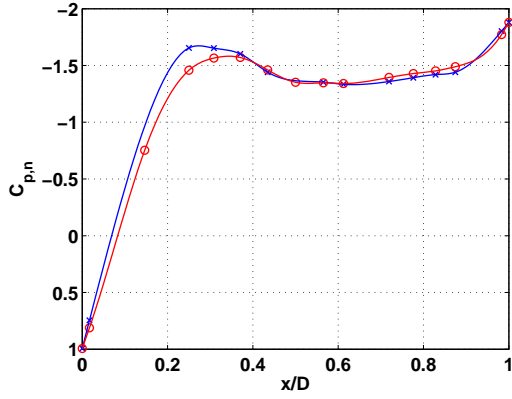


Fig. 4.145: $C_{p,n}$ vs. x/D , $\Lambda = 45^\circ$, baseline, $Re_n = 35000$, $C_{dp,n} = 1.456$

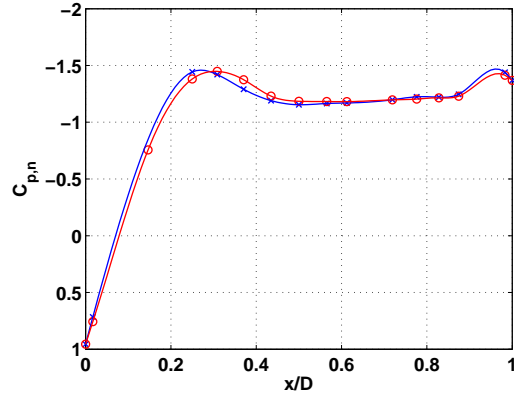


Fig. 4.146: $C_{p,n}$ vs. x/D , $\Lambda = 60^\circ$, baseline, $Re_n = 35000$, $C_{dp,n} = 1.196$

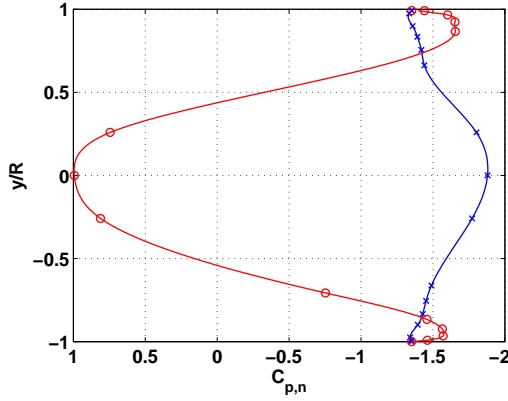


Fig. 4.147: y/R vs. C_p , $\Lambda = 45^\circ$, baseline, $Re_n = 35000$

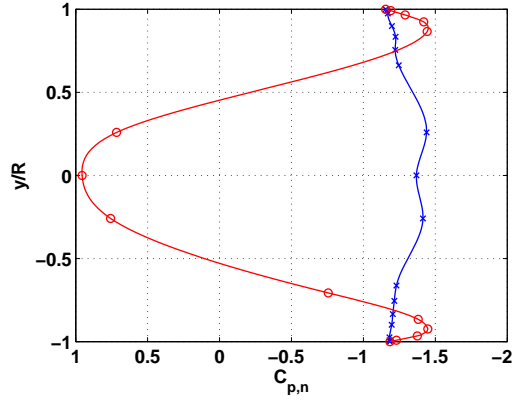


Fig. 4.148: y/R vs. C_p , $\Lambda = 60^\circ$, baseline, $Re_n = 35000$

only be explained by three-dimensional effects. Vorticity is accumulated behind the cylinder and is concurrently convected away. In comparison to the 2-D case the vortices grow therefore over a relatively long time until they finally separate from the cylinder. The separation does not occur homogeneously along the span like in the 2-D case (3-D effects neglected), instead the vortices peel off slowly along the span. This peel-off process becomes quasi stationary for the larger sweep-back angle of $\Lambda = 60^\circ$, but it is obviously instationary for $\Lambda = 45^\circ$.

At $\Lambda = 60^\circ$ vortices peel off the cylinder once they grew to a critical size, further downstream in spanwise direction the process of accumulation of vorticity restarts and a periodicity of vortex peel-off can be observed in spanwise direction. Compared to $\Lambda = 60^\circ$ the convection of vorticity along the span is reduced for $\Lambda = 45^\circ$. At this sweep-back angle the vortices peel off the downstream end of the cylinder after they grew to a critical size. They are displaced into regions of higher streamwise velocity and thus forced away from the cylinder's surface, causing the point of separation to move slowly along the span until its most upstream location is reached, potentially close to the upstream end of the cylinder. It is extremely unlikely that the vortices forming on opposite sides of the cylinder separate synchronously along the span, the slightest imbalance in accumulation of vorticity will result in alternating peel-off process. This interpretation is consistent with all observations presented above. The slow separation of a strong vortex from the cylinder will result in a significant increase of vortex drag, the alternating peel-off results in an overlapping effect of the two vortices in the wake and explains the minimum in $C_{p,n}$ at $y/R = 0$ in figure 4.150.

For a cylinder with larger aspect ratio this scenario might be repeated exactly as described with a slow peel-off along the span from wall to wall, or, depending on the sweep-back angle, a cell-wise peel-off over fractions of the span.

The cylinder is considered to be “infinite”, but actually it is enclosed between the tunnel walls.

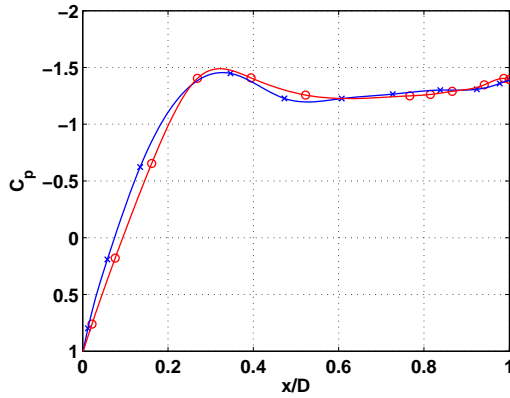


Fig. 4.149: C_p vs. x/D , $\Lambda = 0^\circ$, baseline, $Re_n = 35000$

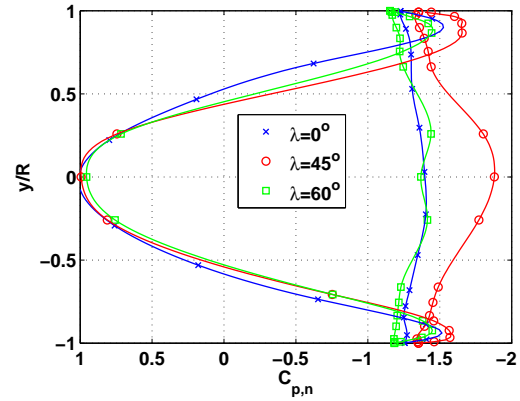


Fig. 4.150: y/R vs. $C_{p,n}$, $Re_n = 35000$, baseline, $\Lambda = 0^\circ$, $\Lambda = 45^\circ$ & $\Lambda = 60^\circ$

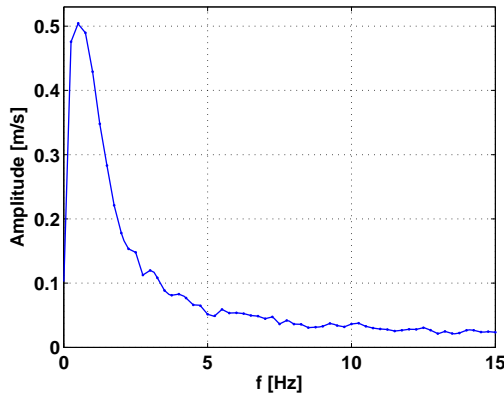


Fig. 4.151: Wake spectrum, $\Lambda = 45^\circ$, baseline, $Re_n = 35000$

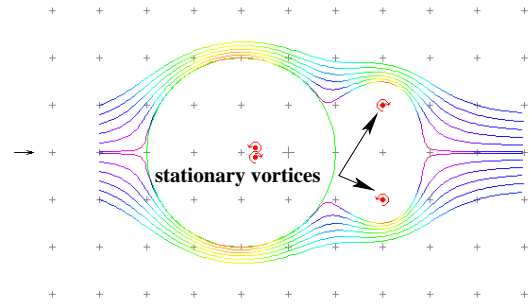


Fig. 4.152: Potential flow, stationary vortices

The upstream wall represents a particular point along the span of the inclined cylinder in the sense that it disturbs the vorticity balance along the span of the cylinder. This is independent of possible disturbances due to the necklace vortex generated at the contact region of cylinder and side wall.

The generation and accumulation of vorticity can start only downstream (in spanwise direction) of the test section wall. Thus the size of the vortices is, among other parameters, determined by the distance from the side wall. The location where the first vortex peels off the cylinder should be determined by this distance, taken a given sweep back angle and velocity. Additionally, the vortices aft of the cylinder are forced away from the cylinder at the downstream end of the cylinder that contacts the opposite test section wall. Vortices that did not grow to a sufficient size and that are still located close to the cylinder are forced to peel off the cylinder and reorient their axes parallel to the free stream. Therefore the end effects on an “infinite” cylinder have to be considered when data are analyzed and interpreted.

4.7.1.2 The Near Wake

To get a brief overview over the coherent structures in the near wake all data were first visualized as described above (pages 14 ff). Experiments indicated that vorticity cannot be not considered to be the most suitable quantity to assess the three-dimensionality of the coherent structures in lee of the cylinder. This is illustrated in figure 3.3, the three-dimensionality of the wake due to vortex peel-off is not apparent. The cores of vortices separating from the cylinder are better described by the minima of the spanwise velocity component W , as illustrated in figures 3.3 and 3.4 by iso-contours of the dimensionless velocity $\frac{W}{U_\infty \sin \Lambda}$. Alternatively $\frac{u'v'}{\sqrt{u'^2}\sqrt{v'^2}}$ was used to visualize the regions of turbulence production and thus high velocity gradients between co-rotating vortices (see figure 3.5). Both quantities enable the tracking of flow structures in the entire investigated

volume.

A combination of $\frac{\Omega_z D}{U_{\infty \cos \Lambda}}$ iso-surfaces and $\frac{W}{U_{\infty \sin \Lambda}}$ contour plots illustrates the good correlation between these two quantities in figure 4.153.

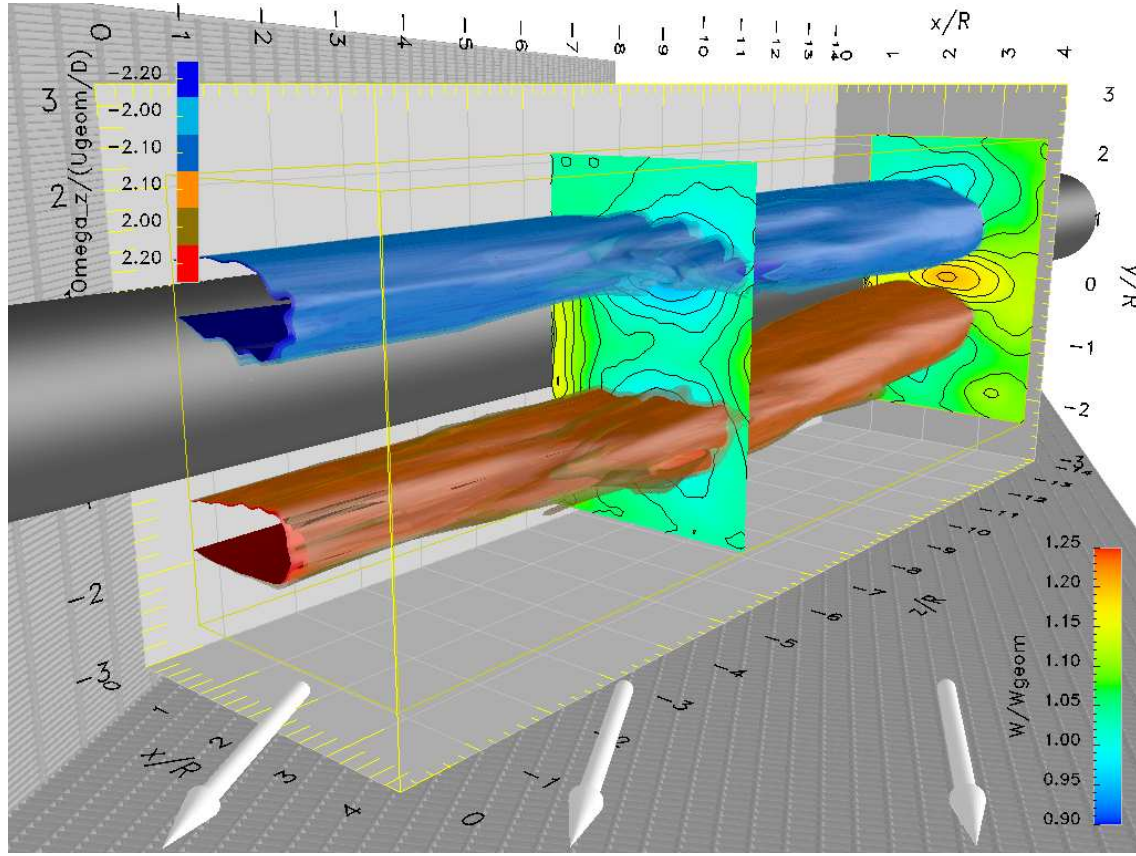


Fig. 4.153: $\frac{\Omega_z D}{U_{\infty \cos \Lambda}}$ (iso-surfaces) and $\frac{W}{U_{\infty \sin \Lambda}}$ (contours), $\Lambda = 60^\circ$, baseline, $Re_n = 35000$

The iso-surfaces in figure 4.153 mark six discrete surfaces of different values of $\frac{\Omega_z D}{U_{\infty \cos \Lambda}}$ in the data volume. The legend for the iso-surfaces is given in the upper left corner of the figure. Three different values per sense of rotation facilitate to estimate of the gradient of vorticity. The interpretation is similar to the contours shown for $\frac{W}{U_{\infty \sin \Lambda}}$ in the 2-D plots. The iso-surfaces are continuous and entirely closed unless intersecting with the boundary of the control volume, as can be seen on the left side where the hollow insides of the shells formed by the iso-surfaces are visible. The two contour plots show the distribution of $\frac{W}{U_{\infty \sin \Lambda}}$ in planes perpendicular to the cylinder. A continuous color bar describing the levels in the contour plots is placed in the lower right.

The good correlation between the two extrema in $\frac{\Omega_z D}{U_{\infty \cos \Lambda}}$ and the minima in $\frac{W}{U_{\infty \sin \Lambda}}$ can be observed easily at the intersection of iso-surfaces and contour plots. Especially on the left plot the minima in $\frac{W}{U_{\infty \sin \Lambda}}$ (blue regions) coincide perfectly with the vortex cores marked by iso-surfaces of $\frac{\Omega_z D}{U_{\infty \cos \Lambda}}$.

Two regions of spanwise velocity visible on the contour plots are of additional interest: On the right plot a region of maximum $\frac{W}{U_{\infty \sin \Lambda}}$ is found between the two counter rotating vortices. Fluid is entrained and then “squeezed” between the vortices and accelerated in spanwise direction. The second region of interest can be observed on the left plane close to the cylinder. A sheet of fluid is accelerated in spanwise direction. This is again caused by entraining fluid between the two vortices and then “squeezing” it in spanwise direction between vortices and cylinder surface. This skewed impinging likely causes the slight increase in base pressure described on page 97 (see figure 4.150).

The shear layers are visible as two thick vortex “sheets” marked by $\frac{\Omega_z D}{U_{\infty \cos \Lambda}}$. They do not show any detailed features. Due to the low-frequent random sampling the individual vortices in the shear layers that separated from the cylinder cannot be resolved in detail. In the zone $z/R < -5$ the

vortex “sheet” extends to larger x/R , but for $z/R < -5$ the coherence in vorticity is decreasing for $x/R > 2$. This is indicated by lower average values and therefore “closing” iso-surfaces. As vortices obviously cannot end in mid-air, the only explanation is a vortex peel-off, causing increased scatter in the location of the vortex cores that diminishes the coherence and thus reduces the average values.

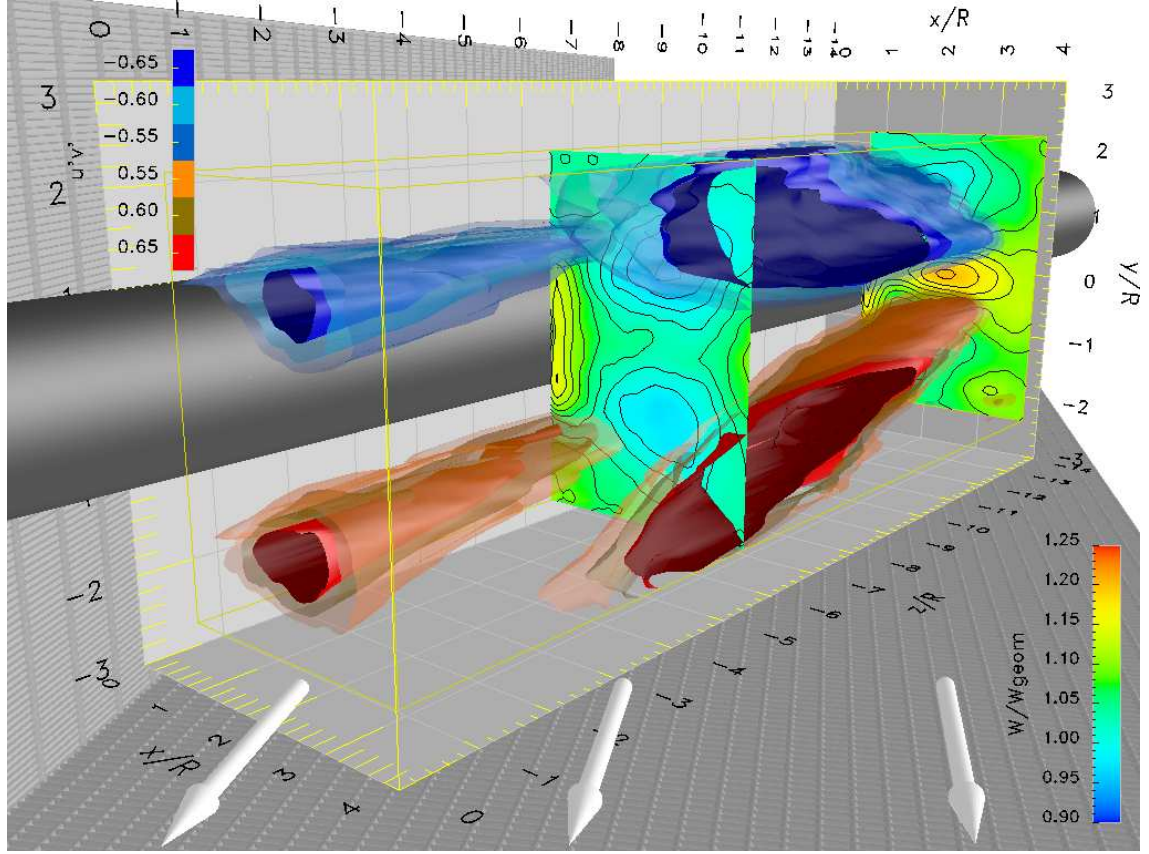


Fig. 4.154: $\frac{\overline{u'v'}}{\sqrt{\overline{u'^2}}\sqrt{\overline{v'^2}}}$ (iso-surfaces) and $\frac{W}{U_{\infty} \sin \Lambda}$ (contours), $\Lambda = 60^\circ$, baseline, $Re_n = 35000$

Contour plots of $\frac{W}{U_{\infty} \sin \Lambda}$ (identical to the ones in figure 4.153) are combined with iso-surfaces of $\frac{\overline{u'v'}}{\sqrt{\overline{u'^2}}\sqrt{\overline{v'^2}}}$ in figure 4.154. A comparison of contour plots and iso-surfaces confirms that maxima of this quantity mark reliably the regions between vortices. In this visualization the vortex peel-off is clearly visible in the entire control volume. The inside of the naturally closed iso-surfaces in figure 4.154 is exposed because all four detected coherent structures are intersecting with boundaries of the visualized volume. Although $\frac{\overline{u'v'}}{\sqrt{\overline{u'^2}}\sqrt{\overline{v'^2}}}$ is not indicating the vortex cores itself, the clear visualization of the spaces between co-rotating vortices is suitable to track their location and spatial development indirectly. It is advantageous compared to visualizations using $\frac{W}{U_{\infty} \sin \Lambda}$ that structures on opposite regions of the wake can be distinguished by the opposite signs of $\frac{\overline{u'v'}}{\sqrt{\overline{u'^2}}\sqrt{\overline{v'^2}}}$. This enables the simple distinction between vortices peeling-off the cylinder in an alternating fashion.

The distribution of $\frac{\Omega_z D}{U_{\infty} \cos \Lambda}$ in the XY-plane at $y/R = -1$ further illustrates that vorticity is not necessarily suitable to track the vortex peel-off (figure 4.155). The lifting vortex can be clearly detected only close to the cylinder. In contrast to this the spanwise peel-off of the vortices is easily traceable in the entire volume using $\frac{W}{U_{\infty} \sin \Lambda}$. The iso-surfaces shown in figure 4.156 were computed in the entire control volume as before, but presented in top-view, not as perspective view as in the 3-D visualizations presented above. The minimum in spanwise velocity (blue) marks the vortex core. The maximum of the spanwise velocity marked in orange visualizes the zones where the

counter-rotating vortices force the entrained fluid to accelerate in spanwise direction. In the top left region fluid is entrained between the vortices and then “squeezed” along the wedge formed between both vortices. In the second region close to the cylinder ($x/R = 1$) fluid is forced to accelerate along the surface of the cylinder.

The fluid motion throughout the entire investigated volume is illustrated in figure 4.157 by means of color coded streamlines (presented as ribbons). The curl of the “stream-ribbons” depicts the local vorticity. At the far end of the cylinder the cores of the vortex pair aft of the cylinder are clearly visible in the contour plot. A second contour plot facilitates the visualization of the orientation of the streamlines close to the downstream end of the cylinder.

Streamlines originating in the XY-plane of the upstream contour plot are drawn in blue. Streamlines originating in the YZ-plane with $y > 0$ and $x = 1$ (top half-plane facing the cylinder) are coded in green and streamlines originating in the YZ-plane with $y < 0$ and $x = 1$ (bottom half-plane) in red.

The data were randomly sampled averaged and thus are “frozen in time”. Therefore streamlines and particle paths coincide. This special situation justifies the selected nomenclature. Only then streamlines can be interpreted as paths of fluid particles entering the control volume from the respective sides: blue from the upstream end, green from above the cylinder and red from below it. Most of the fluid entering at the upstream side is swept through the investigated volume parallel to the cylinder. The top vortex ($\frac{\Omega_z D}{U_\infty \cos \Lambda} < 0$) is mainly formed by fluid crossing the plane above the cylinder (green), visible as a “bundle” of “green streamline” on the left side. Accordingly the bottom vortex consists mostly of fluid entering through the plan below the cylinder. The wake is relatively wide and the spanwise motion in it is pronounced.

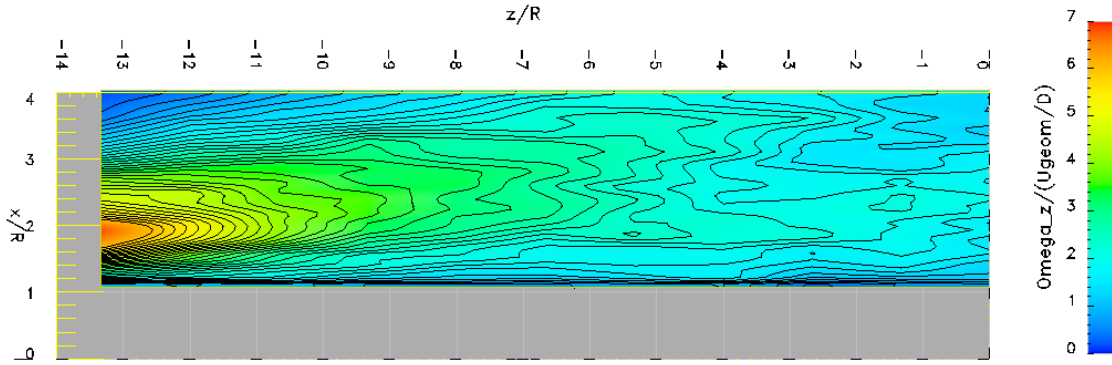


Fig. 4.155: baseline, $\frac{\Omega_z D}{U_\infty \cos \Lambda}$ contours, top view, $\Lambda = 60^\circ$, baseline, $Re_n = 35000$

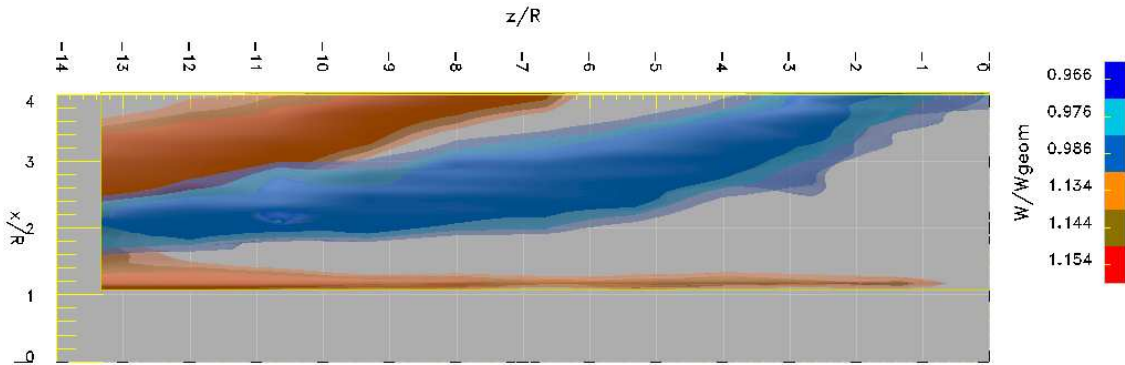


Fig. 4.156: $\frac{W}{U_\infty \sin \Lambda}$ iso-surfaces, top view, $\Lambda = 60^\circ$, baseline, $Re_n = 35000$

The PIV data were analyzed quantitatively by integrating different quantities over the entire cross-section (XY-planes) for every spanwise position z/R . The circulation was computed for both sides of the wake independently. To do so the wake was first bisected by determining the minimum of U for each x/R in the averaged data. Based on the identified center of the wake, the vorticity Ω_z was integrated separately for both sides. Consistent with the vortex peel-off described in figures

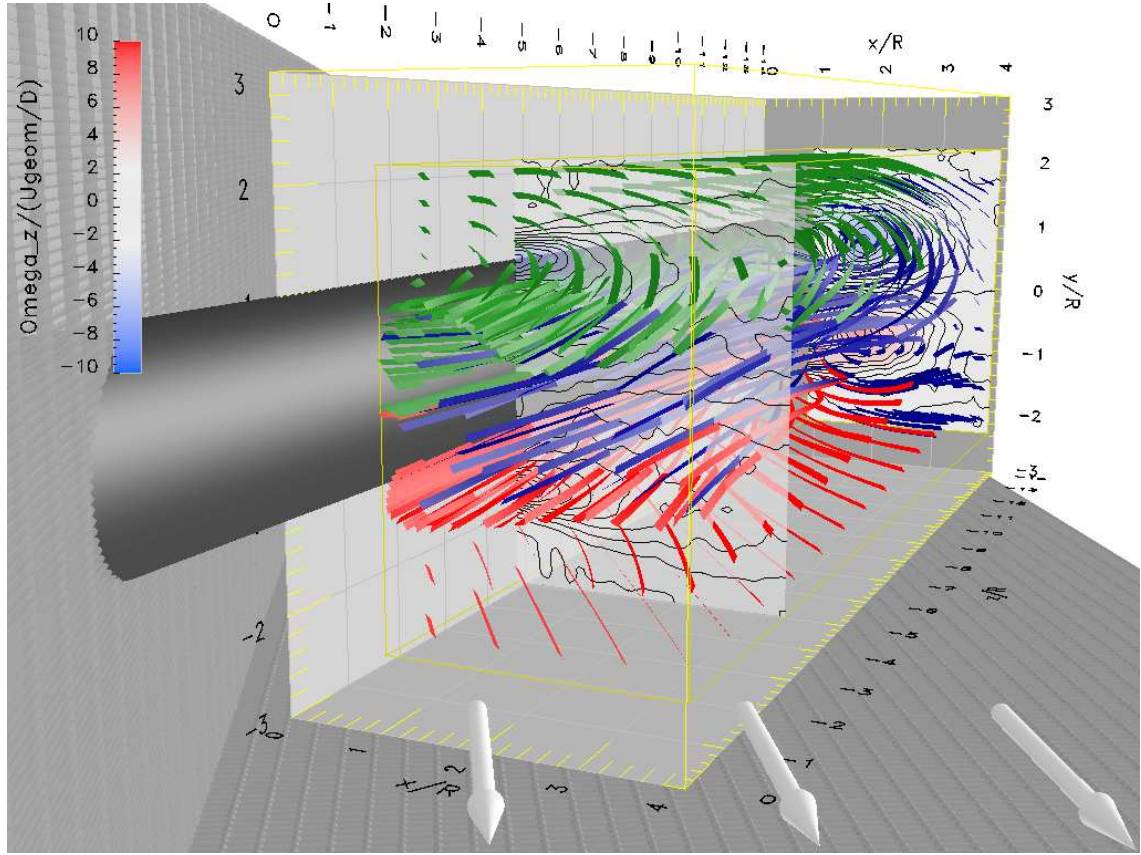


Fig. 4.157: Streamlines and $\frac{\Omega_z D}{U_\infty \cos \Lambda}$ contours, $\Lambda = 60^\circ$, baseline, $Re_n = 35000$

4.154 and 3.4 the dimensionless circulation $\frac{\Gamma_z}{U_\infty \cos \Lambda R}$ decreases along the span (see figure 4.158). The peel-off process is nearly symmetric for top and bottom sides of the wake.

The spanwise velocity component decreases as well over most of the span. It is presented in figure 4.159 as flow rate per area, $\frac{\dot{V}_z}{A_{xy} U_\infty}$. The reduction of the spanwise flow seems to contradict the observation that a minimum in W is found in the vortex cores. Therefore rather an increase in W should be detected in spanwise direction. A closer look at figure 4.156 resolves this disagreement. Together with the minimum of $\frac{W}{U_\infty \sin \Lambda}$ in the vortex cores the maximum of the dimensionless spanwise velocity found on the outside of the vortex pair is moving out of the investigated volume. Both effects nearly compensate each other. The decrease by approximately 3.5% in the axial velocity along the span is therefore considered negligible.

The X-component x_c as defined in equations 4.8 on 47 of the center of vorticity (compare figure 4.160) is increasing until the midspan of the investigated volume. For $z/R > -6$ x_c started to decrease. This matches well with the observed vortex peel-off. As might be seen in figure 4.155 in the bottom right, vorticity accumulation restarts close to the cylinder, while the peeled-off vortex pair is leaving the control volume. The horizontal distance x_c is decreasing as soon as the strength of these vortices is not negligible any more.

The maximum displacement of the center of vorticity along the cylinder is in X-direction $0.4 R$, in Y-direction (see figure 4.161) it is $0.2 R$. The vortices peel-off in X-direction and leave the control volume entirely, thus the larger value of x_c . However, the extrema of the location of the vortices in Y-direction is limited by the diameter of the cylinder. Additionally, the newly forming vortex is forced away from the cylinder in Y-direction by the velocity induced on it by the vortex that peeled-off upstream (in spanwise direction). Thus the Y-distance keeps on increasing over a longer portion of the peel-off cycle than the X-distance. Although the “center of vorticity” provides only a rough estimate for determining the location of vortices, it proved to be a valid procedure for basic analysis of the near wake.

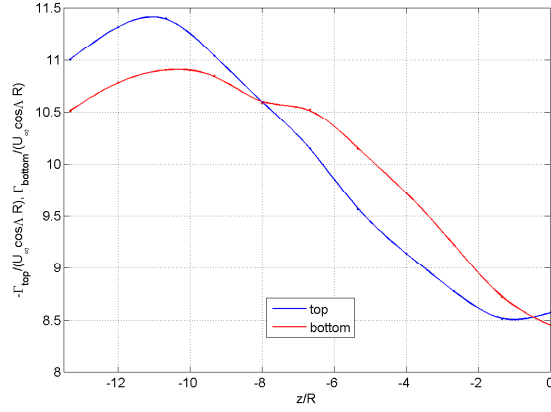


Fig. 4.158: $\frac{\Gamma_z}{U_{\infty} \cos \Lambda R}$ vs. z/R , $\Lambda = 60^\circ$, baseline, $Re_n = 35000$

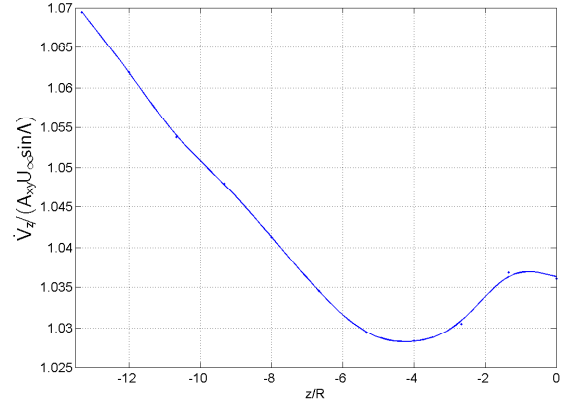


Fig. 4.159: $\frac{\dot{V}_z}{A_x U_{\infty} \sin \Lambda}$ vs. z/R , $\Lambda = 60^\circ$, baseline, $Re_n = 35000$

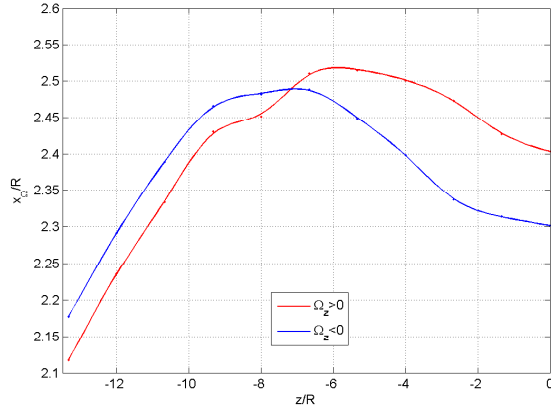


Fig. 4.160: Center of Ω_z , X coordinate, $\Lambda = 60^\circ$, baseline, $Re_n = 35000$

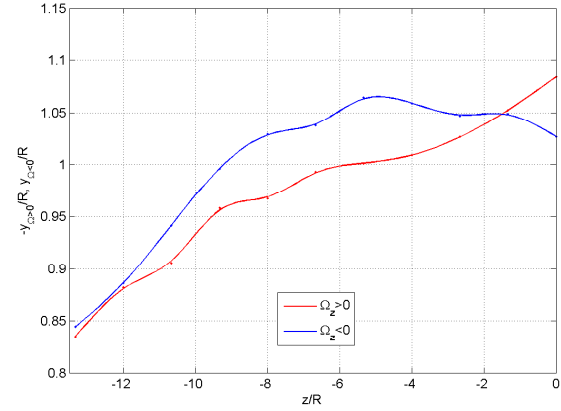


Fig. 4.161: Center of Ω_z , Y coordinate, $\Lambda = 60^\circ$, baseline, $Re_n = 35000$

Based on literature [35] and the fact that it was not possible to detect any characteristic frequencies for $\Lambda = 60^\circ$ it was assumed so far that the coherent structures in the near wake of the inclined cylinder are quasi-stationary. On the other hand it is obvious that the location of these structures oscillates around a mean value if $\frac{u'v'}{\sqrt{u'^2}\sqrt{v'^2}}$ can be used as a criterion to describe the peel-off process. This motion of the vortices cannot be assessed by standard PIV data processing. The low sampling rate of only 6Hz does not allow any true temporal analysis the field information obtained by PIV, nevertheless the PIV data provided an excellent base for the advanced data processing described below.

In a first step the velocity component on opposite sides of the wake were correlated. The Y-coordinate of the center of the wake was determined for all x values as described above. Then for each velocity component the cross correlation at opposite locations was computed with respect to the center of the wake. The spatial distribution of this correlation is presented for W in figure 4.162. Iso-surfaces and contour plot both show the cross correlation $\frac{w'_{top} w'_{bottom}}{\sqrt{w'^2_{top}} \sqrt{w'^2_{bottom}}}$. The red band in the contour plots represents the center of the wake. The visualized structures follow the location of the vortex cores identified before. They grow along the span in size and magnitude, indicating that the fluctuations increase with growing distance from the cylinder's surface. The negative correlation of $\frac{w'_{top} w'_{bottom}}{\sqrt{w'^2_{top}} \sqrt{w'^2_{bottom}}} \leq -0.6$ indicates clearly that the vortex cores oscillate in anti-phase in spanwise direction. These newly detected dynamics require further detailed analysis.

4.7.1.3 Near Wake Dynamics

After the coherent motion of the vortex cores was clearly detected by correlation, the PIV data were further analyzed by Proper Orthogonal Decomposition (see page 17) to assess the details of

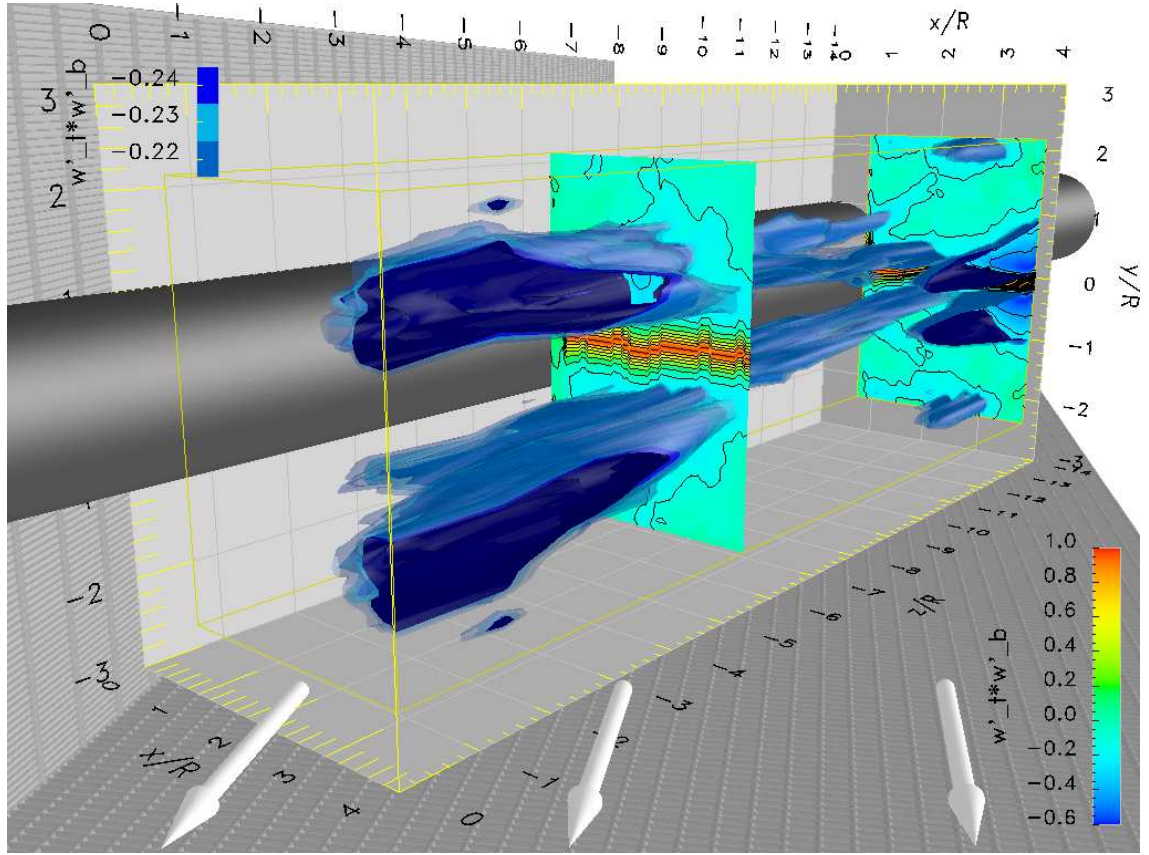


Fig. 4.162: Correlation of w' across the wake, $\frac{w'_{top} w'_{bottom}}{\sqrt{w'^2_{top}} \sqrt{w'^2_{bottom}}}$, $\Lambda = 60^\circ$, baseline, $Re_n = 35000$

the dynamics of the coherent structures in the near wake. For the baseline case the turbulent kinetic energy contained in the first mode was around 30% (see figure 4.163). A minimum of 50% of the turbulent kinetic energy was contained in the first 4-6 modes for all of the 11 baseline data sequences (figure 4.164) acquired along the span. Based on the first POD Eigenflow, phases were computed for every individual data set in the sequence as explained in detail on page 19. According to these POD phases the data sequences were divided into 19 classes. A typical histogram for this distribution is shown in figure 3.7.

In figures 4.165 to 4.167 iso-surfaces of the spanwise velocity component $\frac{w}{U_\infty \sin \Lambda}$ illustrate the spatial and temporal evolvement of the vortices peeling off the cylinder based on the POD phases. Data are presented for the representative phases $\phi = -40^\circ$, $\phi = 0^\circ$ and $\phi = 40^\circ$. Low values of $\frac{w}{U_\infty \sin \Lambda}$ are presented in blue, large ones in red. The “open” iso-surfaces indicate an intersection of the visualized structures with the boundaries of the control volume. The red maximum intersects over its entire length with the YZ-plane at $x/R = 4$. The blue minima intersect with the same plane for $z/R > 5$ and additionally with the XY-plane at the downstream end.

The magnitude of the spanwise velocity component varies significantly over the presented range of ϕ . The wake is deflected downwards at the POD phase of $\phi = -40^\circ$. The lower vortex (blue, $y/R < 0$) is grown to its maximum size, pushing the region with increased spanwise velocity (red) to $y/R > 0$. The upper vortex shrunk and is stretched between the lower vortex (blue) and the cylinder’s surface, thus its spanwise velocity component cannot be detected at this iso-level at $z/R > -10$. Both vortices are approximately balanced at a POD phase angle of $\phi = 0^\circ$, the structure of the wake correspond to the averaged wake (compare figure 3.4 on page 16, notice the different iso-levels). The two vortices are significantly weaker than in their most pronounced states. The pattern of coherent structures at $\phi = 40^\circ$ mirrors the situation found at $\phi = -40^\circ$. At this POD phase angle the upper vortex (blue, $y/R > 0$) is dominant and the maximum in spanwise velocity is displaced towards $y/R < 0$. Both spanwise vortices are quasi stationary during this cycle in the peel-off process although their magnitude fluctuates significantly. The fact that the

position of the vortices seems to be virtually static agrees well with literature [29]. Nevertheless the spanwise oscillations contradict the model that the vortices peeling-off in lee of an inclined cylinder are quasi-static. A possible explanation for the fluctuations lies in the deficit of spanwise velocity

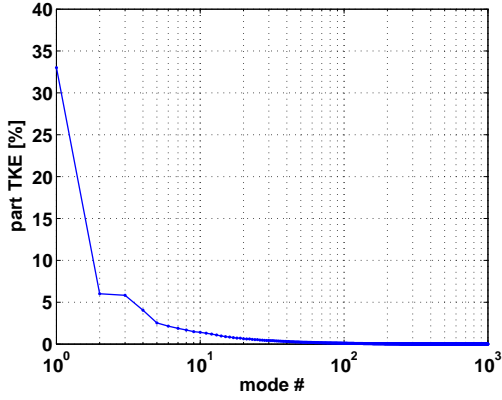


Fig. 4.163: POD Eigenvalues,
 $\Lambda = 60^\circ$, baseline, $Re_n = 35000$

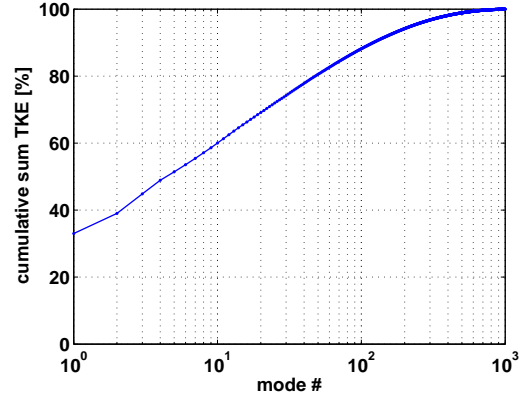


Fig. 4.164: POD Eigenvalues, cumulative sum,
 $\Lambda = 60^\circ$, baseline, $Re_n = 35000$

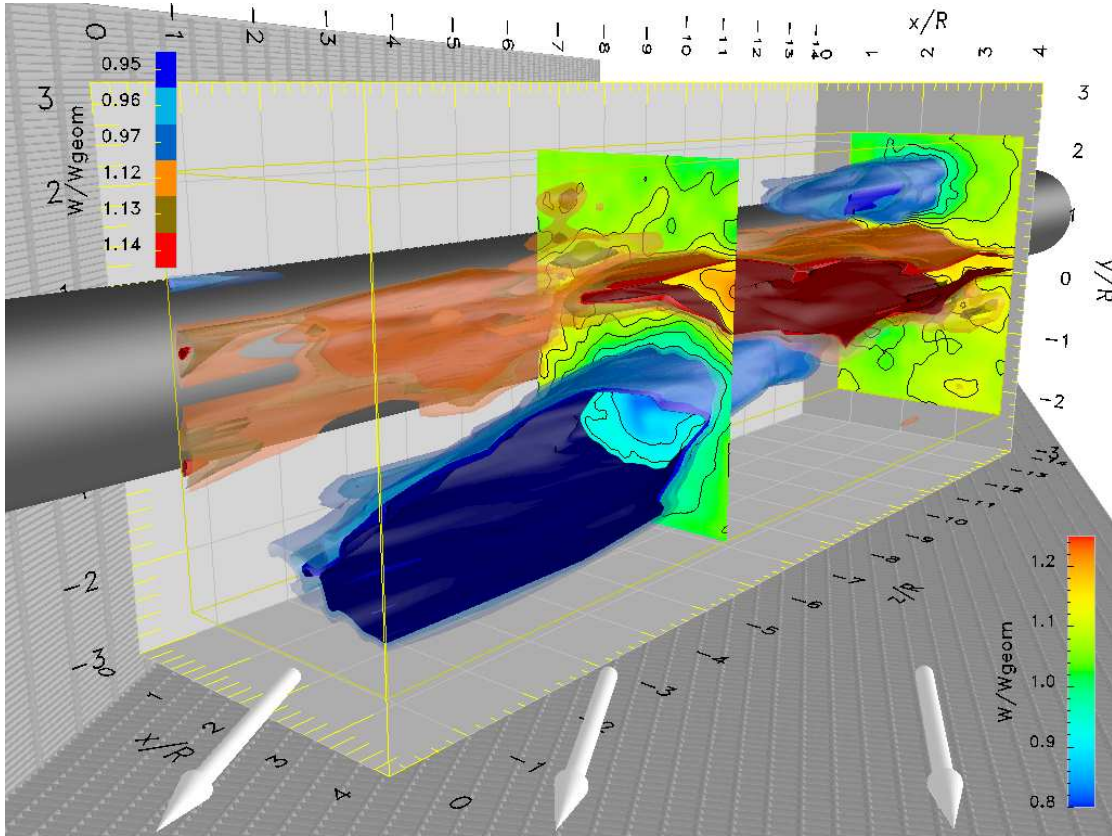


Fig. 4.165: Iso-surfaces of $\frac{W}{U_\infty \sin \Lambda}$, POD $\phi = -40^\circ$, $\Lambda = 60^\circ$, baseline, $Re_n = 35000$

in the vortex cores. The larger the vortices are the larger is the deficit in W , and therefore the less vorticity is convected along the cylinder. Thus the growth rate of the vortices should correlate positively with their size until a critical size is reached. The vortices can grow only to this critical size. Concurrently to the accumulation of vorticity the location of the vortices is altered by vortex induction.

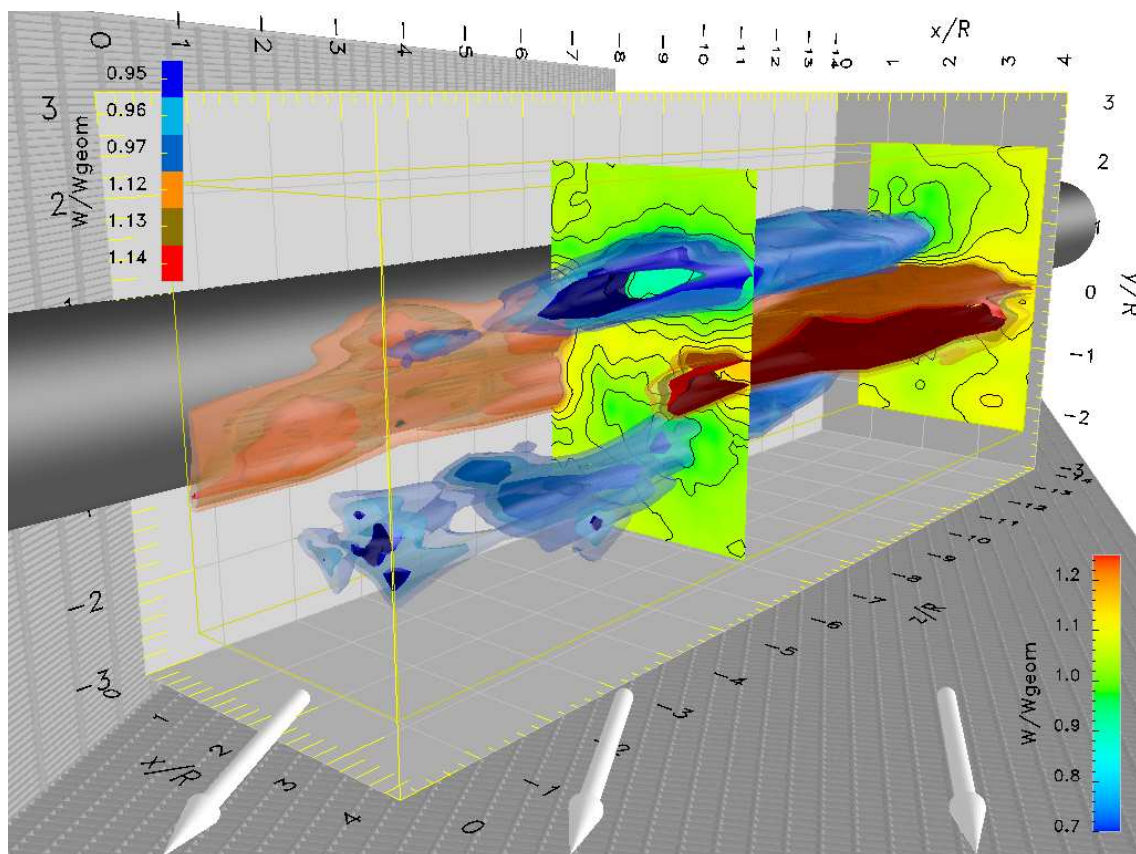


Fig. 4.166: Iso-surfaces of $\frac{W}{U_{\infty} \sin \Lambda}$, POD $\phi = 0^\circ$, $\Lambda = 60^\circ$, baseline, $Re_n = 35000$

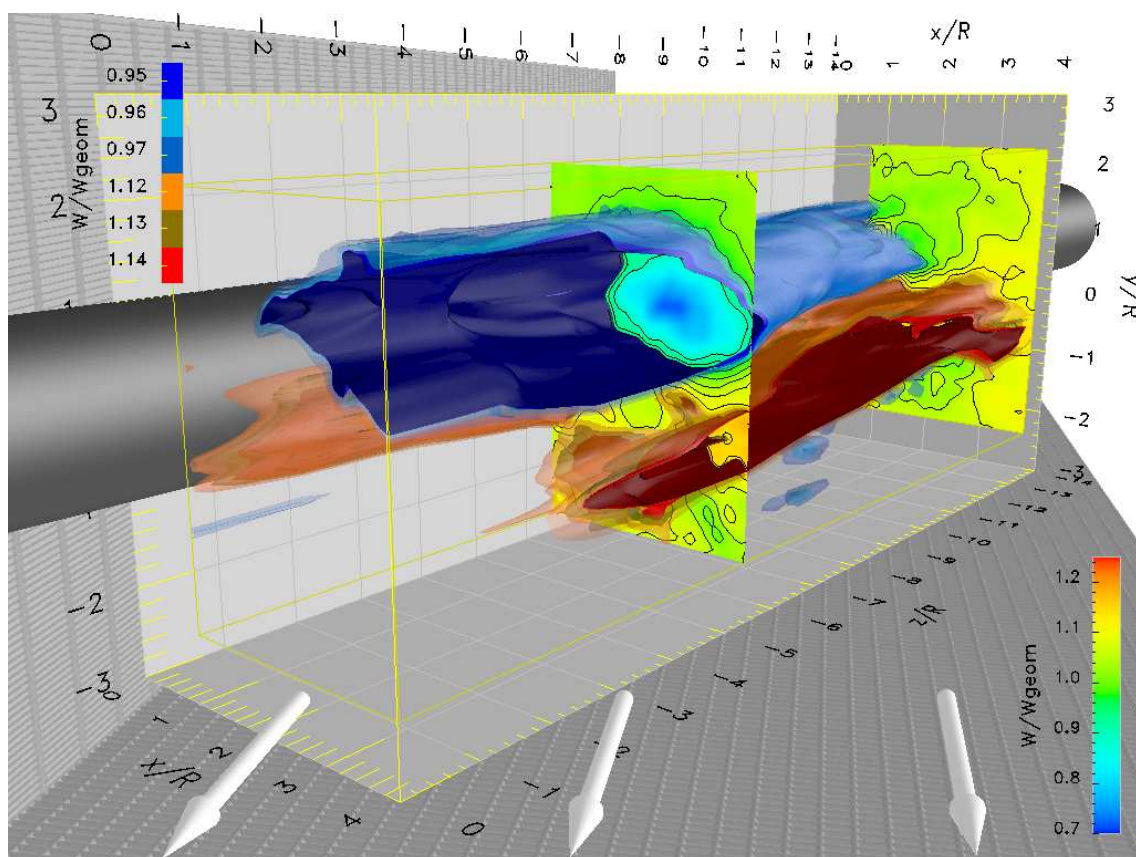


Fig. 4.167: Iso-surfaces of $\frac{W}{U_{\infty} \sin \Lambda}$, POD $\phi = 40^\circ$, $\Lambda = 60^\circ$, baseline, $Re_n = 35000$

The dominant vortex induces on the vorticity accumulated on the opposite side of the wake and pushes it closer to the cylinder's surface. During this process the smaller vortex is stretched between the larger one and the cylinder's surface and fluid is accelerated along the span. Therefore it is not detected in the visualizations using iso-surfaces of the spanwise velocity component. The smaller vortex, displaced towards the cylinder, pushes in return the larger vortex from towards the free stream, i.e. larger velocities. This causes an increased rate of convection along the span and the larger vortex begins to shrink, it is "drained" by the free stream. Once it reaches a size that can no longer provide the induction to keep the other vortex close to the cylinder the process is reversed and the vortex on the opposite side starts to grow. In contrast to the vortex shedding on a 2-D cylinder the vortices in lee of an inclined cylinder oscillate only by a fraction of a diameter of such a vortex around a mean position. The peel-off location is quasi-stationary, but the strength of the vortices fluctuates considerably.

The iso-surfaces of $\frac{W}{U_\infty \sin \Lambda}$ presented in figures 4.168 to 4.170 confirm the constant peel-off angle of the vortices. Different from the perspective presentation before, the iso-surfaces are shown from the top, the cylinder, tunnel wall and floor were removed. The horizontal and vertical position of the vortices (blue) very close to the cylinder vary by less than $\pm \frac{R}{2}$. This is visible at the intersection of the blue iso-surface marking the top vortex and the upstream contour plot in figures 4.165 to 4.167, and for the horizontal displacement on the left side of figures 4.168 to 4.170. The position of the maximum spanwise velocity (red) moves mostly vertically. The stronger lower vortex in figure 4.165 forces the maximum in $\frac{W}{U_\infty \sin \Lambda}$ up to a position of $y/R = 1$ at $z/R = -4$, visible at the intersection of the red iso-surfaces and the contour plot at $z/R = -4$. During the complementary phase shown in figure 4.167 this displacement is reversed to $y/R = -1$.

Instead of the alternating vortex shedding perpendicular to the vortex cores behind the two-dimensional cylinder the fluctuations in the wake at $\Lambda = 60^\circ$ are caused by an oscillation, mainly in direction of the vortex core, causing and alternating strengthening and weakening of the vortices at only small movements perpendicular to the vortex axes. To quantify this oscillation Γ_z was calculated individually for both sides of the wake, as described on page 102 and plotted over the spanwise position. The dimensionless circulation $\frac{\Gamma_z}{U_\infty R}$ presented in figures 4.171 and 4.172 fluctuates indeed by a maximum of approximately 50% of the average value. Vortices on opposite sides of the wake oscillate with 180° phase delay, as can be seen by comparing the color coded curves for different POD phases angles ϕ in both figures. The maximum fluctuation is located at $z/R = -7$. Up to this location negative vorticity is accumulated in the upper part of the wake. From this location onwards the large negative vortex exits the interrogated control volume, thus the circulation decreases again.

The graphs for different φ cross over at approximately $z/R = -2$ in both figures. This is caused by the second (in spanwise direction inside the control volume) vortex that forms at the downstream end of the cylinder, similar to the alternating vortex peel-off from opposite sides described for asymmetric forcing. Once a vortex is peeling-off, vorticity is accumulated downstream of the peel-off location and a new vortex is formed. If the vortex located upstream in spanwise direction is weak it accumulates vorticity at a relatively low rate. Thus the vorticity remains closer to the surface of the cylinder (it is not being "wrapped up"), is convected along the span and incorporated into the vortex downstream of the first one. Therefore a weak upstream vortex ($\varphi < 0$ in figure 4.171) causes an increased growth rate in the downstream vortex.

The total circulation (sum of the absolute values) for the individual POD phases in figure 4.173 follows approximately the curve of the average circulation (figure 4.158). This confirms that the peel-off location moves only little in spanwise direction. The oscillations are nearly symmetric in magnitude, as the difference between the circulation of both sides (difference of the absolute values) presented in figure 4.174 reveals. Around $z/R = -2$ the difference in Γ_z vanishes for all phases and all curves cross over. This is caused by a new pair of vortices that begins to form close to the cylinder upstream of this spanwise location, as discussed above. The maximum difference between the individual POD phases is located around $z/R = -7$. This is approximately the spanwise location where the peeling-off vortices exit the control volume therefore the magnitude of the circulation starts to decrease significantly in spanwise direction. The fluctuations of the difference in circulation with the POD phase angle are with $\pm 75\%$ of the average value considerable.

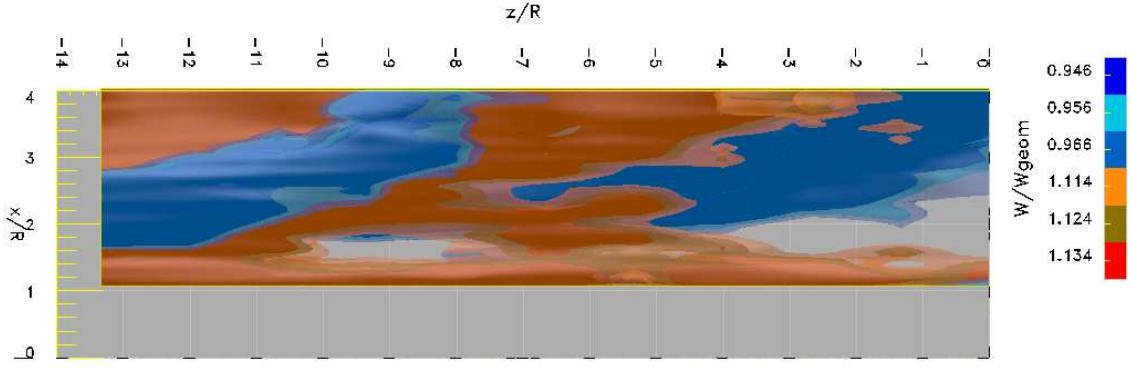


Fig. 4.168: Iso-surfaces of $\frac{W}{U_{\infty} \sin \Lambda}$, POD $\phi = -40^\circ$, top view, $\Lambda = 60^\circ$, baseline, $Re_n = 35000$

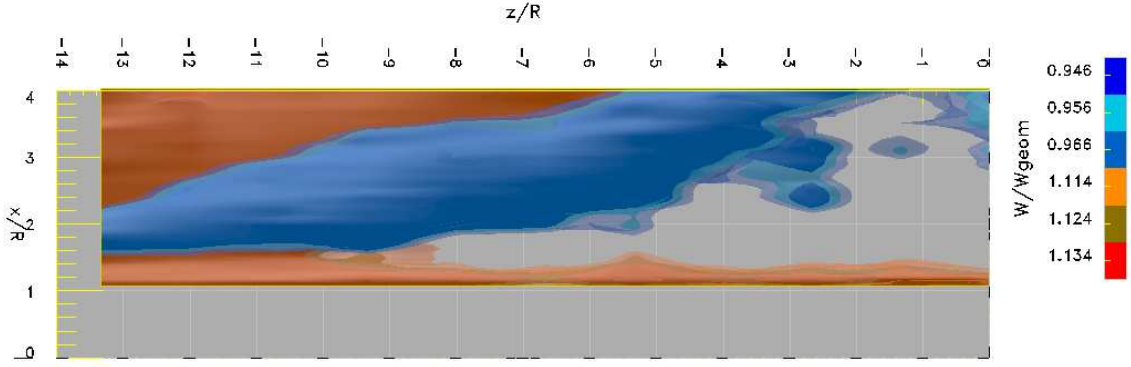


Fig. 4.169: Iso-surfaces of $\frac{W}{U_{\infty} \sin \Lambda}$, POD $\phi = 0^\circ$, top view, $\Lambda = 60^\circ$, baseline, $Re_n = 35000$

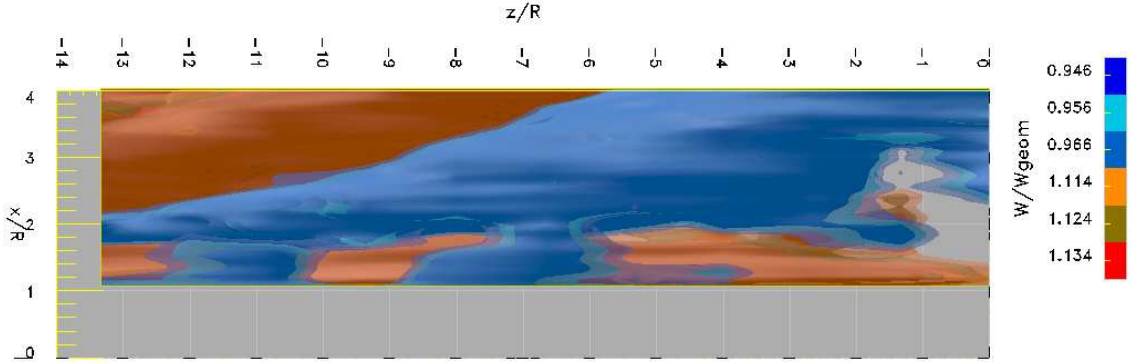


Fig. 4.170: Iso-surfaces of $\frac{W}{U_{\infty} \sin \Lambda}$, POD $\phi = 40^\circ$, top view, $\Lambda = 60^\circ$, baseline, $Re_n = 35000$

The total average spanwise velocity (see figure 4.175) does not vary significantly between the different phases and follows again the average curve presented above. Deviations from the average curve were found for some larger POD phases. This is considered to be caused by insufficient numbers of data sets entering the average. Comparison of figures 4.171 and 4.176 confirms a phase delay of 180° between Γ_z and spanwise velocity. The spanwise velocity computed for the upper part of the wake depends on the POD phase angle φ , in contrast to the mean spanwise velocity. This confirms the observations and interpretation of the results presented in figures 4.165 to 4.167.

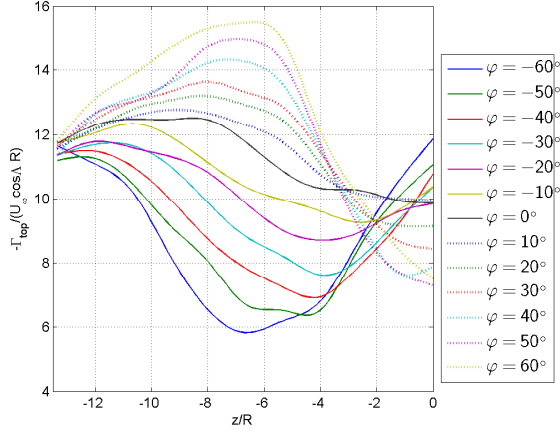


Fig. 4.171: $\frac{\Gamma_{z,top}}{U_{\infty} \cos \Lambda R}$ vs. z/R , $\Lambda = 60^\circ$, baseline, $Re_n = 35000$

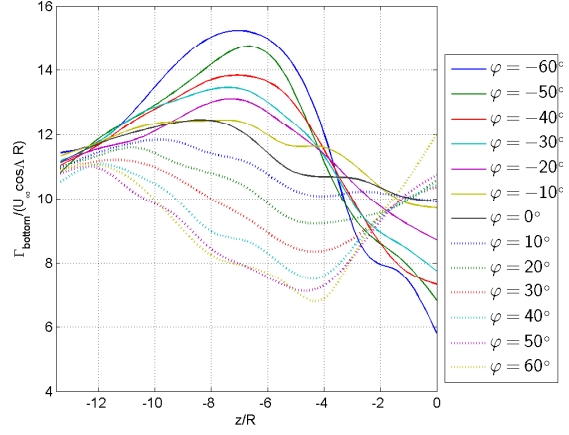


Fig. 4.172: $\frac{\Gamma_{z,bottom}}{U_{\infty} \cos \Lambda R}$ vs. z/R , $\Lambda = 60^\circ$, baseline, $Re_n = 35000$

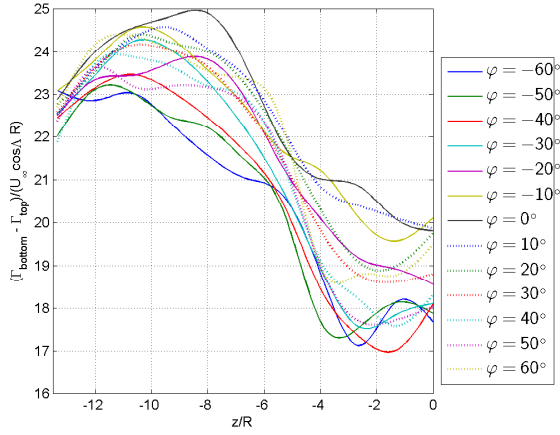


Fig. 4.173: $\frac{\Gamma_{z,total}}{U_{\infty} \cos \Lambda R}$ vs. z/R , $\Lambda = 60^\circ$, baseline, $Re_n = 35000$

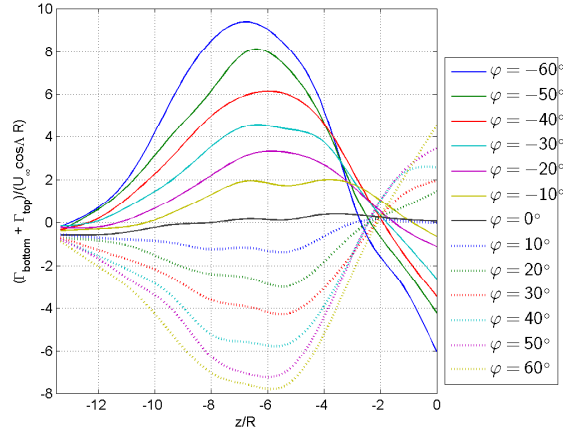


Fig. 4.174: $\frac{\Gamma_{z,diff}}{U_{\infty} \cos \Lambda R}$ vs. z/R , $\Lambda = 60^\circ$, baseline, $Re_n = 35000$

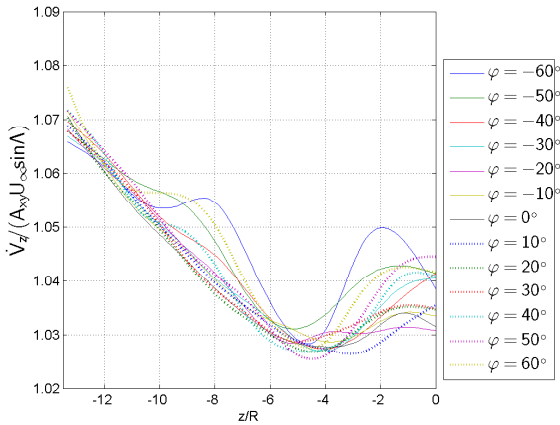


Fig. 4.175: $\frac{\dot{V}_z}{A_{xy} U_{\infty}}$ vs. z/R , $\Lambda = 60^\circ$, baseline, $Re_n = 35000$

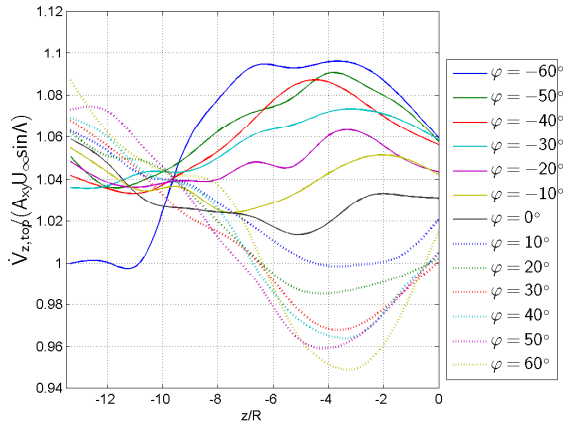


Fig. 4.176: $\frac{\dot{V}_{z,top}}{A_{xy} U_{\infty}}$ vs. z/R , $\Lambda = 60^\circ$, baseline, $Re_n = 35000$

The motion of the center of $\Omega_z > 0$ (see equations 4.8 (page 47) with the POD phase angle at different spanwise stations is presented in figure 4.177. The black circles mark the largest downward deflection of the wake at the most negative POD phase angle. In this case this is counter-intuitive at first sight because for most spanwise stations the black circles are located at the top-most location in figure 4.177. This is due to the fact that the reference phase angle is determined at the downstream end of the cylinder. The expected bottom-most location is found for $z/R > -4$, as defined on page 19 for the consistency check of the phase angle. The phase angle is determined with φ at $z/R = 0$ as reference, based on the continuity of the spanwise motion. In this case the direction of the oscillations of the wake vary along the span, thus the wake is meandering in a twisting motion with a 180° phase delay between the opposing ends of the control volume. This can be confirmed by taking iso-contours of $\frac{U}{U_\infty \cos \Lambda}$ to visualize the orientation of the wake (figure 4.178). The distortion of the wake along the span is caused by induction from the peeling-off vortices. The location of the center of vorticity varies by a maximum of $\pm 0.5R$ in Y-direction and $\pm 0.75R$ in X-direction. This is less than 50% of the maximal diameter of the vortices at the downstream end of the control volume.

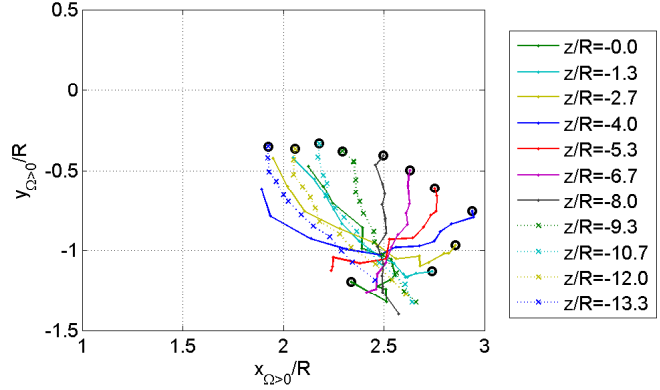


Fig. 4.177: Center of Ω_z , $\Lambda = 60^\circ$, baseline, $Re_n = 35000$

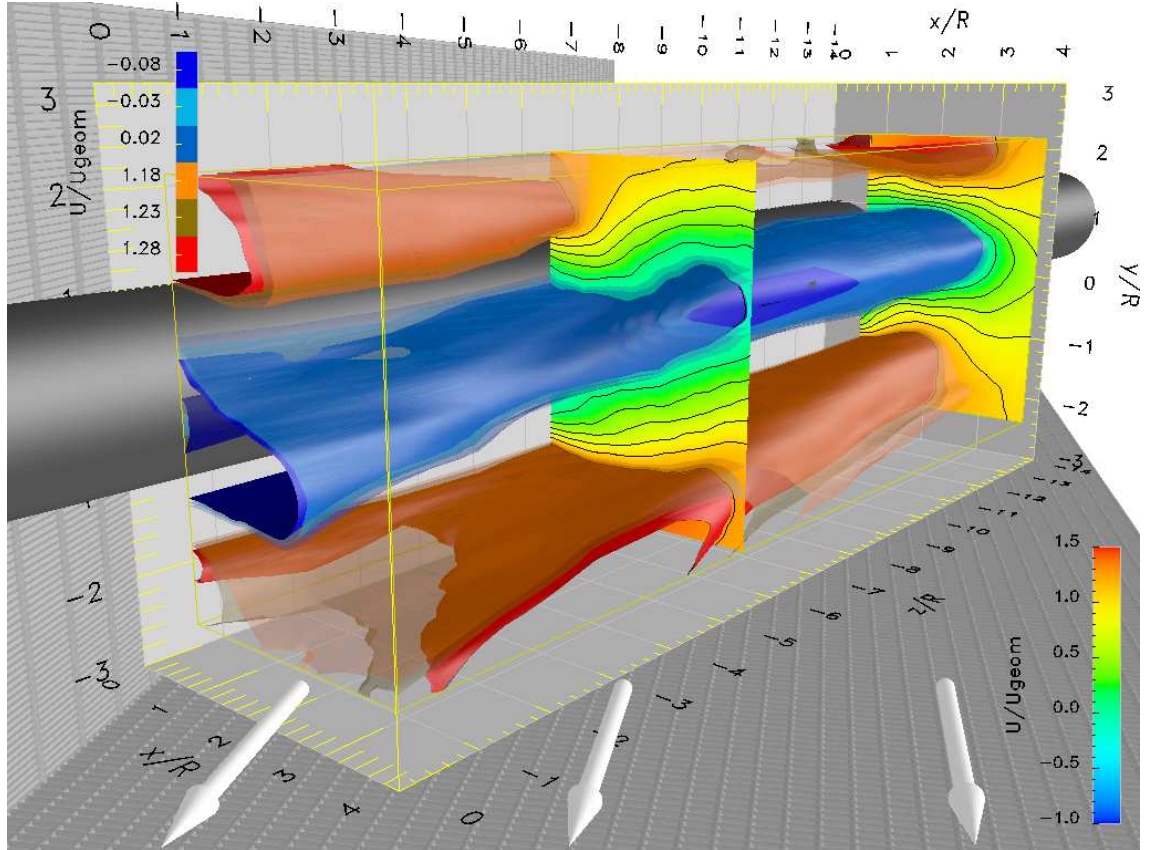


Fig. 4.178: $\frac{U}{U_\infty \cos \Lambda}$, POD $\phi = -40^\circ$, $\Lambda = 60^\circ$, baseline, $Re_n = 35000$

4.7.1.4 The Far Wake

Figures 4.179 and 4.180 present velocity data taken in the far wake behind the cylinder. The two left figures are scaled identically in both figures. The scaling of the right figure is optimized individually for best visualization. A large velocity deficit was found for both sweep-back angles at the downstream side of the cylinder (left side of figures 4.179 and 4.180 b & c). The velocity deficit is greatly reduced across the test section. Close to the opposite side wall (holding the cylinder upstream) two distinct additional minima can be observed in figure 4.179 and two weak ones in figure 4.180.

These minima were caused by the upstream necklace vortex that was prevented from attaching itself to the base of the cylinder and therefore extended close to the wall along the entire test section. In this location the necklace vortices were detected by the wake rake in its rightmost position. The necklace vortex is shed from the cylinder by the fence mounted at a distance of 1" (2.5cm) to the wall. The minimum distance of the wake rake to the side wall is 4" (10cm) and the distance between the rake and the upstream end of the cylinder is approximately 9' (2.75m). The increase in diameter of the disturbances by diffusion is therefore smaller than one degree. Low speed fluid is moved by the now streamwise vortices away from the wall, causing a significant velocity deficit. This has to be taken into account when comparing the disturbance at the wall with the maximum velocity deficit in the wake of the cylinder of only 15%. Actually, the presence of the velocity deficit at the wall can be considered to be a confirmation of the effectiveness of the boundary layer shedding fence at the upstream end of the cylinder.

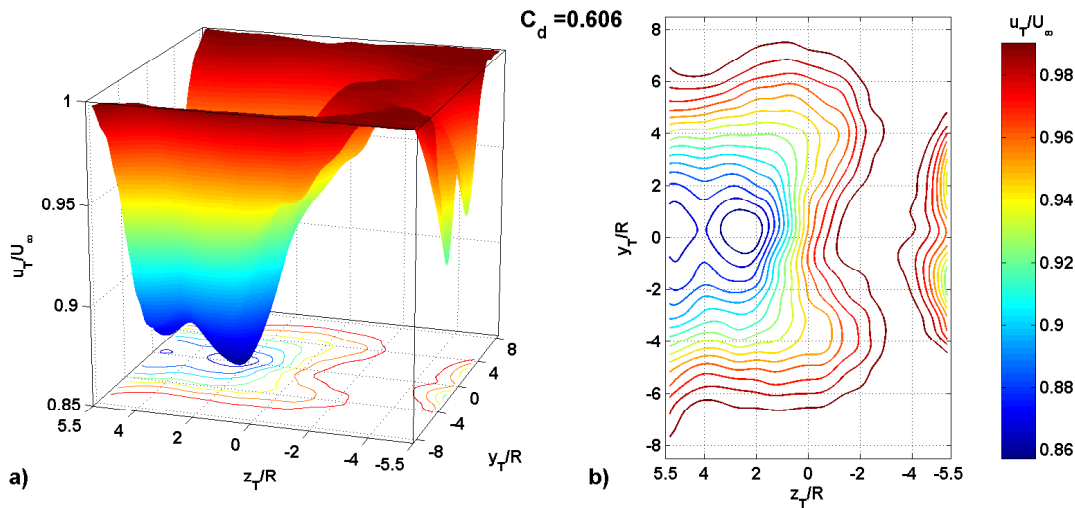


Fig. 4.179: Far wake, $\frac{U_T}{U_\infty}$, baseline, $\Lambda = 45^\circ$, $Re_n = 35000$

As can be seen in figure 4.180, the velocity deficit at the trailing edge of the cylinder remains close to its surface until it impinges in a skewed fashion on the tunnel wall and fans out significantly. Particularly in the $\Lambda = 60^\circ$ case neither the location nor the value of the velocity minimum can be detected properly.

This is due to the fact that within a certain range of Λ the vortices aft of the cylinder do not shed, but peel-off slowly from the cylinder. The larger the sweep angle, the stronger the convection of vorticity, diminishing the accumulation of vorticity. Therefore the vortices stay attached to the cylinder further along the span or even do not separate at all. Thus the velocity deficit found in the vortex cores is detected close to the downstream end of the cylinder and therefore close to the side wall.

As often is the case, the limitations of the setup concerning the minimum dimensions of the model and the dimensions of the test section forced a compromise in the model geometry with a length-to-diameter ratio of $\frac{L}{D} = 16$. Ideally this ratio should be several times larger, but this is almost impossible to achieve in combination with internal zero-mass-flux actuators. Therefore the length-to-diameter ratio is not sufficient to avoid considerable wall interference and to enable accurate measurements of C_d in the far wake in the infinite configuration. Thus the drag coefficient

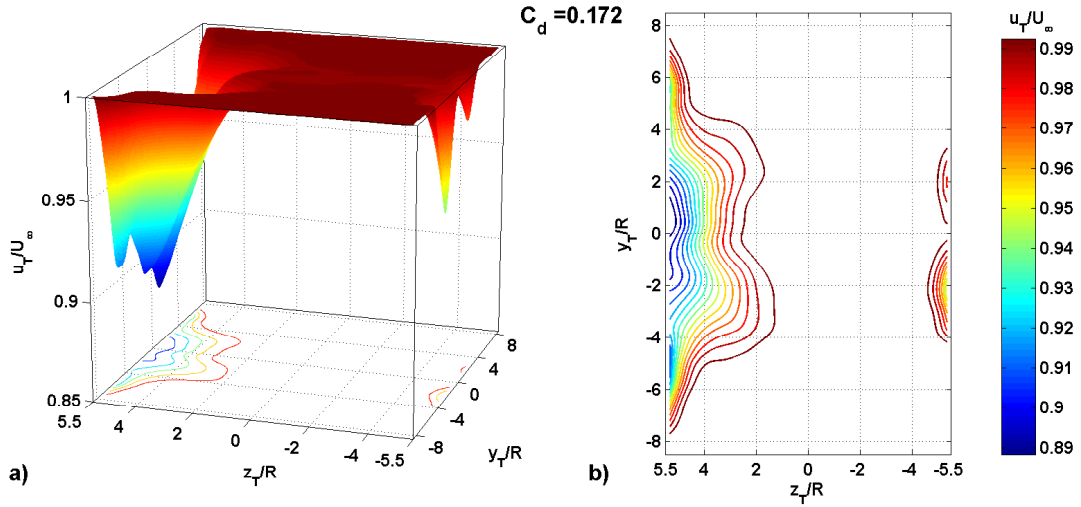


Fig. 4.180: Far wake, $\frac{U_T}{U_\infty}$, baseline, $\Lambda = 60^\circ$, $Re_n = 35000$

averaged across the entire examined area, $C_{d,avg} = 0.172$ $\Lambda = 60^\circ$, has to be considered inaccurate when compared to the form drag determined from the pressure distribution of $C_{dp} = 0.299$ (a difference of 40%).

The situation improves when the sweep-back angle is reduced to $\Lambda = 45^\circ$ (figure 4.179). Although the velocity deficit is still substantial at the left boundary of the investigated area, the location of the minima can be properly determined. Nevertheless the averaged drag coefficient $C_{d,avg} = 0.606$ can be seen only as approximation. The difference to C_{dp} is 20%. Interesting is the fact that at $\Lambda = 60^\circ$ two separate velocity minima can be found side-by-side for $z_T/R > 2$ (figure 4.180). For the smaller sweep-back angle of $\Lambda = 45^\circ$ a corresponding pair of velocity minima is located at $z_T/R = 0$. For $\Lambda = 45^\circ$ additional two minima exist close to $y_T/R = 0$. When comparing the overall shape of the two wakes it seems that in the $\Lambda = 60^\circ$ case the entire wake is shifted towards the wall by $2R$.

Measurements of the velocity deficit in the far wake of the inclined cylinder show a highly non-uniform distribution across the test section. Therefore the velocity deficit has to be integrated across the entire test section to get an approximation for the total drag. The aspect ratio of $\frac{L}{D} = 16$ would have to be increased significantly to avoid wall interference and ensure accurate measurements. This differs largely from the 2-D case where the measurement of the velocity deficit in the far wake at a single spanwise position and at a moderate aspect ratio enables accurate determination of the total drag.

4.7.2 The Finite Cylinder

The finite cylinder at $\Lambda = 60^\circ$ was investigated to determine the total drag of the inclined cylinder. A distance of 6" (152 mm) was obtained by pulling the model 12" (305 mm) out of the test section. An elliptical endplate was mounted on the downstream end of the cylinder extending from the cylinder 4" (100mm) in downstream direction. Changing the configuration moved the velocity minimum in the far wake to a sufficient distance to the wall. A valid approximation of the total drag was established. The relocation of the cylinder moved the row of pressure taps to a spanwise distance of 12" to the wall (6" perpendicular).

As the pressure distribution had to be measured at a different spanwise position, the comparison to the results for the infinite cylinder shown in figure 4.181 is not be representative for the change in configuration. A spanwise variation of strength as well as location of the vortices in lee of the cylinder would cause such considerable differences. An indicator for such a variation might be seen in the fact that the strongest vortices found in the volume investigated by PIV are the ones entering at the upstream end, close to the surface of the cylinder.

Based on the observed spanwise variation of the pressure distributions it has to be stated that several rows of pressure taps would have been necessary to obtain accurate information about

spanwise gradients. Due to the constructive constraints caused by the internal actuation this was not possible. The alternative of building a separate model for the investigation of the different baseline cases was not considered because this study focussed on the effects of active flow control instead the determination of reference baseline data.

The combination of PIV data taken in the near wake and surface pressure data taken at the single available row of pressure taps proved to be suitable to investigate and analyze the modifications of the base flow by active flow control in detail.

4.7.2.1 Forces on the Cylinder

The location of the pressure taps is well outside the volume that could have been investigated with PIV. Therefore it is not possible to verify assumptions about vortices in lee of the cylinder directly by flow field measurements. In figure 4.181 pressure distributions for the infinite and finite configurations are compared.

The pressure distribution taken in the finite case deviates significantly from data taken in the center plane of the test section. Especially the increase in pressure at $y/R = 0$ can be caused only by a pair of strong stationary vortices close to the cylinder. These vortices were identified in the infinite configuration and peeled-off in the investigated control volume (see figure 4.153). The stationary vortex pair causes a significant increase in vortex drag, resulting from a decrease in all pressures measured around the cylinder. The form drag in the finite case was increased to $C_{dp} = 0.336$ compared to $C_{dp} = 0.299$ for the infinite case, a difference of more than 10%.

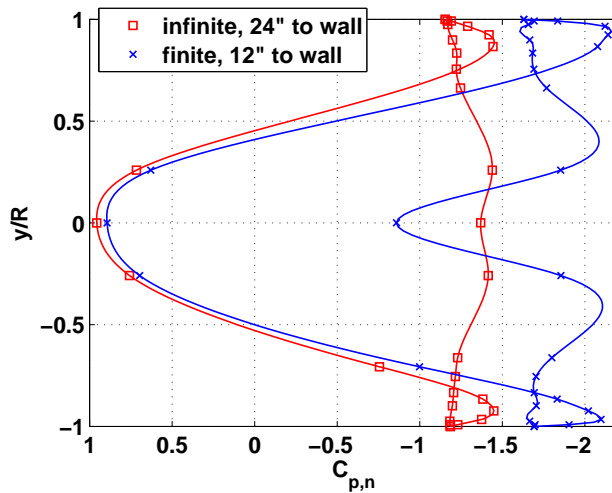


Fig. 4.181: y/R vs. $C_{p,n}$, baseline, $\Lambda = 60^\circ$, infinite & finite, $Re_n = 35000$

4.7.2.2 The Far Wake

The total drag determined from the velocity deficits ($C_d = 0.314$) in the far wake of the finite cylinder at $\Lambda = 60^\circ$ agrees well with the form drag computed from pressure distributions ($C_{dp} = 0.299$) for the infinite cylinder at the same sweep-back angle. The difference between both measurements is less than 2%. The extrema in the velocity deficit can be localized accurately in the finite configuration, as shown in figure 4.182. The values of the velocity deficit at the boundaries of the investigated area are sufficiently small so that a good approximation of the total drag can be obtained by averaging the velocity deficit over the cross section.

Interesting is the existence of two secondary minima at approximately $z_T/R = -3$. This illustrates clearly that the vortices peeling-off opposite sides of the cylinder remain separated along the span. The single central minimum in the velocity is caused by the endplate, causing the spanwise flow to separate from the cylinder at a defined spanwise location.

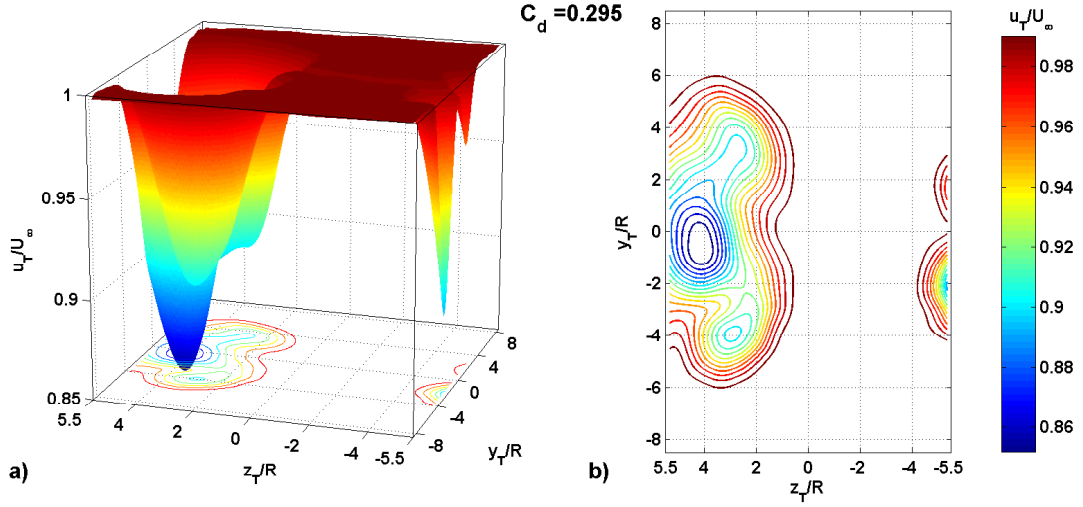


Fig. 4.182: Far wake, $\frac{U_T}{U_\infty}$, baseline, finite cylinder, $\Lambda = 60^\circ$, $Re_n = 35000$

4.8 Conclusions

This investigation shows that drag and lift on an inclined cylinder can be controlled proportionally to the level of excitation using oscillatory zero-mass-flux actuation. Lift can be generated by forcing asymmetrically from a single slot location and the total drag can be reduced efficiently by using two slots located symmetrically on the circumference of the cylinder. By applying a combination of both types of actuation with oscillatory jets emanating at different strengths from slots on opposing sides of the cylinder, these two forces can be, within limits, controlled independently of each other.

The coherent structures in the wake of the cylinder modify the pressure distribution around the body and thus affect the forces acting on it. In particular the large quasi-stationary spanwise vortices peeling off cylinders at large incidence ($\Lambda \leq 60^\circ$) are of interest for understanding the flow around inclined cylinders. Accumulated in these vortices is the vorticity generated in the boundary layers on the cylinder. Concurrently to the generation of vorticity the spanwise velocity component is reduced due to skin friction at the surface of the cylinder. Thus the vortex cores with maxima in vorticity can also be detected by minima of the spanwise velocity component, provided that the vortex was not stretched locally.

An acceleration in spanwise direction occurs in regions where fluid is entrained between two counter rotating vortices or between a large vortex and the cylinder itself. In these situations fluid is pulled in azimuthally by a vortex and then pushed forward in spanwise direction, either between two vortices or between the vortex and the surface of the cylinder. Stretching of a vortex occurs in a largely asymmetric configuration of the wake where a vortex on one side of the cylinder is pulled in between the opposing counter-rotating vortex and the cylinder itself. Such an asymmetric configuration of the flow is observed only for strong asymmetric forcing.

The spanwise vortices aft of an inclined cylinder at large incidence are not shed but rather slowly peel off its surface. In contrast to the situation described by Thomson & Morrison [29] and Zdravkovich [35], the vortices are quasi-stationary but unsteady. Their locations fluctuate by less than $R/2$ due to the meandering of the wake. This correlates with an oscillation of the spanwise velocity in the vortex cores. The resulting variations of the spanwise velocity in the absence of actuation are larger than $\pm 30\%$ of $U_\infty \sin \Lambda$. This observation is consistent with the wall pressure spectra presented by Snarski [25]. The fluctuations in the vortex cores are reduced when forcing is applied above a critical level. The meandering of the wake is reduced, including its spanwise variations.

Actuation below the critical level actually increased fluctuations and spanwise variations. This was observed in the three-dimensional pseudo-visualizations of PIV data as well as in the surface pressure data. It is due to only local reattachment of the flow, resulting in local asymmetries of the wake and large spanwise variations of the flow field. At such low levels of actuation the flow is

disturbed by the actuation and therefore the drag increases.

Based on the (local) form drag three different states of the flow were identified with respect to the actuation level. Below a first critical value of C_μ the flow is disturbed and the form drag increases. Beyond this first critical value the flow reattaches upstream of the slot and only small and shallow three-dimensional separation bubbles remain at the second critical value of C_μ and the flow is considered to be saturated. The gradient $\frac{dC_{dp}}{dC_\mu}$ is strongly negative in this region. Further increase of the excitation level reattaches the flow further downstream of the slot and mainly intensifies the pressure minima on the surface. The additional reduction of the form drag is small.

The vortices peeling off the cylinder greatly contribute to the total drag. The peel-off angle is increased by the excitation. Concurrently, the spanwise vortex peel-off frequency is increased with asymmetric as well as symmetric actuation and the size of the vortices separating in an alternating fashion from opposite sides of the cylinder is reduced. Thus the drag is not only diminished by active flow control but also redistributed along the span. The spanwise flow decreases according to the reduction of the drag.

The control of the forces acting on inclined cylinders and the ability to actively reduce their fluctuations and spanwise variations is of technical relevance not only for the application that initiated this investigation but also for configurations like landing gear struts, oil drilling rigs, pipelines and more.

A severe restriction of this project was the limited ratio of $\frac{L}{D}$. The model of an “infinite” cylinder is always impaired by end effects and a “finite” inclined cylinder is still affected by upstream flow conditions. The available $\frac{L}{D}$ proved to be sufficient for advancing the understanding of this flow. Nevertheless the quantitative results could be improved by increasing the length-to-diameter ratio.

4.9 Outlook and Potential Continuation

Not all questions of interest that emerged during this investigation were answered in detail. The experiments carried out on a cylinder swept-back at $\Lambda = 45^\circ$ were initially intended only as complement for comparison. As the dynamics in the wake at this angle are significantly different, it would be advisable to investigate this configuration with PIV in the near wake as well as in a cross section of the tunnel in the far wake. This would reveal the details of the dynamic peel-off process along the span of the cylinder.

PIV in the far wake of the cylinder with $\Lambda = 60^\circ$ could confirm assumptions concerning the dynamics at this sweep-back angle. In particular the complex flow structure close to the tip of the finite cylinder with its accumulation of individual vortices should be investigated more in detail. This could include the testing of different end pieces on the cylinder. A motorized traverse for the wake rake would be absolutely necessary for a more detailed analysis of the far wake. This should include sufficiently resolved measurements in the boundary layers on the side walls of the test section.

The effect of the slot location was extensively studied for asymmetric excitation and the results made a slot angle of $\Theta = \pm 110^\circ$ the natural choice for the study of symmetric actuation. Nevertheless, the investigation of additional azimuthal slot locations could confirm this decision.

Dynamic surface pressure measurement might improve the understanding of the dynamics in the wake in all configurations. Time resolved PIV would require a suitable light source for the available high-speed cameras, but it would greatly help to fully understand the processes in the near wake of the inclined cylinder.

A significantly increased $\frac{L}{D}$ would help to overcome the flaws of the model of an “infinite” inclined cylinder. This is problematic because a reduction of the diameter is not possible with the existing voice-coil based actuators and the maximal length of a cylinder holding these actuators is limited due to the necessary cabling. Individual cabling is required in this case to enable the fine-adjustment of the excitation system to ensure spanwise uniformity. A possible solution for this dilemma could be the use of compact fluidic actuators.

Last but not least the use of load cells would be advisable to enable direct measurements of the forces on the cylinder to eliminate inaccuracies due to spanwise variations of the flow.

List of Figures

1.1	The refuelling boom	2
2.1	Test section, side view	5
2.2	Geometry and coordinate systems, top view	6
2.3	Actuation slots	7
2.4	Finite cylinder with endplate	7
2.5	Internal beam	7
2.6	The swiveling cylinder	8
3.1	Calibration data	11
3.2	Transformation of C_p	12
3.3	PIV, $\frac{\Omega_z D}{U_\infty \cos \Lambda}$, baseline	15
3.4	PIV, $\frac{W}{U_\infty \sin \Lambda}$, baseline	16
3.5	PIV, $\frac{u'v'}{\sqrt{u'^2}\sqrt{v'^2}}$, baseline	16
3.6	Eigenflow	18
3.7	POD histogram	18
3.8	POD phases, baseline	20
3.9	PIV check, symmetric, $\frac{\dot{W}_{90^\circ} - \dot{W}_{4ph.}}{W_{4ph.}}$	21
3.10	PIV check, symmetric, $\frac{U_{90^\circ} - U_{4ph.}}{U_{4ph.}}$	22
3.11	PIV check, symmetric, $\frac{U_{90^\circ} - U_{4ph.}}{\max(U_{4ph.})}$	22
3.12	PIV check, symmetric, $\frac{V}{V_{max}}$	23
3.13	PIV check, symmetric, $\frac{W}{U_\infty \sin \Lambda}$, $F_n^+ = 1.52$, $C_{\mu,n} = 7\%$	23
3.14	PIV check, symmetric, $\frac{W}{U_\infty \sin \Lambda}$, $F_n^+ = 1.52$, $C_{\mu,n} = 7\%$	24
3.15	PIV check, symmetric, $\frac{W}{U_\infty \sin \Lambda}$, $F_n^+ = 1.52$, $C_{\mu,n} = 7\%$	24
4.1	Swiveling cylinder, $25m/s$	26
4.2	Swiveling cylinder, $100m/s$	27
4.3	Swiveling cylinder, yaw moment	27
4.4	Boundary layer shedding fence	28
4.5	Baseline, $C_{p,n}$, fence mis-aligned	28
4.6	Visualization, $\Lambda = 60^\circ$, $Re_n = 35000$	29
4.7	Visualization (detail), $\Lambda = 60^\circ$, $Re_n = 35000$	29
4.8	Visualization (detail), $\Lambda = 64^\circ$	30
4.9	Visualization (end effect), $\Lambda = 64^\circ$	30
4.10	Visualization, $\Lambda = 64^\circ$	30
4.11	2-D cylinder, C_l	31
4.12	2-D cylinder, C_{dp}	31
4.13	Asymmetric, C_l vs. $C_{\mu,n}$, $\Theta = 110^\circ$	32
4.14	Asymmetric, C_{dp} vs. $C_{\mu,n}$, $\Theta = 110^\circ$	32
4.15	Asymmetric, C_l , $\Theta = 105^\circ$	32
4.16	Asymmetric, C_l vs. $C_{\mu,n}$, $F_n^+ = 1.78$	33
4.17	Asymmetric, C_{dp} vs. $C_{\mu,n}$, $F_n^+ = 1.78$	33

4.18	Asymmetric, C_l , collapsed, $F_n^+ = 1.78$	34
4.19	Asymmetric, C_{dp} , collapsed, $F_n^+ = 1.78$	34
4.20	Asymmetric, $C_{p,n}$, 110° , baseline	35
4.21	Asymmetric, $C_{p,n}$, 110° , $C_{\mu,n} = 11\%$	35
4.22	Asymmetric, $C_{p,n}$, perpendicular, 110° , baseline	35
4.23	Asymmetric, $C_{p,n}$, perpendicular, 110° , $C_{\mu,n} = 11\%$	35
4.24	Asymmetric, $C_{p,n}$, 130° , $C_\mu = 1.0\%$	36
4.25	Asymmetric, $C_{p,n}$, 130° , $C_\mu = 2.75\%$	36
4.26	Asymmetric, $C_{p,n}$, perpendicular, 130° , $C_{\mu,n} = 4\%$	36
4.27	Asymmetric, $C_{p,n}$, perpendicular, 130° , $C_{\mu,n} = 11\%$	36
4.28	Correction for U_n	37
4.29	Asymmetric, C_l , $\Lambda = 45^\circ$	37
4.30	Asymmetric, C_{dp} , $\Lambda = 45^\circ$	37
4.31	Asymmetric, C_l vs. $C_{\mu,n}$, different Λ	38
4.32	Asymmetric, C_{dp} , different Λ	38
4.33	PIV, asymmetric, $\frac{\Omega_z D}{U_{\infty \cos \Lambda}}$ contours	40
4.34	PIV, asymmetric, $\frac{W}{U_{\infty \sin \Lambda}}$ contours	40
4.35	PIV, asymmetric, $\frac{U}{U_{\infty \cos \Lambda}}$ contours	40
4.36	PIV, asymmetric, $\frac{\Omega_z D}{U_{\infty \cos \Lambda}}$, 110°	42
4.37	PIV, asymmetric, $\frac{W}{U_{\infty \sin \Lambda}}$, 110°	42
4.38	PIV, asymmetric, $\frac{\Omega_z D}{U_{\infty \cos \Lambda}}$, 130° , $C_{\mu,n} = 4\%$	43
4.39	PIV, asymmetric, $\frac{U}{U_{\infty \cos \Lambda}}$, 130° , $C_{\mu,n} = 4\%$	43
4.40	PIV, asymmetric, $\frac{\Omega_z D}{U_{\infty \cos \Lambda}}$, 130° , $C_{\mu,n} = 11\%$	44
4.41	PIV, asymmetric, $\frac{U}{U_{\infty \cos \Lambda}}$, 130° , $C_{\mu,n} = 11\%$	44
4.42	PIV, asymmetric, k , 110°	46
4.43	PIV, asymmetric, k , 130°	46
4.44	PIV, asymmetric, $\frac{\Gamma_z}{U_{\infty \cos \Lambda R}}$, $\Theta = 110^\circ$	47
4.45	PIV, asymmetric, $\frac{\Gamma_z}{U_{\infty \cos \Lambda R}}$, $\Theta = 130^\circ$	47
4.46	PIV, asymmetric, x_c/R , $\Theta = 110^\circ$, $F_n^+ = 1.78$, $C_{\mu,n} = 11\%$	47
4.47	PIV, asymmetric, $\frac{U}{U_{\infty \cos \Lambda}}$, POD $\varphi = 0^\circ$, $\Theta = 110^\circ$	48
4.48	PIV, asymmetric, $\frac{U}{U_{\infty \cos \Lambda}}$, POD $\varphi = -40^\circ$, $\Theta = 110^\circ$	49
4.49	PIV, asymmetric, $\frac{U}{U_{\infty \cos \Lambda}}$, POD $\varphi = 40^\circ$, $\Theta = 110^\circ$	49
4.50	PIV, asymmetric, $\frac{\Omega_z D}{U_{\infty}}$, $\Theta = 110^\circ$, POD $\varphi = 0^\circ$	50
4.51	PIV, asymmetric, $\frac{\Omega_z D}{U_{\infty}}$, $\Theta = 110^\circ$, POD $\varphi = -40^\circ$	51
4.52	PIV, asymmetric, $\frac{\Omega_z D}{U_{\infty}}$, $\Theta = 110^\circ$, POD $\varphi = 40^\circ$	51
4.53	PIV, asymmetric, $\frac{\Omega_z D}{U_{\infty}}$, $\Theta = 130^\circ$, $C_{\mu,n} = 11\%$, POD $\varphi = -40^\circ$	53
4.54	PIV, asymmetric, $\frac{\Omega_z D}{U_{\infty}}$, $\Theta = 130^\circ$, $C_{\mu,n} = 11\%$, POD $\varphi = 0^\circ$	53
4.55	PIV, asymmetric, $\frac{\Omega_z D}{U_{\infty}}$, $\Theta = 130^\circ$, $C_{\mu,n} = 11\%$, POD $\varphi = 40^\circ$	54
4.56	PIV, asymmetric, $\frac{\Omega_z D}{U_{\infty}}$, $\Theta = 130^\circ$, $C_{\mu,n} = 4\%$, POD $\varphi = -40^\circ$	54
4.57	PIV, asymmetric, $\frac{\Omega_z D}{U_{\infty}}$, $\Theta = 130^\circ$, $C_{\mu,n} = 4\%$, POD $\varphi = 0^\circ$	55
4.58	PIV, asymmetric, $\frac{\Omega_z D}{U_{\infty}}$, $\Theta = 130^\circ$, $C_{\mu,n} = 4\%$, POD $\varphi = 40^\circ$	55
4.59	PIV, asymmetric, streamlines, $\Theta = 130^\circ$, $C_{\mu,n} = 11\%$, POD $\varphi = 0^\circ$	56
4.60	PIV, asymmetric, streamlines, $\Theta = 130^\circ$, $C_{\mu,n} = 11\%$, POD $\varphi = 40^\circ$	56
4.61	PIV, asymmetric, center of $\Omega_z < 0$, $F_n^+ = 1.78$, $C_{\mu,n} = 11\%$	57
4.62	PIV, asymmetric, center of $\Omega_z > 0$, $F_n^+ = 1.78$, $C_{\mu,n} = 11\%$	57
4.63	Far wake, asym., $\frac{U_T}{U_{\infty}}$, $\Theta = 110^\circ$, baseline	59
4.64	Far wake, asym., $\frac{U_T}{U_{\infty}}$, $\Theta = 110^\circ$, $C_{\mu,n} = 2\%$	59
4.65	Far wake, asym., $\frac{U_T}{U_{\infty}}$, $\Theta = 110^\circ$, $C_{\mu,n} = 4\%$	60
4.66	Far wake, asym., $\frac{U_T}{U_{\infty}}$, $\Theta = 110^\circ$, $C_{\mu,n} = 11\%$	60
4.67	Far wake, asym., $\frac{U_T}{U_{\infty}}$, $\Theta = 130^\circ$, $C_{\mu,n} = 4\%$	61
4.68	Far wake, asym., $\frac{U_T}{U_{\infty}}$, $\Theta = 130^\circ$, $C_{\mu,n} = 11\%$	61

4.69	Far wake, asym., $\frac{U_T}{U_\infty}$, $\Theta = 110^\circ$, $\Lambda = 45^\circ$, baseline	62
4.70	Far wake, asym., $\frac{U_T}{U_\infty}$, $\Theta = 110^\circ$, $\Lambda = 45^\circ$, $C_{\mu,n} = 4\%$	63
4.71	Far wake, asym., $\frac{U_T}{U_\infty}$, $\Theta = 110^\circ$, $\Lambda = 45^\circ$, $C_{\mu,n} = 11\%$	63
4.72	Far wake, $\frac{U_T}{U_\infty}$, $\Theta = 110^\circ$, $\Lambda = 45^\circ$, C_d	64
4.73	Vortex spacing	64
4.74	Vortex location, baseline, finite-infinite	65
4.75	Vortex location, asymmetric, finite-infinite	66
4.76	Asymmetric, Ω_z , $z/R = -5.3$ (finite)	66
4.77	Asymmetric, Ω_z , $z/R = -12.0$ (infinite)	66
4.78	C_l , finite-infinite	67
4.79	C_{dp} , finite-infinite	67
4.80	Far wake, asym., $\frac{U_T}{U_\infty}$, $\Theta = 110^\circ$, baseline, finite	68
4.81	Far wake, asym., $\frac{U_T}{U_\infty}$, $\Theta = 110^\circ$, $C_{\mu,n} = 2\%$, finite	68
4.82	Far wake, asym., $\frac{U_T}{U_\infty}$, $\Theta = 110^\circ$, $C_{\mu,n} = 4\%$, finite	68
4.83	Far wake, asym., $\frac{U_T}{U_\infty}$, $\Theta = 110^\circ$, $C_{\mu,n} = 6\%$, finite	69
4.84	Far wake, asym., $\frac{U_T}{U_\infty}$, $\Theta = 110^\circ$, $C_{\mu,n} = 11\%$, finite	69
4.85	Far wake, asym., C_d & C_{dp} , finite & infinite	70
4.86	Far wake, asym., averaged C_l , finite & infinite	70
4.87	Symmetric, C_p , baseline	70
4.88	Symmetric, C_p , axial blowing	70
4.89	Symmetric, C_p vs. x/R , $C_{\mu,n} = 7\%$	71
4.90	Symmetric, y/R vs. C_p , $C_{\mu,n} = 7\%$	71
4.91	Symmetric, C_l vs. $C_{\mu,n}$	72
4.92	Symmetric, C_{dp} vs. $C_{\mu,n}$	72
4.93	Symmetric, C_l vs. $C_{\mu,n}$, $Re_n = 47000$	72
4.94	Symmetric, C_{dp} vs. $C_{\mu,n}$, $Re_n = 47000$	72
4.95	Symmetric, C_l vs. $C_{\mu,n}$, $\Lambda = 45^\circ$	73
4.96	Symmetric, C_{dp} vs. $C_{\mu,n}$, $\Lambda = 45^\circ$	73
4.97	PIV, symmetric, $\frac{W}{U_\infty \sin \Lambda}$, $F_n^+ = 1.78$, $C_{\mu,n} = 3\%$	74
4.98	PIV, symmetric, $\frac{W}{U_\infty \sin \Lambda}$, $F_n^+ = 1.52$, $C_{\mu,n} = 4\%$	75
4.99	PIV, symmetric, $\frac{W}{U_\infty \sin \Lambda}$, $F_n^+ = 2.29$, $C_{\mu,n} = 4\%$	75
4.100	PIV, symmetric, $\frac{W}{U_\infty \sin \Lambda}$, $F_n^+ = 1.52$, $C_{\mu,n} = 7\%$	76
4.101	PIV, symmetric, $\frac{W}{U_\infty \sin \Lambda}$, $F_n^+ = 1.78$, $C_{\mu,n} = 11\%$	76
4.102	PIV, symmetric, $\frac{\Omega_z D}{U_\infty \cos \Lambda}$, $F_n^+ = 1.78$, $C_{\mu,n} = 11\%$	77
4.103	PIV, symmetric, streamlines, $F_n^+ = 1.78$, $C_{\mu,n} = 3\%$	78
4.104	PIV, symmetric, streamlines, $F_n^+ = 1.78$, $C_{\mu,n} = 4\%$	78
4.105	PIV, symmetric, streamlines, $F_n^+ = 1.78$, $C_{\mu,n} = 11\%$	79
4.106	PIV, $\frac{u'^2 + v'^2 + w'^2}{U_\infty^2}$, baseline	80
4.107	PIV, symmetric, $\frac{u'^2 + v'^2 + w'^2}{U_\infty^2}$, $F_n^+ = 1.78$, $C_{\mu,n} = 3\%$	80
4.108	PIV, symmetric, $\frac{u'^2 + v'^2 + w'^2}{U_\infty^2}$, $F_n^+ = 1.78$, $C_{\mu,n} = 4\%$	81
4.109	PIV, symmetric, $\frac{u'^2 + v'^2 + w'^2}{U_\infty^2}$, $F_n^+ = 1.78$, $C_{\mu,n} = 7\%$	82
4.110	PIV, symmetric, center of $\Omega_z < 0$, $F_n^+ = 1.78$, $C_{\mu,n} = 3\%$	82
4.111	PIV, symmetric, center of $\Omega_z < 0$, $F_n^+ = 1.78$, $C_{\mu,n} = 4\%$	83
4.112	PIV, symmetric, center of $\Omega_z < 0$, $F_n^+ = 1.78$, $C_{\mu,n} = 7\%$	83
4.113	Far wake, symmetric, baseline	83
4.114	Far wake, symmetric, $C_{\mu,n} = 2\%$	84
4.115	Far wake, symmetric, $C_{\mu,n} = 4\%$	84
4.116	Far wake, symmetric, $C_{\mu,n} = 7\%$	84
4.117	Far wake, symmetric, C_d	85
4.118	Far wake, symmetric, far wake, $\Lambda = 45^\circ$, baseline	86
4.119	Far wake, symmetric, far wake, $\Lambda = 45^\circ$, $C_{\mu,n} = 1\%$	86

4.120	Far wake, symmetric, $\Lambda = 45^\circ$, $C_{\mu,n} = 2\%$	86
4.121	Far wake, symmetric, $\Lambda = 45^\circ$, $C_{\mu,n} = 3\%$	87
4.122	Far wake, symmetric, C_d , $\Lambda = 45^\circ$	87
4.123	Symmetric, vortex spacing	88
4.124	Symmetric, y/R vs. $C_{p,n}$, finite, baseline	88
4.125	Symmetric, y/R vs. $C_{p,n}$, finite, $F_n^+ = 1.78$, $C_{\mu,n} = 11\%$	88
4.126	Far wake, symmetric, baseline	89
4.127	Far wake, symmetric, finite, $C_{\mu,n} = 2\%$	90
4.128	Far wake, symmetric, finite, $C_{\mu,n} = 4\%$	90
4.129	Far wake, symmetric, finite, $C_{\mu,n} = 7\%$	90
4.130	Far wake, symmetric, finite, C_d	91
4.131	Asymmetric, $C_{p,n}$ vs. x/D , both slots open	92
4.132	Asymmetric, $C_{p,n}$ vs. x/D , inactive slot taped	92
4.133	Symmetric, $\delta = 90^\circ$, C_l vs. $C_{\mu,n}$	93
4.134	Symmetric, $\delta = 90^\circ$, C_{dp} vs. $C_{\mu,n}$	93
4.135	Symmetric, $\delta = 90^\circ$, C_l vs. $C_{\mu,n}$	93
4.136	Symmetric, $\delta = 180^\circ$, C_{dp} vs. $C_{\mu,n}$	93
4.137	Bi-frequent, $C_{p,n}$ vs. x/D	94
4.138	Bi-frequent, y/R vs. $C_{p,n}$, $C_{\mu,n} = 7\%$	94
4.139	PIV, bi-frequent, $\frac{\Omega_z D}{U_\infty \cos \Lambda}$, $C_{\mu,n} = 7\%$	95
4.140	PIV, bi-frequent, $\frac{\Omega_z D}{U_\infty \cos \Lambda}$, $C_{\mu,n} = 7\%$	95
4.141	Baseline, C_p vs. x/D , $\Lambda = 45^\circ$	97
4.142	Baseline, C_p vs. x/D , $\Lambda = 60^\circ$	97
4.143	Baseline, y/R vs. C_p , $\Lambda = 45^\circ$	97
4.144	Baseline, y/R vs. C_p , $\Lambda = 60^\circ$	97
4.145	Baseline, $C_{p,n}$ vs. x/D , $\Lambda = 45^\circ$	98
4.146	Baseline, $C_{p,n}$ vs. x/D , $\Lambda = 60^\circ$	98
4.147	Baseline, y/R vs. $C_{p,n}$, $\Lambda = 45^\circ$	98
4.148	Baseline, y/R vs. $C_{p,n}$, $\Lambda = 60^\circ$	98
4.149	2-D baseline C_p vs. x/D	99
4.150	Baseline, y/R vs. $C_{p,n}$, $\Lambda = 0^\circ, 45^\circ \& 60^\circ$	99
4.151	Spectrum, $\Lambda = 45^\circ$	99
4.152	Potential flow	99
4.153	PIV, baseline, $\frac{\Omega_z D}{U_\infty \cos \Lambda}$ and $\frac{W}{U_\infty \sin \Lambda}$	100
4.154	PIV, baseline, $\frac{u'v'}{\sqrt{u'^2}\sqrt{v'^2}}$ and $\frac{W}{U_\infty \sin \Lambda}$	101
4.155	PIV, baseline, $\frac{\Omega_z D}{U_\infty \cos \Lambda}$, top view	102
4.156	PIV, baseline, $\frac{W}{U_\infty \sin \Lambda}$, top view	102
4.157	PIV, baseline, streamlines	103
4.158	PIV, baseline, $\frac{\Gamma_z}{U_\infty \cos \Lambda R}$	104
4.159	PIV, baseline, $\frac{\dot{V}_z}{A_{xy} U_\infty}$, average	104
4.160	PIV, baseline, center of Ω_z , X coordinate	104
4.161	PIV, baseline, center of Ω_z , Y coordinate	104
4.162	PIV, baseline, $\frac{w'_{top} w'_{bottom}}{\sqrt{w'^2_{top}} \sqrt{w'^2_{bottom}}}$	105
4.163	PIV, baseline, POD Eigenvalues	106
4.164	PIV, baseline, sum of POD Eigenvalues	106
4.165	PIV, baseline, POD $\phi = -40^\circ$	106
4.166	PIV, baseline, POD $\phi = 0^\circ$	107
4.167	PIV, baseline, POD $\phi = 40^\circ$	107
4.168	PIV, baseline, POD $\phi = -40^\circ$, top view	109
4.169	PIV, baseline, POD $\phi = 0^\circ$, top view	109
4.170	PIV, baseline, POD $\phi = 40^\circ$, top view	109
4.171	PIV, baseline, $\frac{\Gamma_{z,top}}{U_\infty \cos \Lambda R}$ vs. z/R	110

4.172	PIV, baseline, $\frac{\Gamma_{z,bottom}}{U_{\infty} \cos \Lambda R}$ vs. z/R	110
4.173	PIV, baseline, $\frac{\Gamma_{z,total}}{U_{\infty} \cos \Lambda R}$ vs. z/R	110
4.174	PIV, baseline, $\frac{\Gamma_{z,diff}}{U_{\infty} \cos \Lambda R}$ vs. z/R	110
4.175	PIV, baseline, $\frac{\dot{V}_z}{A_{xy} U_{\infty}}$ vs. z/R	110
4.176	PIV, baseline, $\frac{V_{z,top}}{A_{xy} U_{\infty}}$ vs. z/R	110
4.177	PIV, baseline, center of Ω_z	111
4.178	PIV, baseline, $\frac{U}{U_{\infty} \cos \Lambda}$, POD $\phi = -40^\circ$	111
4.179	Far wake, baseline, $\frac{U_T}{U_{\infty}}$, $\Lambda = 45^\circ$	112
4.180	Far wake, baseline, $\frac{U_T}{U_{\infty}}$, $\Lambda = 60^\circ$	113
4.181	Baseline, y/R vs. $C_{p,n}$, infinite & finite, $\Lambda = 60^\circ$	114
4.182	Far wake, baseline, $\frac{U_T}{U_{\infty}}$, finite	115

Bibliography

- [1] M. A. Bennington and K. D. Visser. Aerial refueling implications for commercial aircraft. *J. of Aircraft*, 42:366–375, 2005.
- [2] J.-C. Bera, M. Michard, M. Sunyach, and G. Compte-Bellot. Changing lift and drag by jet oscillation: Experiments on a circular cylinder with turbulent separation. *European. J. of Mechanics B-Fluids*, 19:575–595, 2000.
- [3] J. E. Bernhardt and D. R. Williams. Closed-loop control of forebody flow asymmetry. *33rd AIAA Aerospace Sciences Meeting and Exhibit*, AIAA-95-0651, 1995.
- [4] J. E. Bernhardt and D. R. Williams. Proportional control of asymmetric forebody vortices. *AIAA Journal*, 36:2087–2093, 1998.
- [5] http://commons.wikimedia.org/wiki/File:Boeing_KC-135Q_refueling_SR-71.JPG, source: http://www.dodmedia.osd.mil/Assets/1983/Air_Force/DF-ST-83-07614.JPG, public domain.
- [6] M. Brede, H. Eckelmann, and Rockwell D. On secondary vortices in the cylinder wake. *Physics of Fluids*, 8:2117–2124, 1996.
- [7] J. Carberry, J. Sheridan, and D. Rockwell. Controlled oscillations of a cylinder: Forces and wake modes. *J. Fluid Mech.*, 538:31–69, 2005.
- [8] D. Degani. Instabilities of flows over bodies at large incidence. *AIAA Journal*, 30:94–100, 1992.
- [9] L. E. Ericsson. Forebody flow control of conditions of naturally occurring separation asymmetry. *J. of Aircraft*, 39:252–261, 2002.
- [10] U. Fey, M. Koenig, and Eckelmann H. A new strouhal-reynolds-number relationship for the circular cylinder in the range $47 < \text{Re} < 2 \times 10^5$. *Physics of Fluids*, 10:1547–1549, 1998.
- [11] N. T. Hoang, O. k. Rediniotis, and D. P. Telionis. Symmetric and asymmetric separation patterns over a hemisphere cylinder at low Reynolds numbers and high incidences. *J. of Fluids and Structures*, 11:793–817, 1977.
- [12] Ideal Flow Machine: <http://www.aoe.vt.edu/devenpor/aoe5104/ifm/ifminfo.html>.
- [13] T. Igarashi. Effect of tripping on the flow around a circular cylinder normal to an airstream. *Bulletin of JSME*, 29:2917–2924, 1986.
- [14] Y. Kim and D. Rockwell. Vortex buffeting of aircraft tail, interpretation via proper orthogonal decomposition. *AIAA Journal*, 43:550–559, 2005.
- [15] R. King. Vortex excited oscillations of yawed circular cylinders. *J. of Fluids Engineering*, pages 495–501, 1977.
- [16] G. V. Lachmann. *Boundary Layer and Flow Control, Vol. 1 and 2*. Pergamon Press Inc., New York, N. Y., 1961.

- [17] J.-C. Lin, J. Towfighi, and D. Rockwell. Near wake of a circular cylinder: Control by steady and unsteady surface injection. *J. of Fluid and Structures*, 9:659–669, 1995.
- [18] S. Margalit, D. Greenblatt, A. Seifert, and I. Wygnanski. Delta wing stall and roll control using segmented piezoelectric fluidic actuators. *J. of Aircraft*, 42:698–709, 2005.
- [19] J. S. Marshall. Wake dynamics of a yawed cylinder. *J. of Fluid Engineering*, 125:97–103, 2003.
- [20] T. Naveh, A. Seifert, A. Tumin, and I. Wygnanski. Sweep effect on parameters governing control of separation by periodic excitation. *J. of Aircraft*, 35:510–512, 1998.
- [21] B. R. Noack, M. Koenig, and H. Eckelmann. Three-dimensional stability analysis of the periodic flow around a circular cylinder. *Physics of Fluids A*, 5:1279–1281, 1993.
- [22] W. H. Press, B. P. Flannery, S. A. Teukolsky, and W. T. Vetterling. *Numerical Recipes in C: The Art of Scientific Computing*. Cambridge University Press, Cambridge, second edition, 1992.
- [23] A. Roshko. On the drag and shedding frequency of two-dimensional bluff bodies. *NACA Technical Note*, 3169, 1954.
- [24] H. Schlichting. *Boundary Layer Theory*. McGraw-Hill, New York, N. Y., 6th edition edition, 1968.
- [25] S. R. Snarski. Flow over yawed circular cylinders: Wall pressure spectra and flow regimes. *Phys. Fluids*, 16:344–359, 2004.
- [26] L. Taubert, P. Kjellgren, and I. Wygnanski. Generic bluff bodies with undetermined separation location. *1st AIAA Flow Control Meeting*, AIAA-2002-3068, 2002.
- [27] L. Taubert and I. Wygnanski. Control of vortex shedding from a cylinder at different sweep back angles. *2nd AIAA Flow Control Meeting*, AIAA-2004-2511, 2004.
- [28] M. C. Thompson and K. Hourigan. The shear layer instability of a circular cylinder wake. *Phys. Fluids*, 17:1–4, 2005.
- [29] K. D. Thomson and D. F. Morrison. The spacing, position and strength of vortices in the wake of slender cylindrical bodies at large incidence. *J. Fluid Mech.*, 50:751–783, 1971.
- [30] H. W. The ONERA water tunnel test possibilities for flow visualization in aeronautical and naval domains. *AGARD CP 413 Mémoire*, 14, 1986.
- [31] A. B. Wardlaw and W. J. Yanta. Multistable vortex patterns an slender, circular bodies at high incidence. *AIAA Journal*, 20:509–515, 1982.
- [32] D. R. Williams and H. Papazian. Forebody vortex control with the unsteady bleed technique. *AIAA Journal*, pages 853–855, 1991.
- [33] C.H.K. Williamson. Vortex dynamics in the cylinder wake. *Annu. Rev. Fluid. Mech.*, 28:477–539, 1996.
- [34] J-Z. Wu, H-Y. Ma, and M-D. Zhou. *Vorticity and Vortex Dynamics*. Springer-Verlag, Berlin, 2006.
- [35] M. M. Zdravkovich. *Flow Around Circular Cylinders, Vol. 1 and 2*. Oxford University Press, Oxford, 1997.